Cooperative Functional Behavior in Stacked Multimetallic Porphyrin Complexes

Zur Erlangung des akademischen Grades eines

DOKTORS DER NATURWISSENSCHAFTEN

(Dr. rer. nat.)

von der KIT-Fakultät für Chemie und Biowissenschaften

des Karlsruher Instituts für Technologie (KIT)

genehmigte

DISSERTATION

von

M. Sc. Michael Rotter

aus Bietigheim-Bissingen

Dekan: Prof. Dr. Martin Bastmeyer

Referent: Prof. Dr. Stefan Bräse

Korreferent: Prof. Dr. Claudia Bizzarri

Tag der mündlichen Prüfung: 18.07.2025

Declaration of Honesty

This work was carried out from June 2022 through June 2025 at the Institute of Organic Chemistry, Faculty of Chemistry and Biosciences at the Karlsruher Institute of Technology (KIT) under the supervision of Prof. Dr. Stefan Bräse.

Die vorliegende Arbeit wurde im Zeitraum von Juni 2022 bis Juni 2025 am Institut für Organische Chemie, Fakultät für Chemie und Biowissenschaften des Karlsruher Instituts für Technologie (KIT) unter der Leitung von Prof. Dr. Stefan Bräse durchgeführt.

Hereby I, MICHAEL ROTTER, declare that I completed this work independently, without any improper help and that all material published by others is cited properly. This thesis has not been submitted to any other university before.

Hiermit erkläre ich, MICHAEL ROTTER*, dass ich diese Arbeit selbstständig, ohne unzulässige Hilfe, angefertigt und alle fremden Quellen ordnungsgemäß zitiert habe. Diese Arbeit wurde bisher an keiner anderen Universität eingereicht.*

Karlsruhe, June 4th, 2025

German Title of the Thesis

Kooperatives Funktionelles Verhalten in Gestapelten Multimetallischen Porphyrin Komplexen

Table of Contents

Abstract

The porphyrin molecular scaffold offers a highly adaptable ligand system with broad functional versatility, fulfilling the key requirements for the design and synthesis of tailor-made multimetallic complexes. Their modular synthesis allows for precisely constructing heterobimetallic active site analogs that mimic enzymatic environments. Dimeric porphyrins, in particular, are ideal for modeling the cooperative magnetic, catalytic, and optical behaviors of closely situated metal centers. Such synthetic analogs serve as valuable models for probing the fundamental principles of metal–metal cooperation, thereby advancing our understanding of functional systems and informing the development of next-generation platforms. This work synthesizes and evaluates a porphyrin dimer designed to position nickel and iron centers in close spatial proximity. An optimized synthetic route was developed to produce ortho-phenylene-linked porphyrin dimers with improved yields, along with a more efficient metalation strategy enabling the rapid formation of heterobimetallic complexes. Electrochemical analysis using cyclic voltammetry revealed distinct redox profiles for each of the two metal centers in the heterobimetallic porphyrin dimer. Photocatalytic experiments demonstrated a marked performance improvement compared to both homobimetallic and monomeric reference compounds, with the heterobimetallic complex achieving a turnover number of up to 2060 for carbon monoxide production and a selectivity of 97%. These findings strongly indicate a cooperative effect between the nickel and iron centers, made possible by their close spatial arrangement within the co-facial dimeric framework. Density functional theory (DFT) calculations further support the emergence of a high-spin state, arising from antiferromagnetic coupling between the individual metal centers, offering deeper insight into the electronic structure of the complex. Furthermore, this work consists of a series of ortho-linked palladium (II) porphyrin complexes capable of generating singlet oxygen upon photoexcitation. The luminescence emission profiles of these compounds display a non-linear relationship with reactive oxygen species (ROS) production, suggesting cooperative interactions between co-facially arranged Pd (II) centers. Comprehensive photophysical characterization using UV-Vis spectroscopy provided further insight into their light-activated properties and a range of biological assays, including MTT viability assays, cellular permeability measurements, intracellular ROS detection, and in vitro evaluations of both dark cytotoxicity and light-induced phototoxicity showed consistent trends in ROS production and confirmed superior biocompatibility and photoinduced cytotoxicity.

Kurzzusammenfassung

Das Porphyrin-Molekülgerüst bietet ein äußerst anpassungsfähiges Ligandensystem mit breiter funktioneller Vielseitigkeit, das die wichtigsten Anforderungen für die Entwicklung und Synthese maßgeschneiderter multimetallischer Komplexe erfüllt. Porphyrine sind hochgradig anpassungsfähige Liganden, die ein breites Spektrum von Metallionen koordinieren können, ohne dass ihre Kernstruktur verändert werden muss. Diese Arbeit befasst sich mit der Synthese und Bewertung eines Porphyrindimers, bei dem Nickel- und Eisenzentren in unmittelbarer räumlicher Nähe zueinander angeordnet sind. Es wurde ein optimierter Syntheseweg entwickelt, um ortho-Phenylen-verknüpfte Porphyrin-Dimere mit verbesserter Ausbeute herzustellen, sowie eine effizientere Metall-Koordination, die die schnelle Bildung heterobimetallischer Komplexe ermöglicht. Die elektrochemische Analyse mittels zyklischer Voltammetrie ergab unterschiedliche Redox-Profile für jedes der beiden Metallzentren im heterobimetallischen Porphyrin-Dimer. Photokatalytische Experimente zeigten eine deutliche Leistungsverbesserung im Vergleich zu homobimetallischen und monomeren Referenzverbindungen, wobei der heterobimetallische Komplex eine Umsatzzahl von bis zu 2060 für die Kohlenmonoxidproduktion und eine Selektivität von 97 % erreichte. Diese Ergebnisse deuten stark auf einen kooperativen Effekt zwischen den Nickel- und Eisenzentren hin, der durch ihre enge räumliche Anordnung innerhalb des ko-fazialen dimeren Gerüsts ermöglicht wird. Berechnungen der Dichtefunktionaltheorie (DFT) belegen außerdem die Entstehung eines High-Spin-Zustands, der durch antiferromagnetische Kopplung zwischen den einzelnen Metallzentren entsteht und einen tieferen Einblick in die elektronische Struktur des Komplexes ermöglicht. Darüber hinaus besteht diese Arbeit aus einer Reihe von ortho-verknüpften Palladium (II)-Porphyrin-Komplexen, die bei Photoanregung Singulett-Sauerstoff erzeugen können. Die Lumineszenz-Emissionsprofile dieser Verbindungen zeigen eine nichtlineare Beziehung zur Produktion reaktiver Sauerstoffspezies (ROS), was auf kooperative Wechselwirkungen zwischen ko-fazial angeordneten Pd (II)-Zentren schließen lässt. Eine umfassende photophysikalische Charakterisierung mittels UV-Vis-Spektroskopie lieferte weitere Einblicke in ihre lichtaktivierten Eigenschaften, und eine Reihe biologischer Tests, darunter MTT-Lebensfähigkeitstests, Messungen der zellulären Permeabilität, intrazelluläre ROS-Detektion und In-vitro-Bewertungen sowohl der Zytotoxizität im Dunkeln als auch der lichtinduzierten Phototoxizität, zeigten konsistente Trends bei der ROS-Produktion und bestätigten eine hervorragende Biokompatibilität und photoinduzierte Zytotoxizität.

1 Introduction

Climate change represents one of the most pressing global challenges of the current century, with profound implications for public health.[1-3] The accelerating rise in atmospheric carbon dioxide (CO_2) levels is a crucial factor driving global climate change.[4] Human activities such as widespread deforestation, the burning of fossil fuels, and large-scale industrial operations are major contributors to this increase in CO_2 concentrations.[5-7] As a consequence, global temperatures are rising, leading to significant threats for both ecosystems and human life.[8, 9] These impacts are evident in the growing frequency and severity of extreme weather events, the acidification of oceans, and widespread ecological disturbances.[10-13] Among its numerous health impacts, the potential influence of climate change on cancer incidence, progression, and treatment has garnered increasing scientific attention.[14, 15] While cancer has traditionally been viewed through the lens of genetic, lifestyle, and direct environmental exposures, emerging evidence suggests that broader climatic and ecological changes may act as upstream determinants of cancer risk and burden.[16-19] Fine particulate matter, volatile organic compounds, and polycyclic aromatic hydrocarbons, many of which are products of fossil fuel combustion and wildfires, are exacerbated by climate change and are established risk factors for various cancers, including lung and bladder cancer.[20-22] Furthermore, disruptions to food and water safety, driven by changing environmental conditions, may increase exposure to contaminants such as aflatoxins, heavy metals, and endocrine-disrupting chemicals, further contributing to cancer risk.[23-26]

To mitigate the effects of climate change, not only must CO_2 emissions be reduced, but existing atmospheric CO_2 must also be captured and transformed into less harmful or even useful products.[27, 28] This has led to intense focus on carbon capture, utilization, and storage.[29-31] Within this framework, CO_2 reduction catalysts are key enablers of carbon utilization, transforming CO_2 into fuels and chemicals through electrochemical or photocatalytic processes.[32, 33] Photodynamic therapy (PDT) has emerged as a highly promising modality in cancer research, offering a selective, minimally invasive, and multifaceted approach to tumor eradication.[34-36] By leveraging the precise activation of photosensitizers with light, PDT induces localized oxidative damage that can directly kill cancer cells, disrupt tumor vasculature, and stimulate anti-tumor immune responses. Unlike conventional therapies, PDT bypasses many resistance mechanisms and causes minimal systemic toxicity, making it an attractive option for treating resistant or recurrent cancers.[37-39]

Tetrapyrrolic macrocycles, such as porphyrins and their derivatives, are fundamental to a wide array of biological processes due to their unique ability to coordinate metal centers.[40-42] These metal–macrocycle complexes enable essential functions including reversible oxygen binding, electron transfer, and redox catalysis. In hemoglobin and myoglobin, for instance, iron-coordinated protoporphyrin IX facilitates oxygen transport and storage, critical to cellular respiration and energy production in aerobic organisms.[43] Beyond oxygen binding, porphyrin cofactors participate directly in electron transport chains. Cytochrome c, a heme-containing protein, acts as an electron carrier within the mitochondrial respiratory chain, enabling efficient oxidative phosphorylation and ATP generation.[44] Similarly, heme-based enzymes such as cytochrome P450 oxidize a variety of organic substrates *via* activation of molecular oxygen, playing a central role in the metabolism of hydrophobic compounds.[45] Other heme enzymes, including catalases and peroxidases, efficiently decompose hydrogen peroxide, protecting cells from oxidative damage through distinct but complementary redox mechanisms.[46] The coordination flexibility and tunability of the porphyrin scaffold are further demonstrated by chlorophylls, which incorporate magnesium ions and drive light-induced electron transfer in photosynthesis. Variations in the porphyrin periphery and fused ring systems adapt the photophysical properties for efficient photon capture and water oxidation in plants and photosynthetic bacteria.[47] In anaerobic organisms, alternative metal centers such as nickel in cofactor F430 enable reductive processes like methanogenesis, while cobalt-based corrinoids such as vitamin B_{12} are essential for DNA synthesis and enzymatic rearrangement reactions.[48] In many biological systems, tetrapyrrolic cofactors are not isolated but are embedded within complex multimetallic active sites. These assemblies, often featuring multiple metal ions in close proximity, are critical to the function of metalloenzymes such as hemocyanin, superoxide dismutase, carbon monoxide dehydrogenase, and cytochrome c oxidase.[49, 50] Particularly, cytochrome c oxidase catalyzes the four-electron reduction of dioxygen to water while concurrently translocating protons across the membrane, thereby contributing directly to the formation of the proton gradient that drives ATP synthesis. This highly evolved architecture ensures complete oxygen reduction without generating harmful reactive oxygen species.

1.1 Structure and nomenclature of porphyrins

Porphyrins represent one of the most widely distributed classes of macrocyclic compounds in nature and are among the most thoroughly investigated molecular frameworks in the field of chemistry.[51-53] The core structure, known as porphin, has the molecular formula $C_{10}H_{14}N_4$ and comprises four pyrrole units interconnected *via* methine bridges to form a planar, cyclic conjugated system.[54, 55]

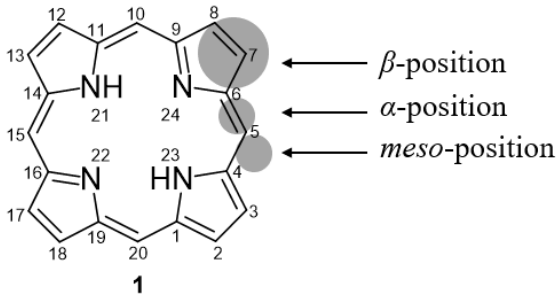

1

Figure 1: Systematic atom numbering in the porphyrin core structure, porphin **1**, with their respective descriptors *α*-, *β*-, and *meso*- to describe their position more precisely.[56]

The 24 atomic positions of the porphin core structure are systematically numbered. Although the descriptors *α*-, *β*-, and *meso*-positions are not officially endorsed by the International Union of Pure and Applied Chemistry (IUPAC) nomenclature standards, they remain widely used within the scientific community to reference specific sites on the macrocycle.[57] The fundamental structure, which contains two inner-core protons associated with the four nitrogen atoms, is referred to as a "free base" porphyrin. Additionally, porphyrins can be classified according to substitution patterns at the *meso*-positions.[58] The commonly employed ABCD system categorizes such derivatives based on their symmetry. In this system, *meso*-substitution at positions 5 and 15 is described as *trans*, while substitution at positions 5 and 10 is termed *cis*, as illustrated by the notation in **Figure 2**.[59]

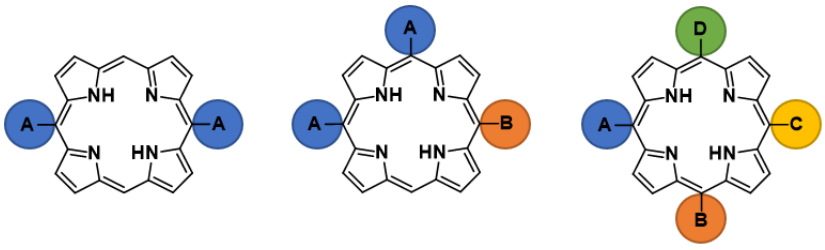

Figure 2: ABCD-nomenclature used to define porphyrin side-groups located at the *meso*-position. A2-type (left), A2B-typ (middle) and ABCD-type (right) are displayed.

In addition to the classical porphyrin framework, numerous structurally diverse porphyrin derivatives have been identified. Among them, the *N*-confused porphyrin represents a notable structural variation, characterized by a rearrangement of the canonical $C_{20}N_4$ macrocyclic framework to yield a 2-aza-21-carbaporphyrin.[60] FURUTA *et al.* first reported this unique motif in 1994 as a minor product arising from the acid-catalyzed condensation of pyrrole with benzaldehyde.[60] The formation of the *N*-confused porphyrin results from the inversion of one pyrrole unit, leading to a 2,4-substitution pattern rather than the conventional 2,5-substitution. This rearrangement alters the inner core of the macrocycle by replacing a tertiary nitrogen with a methine group, effectively relocating a nitrogen atom to a *β*-position on the macrocycle. Consequently, the hydrogen-bonding network and electronic distribution within the macrocyclic cavity are significantly modified.[61] Notably, the traditional porphyrin nomenclature is retained for these derivatives, despite the structural rearrangement of two heteroatoms.

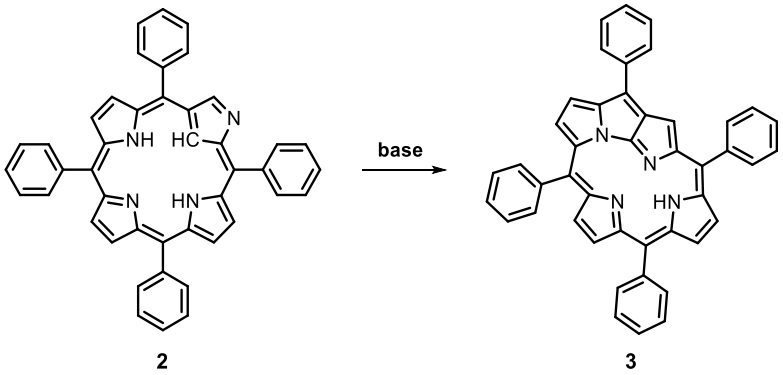

Scheme 1: Structural motif of the *N*-confused porphyrin (left, **2**) and the transition to its fused counterpart the *N*-fused porphyrin (right, **3**).

Upon stirring of the *N*-confused porphyrin in a base of choice, a structural rearrangement occurs, yielding the *N*-fused porphyrin (**Scheme 1**).[62, 63] This transformation involves the rotation of the confused pyrrole ring followed by a nucleophilic attack from an adjacent pyrrole unit, resulting in a fused macrocyclic system. The resulting structure is characterized by a [5,5,5]-fused tri-pentacyclic ring system incorporating two tertiary nitrogen atoms within the macrocyclic core. This novel scaffold significantly expands the coordination chemistry of the porphyrin center, offering new possibilities for metal complexation and functionalization.[64, 65] The IUPAC-recommended atom numbering for this system differs slightly from that of the classical porphyrin. Numbering begins at the carbon atom connected to the methine bridge of the inverted pyrrole, with the inner nitrogen atoms subsequently designated as positions 2, 22, 23, and 24.[64]

1.2 Properties of porphyrins

1.2.1 Conjugation effects

The distinctive electronic properties of porphyrins are fundamentally attributed to their extended π-electron system, which comprises a total of 26 π-electrons, of which 18 are delocalized over the macrocyclic conjugated pathway.[66] This delocalization confers aromatic character to the core of the molecule. For the porphin structure, four principal resonance structures can be proposed to describe the electronic distribution (**Figure 3**).[67, 68]

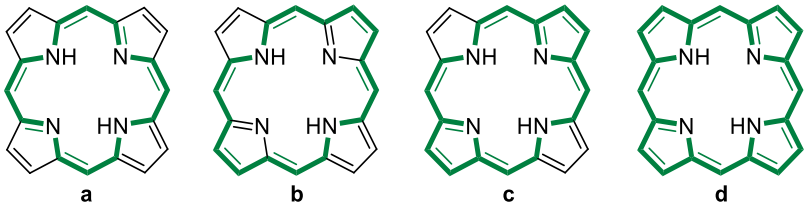

Figure 3: Different pathways to describe the resonance forms of porphin. a: The 18π-[16]annulene internal cross pathway, b: the 18π-[18]annulene pathway, c: the 22π-electron pathways, d: the 26π-electron aromatic pathway.

The aromatic nature of the macrocycle manifests in its nuclear magnetic resonance (NMR) characteristics. Most proton resonances appear in the typical downfield region associated with aromatic systems due to the ring current effect. However, an anomalous high-field signal at approximately –3.5 ppm is observed, corresponding to the inner N–H protons of the porphyrin core.[69] This chemical shift anomaly is explained by the diamagnetic ring current induced in the delocalized π-system under the influence of an external magnetic field applied during ^{1}H NMR spectroscopy. The resulting induced magnetic field reinforces the external field at the periphery of the molecule, deshielding the β-protons and causing downfield shifts above 10 ppm, while opposing it at the center, where the inner N-H protons reside. This leads to significant shielding of these internal protons, resulting in their characteristic upfield resonance.[70, 71]

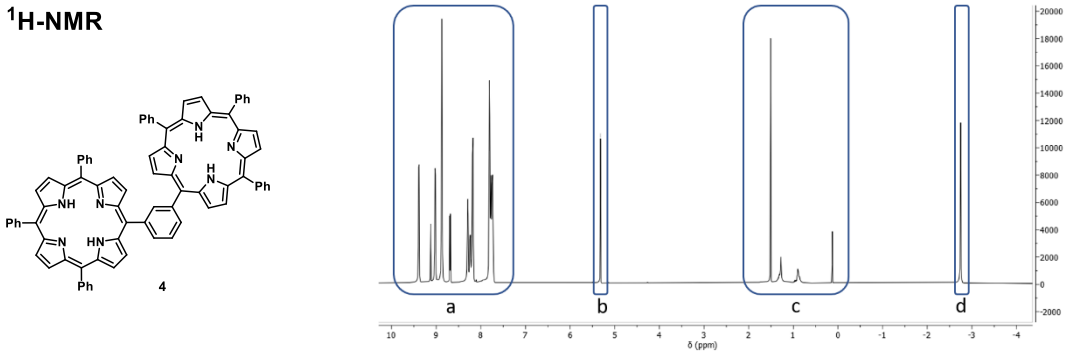

Figure 4: ^{1}H-NMR example of 1,3-Phenylene-bis-5-(10,15,20-triphenylporphyrin) **4**. Part **a** represents the aromatic section within all ^{1}H atoms of the whole structure except the inner NH protons, part **b** is the solvent signal CD_2Cl_2, part **c** the typical impurity section (water (1.54 ppm), H-grease (1.28, 0.94-0.82 ppm) and silicon grease (0.1 ppm)) of porphyrin reactions and part **d** the characteristic upfield resonance of the inner NH protons.

The in **Figure 5** illustrated spectrum shows a typical porphyrin ^{1}H-NMR containing all product signals in the extreme high- and low-field splitting sections **a** and **d** as well as the solvent and impurity sections in between in section **b** and **c**.

1.2.2 Photophysical properties

Porphyrins are among the most efficient chromophores, exhibiting exceptionally high molar extinction coefficients. For example, tetraphenylporphyrin (TPP, **5**) displays an extinction coefficient of $\varepsilon = 3.72 \times 10^5$ cm$^{-1}\cdot$M^{-1} in diethyl ether, placing it among the strongest known light-absorbing organic molecules.[72] As a result, even low concentrations of porphyrins produce intensely colored solutions. The underlying photophysical behavior is elucidated by the UV-Vis absorption spectra.[73] The spectrum of TPP **5** is characterized by two distinct absorption regions (**Figure 5**). The most intense feature is the *Sorét* band (S-band), spanning 380–430 nm, which arises from π–π* transitions associated with the $S_0 \rightarrow S_2$ electronic excitation. A series of lower-intensity absorption peaks appear in the 500–650 nm region, collectively known as the Q-bands, corresponding to transitions from the ground state S_0 to the first excited singlet state S_1. The splitting of the Q-band into multiple sub-bands is attributed to the D_2h symmetry of the free-base porphyrin core.[74]

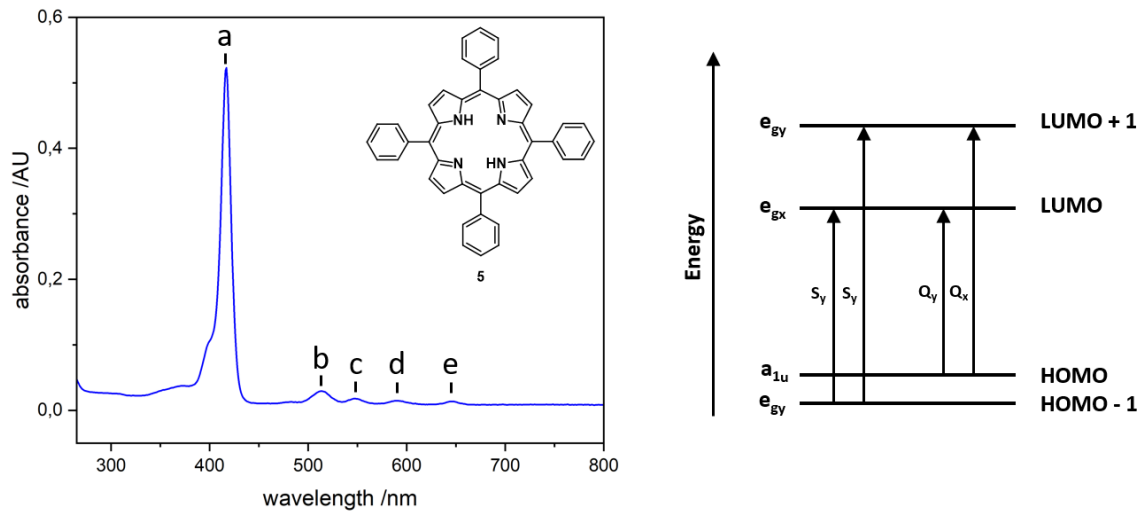

Figure 5: UV-Vis spectrum of TPP (**5**) with the characteristic *Sorét* band (**a**) at 417 nm and the Q-bands at 515 (b), 550 (c), 592 (d) and 646 (e) nm (left). The energy diagram of the relevant frontier orbitals and the transition leading to the respective bands are illustrated (right).

Substitution at the *meso*-positions with electron-donating groups induces a bathochromic shift (red shift) of both S- and Q-band absorptions. This is due to enhanced delocalization of the π-electron system as the lone pairs from the substituents contribute to the conjugated macrocycle.[75]

1.2.3 Properties of metalloporphyrins

The presence of four nitrogen donor atoms within the porphyrin core facilitates robust coordination with a wide range of metal ions. Among these, two nitrogen atoms function as acidic π-donors, while the remaining two act as basic π-acceptors, collectively rendering the porphyrin an excellent tetradentate ligand for metal complexation.[76] The resulting coordination geometry is primarily governed by the ionic radius and electronic configuration of the central metal ion. Consequently, porphyrins can adopt a variety of metal coordination environments depending on the size and charge of the coordinated metal species (**Figure 6**).[76, 77]

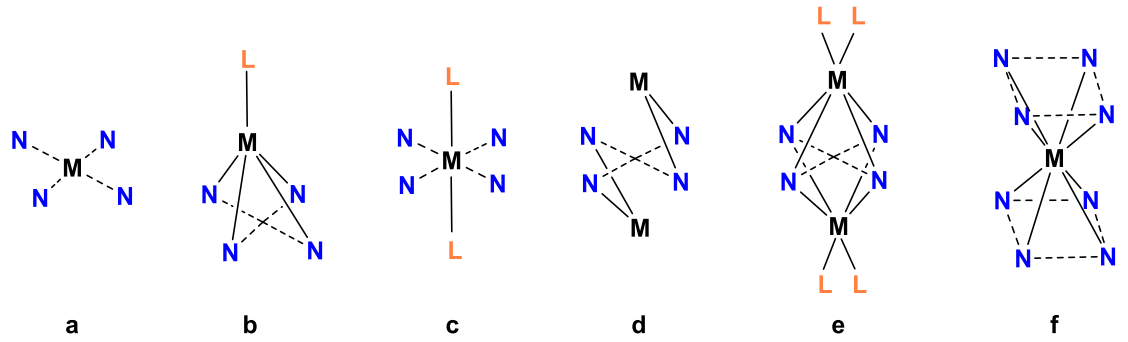

Figure 6: The different coordination geometries of porphyrin-based metal complexes. With **a**: square-planar, **b**: square-pyramidal, **c**: distorted octahedral, **d**: angled, **e**: square-bipyramidal, **f**: square-antiprismatic coordination displayed. M: metal, N: inner nitrogen of the porphyrin scaffold, L: Ligand.

The most prevalent coordination motif is square-planar, which is compatible with a broad range of non-radioactive metal ions spanning from Si (IV) to Pb (II). In this configuration, the metal ion typically adopts a +2 oxidation state and resides coplanar with the porphyrin ligand.[78, 79] In cases where the metal ion is sterically too large to fit within the plane of the macrocycle, square-pyramidal geometry may emerge *via* a "sitting-atop" mode. This out-of-plane coordination is frequently observed with lanthanides due to their comparatively large ionic radii and limited space within the porphyrin cavity.[80] Distorted octahedral geometries are characteristic of biologically relevant systems such as cytochromes and heme proteins, where axial ligands above and below the porphyrin plane differ in bond length and identity, resulting in asymmetry.[81] Less common are the angled and square-bipyramidal geometries, typically arising in complexes with monovalent cations such as alkali metals or silver (I).[82] For large metal ions, eight-coordinate square-antiprismatic geometries can be achieved, forming sandwich-type complexes where the metal is encapsulated between two porphyrin ligands.[83]

1.2.4 Properties of the N-confused and N-fused porphyrin derivatives

N-confused porphyrins exhibit a distinctive and rare property: tautomerization between two inner protonation states, the inner 3H and 2H forms.[84] This tautomerism is highly dependent on the polarity of the solvent. In nonpolar solvents, the 3H-tautomer predominates, whereas in polar solvents, the equilibrium shifts toward the 2H-tautomer (**Scheme 2**).[85]

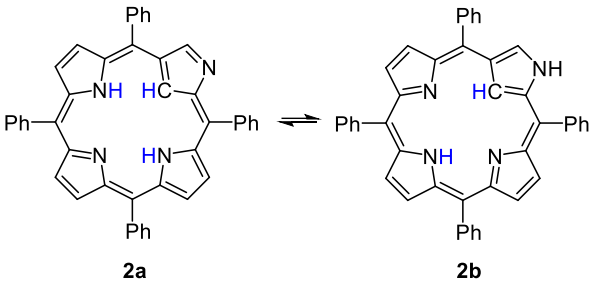

Scheme 2: Solvent-dependent tautomerization of the N-confused porphyrin with its 3H tautomer (2a) and 2H tautomer (2b).

The primary structural difference between the two tautomers lies in the degree of aromaticity. Compound **2a** retains a fully delocalized 18π-electron system and thus maintains aromatic character. In contrast, compound **2b** has disrupted conjugation due to the twisted orientation of the confused pyrrole moiety, resulting in diminished aromatic stabilization. Despite their structural divergence from regular porphyrins, *N*-confused porphyrins preserve the capacity for metal coordination in various geometries previously described.[86, 87] Numerous metal complexes have been synthesized and characterized, including those incorporating iron and rhodium centers.[88, 89] Analogous tautomerism is also observed in *N*-fused porphyrins, though with a crucial distinction: both tautomeric forms retain aromatic character due to uninterrupted π-conjugation throughout the macrocyclic framework (**Scheme 3**).[90]

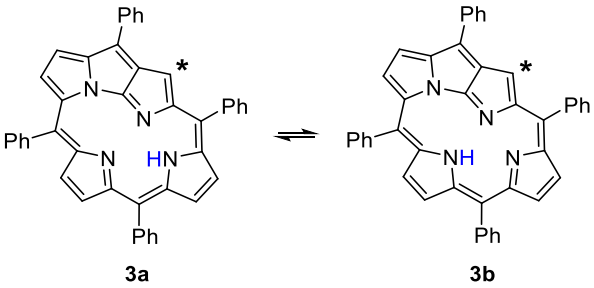

Scheme 3: Tautomerization of the N-fused porphyrin with position C21 (*) as preferred substitution position.

In the unsubstituted form, tautomer **3a** is typically more stable. However, specific substitutions, such as a bromination at position C_{21}, can shift the equilibrium in favor of the alternate tautomer, rendering it thermodynamically preferred. Given that both tautomers are aromatic, their relative stabilities are comparable under standard conditions (20°C, 1 atm). Metal

coordination in *N*-fused porphyrins predominantly occurs *via* an out-of-plane "sitting-atop" geometry, though in-plane coordination is also feasible, particularly with small metal ions possessing compact ionic radii.[63]

Comparing the UV-Vis spectrum of *N*-confused and *N*-fused porphyrins (**Figure 10**) to the conventional absorption of TPP, only a disruption of the Q-bands of the *N*-confused spectrum could be observed while the *Sorét* band stays similar in shape, position and intensity.[91-93]

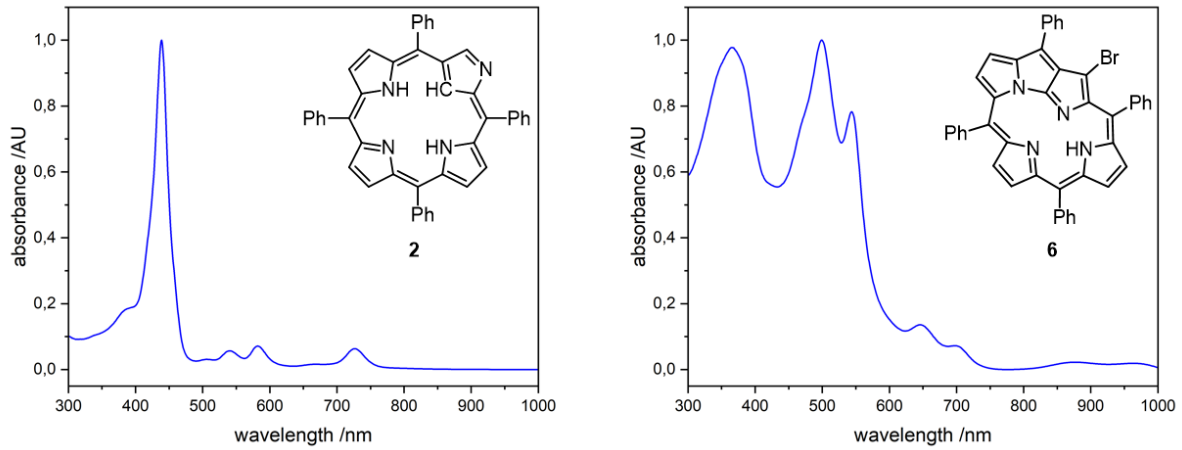

Figure 7: Absorption spectrum of 5,10,15,20-Tetraphenyl-2-aza-21-carbaporphyrin (*N*-confused porphyrin (**2a**)) and 19-Bromo-3,8,13,16-tetraphenyl-4,7-imino-2,17-methano-9,12-nitrilo[1,3]diazacyclohexadecino[2,1,16-cd]pyrrolizine (Bromo-*N*-fused porphyrin (**4**)).

A more impactful derivative concerning the absorption is the *N*-fused scaffold. The fusion of two adjacent pyrrole units within the porphyrinoid framework leads to a notable reduction in the HOMO–LUMO energy gap, without altering the total number of π-electrons or significantly affecting the fundamental aromatic π-system.[94] This structural modification results in distinct optical properties, characterized by intense absorption bands at 360, 499, and 545 nm, alongside weaker transitions at 647, 704, 852, and 941 nm. Remarkably, despite retaining an 18π-electron aromatic configuration, the absorption tail extends beyond 1000 nm, indicating substantial electronic delocalization and enhanced near-infrared absorption.[63]

1.3 Syntheses of porphyrins

1.3.1 The history of porphyrin synthesis

The first synthetic access to porphyrins was achieved in the early 20th century by WILLSTÄTTER, STOLL, and KÜSTER.[95] At the time, structural elucidation posed a significant challenge due to limited analytical techniques. Nevertheless, Hans Fischer later confirmed the proposed structure with experimental evidence, solidifying the foundational understanding of porphyrins.[96] A major advancement occurred in 1935, when ROTHEMUND reported the first systematic synthesis by reacting equimolar amounts of pyrrole and various aldehydes in methanol or pyridine (**Scheme 4**).[97] Reaction temperature played a crucial role in product distribution: prolonged stirring at 90 °C yielded porphin (1) and tetramethylporphyrin (15), while heating the mixture to 220 °C led to the formation of TPP.[98, 99]

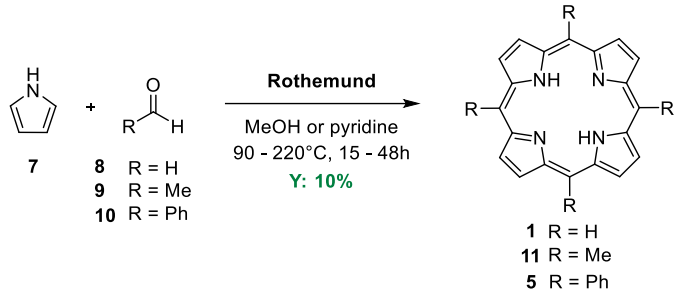

Scheme 4: Reaction scheme of ROTHEMUNDS approach to synthesize porphyrins from 1935.

After several decades with limited progress, ADLER and LONGO introduced a modified method in 1964 that increased yields to approximately 20% by employing propionic acid under reflux conditions (**Scheme 5**).[100] However, the harsh acidic and thermal environment restricted the scope of compatible functional groups.

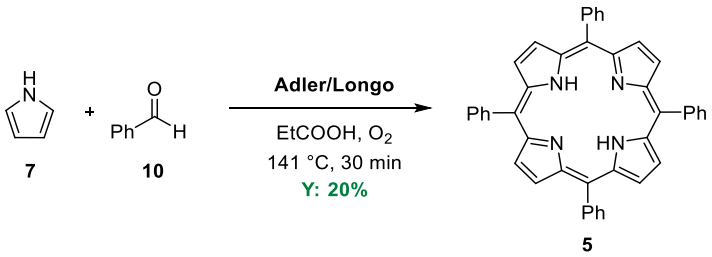

Scheme 5: Reaction scheme of the optimization of ADLER and LONGO from 1964.

A significant breakthrough in porphyrin synthesis came in 1986 when LINDSEY and co-workers developed a high-dilution methodology, operating at low concentrations of 10^{-2} M.[101] Pyrrole and benzaldehyde were dissolved in dry, chlorinated solvents and subjected to acid catalysis using trifluoroacetic acid (TFA) or boron trifluoride diethyl etherate ($BF_3{\cdot}OEt_2$) under inert

conditions. The intermediate porphyrinogen was then oxidized in situ using *p*-chloranil or 2,3-dichloro-5,6-dicyano-1,4-benzoquinone (DDQ), yielding the desired porphyrin product (**Scheme 6**). This approach not only increased yields up to 50% but also enabled the incorporation of sensitive functional groups such as azides due to the milder conditions employed.

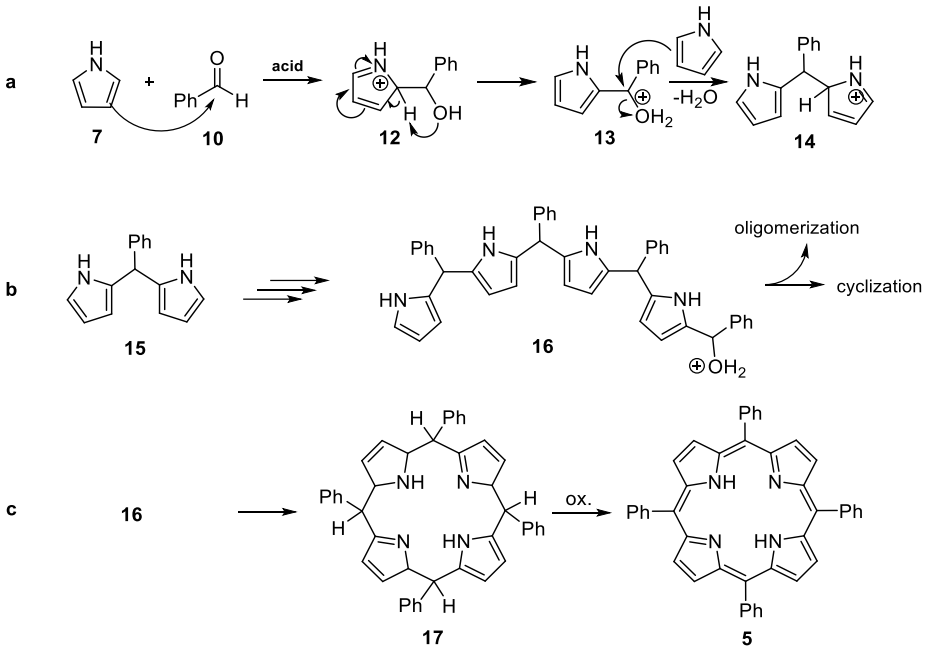

Scheme 6: Reaction mechanism elaborated by LINDSEY et al. to yield TPP with up to 50% yield.[101]

The reaction proceeds through an acid-catalyzed electrophilic substitution of benzaldehyde **10** at the *α*-position of pyrrole **7**, forming the intermediate protonated phenyl(2H-pyrrol-2-yl)methanol **12**. Subsequent nucleophilic attack by a second pyrrole molecule results in hydrolysis and formation of a dipyrromethane derivative **15**. Iterative condensation leads to the bilane carbenium ion intermediate **16**, which can either cyclize to form the desired porphyrinogen **17** or proceed through oligomerization pathways to undesired by-products. Upon oxidation with DDQ, the porphyrinogen **17** is converted to the final porphyrin macrocycle **5**. This method is particularly well-suited for synthesizing symmetrical porphyrins. However, by carefully controlling the stoichiometry of the reactants, asymmetrical porphyrins can also be accessed. Alternatively, a stepwise approach involving pre-formed dipyrromethane intermediates is often preferred for synthesizing porphyrins with defined substitution patterns.

1.3.2 Synthesis of non-symmetric porphyrins

The synthesis of non-symmetrical porphyrins can be effectively achieved by introducing distinct substituents at the *meso*-positions. In this approach, equimolar amounts of 2,2′-

dipyrromethane **18** and various aldehydes are employed under *Lewis* acid (LA) catalysis to promote macrocyclization. The use of pre-functionalized dipyrromethane intermediates provides a high degree of control over the final substitution pattern of the porphyrin core.[102, 103]

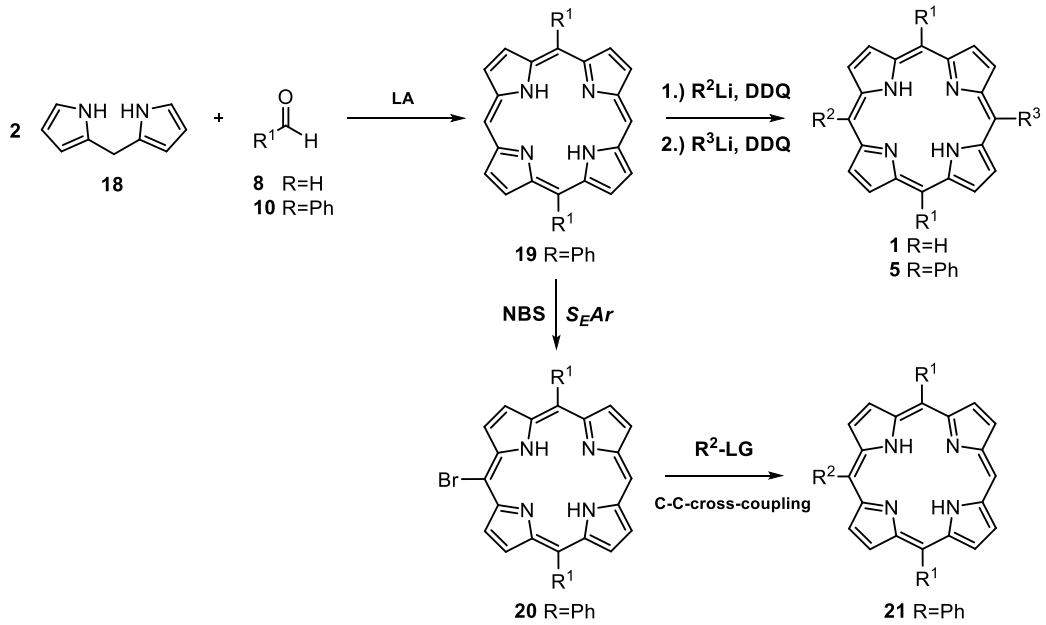

Scheme 7: Effective reaction pathways to synthesize defined unsymmetrical porphyrins.

SENGE and co-workers have demonstrated that organolithium reagents can be utilized in addition-oxidation sequences, followed by nucleophilic aromatic substitution, to selectively functionalize the porphyrin framework.[104] Among the available sites, the *meso*-position exhibits the highest reactivity, making it a preferred locus for post-synthetic modifications. Furthermore, non-symmetrical porphyrins can also be accessed *via* selective bromination of the *meso*-positions, followed by palladium-catalyzed C–C cross-coupling reactions, such as SUZUKI or SONOGASHIRA couplings. These methodologies expand the structural diversity and functional utility of porphyrinoid systems.[104]

1.4 Photochemical catalysis

Photochemical catalysis offers a promising route to address global energy and environmental challenges by enabling the light-driven conversion of CO_2 into fuels and value-added chemicals. Although direct one-electron reduction of CO_2 to its radical anion requires a prohibitively high potential, coupling CO_2 reduction with proton transfer allows the formation of more stable products, such as carbon monoxide, formic acid, methanol, and methane, at significantly lower redox potentials (**Scheme 8**).[105, 106]

			Redox potential (V)	
$CO_2 + 1e^-$	⟶	$CO_2^{-\bullet}$	- 1.90	(1)
$CO_2 + 2H^+ + 2e^-$	⟶	$CO + H_2O$	- 0.53	(2)
$CO_2 + 2H^+ + 2e^-$	⟶	$HCOOH$	- 0.61	(3)
$CO_2 + 4H^+ + 4e^-$	⟶	$HCHO + H_2O$	- 0.48	(4)
$CO_2 + 6H^+ + 6e^-$	⟶	$CH_3OH + H_2O$	- 0.38	(5)
$CO_2 + 8H^+ + 8e^-$	⟶	$CH_4 + 2H_2O$	- 0.24	(6)

Scheme 8: Possible conversion of the reduction of CO_2 with its redox potentials vs. NHE at pH = 7.

A catalytic system is required to achieve such conversions. The photocatalytic approach to CO_2 reduction offers a highly versatile and tunable platform. These systems typically comprise a molecular photosensitizer (PS), a molecular catalyst (CAT), and a sacrificial electron donor (SED). The photocatalytic cycle is initiated by the excitation of PS to its electronically excited state (PS*), from which electron transfer proceeds *via* either oxidative or reductive quenching pathways (**Figure 18**).[107]

In oxidative quenching, PS* transfers an electron to CAT, generating the catalytically active one-electron-reduced species ($CAT^{-\bullet}$) and an oxidized photosensitizer (PS^+), which is subsequently regenerated by interaction with the SED. For this pathway to be thermodynamically viable, the excited-state oxidation potential of the PS must be more negative than the reduction potential of CAT. This condition is often challenging to meet in the

context of CO_2 reduction due to the typically very negative redox potentials required to activate CO_2. In the reductive quenching mechanism, the electron donor transfers an electron to PS*, forming a reduced photosensitizer ($PS^{-\cdot}$) and an oxidized donor species (SED^{+}). The $PS^{-\cdot}$ then reduces CAT to $CAT^{-\cdot}$. Thermodynamic feasibility in this case requires that the reduction potential of PS* must be more positive than that of the donor. Kinetically, this pathway is often favored due to the higher concentrations of the sacrificial donor relative to the catalyst.

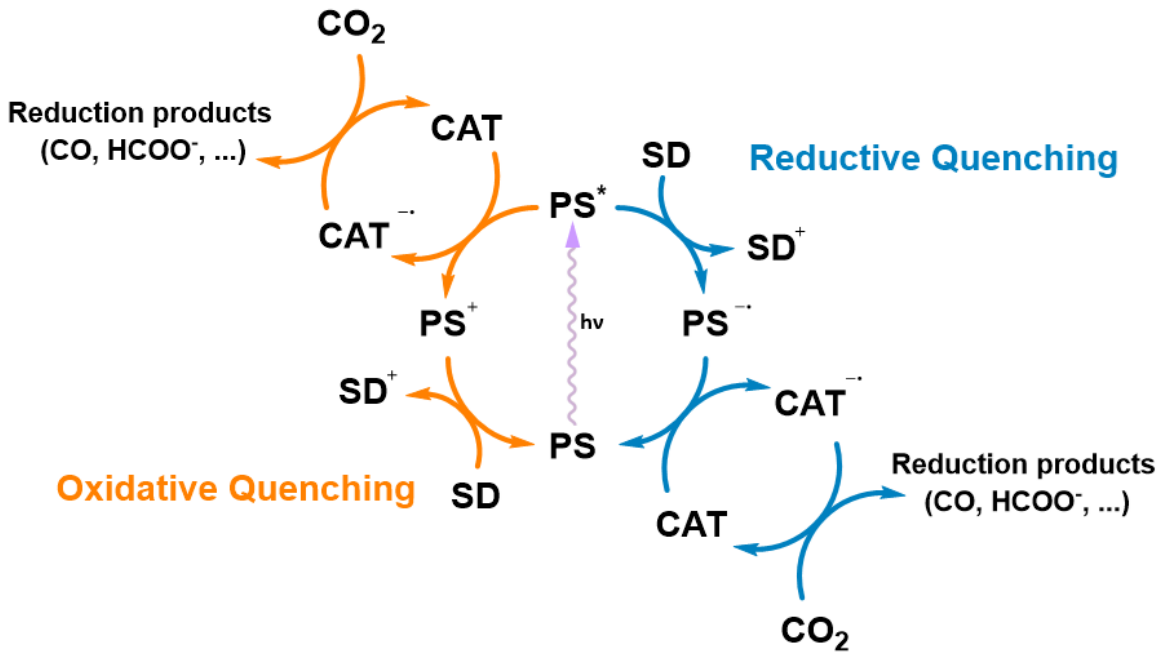

Figure 8: General mechanism of the reduction of CO_2 *via* reductive quenching (blue) and oxidative quenching (orange).[105]

Despite these differing mechanisms, both routes converge on the generation of $CAT^{-\cdot}$, the active intermediate that binds and reduces CO_2. In analogy to electrochemical systems, this reduced catalyst typically undergoes ligand dissociation to create a vacant coordination site for CO_2 binding, forming a catalytically competent CO_2 adduct. However, photochemical systems depend on discrete, diffusion-controlled photoinduced electron-transfer events. These processes typically deliver only one electron per excitation event, necessitating a second electron from additional mechanisms such as sequential photoinduced electron transfer (PET) steps, strongly reducing SED-derived species, or catalyst disproportionation.[108-110]

1.5 Photodynamic therapy

Photodynamic therapy is a well-established, minimally invasive clinical strategy for the treatment of malignant tissues.[111] Unlike conventional modalities such as surgery, chemotherapy, or radiotherapy, PDT offers unique advantages, including spatiotemporal control, reduced systemic toxicity, and the potential for repeated treatments without cumulative adverse effects.[34] Its therapeutic effect relies on the interplay of three individually non-toxic components: a photosensitizer, light of an appropriate wavelength, and molecular oxygen.[112]

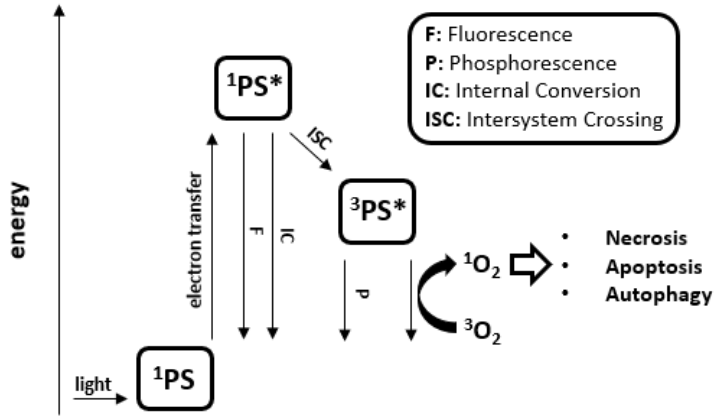

Figure 9: Simplified *Jablonski* diagram for the general mechanism of the excitation and energy transfer of a PS to produce ROS.[113]

The PDT process begins with the systemic, local, or topical administration of a photosensitizer, which preferentially accumulates in neoplastic tissues. Upon localized irradiation with low-energy light, the PS is excited from its ground state to a singlet excited state, followed by intersystem crossing (ISC) to a long-lived triplet state. In this state, the PS can transfer energy to ground-state molecular oxygen ($^3O_2$), producing reactive oxygen species primarily singlet oxygen ($^1O_2$) *via* a type II photochemical pathway.[113] These ROS exert oxidative stress, ultimately triggering cellular damage through mechanisms such as apoptosis, necrosis, or autophagy. An ideal photosensitizer should combine high singlet oxygen quantum yield, strong absorption in the therapeutic window, photochemical and thermal stability, and selective accumulation in tumor tissues. Several porphyrin-based compounds have been approved by the U.S. Food and Drug Administration (FDA) for clinical PDT applications, owing to their favorable photophysical properties and tumor-targeting capabilities. Given that ROS generation is a key determinant of PDT efficacy, the design and optimization of next-generation PSs remain a central focus of research.[114, 115]

1.5.1 Porphyrins as photosensitizers in photodynamic therapy

Porphyrins form the cornerstone of PDT photosensitizer development due to their distinct optical and photochemical features, including strong absorbance in the therapeutic window, high triplet quantum yields, and generally low systemic toxicity.[116-118] Several porphyrin-based agents, such as *Photofrin*® (**22**), *Fotolon*® (**23**), and *Tookad*® (**24**), have attained regulatory approval, underscoring their clinical relevance and translational potential.[119, 120]

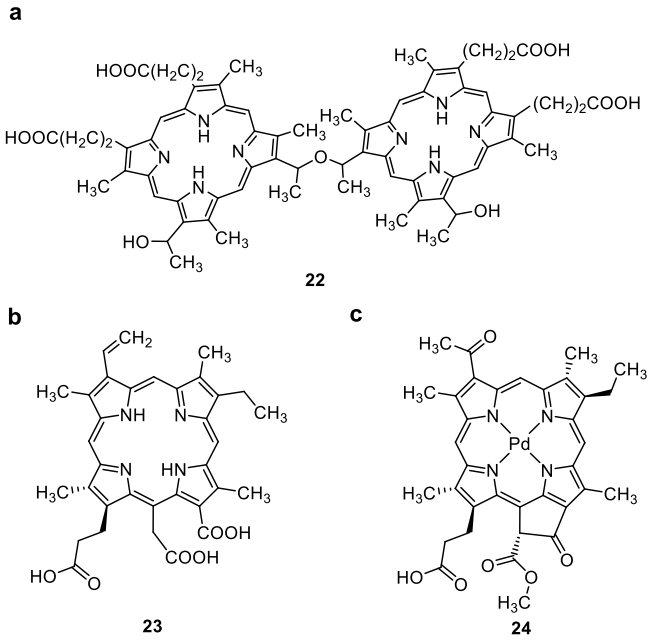

Figure 10: Chemical structure of the commercially available porphyrin-based photosensitizers Photofrin® (**a**), Fotolon® (**b**), and Tookad® (**c**) for PDT.

Moreover, cationic porphyrin derivatives demonstrate enhanced water solubility and improved cellular uptake, further enhancing their therapeutic efficiency.[121, 122] However, despite their clinical success, first-generation porphyrin PSs are limited by modest biocompatibility, low ROS production, and limited tumor selectivity. These limitations underscore the need for improved porphyrinoid systems with enhanced photochemical performance and optimized pharmacokinetics.[123] One promising strategy to enhance the properties of porphyrin-based PSs involves coordinating metal ions within the macrocyclic core.[124] The tetrapyrrolic coordination environment and extended π-conjugation of porphyrins facilitate complexation with a broad range of metal ions. This modification can significantly modulate the photophysical and electrochemical characteristics of the molecule. Importantly, metallation enhances ISC *via* the heavy atom effect, thereby increasing triplet-state population and subsequent ROS generation. Metalloporphyrins incorporating transition metals such as platinum and palladium are especially compelling due to their dual functionality: they act as both effective photosensitizers

and molecular oxygen sensors. The rational design of such metallated porphyrin systems offers considerable promise for the development of next-generation PDT agents with superior selectivity, higher phototoxicity, and integrated diagnostic capabilities.[125, 126]

2 Aim of the Work

A novel platform for investigating cooperative effects was developed by the BRÄSE group, featuring a porphyrin dimer composed of a conventional *ortho*-phenyl-linked tetraphenylporphyrin and an *N*-fused porphyrin unit. This unique scaffold represents the first ligand system capable of simultaneously coordinating two metal centers in different oxidation states within close spatial proximity. Although the initial synthesis was successfully achieved, comprehensive characterization of the resulting compounds remains incomplete, and no standardized reaction conditions were established to ensure product formation reliably. The initial objective of this work was to reproduce the synthesis of 1,2-phenylene(*N*-fused-tetraphenylporphyrin-triphenylporphyrin) **25** and to optimize each step to establish robust and reproducible reaction conditions. Careful purification and thorough analysis of the intermediates and final products are essential to generate definitive analytical evidence confirming the structure of the target compound (**Scheme 9**).

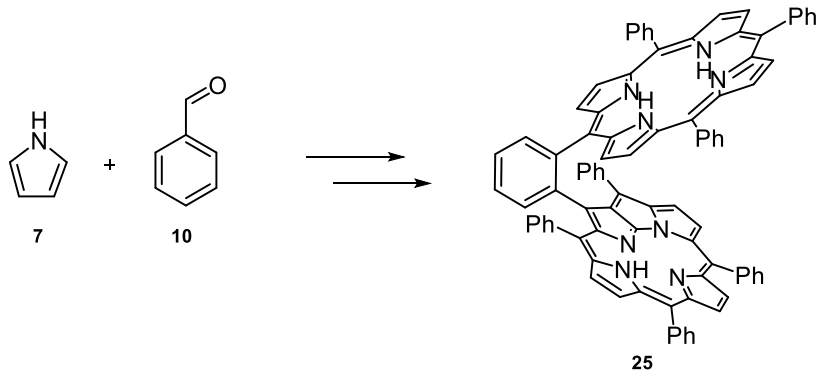

Scheme 9: General representation of the synthesis to produce the target compound 1,2-phenylene(*N*-fused-tetraphenylporphyrin-triphenylporphyrin) from pyrrole and benzaldehyde as starting substances.

Another previous study conducted by the BRÄSE research group was the successful synthesis of *ortho*-linked porphyrin di- and trimers. The coordination chemistry of these systems was thoroughly explored by attaching a wide range of transition metals as homo- and hetero-bi- and tri-metallic complexes. The present work aims to reproduce and optimize these synthetic protocols in order to generate sufficient quantities of the stacked porphyrin scaffolds for subsequent investigations into the cooperative electronic and catalytic effects arising from their multimetallic architectures. As a foundational step, the synthesis of the asymmetrically functionalized 5,10,15,20-tetraphenylporphyrin monomer will be repeated and refined. This monomer serves as a key precursor for the stepwise construction of *ortho*-phenylene-bridged bis- and tris-porphyrin assemblies. Particular emphasis will be placed on scaling up and

optimizing the condensation reactions to ensure high yields and reproducibility for further application in coordination studies (**Scheme 10**).[127, 128]

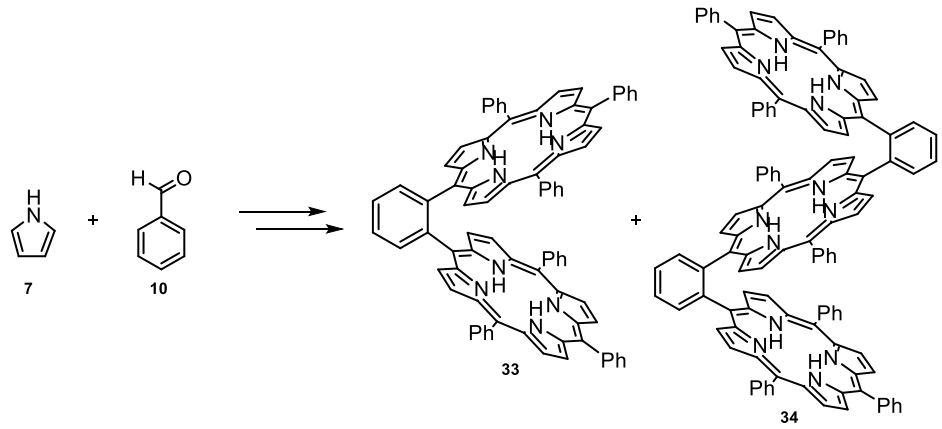

Scheme 10: General representation of the synthesis to produce the target compounds *ortho*-phenylene bis- and tris-porphyrins from pyrrole and benzaldehyde as starting substances.

Several of the synthesized metal complexes exhibit promising potential for targeted applications. Notably, the heterobimetallic 1,2-phenylene-bis-5-(10,15,20-triphenylporphyrin)-nickel(II)iron(III) complex structurally mimics the active site of carbon monoxide dehydrogenase (CODH), a metalloenzyme known to catalyze the reduction of carbon dioxide under physiological conditions.[129] To enable a comprehensive investigation of this biomimetic system, a robust synthetic route must be established to obtain sufficient quantities of the dimeric porphyrin ligand. Once adequate amounts of the ligand are available, its coordination chemistry can be systematically explored to form heterobimetallic complexes more efficiently. Of particular interest is the Ni(II)/Fe(III) complex, due to its structural and electronic resemblance to the native CODH active site. The synthesis and subsequent evaluation of this complex as a functional mimic for CO_2 reduction constitute a central objective of this thesis. To assess its catalytic potential, the electrochemical properties of the complex will be examined using cyclic voltammetry. Should these electrochemical studies confirm activity toward CO_2 reduction, further investigations will be conducted to explore its application in photochemical CO_2 conversion systems.

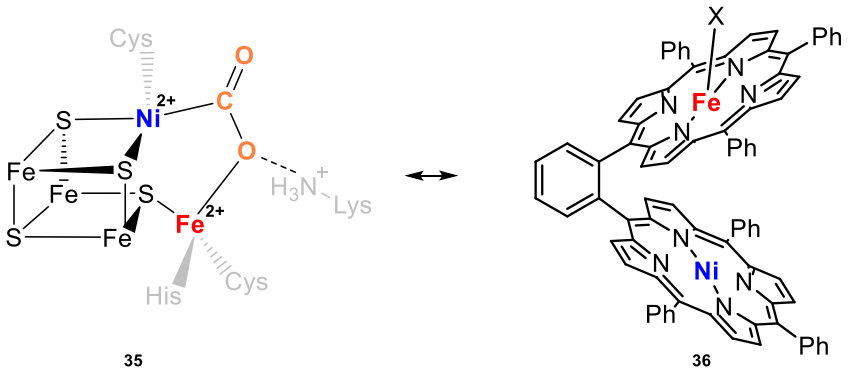

Figure 11: Structural motif and predicted coordination of CO_2 of the active center of the CODH (left)[129] and the porphyrin-based mimic forcing Ni and Fe in spatial proximity (right).[127]

Another compound of significant interest is the *ortho*-linked tris-porphyrin derivative, 5,15-bis(2-(10,15,20-triphenylporphyrinyl)phenyl)-10,20-diphenylporphyrin. This molecular architecture enables the spatial arrangement of up to three metal centers in close proximity, providing a well-defined platform for probing cooperative interactions between multiple metal sites. One particularly promising application of this scaffold is its use in photodynamic therapy. The palladium (II) complex of the tris-porphyrin has demonstrated notable potential as a photosensitizer. Comparative analysis of semi-quantitative emission spectra from the monomeric, dimeric, and trimeric complexes revealed a non-linear enhancement in singlet oxygen generation with increasing porphyrin units. This behavior suggests a synergistic effect in the trimeric system, highlighting its suitability for the efficient production of reactive oxygen species, particularly singlet oxygen, which is a key cytotoxic agent in cancer phototherapy. To evaluate the photosensitizing potential of the palladium complexes, it is necessary to resynthesize these compounds and perform quantitative assessments of their singlet oxygen generation efficiency. One suitable analytical approach is the dichlorofluorescein (DCF) assay. In this method, non-fluorescent DCF is oxidized by reactive oxygen species to form the fluorescent product dichlorodihydrofluorescein (DCFH). The resulting fluorescence, typically monitored at an emission maximum of 522 nm, provides a quantitative measure of ROS production. This assay enables the comparative evaluation of the singlet oxygen yield of different Pd (II) porphyrin complexes under controlled irradiation conditions.[120]

3 Main Part

3.1 Elaboration of dimeric structures with porphyrin derivatives

3.1.1 Synthesis approach

To start the journey of synthesizing a porphyrin dimer with alternative porphyrin scaffolds, the synthesis of the *N*-confused porphyrin (NCP) was carried out under conditions following a procedure of *Lindsey et al.* The strategy in this was to take the well-established synthesis of tetraphenylporphyrin and switch the catalyst from TFA/$BF_3 \cdot OEt_2$ to methanesulfonic acid ($MeSO_3H$) and stir the starting substances pyrrole and benzaldehyde together with the catalyst at room temperature for 30 minutes in the absence of light. This conversion could be achieved with a yield of 29% (**Scheme *11***).[84]

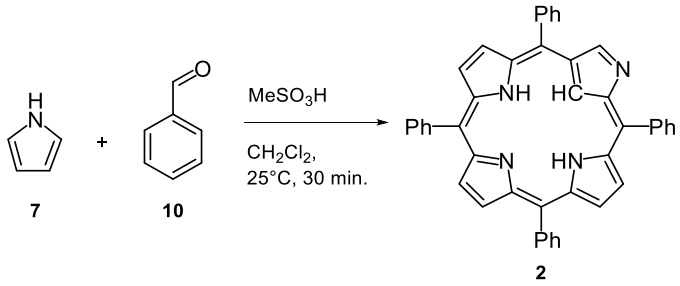

Scheme 11: Synthesis of the first precursor, the *N*-confused porphyrin.

To achieve a bromination of this substance, NCP was treated with N-bromosuccinimide (NBS) and stirred for 5 minutes. The crude product was then passed through a short silica pad and re-dissolved in pyridine. Upon stirring at room temperature for 1 hour, the reaction proceeded to form the bromo-*N*-fused porphyrin, affording a 55% yield over two steps *via* a presumed [5,5,5] tri-pentacyclic ring fusion (**Scheme *12***).

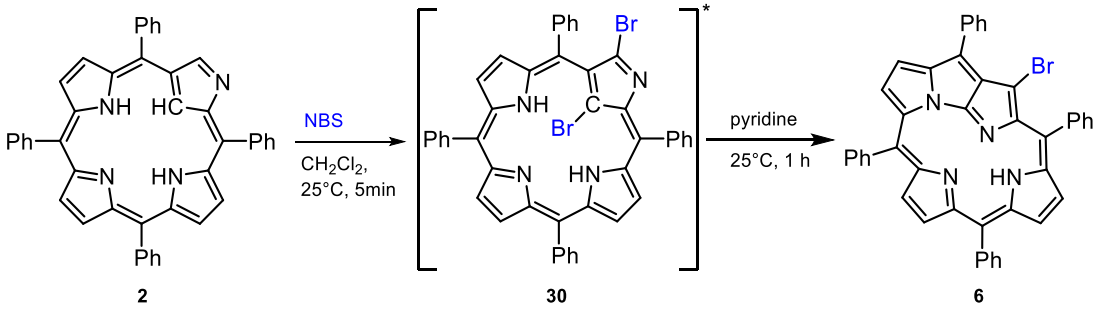

Scheme 12: Synthesis pathway towards the brominated *N*-fused porphyrin.

Subsequently, compound **6** was subjected to a *Suzuki–Miyaura* cross-coupling reaction to yield the formyl-phenyl-*N*-fused porphyrin in 24% yield. Optimal conditions involved 2-

formylphenylboronic acid, $Pd(PPh_3)_4$, and K_3PO_4 in degassed THF, heated to 110 °C for 15 minutes in a sealed pressure vial, following protocols used for analogous porphyrin derivatizations (**Scheme *13***).[104]

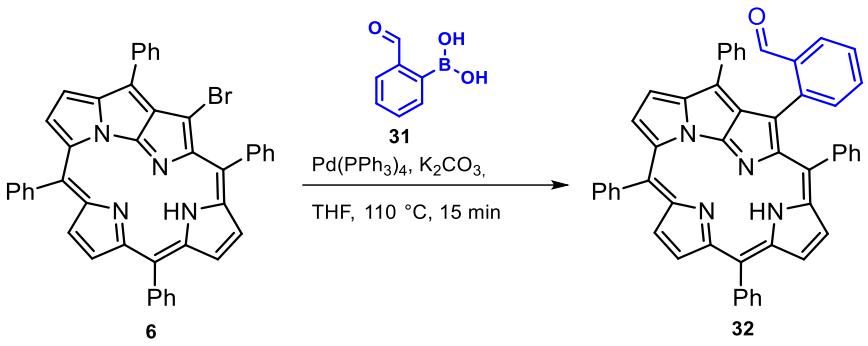

Scheme 13: *SUZUKI-MIYAURA* cross-coupling step to form the formyl-phenyl-*N*-fused porphyrin.

The aldehyde-functionalized porphyrin was subsequently used in a condensation reaction to synthesize a dimeric construct, comprising an *N*-fused porphyrin (NFP) and a regular porphyrin unit, referred to as the "*N*-fused–regular dimer". To a degassed solution of compound **32** in CH_2Cl_2, pyrrole, benzaldehyde, and TFA as an acid catalyst were added dropwise over a period of 48 hours, ensuring a controlled and gradual formation of the dimeric ligand. The reaction progress was continuously monitored *via* TLC. Upon observing a deceleration in the conversion of the starting material, additional portions of the reactants were introduced in their respective stoichiometric ratios to maintain reaction efficiency (**Scheme *14***).

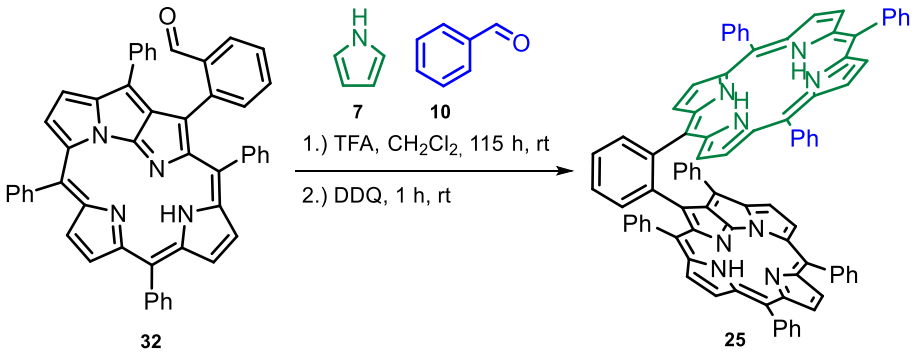

Scheme 14: Mixed-condensation step to form 1,2-phenylene(*N*-fused-tetraphenylporphyrin-triphenylporphyrin).

3.1.2 Characterization of the novel compounds

The general characterization of these compounds was carried out using NMR spectroscopy, mass spectrometry, and UV-Vis absorption spectroscopy. The precursor compounds exhibited spectral features consistent with those reported in the literature and were unambiguously identified based on these analytical data. The dimeric structure, however, poses considerable analytical challenges when using conventional techniques such as ^{1}H-NMR spectroscopy, largely due to the high density of proton signals within overlapping chemical shift regions, compounded by pronounced π–π stacking interactions and aggregation tendencies typical of extensively conjugated systems. Furthermore, attempts at crystallization have been unsuccessful, likely due to the molecule's pronounced asymmetry and substantial conformational flexibility. These characteristics hinder its ability to adopt a stable, periodically repeating arrangement necessary for the formation of a crystalline lattice suitable for X-ray diffraction analysis. Additional analytical techniques, such as ion mobility measurements, were employed to confirm the proposed structure.

3.1.2.1 NMR analysis

The ^{1}H NMR spectrum of compound **2** displays a singlet at 8.77 ppm, attributable to the outer *β*-proton of the twisted pyrrole ring. In the high-field region, a broad singlet at –2.43 ppm corresponds to the NH protons, while a sharper singlet at –4.99 ppm is assigned to the inner CH proton (**Figure 12**).

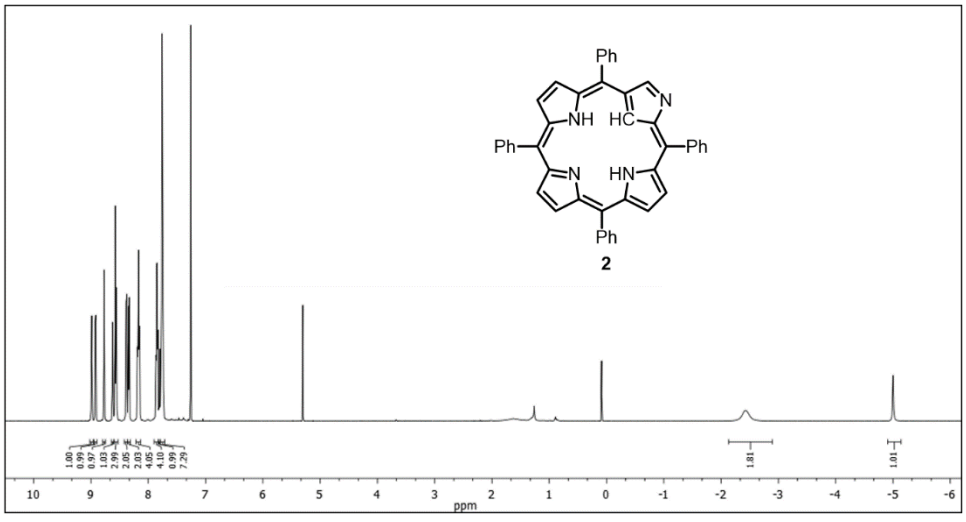

Figure 12: ^{1}H-NMR spectrum of the *N*-confused porphyrin **2** in $CDCl_3$ measured at a 500 MHz spectrometer with 64 scans.

The ^{1}H NMR spectrum of **3** shows doublets in the 7–8 ppm range with an increased coupling constant (J = 5.1 Hz) compared to typical porphyrins (e.g., diphenylporphyrin, J = 4.6 Hz), which is attributed to the slightly distorted macrocyclic framework (**Figure 13**).[130]

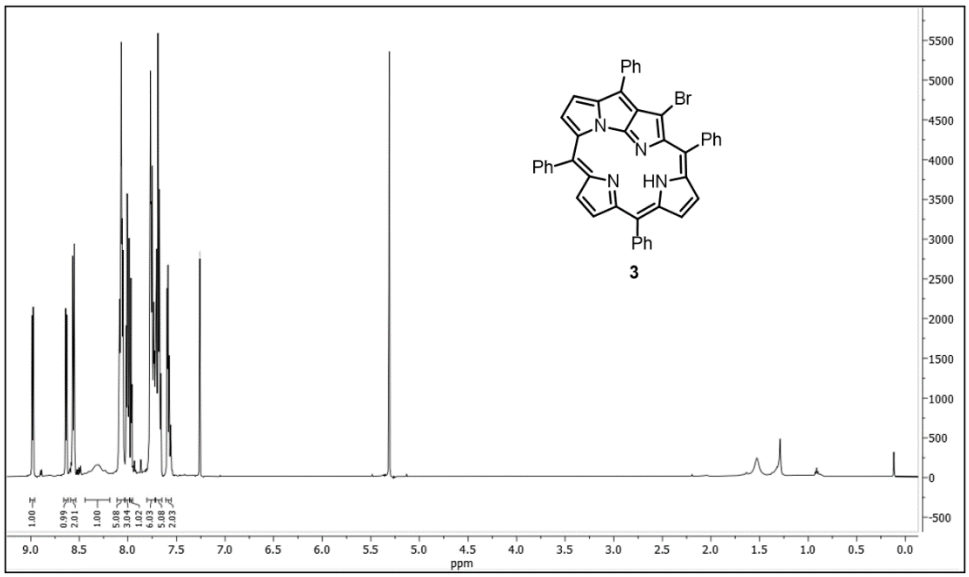

Figure 13: ^{1}H-NMR spectrum of the *N*-fused porphyrin bromide **3** in $CDCl_3$ measured at a 500 MHz spectrometer with 64 scans.

The ^{1}H NMR spectrum of compound **32** displayed broad signals corresponding to the pyrrolic protons, indicative of significant π–π stacking interactions in solution. These signals could be noticeably sharpened by the addition of 1 M aqueous HCl in a 1:10 ratio, effectively disrupting the aggregation behavior.[131] In contrast, analogous deuterated solvents did not produce a comparable effect. However, substituting $CDCl_3$ with CD_2Cl_2 as the solvent led to improved spectral resolution and narrower signals. In the optimized spectrum, a distinct singlet at 10.16 ppm confirmed the presence of the aldehyde functional group. Additionally, a broad singlet at 8.00 ppm was attributed to the NH proton, which, unlike in conventional porphyrin systems, appears in the downfield region. This downfield shift is characteristic of the *N*-fused porphyrin architecture, underscoring its electronic and structural deviation from regular porphyrins (**Figure 14**).[65]

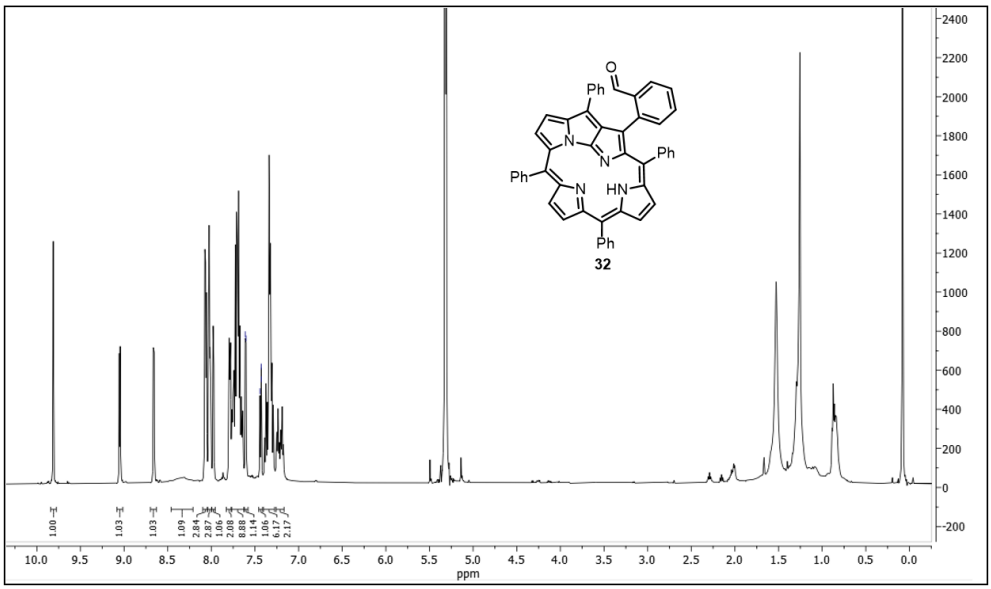

Figure 14: ^{1}H-NMR spectrum of the *N*-fused porphyrin aldehyde **32** in $CDCl_3$ measured at a 500 MHz spectrometer with 64 scans.

The ^{1}H NMR spectrum of the compound **25** exhibits pronounced line broadening, attributable to π-stacking interactions. This aggregation-induced broadening can be mitigated by the addition of either an acid or pyridine-d_5 as a basic disruptor of the stacking. A detailed investigation by *Shimizu et al.* into *N*-heterocyclic π–π interactions involving various pyridines provides a thorough foundation for understanding this behavior.[131] The optimal concentration of pyridine-d_5 was determined empirically by acquiring ^{1}H NMR spectra at varying solvent ratios. Increasing the proportion of pyridine-d_5 relative to CD_2Cl_2 led to significant sharpening of the pyrrolic, and aromatic signals indicating a reduction in aggregation and improved spectral resolution (**Figure 15**).

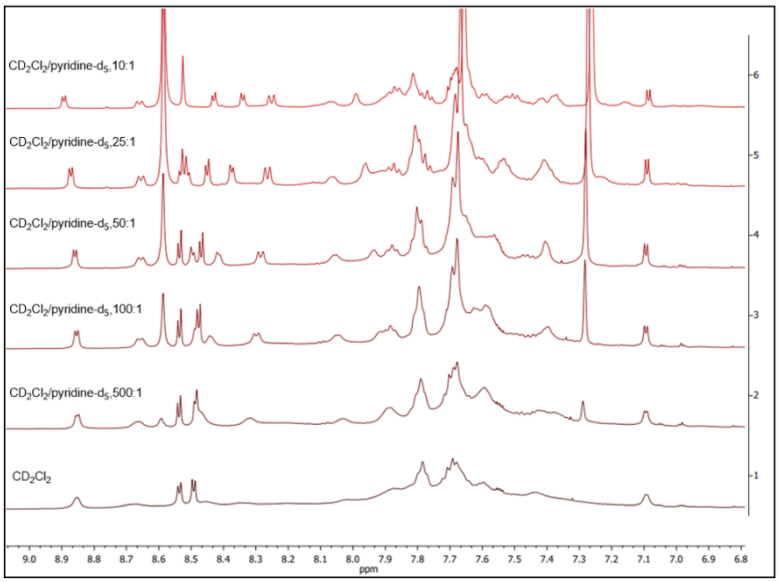

Figure 15: ^{1}H-NMR of the downfield region of the *N*-fused porphyrin dimer **25** in CD_2Cl_2 and different ratios of pyridine-d_5.

The optimal spectral resolution was achieved at a CD_2Cl_2 to pyridine-d_5 ratio of 25:1. Consequently, the subsequent ^{1}H NMR measurement was conducted using this solvent mixture to ensure optimal signal clarity and representation (**Figure 18**).

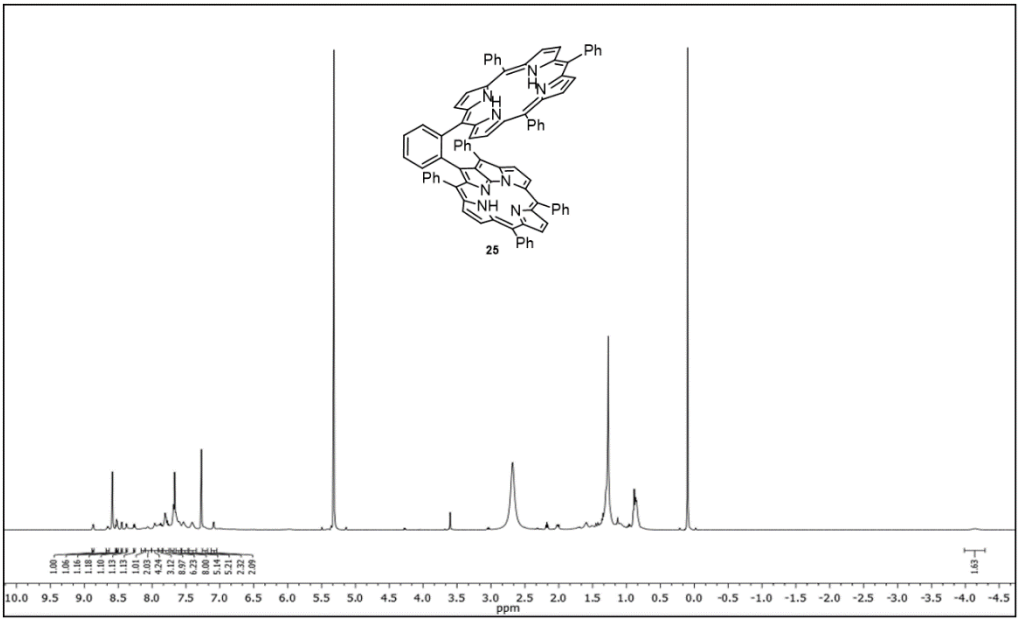

Figure 16: ^{1}H-NMR spectrum of the *N*-fused porphyrin dimer **25** in CD_2Cl_2/pyridine-d_5 (25:1) measured at a 500 MHz spectrometer with 64 scans.

To address potential π–π stacking or aggregation effects, variable-temperature ^{1}H-NMR spectroscopy was conducted. It is well-established in the literature that elevated temperatures can disrupt intermolecular aggregation, thereby improving spectral resolution.[132, 133] Accordingly, the dimeric compound was dissolved in DMF-d_7 and subjected to ^{1}H-NMR

measurements at various temperatures to assess changes in signal sharpness and chemical shift behavior (**Figure 17**).

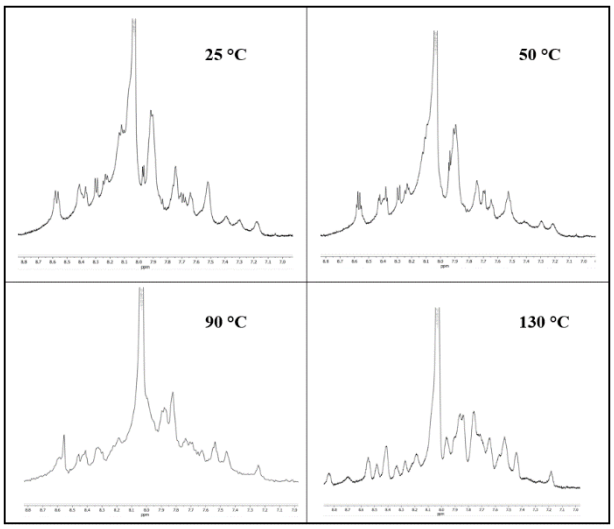

Figure 17: ^{1}H-NMR spectrum of the *N*-fused porphyrin dimer **25** in DMF-d_7 at 25°C, 50°C, 90°C, and 130°C.

3.1.2.2 UV-Vis absorption spectra analysis

UV-Vis absorption spectroscopy of NCP in CH_2Cl_2 reveals that the absorption bands have a bathochromic shift compared to the standard TPP. The *Sorét* band appears at 439 nm, and the *Q*-bands exhibit maxima at 541 nm, 582 nm, and 726 nm. This characteristic absorption of the NCP fits in well with the other analytics and confirms the predicted structure (**Figure 18**).

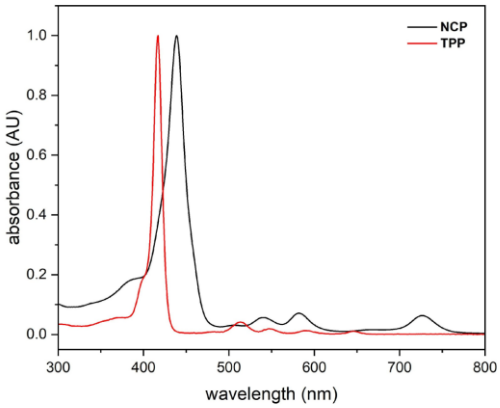

Figure 18: Comparison of the normalized UV-Vis absorption spectrum of NCP (black) and TPP (red).

The UV-Vis absorption spectra of compounds **2** and **5** corroborate the characteristic features reported in the literature for *N*-fused porphyrin frameworks.[132, 133] For the *N*-fused bromo derivative, intense absorption bands are observed at 360 nm, 489 nm, and 561 nm, along with weaker bands at 647 nm, 707 nm, and 885 nm. In comparison, the *N*-fused aldehyde derivative

exhibits slightly red-shifted absorption maxima at 367 nm, 500 nm, 545 nm, 648 nm, 707 nm, 879 nm, and 972 nm (**Figure 19**).

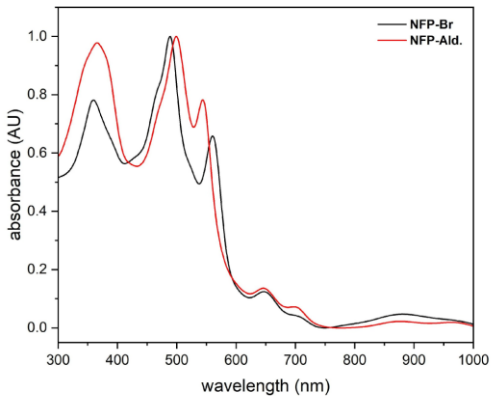

Figure 19: Comparison of the normalized UV-Vis absorption spectrum of NFP-Bromide (black) and NFP-Aldehyde (red).

The UV-Vis absorption spectrum of the dimeric ligand distinctly displays characteristic *Q*-bands in the 500–580 nm range, along with additional weak, *Stokes*-shifted *Q*-like bands around 650 and 720 nm. These latter absorptions can be attributed to the $S_0 \rightarrow S_1$ transition of the *N*-fused porphyrin subunit.

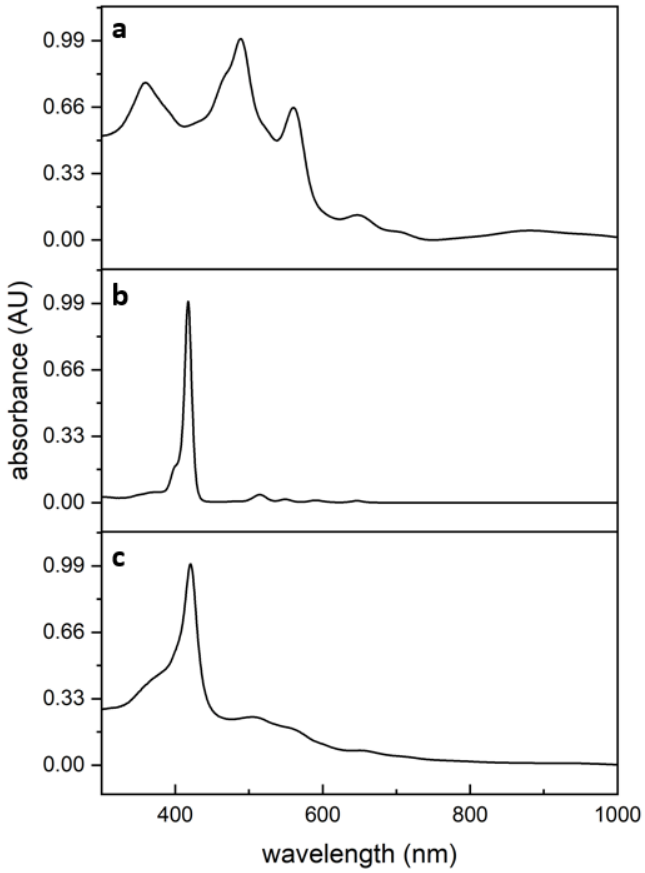

Figure 20: Comparison of the normalized UV-Vis absorption spectrum of NFP-aldehyde (**a**), TPP (**b**) and *N*-fused dimer (**c**).

By comparing the dimeric absorption to its monomeric counterparts, one can see that the dimeric spectrum is a combination of both the monomeric ones with the characteristic *Sorét*-band of TPP at 420 nm and a combination of TPPs *Q*-bands and NFPs bands at 505 nm, 564, and 660 nm (**Figure 12**). This further proves the existence of the N-fused porphyrin in the dimeric compound.

3.1.2.3 Ion mobility measurements, mass spectrometry, and DFT calculations

Due to the inability to crystallize the dimeric compound and determine its solid-state structure, ion mobility spectrometry (IMS) coupled with mass spectrometry was employed to gain further structural insights into the singly protonated dimer species in the gas phase. The analytical approach utilized here follows previously established protocols developed for related porphyrin and porphyrin-oligomer systems.[127, 134] Measurements were conducted using a trapped ion mobility spectrometry-time-of-flight mass spectrometer (TIMS-TOF MS) equipped with an electrospray ionization source. The operating principles of trapped ion mobility spectrometry (TIMS), a high-resolution IMS technique, have been extensively described elsewhere.[135] Briefly, TIMS separates ions based on their mobility through a nitrogen gas stream, where ions are retained by an opposing electric field. By gradually reducing the electric field, ions elute sequentially in accordance with their mobility. The resulting mobilogram provides elution times that are converted into collision cross section (CCS) values *via* calibration against reference CCS data obtained from Agilent TuneMix™, as reported by *Stow et al.*[136] The CCS represents the rotationally averaged interaction cross-section of an ion with the buffer gas (N_2), offering insight into the compactness of the molecular structure: smaller CCS values correspond to more compact conformations. The high resolution of TIMS enables a qualitative estimation of the spatial separation between the porphyrin units in the dimeric ligand.

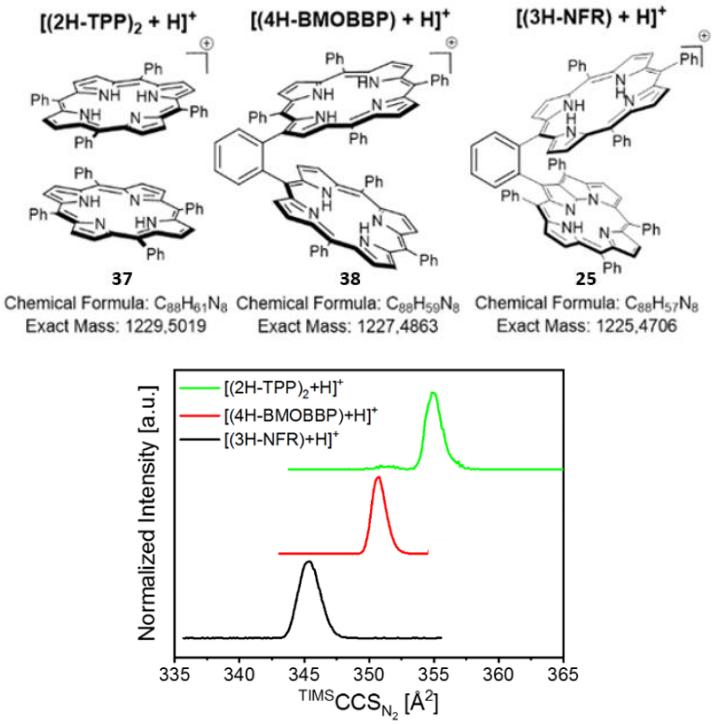

Figure 21: Structure, chemical formula, and exact masses of the target compound **25** ([(3H-NFR)+H]$^+$), two non-linked TPP molecules **37** ([(2H-TPP)$_2$+H]$^+$), and a *β-meso*-linked ortho-phenylene bisporphyrin **38** ([(4H-BMOBBP]+H]$^+$) as references.

As illustrated in **Figure 21**, the ion [(H$_2$+TPP)$_2$+H]$^+$ exhibits the largest $^{TIMS}CCS_{N2}$ value among the three dimeric species analyzed. In the absence of covalent bonds between the two porphyrin subunits, the [(H$_2$+TPP)$_2$+H]$^+$ complex is stabilized predominantly by non-covalent dispersion interactions, leading to a co-facially stacked dimeric configuration. This structural motif closely resembles that proposed for porphyrin H-aggregates in solution.[137, 138]

In a previous study, *Schissler et al.* reported that the gas-phase structure of the protonated BMOBBP dimer adopts a similar, albeit slightly more compact, co-facial arrangement.[127] Given that the protonated *N*-fused–regular porphyrin dimer (NFR) exhibits an even lower CCS value, one could infer that it likewise adopts a co-facial architecture, but with a reduced interplanar distance between the porphyrin cores compared to both [(H$_2$+TPP)$_2$+H]$^+$ and [(4H-BMOBBP)+H]$^+$.

The free-base *N*-fused porphyrin monomer can coordinate a Mn(I)(CO)$_3$ moiety, resulting in a distorted tetrahedral "on-top" complex. In this configuration, the Mn(I) center interacts with three of the four porphyrinic nitrogen atoms, leading to an overall distorted octahedral geometry around the metal center.[65] Upon reaction of the triamino-substituted *N*-fused–regular porphyrin dimer with Mn(CO)$_5$Br in DMF, a new species is formed that is detected by ESI-

MS as $[2Mn–3(CO)–NFR]^+$ and further proves the existence of the *N*-fused moiety in the dimeric compound. The $[2Mn–3(CO)–NFR]^+$ species is most plausibly a heterobimetallic complex in which a $Mn(I)(CO)_3$ unit is coordinated to the *N*-fused porphyrin, while a Mn(III) ion is coordinated to the regular porphyrin unit. This assignment is further supported by the detection of minor amounts of $[Mn–H–NFR]^+$ in the ESI-MS spectrum, consistent with a Mn(III)–porphyrin complex coexisting with an uncoordinated NFP moiety.

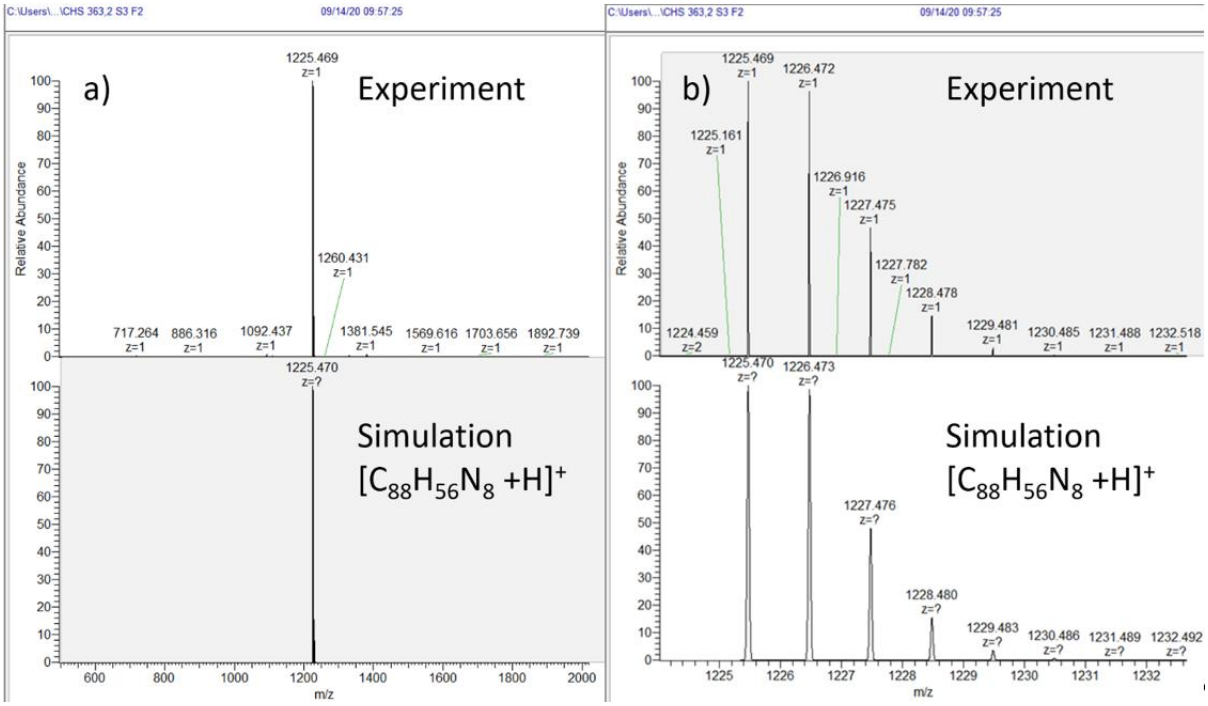

Figure 22: Simulated and actual ESI mass spectrum of the NFR dimeric ligand **25** ($[(3H\text{-}NFR)+H]^+$).

The ESI-MS spectrum of the ligand reveals that both the experimentally observed exact mass and the corresponding isotopic distribution match precisely with the simulated values, thereby providing strong confirmation of the proposed molecular structure for the NFR ligand

(**Figure 24**) as well as for the respective Mn(I)/Mn(III) complex (**Figure 25**).

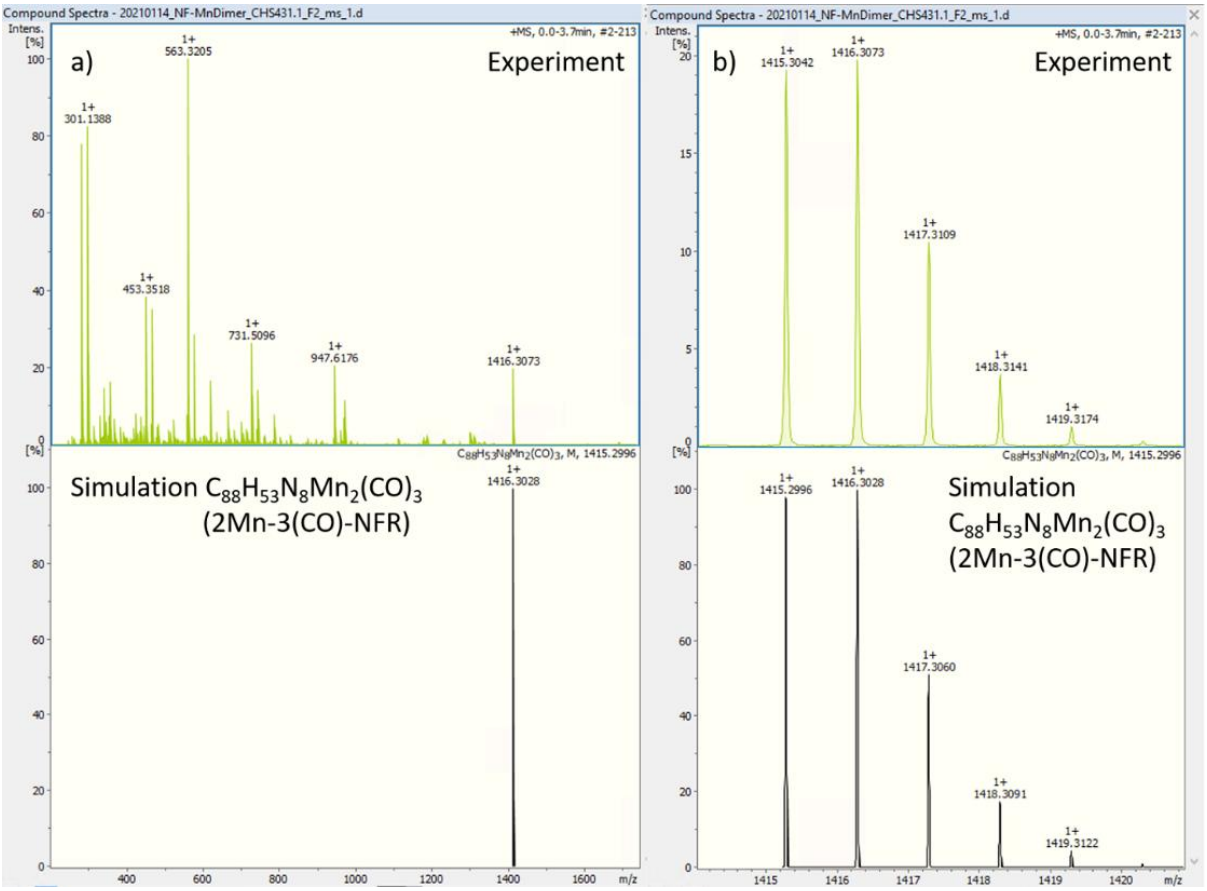

Figure 23: Simulated and actual ESI mass spectrum of the NFR-Mn dimeric complex ([2Mn-3(CO)-NFR]$^+$) complex.

Two isomeric forms of the complex are theoretically possible: An "internal" coordination mode in which the Mn(I)$(CO)_3$ fragment is located between the two porphyrin planes, bound to the NFP from the inside, or an "external" coordination mode where the Mn(I)$(CO)_3$ unit is bound to the NFP on the outer side of the dimer. Assuming that the NFR ligand adopts a co-facial arrangement in DMF, analogous to the configuration inferred in CD_2Cl_2, the formation of the external isomer is expected to proceed without significant steric hindrance. In contrast, the generation of the internal isomer would likely require a substantial activation barrier due to the need to disrupt the "clam shell" structure. Consequently, the [2Mn-3(CO)-NFR]$^+$ complex is anticipated to predominantly exist as a single, externally coordinated isomer. To evaluate this hypothesis, a TIMS analysis of the [2Mn-3(CO)-NFR]$^+$ complex was performed.

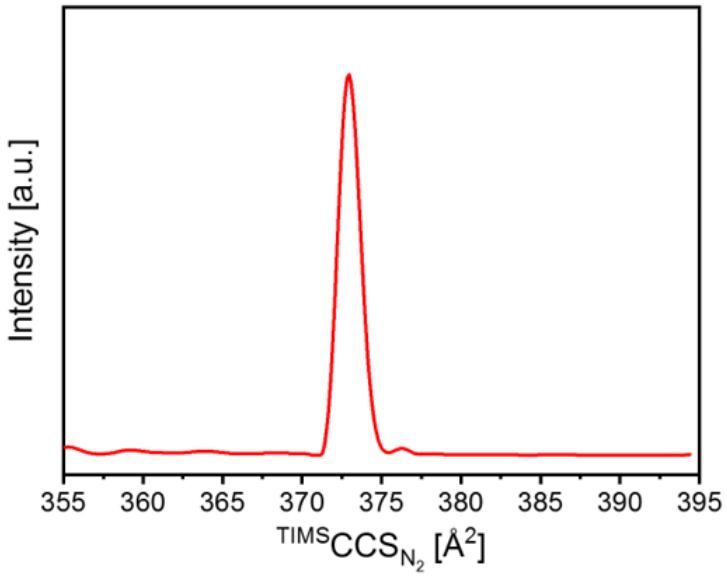

Figure 24: TIMS experiment of [2Mn-3(CO)-NFR]$^+$ revealing in a single mobilogram.

The resulting mobilogram displays a single, well-defined peak. This observation suggests one of three possibilities: (i) only one isomer is present, (ii) multiple isomers possess indistinguishable collision cross sections (CCS) under the resolution provided by TIMS, or (iii) different isomers undergo rapid interconversion on the experimental timescale. The third scenario appears unlikely, as the structural rearrangements required to convert between internal and external isomers would necessitate high activation energies not compatible with the thermal energy available under the experimental conditions.

To evaluate whether TIMS could distinguish between the external and internal isomers, if both were present, DFT calculations were carried out on the two di-manganese complexes. These computations were performed using the *Turbomole* software package[139], employing the def2-SVP basis set and the TPSS functional, along with D3-BJ dispersion correction. Given that Mn(I) and Mn(III) are open-shell species, various spin states of the [2Mn-3(CO)-NFR]$^+$ ion had to be considered to accurately model the system's electronic structure.

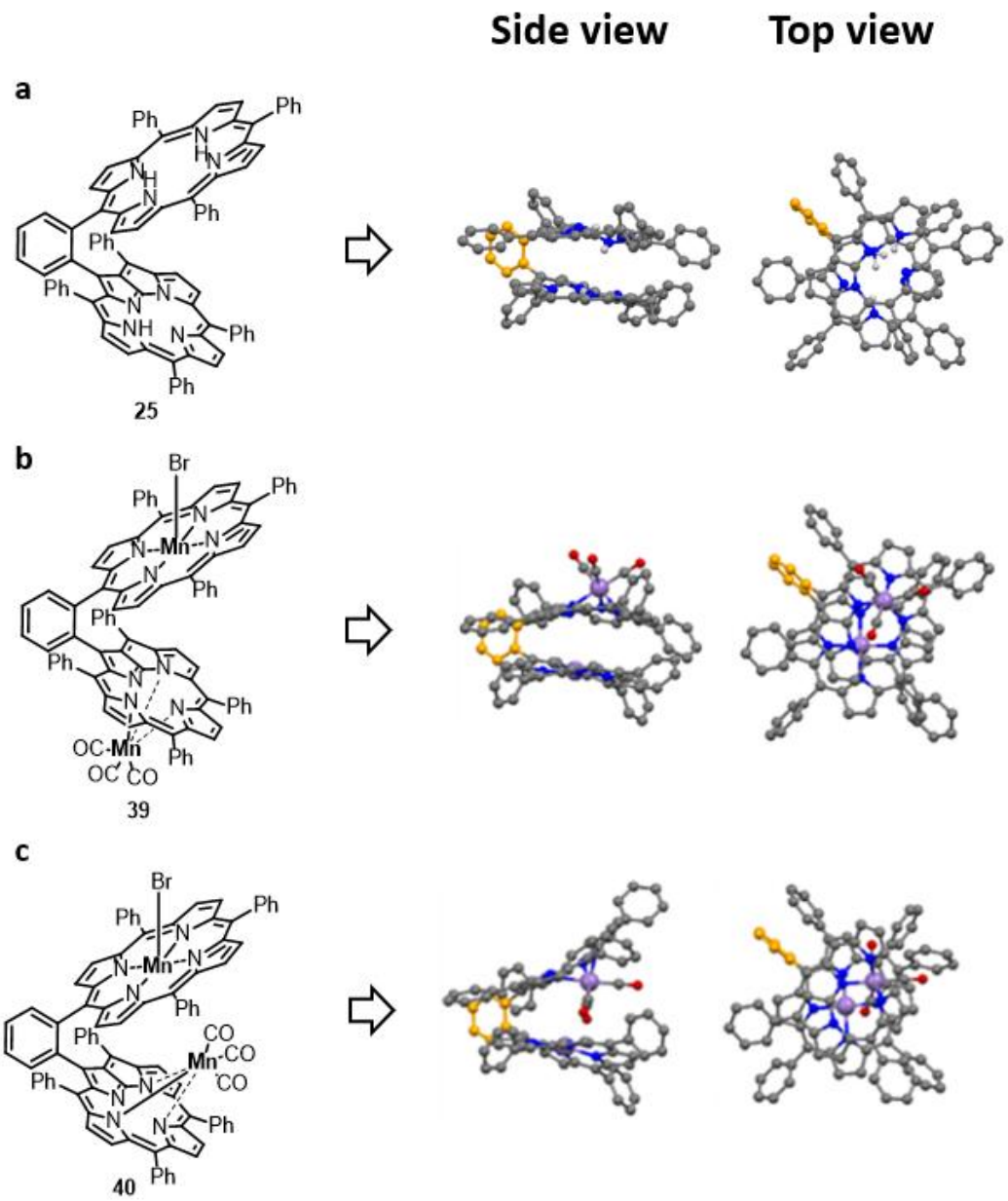

Figure 25: DFT-calculated structure of the NFR ligand (**a**) and Mn(I)Mn(III) complexes for the external (**b**) and internal (**c**) coordination, presented in side view and top view, as a model for [2Mn-3(CO)-NFR]+. The calculations were carried out in *Turbomole* with def2-SVP, TPSS and D3-BJ. The carbon atoms are shown in grey (with an orange linker-phenyl for clarity), the nitrogen atoms are plotted in light blue, the oxygen atoms in red and the manganese atoms in purple. They represent the structures in their respective lowest energy quintet configuration.

3.2 Effective reduction of carbon dioxide with a heterobimetallic porphyrin complex

3.2.1 Current state of research

Porphyrins are highly versatile ligands, capable of coordinating a broad spectrum of metal ions without requiring alterations to their core structure. Their modular synthesis makes them ideal candidates for constructing heterobimetallic active site analogs that mimic enzymatic environments. In particular, dimeric porphyrins offer valuable platforms for modeling cooperative magnetic, catalytic, and optical interactions between closely spaced metal centers.[127] In 2015, *Naruta et al.* introduced the first ortho-phenylene-linked porphyrin dimer capable of efficiently reducing CO_2 to CO, outperforming its monomeric counterparts.[140] They demonstrated that co-facial interactions between the porphyrin units promoted synergistic behavior between the metal centers, significantly enhancing catalytic activity. Building on this work, they reported in 2016 that modifying peripheral substituents allowed for fine-tuning of the catalyst's overpotential.[141] A subsequent 2017 study further advanced this platform by immobilizing the catalyst onto FTO surfaces.[142] However, these investigations were limited to homobimetallic systems, leaving unanswered how heterobimetallic combinations might interact within a co-facial geometry.

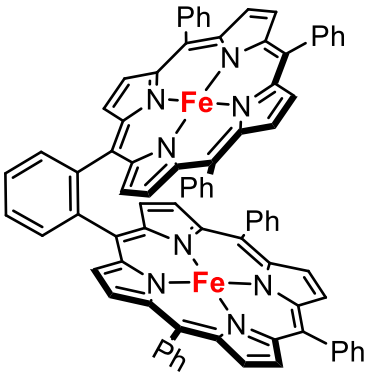

41

Figure 26: First *ortho*-phenylene-linked porphyrin dimer designed, synthesized and tested for photochemical CO_2 reduction by *Naruta et al.*

A novel direction was taken in 2023 by *Zhang* and colleagues with the introduction of a phenylene-linked porphyrin dimer incorporating a urea moiety, designed to provide hydrogen-bonding sites for enhanced CO_2 binding.[143] This system allowed for the incorporation of different metals into each porphyrin core to investigate potential cooperative effects. However, experiments involving Zn(II) and Fe(II) did not reveal any improvement in catalytic activity, suggesting that the metal centers did not exhibit meaningful cooperative interactions, likely due to insufficient spatial proximity.

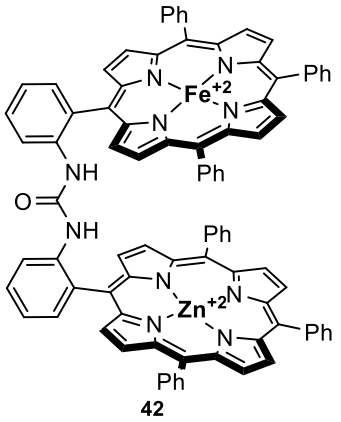

42

Figure 27: First porphyrin-based heterobimetallic complex designed, synthesized, and tested for photochemical CO_2 reduction by *Zhang et al.*

Notably, what porphyrin-based systems have not yet accomplished was recently demonstrated using an alternative approach. In 2024, a phenanthroline-based Fe/Ni complex reported by *Xiao* and co-workers was shown to activate CO_2 through a dual-site mechanism involving a key intermediate.[144] This complex achieved turnover numbers as high as 670, with minimal generation of H_2 or formate byproducts. Despite this progress, its overall catalytic efficiency remains modest, highlighting room for further development and optimization.

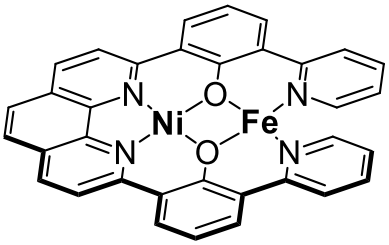

43

Figure 28: First non-porphyrin-based heterobimetallic Fe/Ni complex designed, synthesized, and tested for photochemical CO_2 reduction by *Xiao et al.*

3.2.2 Optimization of ortho-linked porphyrin structures

Over the past five decades, chemists have explored various strategies for constructing co-facial bisporphyrins. Early approaches employed relatively flexible linkers, such as double urea or amide bridges connecting porphyrins at the *meso*- or *β*-positions, resulting in sandwich-like assemblies. Later developments introduced metalloporphyrins connected *via* single imidazole or oxo bridges, requiring only one linker and one bridging ligand.[145-147] To enhance structural rigidity and enforce co-facial geometry, more robust linkers such as anthracene, bisphenylene, dibenzofuran, and xanthene were incorporated, with each scaffold bearing two porphyrin units. These systems were designed to encourage face-to-face alignment of the porphyrin cores.[148-151] A parallel advancement came from *Kobuke* and co-workers, who pioneered the synthesis of ortho-phenylene-bridged bisporphyrins.[152] Despite the intrinsic 60° angle between ortho-substituents on a benzene ring, *Osuka et al.* successfully demonstrated through X-ray crystallography that a co-facial arrangement could be achieved, with the porphyrin planes separated by approximately 3.43 Å.[153] However, these foundational methods typically yielded low overall product quantities. For instance, the highest reported total yield for a symmetrical o-phenylene-linked porphyrin dimer stands at just 0.65%.[152] A promising synthetic strategy was introduced by *Schissler et al.* in 2021, involving a stepwise condensation of 5-(2-formylphenyl)-10,15,20-triphenylporphyrin. This approach enhanced the overall yield to 4.4%, representing nearly a sevenfold improvement over previously reported methods.[127] While this method offered a much better synthetic practice to yield the target scaffold, it remained limited by low yields in the final condensation step required to form the porphyrin dimer.

3.2.2.1 Synthesis approach *via Suzuki-Miyaura* cross-coupling

The previously established approach has proven difficult to control, reproduce, and optimize. This limitation primarily stems from the necessity of adding reagents dropwise using disposable syringes in order to maintain stoichiometric precision. While this method initially enabled the successful synthesis of the target structure, it has proven impractical for broader application in follow-up studies. More precise reagent handling techniques, such as Hamilton syringes or syringe pumps, are unsuitable in this case due to the corrosive nature of the TFA catalyst employed. TFA rapidly degrades these devices, leading to inconsistent reagent delivery and premature wear of the equipment. Although disposable syringes mitigate corrosion issues, they introduce new challenges, particularly inaccuracies associated with droplet formation and the significant viscosity differences between reagents. Consequently, the development of a

more robust and scalable synthetic strategy for ortho-linked porphyrin dimers is both necessary and desirable.

The starting material for the cross-coupling reaction, 5-bromo-10,15,20-triphenylporphyrin was synthesized following the procedure described by *Schissler et al.* Briefly, 2,2′-dipyrromethane was condensed with benzaldehyde under trifluoroacetic acid catalysis to afford a porphyrinogen, which was then oxidized with DDQ to yield 5,15-diphenylporphyrin. This intermediate underwent nucleophilic aromatic substitution with phenyl-lithium to produce 5,10,15-triphenylporphyrin, which was subsequently brominated using *N*-bromosuccinimide to afford the target brominated porphyrin with an overall yield of 32% over four steps (**Figure *29***).

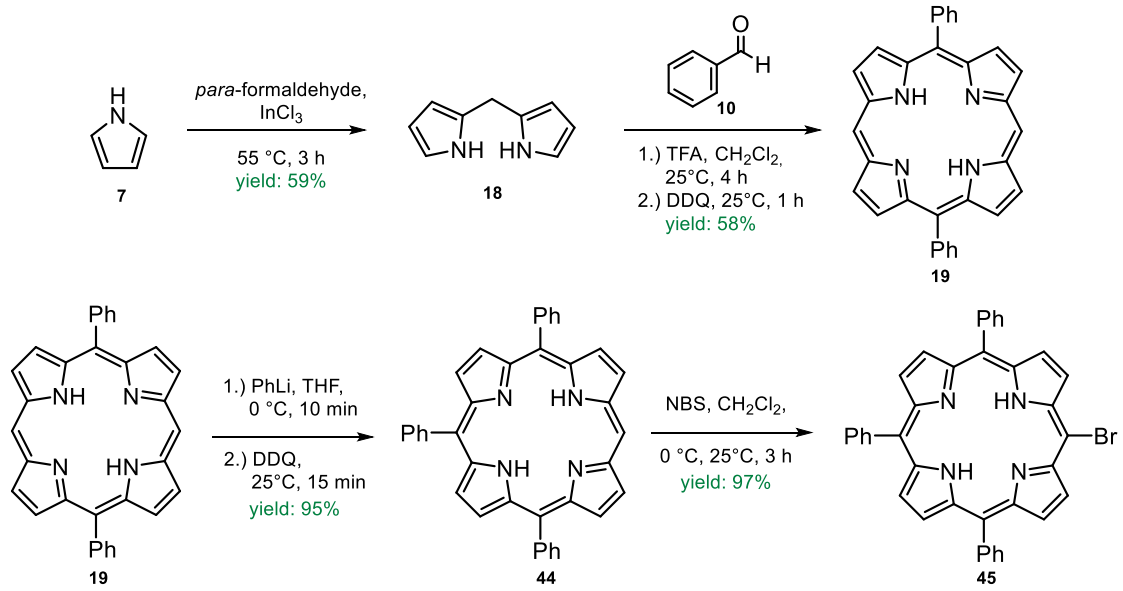

Figure 29: Four-step synthesis of compound **45** as simple access to the monomeric precursor for the subsequent cross-coupling step.

To access the coupling intermediate, compound **45** was subjected to *Suzuki–Miyaura* cross-coupling using 1,2-phenylenediboronic acid as coupling partner, enabling a following coupling reaction with a halide species. Upon workup and separation, three fractions were collected and analyzed *via* ESI-MS. The desired mono-coupled intermediate could not be detected; however, the fully coupled *ortho*-phenylene-bisporphyrin (OBBP) was clearly present in the crude mixture. This suggests that both coupling steps can proceed consecutively within a single reaction sequence under these conditions. Given the successful one-step formation of OBBP, systematic optimization of the coupling protocol was pursued. Classical strategies for improving *Suzuki* cross-couplings were applied, including screening of alternative palladium catalysts, introduction of ancillary ligands to alter the coordination environment and improve

catalytic activity, and the implementation of milder conditions through the use of weaker bases and reduced reaction temperatures.[154-156]

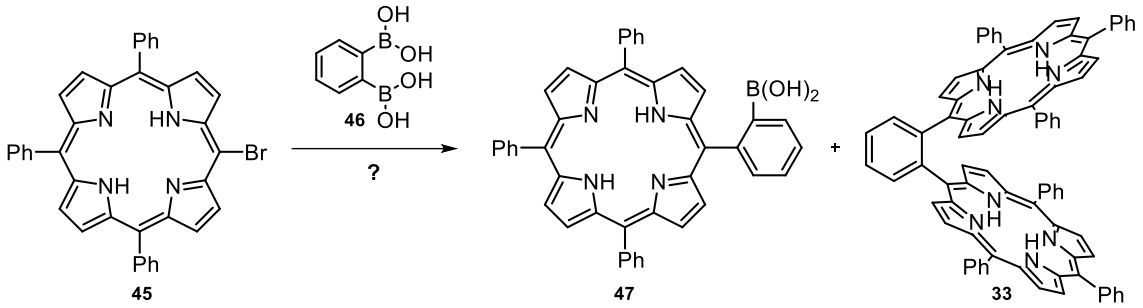

Figure 30: General reaction scheme for the cross-coupling reaction of compound **45** with reactant **46**.

Initially, four different palladium-based catalysts were screened for their effectiveness in promoting the cross-coupling reaction. To streamline the evaluation process and maximize the number of tested conditions, the crude reaction mixtures were analyzed directly by ESI-MS prior to purification. Previous experiments had demonstrated that the target product is detectable in the unpurified reaction mixture, allowing rapid exclusion of conditions under which product formation does not occur, thereby improving overall screening efficiency.

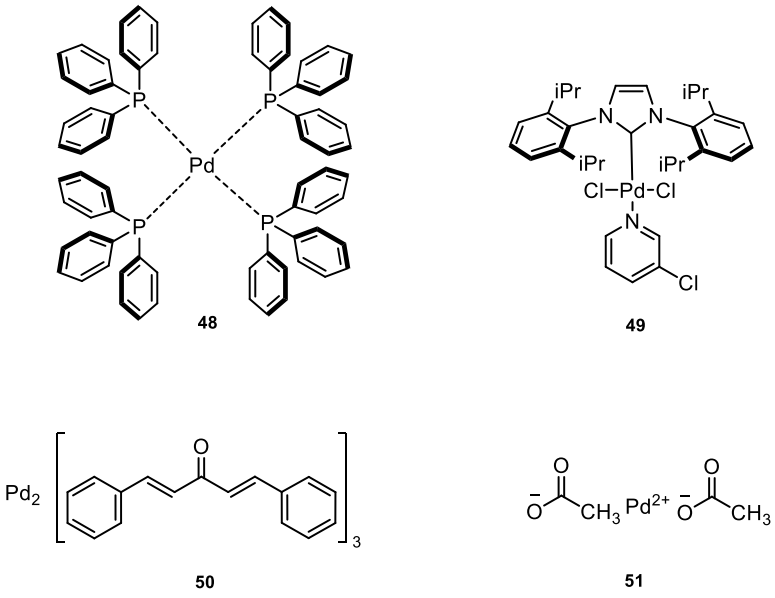

Figure 31: The four different palladium-based catalysts tested. Among them, Tetrakis(triphenylphosphin)palladium(0) (**48**), Dichloro-[1,3-bis-(2,6-di-3-pentylphenyl)-imidazol-2-yliden](3-chlorpyridyl)-palladium(II) (**49**, Pd-PEPPSI), Tris(dibenzylideneacetone)dipalladium(0) (**50**, $Pd_2(dba)_3$), and Palladium(II)-acetate (**51,** $Pd(OAc)_2$).

Among the four catalysts initially tested, only $Pd_2(dba)_3$ and $Pd(OAc)_2$ facilitated the formation of the desired product. These two catalysts were subsequently selected for further optimization under milder reaction conditions. To investigate the influence of additional ligands and temperature, a series of reactions were conducted using either K_3PO_4 or the weaker base

K_2CO_3. For each base, reactions were performed in the absence of additional ligands (**a**), as well as in the presence of XPhos (**b**) or SPhos (**c**), at reaction temperatures of 25 °C, 40 °C, and 80 °C.

Table 1: The temperature, base, and ligand variation screening results. Successful attempts are marked in green and failed attempts in red.

	$Pd_2(dba)_3$									**$Pd(OAc)_2$**								
	25°C			**40°C**			**80°C**			**25°C**			**40°C**			**80°C**		
	a	**b**	**c**	**a**	**b**	**c**	**a**	**b**	**c**	**a**	**b**	**c**	**a**	**b**	**c**	**a**	**b**	**c**
K_3PO_4																		
K_2CO_3																		

The systematic screening of reaction conditions for the *Suzuki* cross-coupling toward OBBP revealed that high temperatures and strong bases, although promoting coupling, lead to undesired side reactions such as linker decomposition and defunctionalization of the porphyrin core. Lowering the reaction temperature and employing weaker bases, along with alternative palladium catalysts, significantly improved selectivity. Among the conditions tested, the combination of $Pd(OAc)_2$, K_3PO_4, and XPhos at room temperature proved most effective for OBBP formation, while $Pd(OAc)_2$ with K_2CO_3 at 40 °C favored intermediate formation. These results emphasize the importance of fine-tuning the catalyst, base strength, ligand, and temperature to achieve efficient and selective dimer formation. Nevertheless, the inability to isolate the target compounds highlights the limitations of small-scale synthesis and potential intermediate instability, suggesting that future efforts should focus on reaction scale-up and more gentle purification protocols to enable reliable product isolation.

An alternative strategy to access the desired dimer *via* cross-coupling involved reversing the functional groups of the coupling partners. In this approach, the boronic ester functionality was introduced onto the porphyrin unit, while the bromine substituent was positioned on the linker. To this end, 5-bromo-10,15,20-triphenylporphyrin was subjected to a borylation reaction with 4,4,5,5-tetramethyl-1,3,2-dioxaborolane (pinacolborane) under palladium catalysis, affording 5,10,15-triphenyl-20-(4,4,5,5-tetramethyl-1,3,2-dioxaborolan-2-yl)porphyrin in 43% isolated yield.

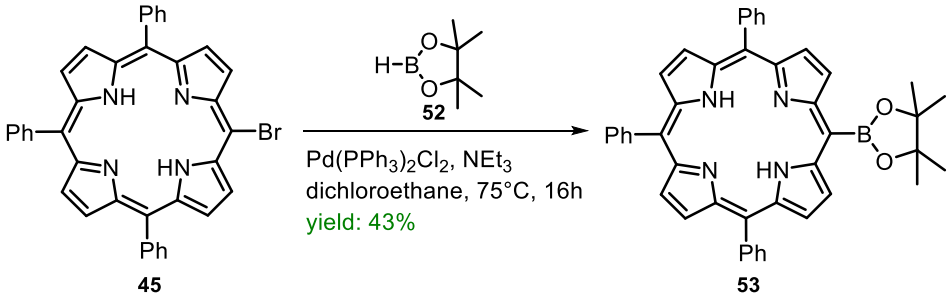

Figure 32: *Suzuki* cross-coupling to produce an asymmetric borylated porphyrin.

Following the successful isolation of the boronated porphyrin, subsequent cross-coupling reactions were conducted under conditions identified as promising in previous optimization studies. Specifically, the borylated porphyrin derivative was reacted with 1,2-dibromobenzene using $Pd(OAc)_2$ as the catalyst, K_3PO_4 as the base, and XPhos as ligand. The reactions were performed at 25 °C, 40 °C, and 80 °C, each for a duration of 16 hours.

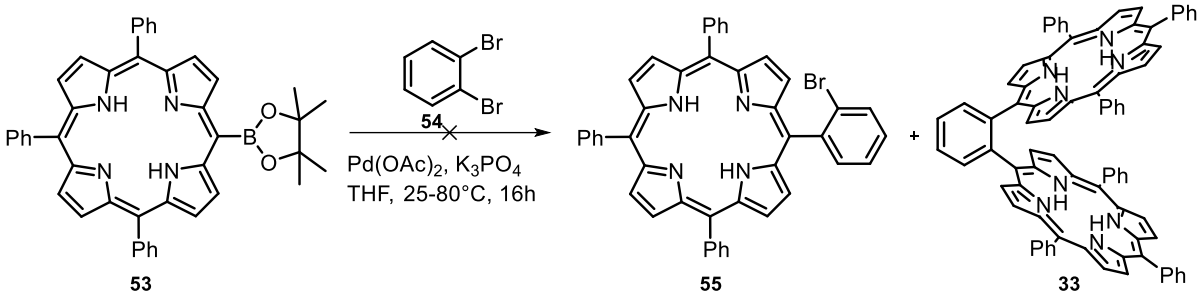

Figure 33: Synthesis approach for the switched functionalization attempt to yield OBBP with a cross-coupling reaction.

The reaction mixtures were analyzed by ESI-MS, revealing that in all cases, the predominant species was TPP. This observation suggests that defunctionalization of the bromine substituent occurred following the initial coupling event. Such decomposition is commonly attributed to overly harsh reaction conditions, highlighting the need for further optimization to enable successful synthesis of the desired product for future projects.

3.2.2.2 Synthesis approach *via* step-wise condensation

The most effective strategy to date for synthesizing OBBP *via* stepwise condensation was reported in previous work by the *Bräse* group.[127] In this approach, 5-(2-formylphenyl)-10,15,20-triphenylporphyrin undergoes a final mixed condensation with pyrrole and benzaldehyde, nominally in a 1:4:3 molar ratio. Depending on the reaction conditions, either $BF_3 \cdot OEt_2$ or TFA was used as the acid catalyst. A key aspect of this protocol is the gradual, sequential addition of pyrrole and benzaldehyde, which is continued until the conversion of the aldehyde-functionalized porphyrin slows, as monitored by TLC. To maximize yield, the

researchers intentionally deviated from the theoretical stoichiometry. Due to the inherent reactivity of pyrrole and benzaldehyde, they preferentially form TPP rather than condense with the aldehyde-functionalized porphyrin. Thus, using an excess of both pyrrole and benzaldehyde is advantageous, ensuring complete conversion of the starting material. The success of this transformation depends critically on the precise concentration of the catalyst. Insufficient catalyst loading fails to trigger the reaction, whereas excessive amounts reduce selectivity by promoting side-product formation.

The objective of optimizing this reaction is to balance catalyst loading to effectively initiate the condensation while maintaining sufficient selectivity for the desired product. A persistent challenge in this approach is the preferential formation of TPP, which arises due to its significantly lower steric hindrance compared to the OBBP framework. As a result, complete suppression of TPP formation is not feasible and remains an intrinsic limitation of the methodology. However, by carefully tuning the catalyst concentration and precisely controlling its rate of addition, it may be possible to minimize the formation of additional side products, such as porphyrin oligomers that lack ring formation. This strategy aims to shift the product distribution toward the targeted dimer by managing the reaction kinetics and reducing undesired pathways.

Table 2: Optimization approach for the stepwise condensation to yield OBBP. The equivalents are compared to 1.00 equiv. of the starting material. The rate is the addition rate of the catalyst and is related to 8h working days, which translates to 1-4 times (8h – 2h) addition over one day.

Catalyst	Equivalent	Rate (h)	Yield (%)
TFA	0.50	2	4
TFA	0.50	4	0
TFA	0.50	8	0
TFA	1.00	2	12
TFA	1.00	4	14
TFA	1.00	8	8
TFA	2.00	2	6
TFA	2.00	4	7
TFA	2.00	8	11
Catalyst	**Equivalent**	**Rate (h)**	**Yield (%)**
$BF_3 \cdot OEt_2$	0.50	2	7
$BF_3 \cdot OEt_2$	0.50	4	3
$BF_3 \cdot OEt_2$	0.50	8	2

$BF_3{\cdot}OEt_2$	1.00	2	18
$BF_3{\cdot}OEt_2$	1.00	4	26
$BF_3{\cdot}OEt_2$	1.00	8	10
$BF_3{\cdot}OEt_2$	2.00	2	7
$BF_3{\cdot}OEt_2$	2.00	4	14
$BF_3{\cdot}OEt_2$	2.00	8	13

To access the influence of time intervals between the addition of all materials, the reactants were added at intervals of 2, 4, and 8 hours until the complete consumption of the starting aldehyde-porphyrin was observed by TLC. For reactions catalyzed by TFA, the average reaction duration was approximately 2 days with 2-hour intervals, 3 days with 4-hour intervals, and 4 days with 8-hour intervals between additions. In contrast, reactions using $BF_3{\cdot}OEt_2$ as the catalyst proceeded more rapidly, with average completion times of 1 day for 2-hour intervals, 2 days for 4-hour intervals, and 4 days for 8-hour intervals. The results in **Table 2** suggest that a concentration of 1.00 equivalent of $BF_3{\cdot}OEt_2$ every 2-4 h leads to the highest overall yield. Subsequent reactions were conducted under more refined reaction control using TLC to further suppress side product formation. Reactants were introduced at three-hour intervals. Upon the first detection of a byproduct, catalyst addition was paused for a duration twice the interval time (6 hours), while the addition of other reactants continued as scheduled. This cycle was repeated over three days, with three reactant additions per day. The catalyst was added three times on the first day and once on each of the following two days. This modified protocol resulted in an average yield of 33%, nearly doubling the yield obtained with the initial method. One experiment yielded a maximum of 44% OBBP, representing the highest conversion observed for the stepwise condensation approach and highlighting the upper limit of efficiency achievable with this methodology.

3.2.3 Metal coordination in a controlled environment

The synthesis of homobimetallic complexes using ligands such as OBBP is often straightforward, as the metal coordination environment closely resembles that of the corresponding monomeric ligand systems. In contrast, the preparation of heterobimetallic complexes typically requires tailored synthetic strategies to achieve high atom economy and satisfactory yields, due to the need for selective and sequential metal incorporation.[157-159] A viable strategy for the synthesis of heterobimetallic OBBP complexes was demonstrated in 2021 by the *Bräse* group, involving stepwise metal coordination before and after dimer formation. In the case of the target Ni(II)/Fe(III) complex, the route begins with metallation of a monomeric porphyrin using $Ni(acac)_2$ under thermal conditions in DMF, affording the corresponding Ni(II)-coordinated species. This intermediate was then subjected to an acid-catalyzed condensation with pyrrole and benzaldehyde, yielding a co-facially linked o-phenylene-bridged bisporphyrin bearing one Ni(II) center and one free-base macrocycle. Subsequent metalation of the remaining free-base porphyrin with $FeCl_2$ under similar thermal conditions furnished the heterobimetallic Ni(II)/Fe(III) complex. Although the overall yield from simple starting materials was modest, the sequence highlights a robust and adaptable approach to constructing structurally defined heterobimetallic porphyrin dimers.[127] Subsequently, the same procedure was translated to ortho-linked trimeric porphyrins, confirming the adaptable approach.[128]

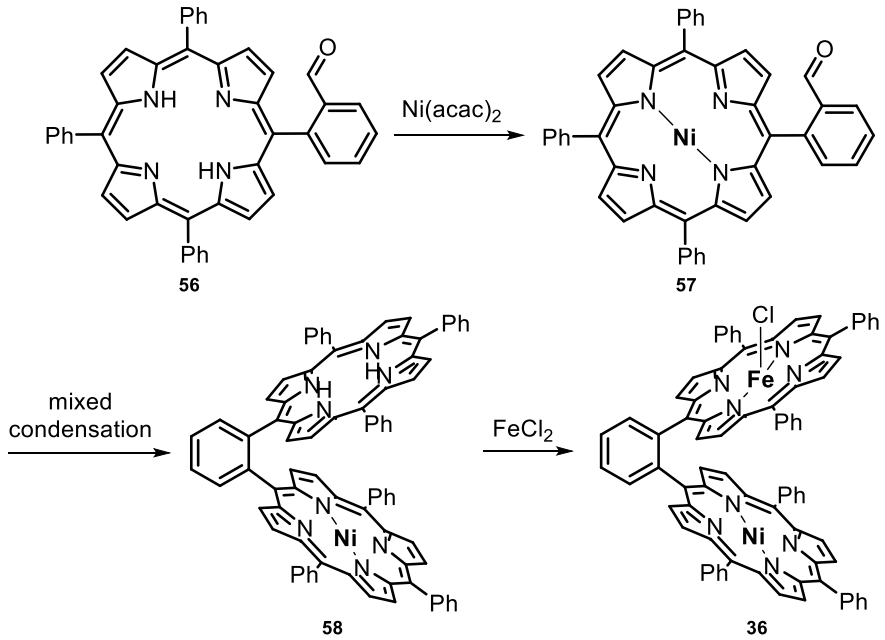

Figure 34: Previously reported reaction pathway to synthesize heterobimetallic OBBP complexes starting from 5-(2-Formylphenyl)-10,15,20-triphenylporphyrin.

However, this strategy frequently compromises the efficiency of the dimerization step, limiting its applicability for the preparative-scale synthesis required for further studies. A more effective approach entails preparing the ligand in its metal-free form, followed by the development of selective metalation conditions to introduce a single metal center post-assembly. To elaborate this, the stepwise coordination of Ni(II) from $Ni(acac)_2$ to form Ni–OBBP complexes was investigated. As a preliminary step, UV-Vis absorption spectroscopy was employed to assess whether the reaction progress could be effectively monitored *via* characteristic spectral changes.

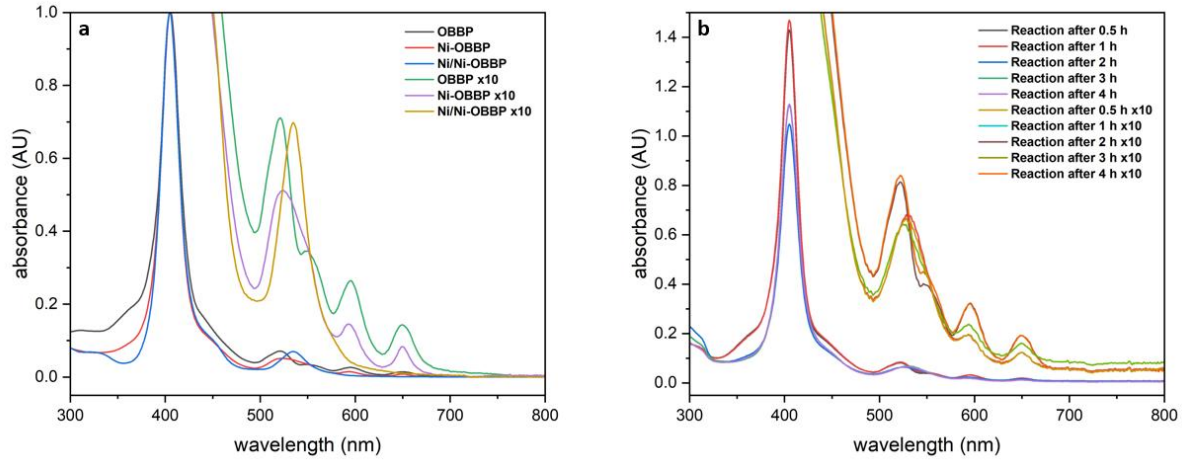

Figure 35: UV-Vis absorption spectra of OBBP, Ni-OBBP, and Ni/Ni-OBBP (**a**). UV-Vis absorption spectra of the reaction of OBBP with 1 Equiv. $Ni(acac)_2$ at 100°C in DMF for 0.5 – 4h (**b**). The *Q*-band regions were enlarged by x 10.

As anticipated, coordination of Ni(II) to the porphyrin core resulted in a progressive loss of *Q*-band signals in the UV-Vis absorption spectrum, reflecting the increased molecular symmetry upon metallation.[160] Specifically, the number of Q-bands decreased from four in the free-base OBBP ligand to three in the mono-Ni(II)-coordinated complex, and ultimately to a single *Q*-band in the fully metallated Ni/Ni–OBBP species. As **Figure 35b** displays, when OBBP is reacted with equimolar amounts of $Ni(acac)_2$, selective coordination of only one porphyrin unit is observed, even after extended reaction times of up to 4 hours. Time-dependent analysis indicates that the metalation occurs within a narrow window between 1 and 2 hours: after 1 hour, only the free-base ligand is detected, whereas after 2 hours, complete conversion to the mono-Ni(II)-coordinated complex is observed. Given the nearly quantitative conversion, the synthesis of the heterobimetallic structure can be achieved with minimal loss of starting material. When combined with the optimized mixed condensation protocol, an overall 2.6-fold increase in yield was obtained, starting from 5-(2-formylphenyl)-10,15,20-triphenylporphyrin. This improvement is primarily attributed to the enhanced efficiency of the dimerization step

rather than the metalation itself. Notably, the ability to generate substantial quantities of the free-base ligand prior to metal insertion offers a more practical and versatile approach for laboratory-scale synthesis, avoiding potential complications associated with premature metal coordination in subsequent steps.

3.2.4 Redox properties of homo- and heterobimetallic porphyrin complexes

Electron transfer processes lie at the core of reactivity in inorganic coordination complexes and play a pivotal role in the development of systems for renewable energy applications.[161-163] Molecular electrochemistry has therefore emerged as a fundamental analytical and mechanistic tool in the study of redox-active species. Electrochemical techniques, particularly cyclic voltammetry (CV), enable the direct observation and quantification of oxidation and reduction events. These processes are typically monitored by modulating the potential of an inert working electrode (e.g., glassy carbon, platinum, gold, or mercury) *via* an external power source such as a potentiostat. The applied potential alters the *Fermi* level of the electrode, allowing electron transfer to or from molecular orbitals of the analyte species when the energy levels become thermodynamically accessible. For instance, in an electrochemical reduction, a species such as ferrocene (Fc^+) can accept an electron from the electrode surface when the energy of the electrode's electrons exceeds the energy of the LUMO of Fc^+. The driving force for this heterogeneous electron transfer is the potential difference between the electrode and the redox-active molecular orbital. Cyclic voltammetry is particularly suited for investigating these redox processes, offering detailed insight into the reversibility, kinetics, and thermodynamics of electron transfer events. It is especially valuable for characterizing redox-active metal complexes and probing electron transfer-coupled chemical transformations, including electrocatalysis.[164]

To investigate the redox properties of our Ni/Fe OBBP complex, CV was conducted with the respective complex as well as his homobimetallic (Fe/Fe-OBBP, Ni/Ni-OBBP) and monomeric counterparts (Fe-TPP, Ni-TPP). CV measurements were carried out in dimethylacetamide (DMA) using 0.1 M tetrabutylammonium hexafluorophosphate ($TBAPF_6$) as the supporting electrolyte. A glassy carbon electrode served as the working electrode, and all redox potentials were referenced against the Fc^+/Fc redox couple as an internal standard.

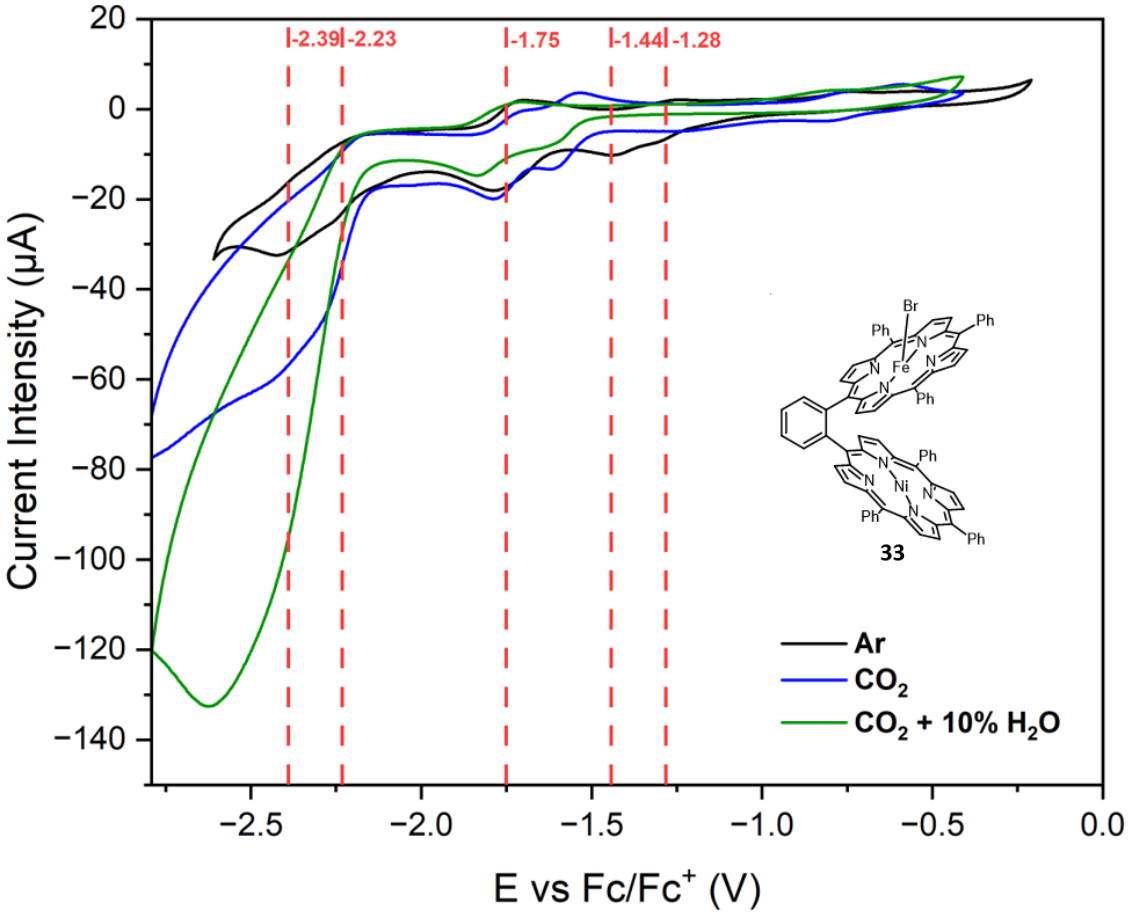

Figure 36: Cyclic voltammogram of the Fe/Ni complex. The measurements were conducted under argon (black), under CO_2 (blue), and under CO_2 + 10% proton source (H_2O, green). The red-scattered line represents the half-wave potentials under argon.

The first reversible reduction process appears at –1.28 V and is assigned to the Fe(III)/Fe(II) redox couple. A second reversible reduction at –1.44 V corresponds to the Fe(II)/Fe(I) couple, followed by a third reduction at –1.75 V, indicating further reduction to a formally Fe(0) state. The nickel center is subsequently reduced in two steps: Ni(II) to Ni(I) at –2.23 V, and Ni(I) to Ni(0) at –2.39 V. Comparison with the corresponding homobimetallic analogues reveals similar electrochemical behavior. The Fe/Fe–OBBP complex exhibits reduction events at –1.40 V (Fe(III)/Fe(II)), –1.86 V (Fe(II)/Fe(I)), and –2.01 V (Fe(I)/Fe(0)). In contrast, the Ni/Ni–OBBP complex undergoes reductions at –1.66 V and –1.76 V for the Ni(II)/Ni(I) transitions of the two nickel centers, and at –2.23 V and –2.41 V for the Ni(I)/Ni(0) transitions, closely resembling the redox profile of the heterobimetallic species.

Table 3: Electrochemical data of Fe/Fe-OBBP, Ni/Ni-OBBP and Fe/Ni-OBBP. Conditions: 3 mL DMA and 0.1 M $TBAPF_6$. Working Electrode: Glassy Carbon, Counter Electrode: Pt-wire, Quasi-Reference Electrode: Ag-wire and internal standard: Ferrocene. The values are reported versus Fc/Fc^+ oxidation.

	Ox.1	Ox.2	Red.1	Red.2	Red.3	Red.4	Red.5
Fe/Fe-OBBP	0.47 V	-	- 1.4 V	- 1.86 V	- 2.01 V	-	-
Ni/Ni-OBBP	0.65 V	-	- 1.66 V	- 1.76 V	- 2.23 V	- 2.41 V	-
Fe/Ni-OBBP	0.64 V	0.85 V	- 1.28 V	- 1.44 V	- 1.75 V	- 2.23 V	- 2.39 V

3.2.5 Photocatalytic carbon dioxide reduction

Photocatalytic CO_2 reduction experiments were conducted in a 21 mL glass vial containing a 5 mL solution of catalyst **33**, a PS, BIH as a sacrificial electron donor, triethylamine (TEA) as a co-base, and a proton source (H^+), all dissolved in dimethylacetamide (DMA). Prior to irradiation, each vial was sealed and purged with CO_2 for 15 minutes to ensure saturation. Irradiation was then carried out using a 450 nm light source, and gaseous products were analyzed at defined intervals using gas chromatography equipped with two dielectric-barrier discharge ionization detectors (GC-BID).

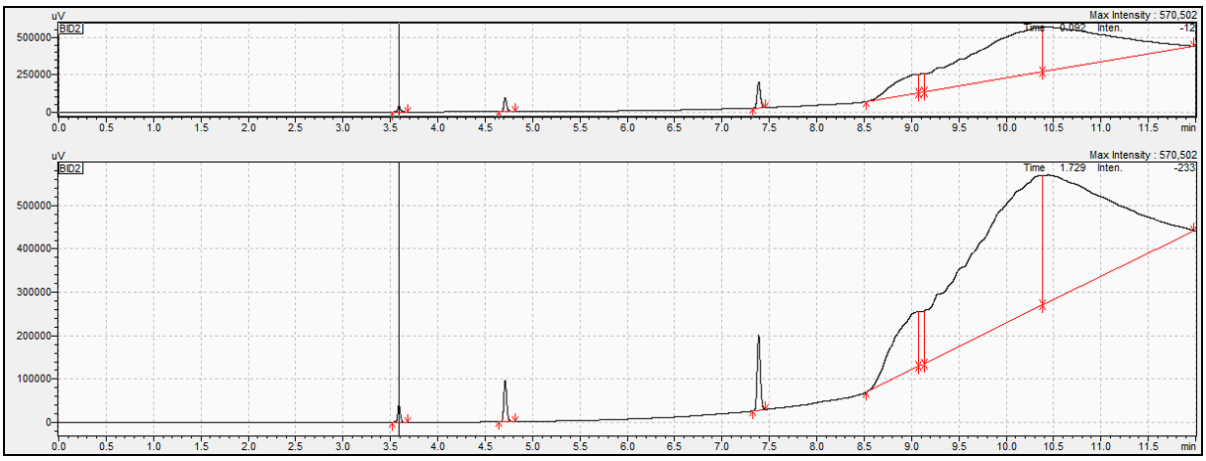

Figure 37: Interface of the GC-BID measurements with a peak at 3.58 min. (Ar/O_2), 4.72 min. (N_2), and 7.44 min (CO) retention time.

Reaction conditions were systematically optimized by varying the photosensitizer, proton source, catalyst concentration, and evaluating reproducibility. Negative control experiments lacking individual components such as CO_2, light, PS, or H^+ confirmed the necessity of all components. All experiments were optimized to achieve the highest turnover number (TON), representing the maximum number of substrate molecules converted to product per active site.

Table 4: Comparison of the proton sources H_2O, trifluoroethanol (TFE) and phenol (PhOH). Conditions: 10µM catalyst, 500 µM PS ($Ru(bpy)_3Cl_2$), 1 mL TEA as base in 5 mL DMA in a 21 mL GC-BID glass vial. The samples were irradiated at 450 nm for 48h.

entry	H^+ source	CO /µmol	H_2 /µmol	CH_4 /µmol	TON (CO)	Sel. (CO) /%
1	H_2O	0.192	0	0	8	100
2	H_2O	0.362	0,576	0	14	39
3	TFE	0	0	0	0	0
4	TFE	0.267	0	0.007	53	98
5	PhOH	1,150	0	0	230	100
6	PhOH	1,293	0	0	259	100

Initial optimization of the proton source was conducted using a 10 µM solution of catalyst and $Ru(bpy)_3Cl_2$ as the PS, with water (H_2O), trifluoroethanol (TFE), and phenol (PhOH) evaluated based on their decreasing pK_a values: 15.7 (H_2O), 12.4 (TFE), and 10.0 (PhOH) (**Table 4**). All three proton sources facilitated photocatalytic CO_2 reduction, yielding CO as the major product. Water demonstrated moderate CO production; however, one trial exhibited poor selectivity, with significant formation of hydrogen (H_2) as a side product. TFE showed higher CO generation and generally good selectivity, but one replicate failed to produce detectable conversion, raising concerns about reproducibility. Phenol provided the most consistent and efficient performance among the three, affording nearly fivefold higher CO production relative to TFE while maintaining 100% selectivity for CO. These findings suggest that lower pK_a proton donors are more suitable for this system, with phenol selected as the optimal proton source for all subsequent photocatalytic studies.

Subsequent optimization focused on the catalyst concentration, a critical parameter for accurate determination of the TON. Systematic variation of the catalyst concentration was performed to identify the optimal conditions for efficient CO_2 reduction. If comparable amounts of CO are produced at lower catalyst concentrations, this indicates that higher concentrations may not be fully utilized under the given CO_2 availability, suggesting the presence of excess catalyst. Therefore, minimizing catalyst loading without compromising activity not only improves TON but also provides insight into the system's catalytic efficiency under CO_2-limited conditions.

Table 5: Comparison of the catalyst concentrations 10 µM, 5 µM, 1 µM and 0.5 µM. Conditions: 500 µM PS ($Ru(bpy)_3Cl_2$), 1 mL TEA as base, 0.25 mL PhOH as proton source in 5 mL DMA in a 21 mL GC-BID glass vial. The samples were irradiated at 450 nm for 48h.

entry	Conc. (CAT)	CO /µmol	H_2 /µmol	CH_4 /µmol	TON (CO)	Sel. (CO) /%
1	10	13.529	0	0	271	100
2	10	14.568	0	0	291	100

3	5	0.915	0	0	37	100
4	5	1.443	0	0	58	100
5	1	7.143	0	0	1429	100
6	1	8.483	0	0	1697	100

Three catalyst concentrations, 10 µM, 5 µM, and 1 µM, were evaluated using $Ru(bpy)_3Cl_2$ as PS and PhOH as H^+. Reactions performed at 10 µM yielded results consistent with previous experiments, confirming the reproducibility of the catalytic setup. Upon decreasing the catalyst loading, CO selectivity remained high; however, overall CO production declined significantly at 5 µM. This reduction in gas-phase product yield may be attributed to competing side reactions yielding non-volatile products such as formate or methanol. Interestingly, the reaction conducted at 1 µM catalyst concentration resulted in the highest CO conversion while maintaining full selectivity, indicating this condition as the most favorable for efficient and selective CO_2 reduction.

The next focus of optimization centered on the selection of an appropriate photosensitizer, a key component influencing photocatalytic efficiency. While ruthenium-based complexes such as $Ru(bpy)_3Cl_2$ remain the benchmark in photocatalysis due to their robust photophysical properties, they rely on rare and expensive metals, prompting the exploration of more sustainable alternatives. Thermally activated delayed fluorescence (TADF) molecules offer a promising class of metal-free or earth-abundant PSs, aligning with the goals of green and sustainable chemistry. To evaluate their potential, two representative compounds were selected: the fully metal-free organic emitter 3,5-tetrakis(carbazol-9-yl)-4,6-dicyanobenzene (4CzIPN), a well-known TADF molecule, and the copper-based complex Cu(bcp)XantphosPF$_6$, which employs an earth-abundant first-row transition metal. These alternatives were directly compared to $Ru(bpy)_3Cl_2$ in photocatalytic CO_2 reduction experiments to assess their activity, selectivity, and practical viability.

Table 6: Comparison of Photosensitizers. 4CzIPN vs. $Ru(bpy)_3$ vs. Cu(bcp)XantphosPF$_6$. Conditions: 1 µM catalyst, 500 µM photosensitizer (PS), 1 mL TEA as base, 0.25 mL PhOH as proton source in 5 mL DMA in a 21 mL GC-BID glass vial. The samples were irradiated at 450 nm for 48h.

entry	**PS**	**CO /µmol**	**H_2 /µmol**	**CH_4 /µmol**	**TON (CO)**	**Sel. (CO) /%**
1	4CzIPN	2.648	11.965	0.014	530	18
2	4CzIPN	2.260	9,040	0.010	452	20
3	$Ru(bpy)_3Cl_2$	11.010	0	0	2202	100
4	$Ru(bpy)_3Cl_2$	7.957	0	0	1591	100

5	Cu(bcp)XantphosPF$_6$	5.565	0	0	1113	100
6	Cu(bcp)XantphosPF$_6$	3.853	0	0.004	771	100

As summarized in **Table 6**, all tested photosensitizers demonstrated viability for driving the photocatalytic reduction of CO_2 under the chosen conditions. The fully metal-free TADF compound 4CzIPN facilitated the formation of multiple gaseous products, including CO, H_2, and trace amounts of CH_4. The detection of methane, representing the most reduced carbon product accessible in this system, underscores the compatibility of 4CzIPN with deep multi-electron reduction processes. However, the product distribution revealed limited selectivity toward CO, the desired primary reduction product, due to significant concurrent hydrogen evolution. In contrast, the copper-based photosensitizer Cu(bcp)XantphosPF$_6$ exhibited markedly improved selectivity toward CO formation, achieving TONs as high as 1113. This highlights its strong potential as a renewable, earth-abundant alternative to noble-metal-based systems. Nonetheless, Ru(bpy)$_3$Cl$_2$ outperformed both alternative PSs, delivering the highest CO yields with exceptional selectivity. These results reaffirm the superior efficiency and reliability of ruthenium-based complexes in photocatalytic CO_2 reduction, albeit at the cost of sustainability and material scarcity.

To benchmark the photocatalytic performance of the Fe/Ni heterobimetallic catalyst, comparative experiments were conducted under analogous conditions using its homobimetallic analogues as well as the corresponding monomeric complexes. This evaluation aimed to demonstrate the enhanced activity and selectivity conferred by the heterobimetallic configuration and possible cooperative activity between both metal centers.

Table 7: Comparison of analogous catalysts tetraphenylporphyrin-nickel(II) (Ni-TPP), tetraphenylporphyrin-iron(III) (Fe-TPP), Ni/Ni-OBBP and Fe/Fe-OBBP. Conditions: 1 µM CAT, 500 µM PS (Ru(bpy)$_3$Cl$_2$), 1 mL TEA as base, 0.25 mL PhOH as proton source in 5 mL DMA in a 21 mL GC-BID glass vial. The samples were irradiated at 450 nm for 48h.

entry	**CAT**	**CO /µmol**	**H_2 /µmol**	**CH_4 /µmol**	**TON (CO)**	**Sel. (CO) /%**
1	Ni-TPP	0.406	2.129	0	81	16
2	Ni-TPP	0.332	3.440	0	66	9
3	Fe-TPP	0.253	0	0	51	100
4	Fe-TPP	0.222	0	0	44	100
5	Ni/Ni-OBBP	0.438	3.900	0	88	10
6	Ni/Ni-OBBP	0.271	3.035	0	54	8
7	Fe/Fe-OBBP	0.144	0	0	29	100
8	Fe/Fe-OBBP	0.198	0	0	40	100

The data presented in **Table 7** highlight the general catalytic activity of the tested complexes toward photocatalytic CO_2 reduction. As anticipated, Fe(III)-based complexes, both monomeric and dimeric, exhibited comparable performance in terms of CO production and selectivity, in line with their established role as efficient CO_2 reduction catalysts.[165-167] In contrast, Ni(II)-containing analogues, which are less commonly associated with such activity, displayed similar CO conversion efficiencies but suffered from significantly lower selectivity due to increased H_2 evolution. When benchmarked against the heterobimetallic Fe/Ni complex, the superiority of the latter becomes evident. The heterobimetallic system achieved turnover numbers nearly 20-fold higher than those of its monometallic counterparts, underscoring the substantial enhancement in catalytic performance conferred by the bimetallic architecture.

To further validate the robustness of the catalytic system, reproducibility studies were conducted. Given the sensitivity of photocatalytic reactions to experimental conditions, particular care was taken to ensure consistency in sample preparation and reaction setup. Eight independent reactions were performed under the optimized conditions, and the resulting TONs were analyzed to assess the degree of variability. The low fluctuation across replicates confirmed the system's reproducibility and reliability under standardized conditions.

Table 8: Test the reproducibility and liquid phase side products ($HCOO^-$) of the best performing conditions. Conditions: 1 µM CAT (**3**), 500 µM PS ($Ru(bpy)_3Cl_2$), 1 mL TEA as base, 0.25 mL PhOH as proton source in 5 mL DMA in a 21 mL GC-BID glass vial. The samples were irradiated at 450 nm for 48h. The detection of $HCOO^-$ is displayed in section 6.

entry	CO /µmol	H_2 /µmol	CH_4 /µmol	TON (CO)	TON ($HCOO^-$)	Sel. (CO_{gas}) /%	Sel. (CO_{liquid}) /%
1	10.634	0	0	2127	36	100	98
2	9.395	0	0	1879	27	100	99
3	12.045	0	0	2409	146	100	94
4	12.261	0	0	2452	52	100	98
5	12.798	0	0	2560	56	100	98
6	7.231	0	0	1446	41	100	97
7	8.347	0	0	1669	53	100	97
8	9.672	0	0	1934	22	100	99

Under optimized conditions, utilizing 1 µM of catalyst, $Ru(bpy)_3Cl_2$ as the photosensitizer, and PhOH as the proton source with 48 hours of irradiation, a TON of 2060 ± 372 was achieved for CO production, with 100% selectivity in the gas phase. The relatively narrow TON standard deviation indicates excellent reproducibility, especially when compared to analogous photocatalytic systems, underscoring the reliability and robustness of the developed catalytic

setup.[168] As shown in **Table 8**, the overall selectivity toward CO in the gas phase was slightly below 100%, indicating the presence of additional CO_2 reduction products in the liquid phase. To assess this, a complementary experiment was conducted to quantify the formation of formate ($HCOO^-$), a well-known two-electron reduction product of CO_2. The analysis was performed using a validated ^1H NMR-based assay.[169] A calibration curve was generated by comparing varying concentrations of formic acid against a fixed concentration of ferrocene as an internal standard, enabling accurate quantification of formate in the reaction mixtures. Afterwards, $HCOO^-$ analysis was conducted after 48 hours of photocatalysis, following termination of the reaction. For each sample, 0.8 mL of the reaction mixture was withdrawn and exposed to ambient conditions for several minutes to allow residual CO_2 to dissipate. Subsequently, 36 µL of 1,8-diazabicyclo[5.4.0]undec-7-ene (DBU) was added, and the mixture was sonicated for 10 minutes. Finally, 1.16 mL of a 1.19 mM ferrocene solution in deuterated acetonitrile (MeCN-d_3) was introduced. The resulting solutions were analyzed by ^1H NMR spectroscopy under previously established conditions to quantify the concentration of formate.

Table 9: Table of the conditions for the calibration of the formation of formate.

Formic acid /mM	Solvent /L	Formic acid /mg	Ferrocene /mM
1	0,1	4,60	1
5	0,1	23,00	1
10	0,1	46,00	1
20	0,1	92,00	1
50	0,1	230,00	1
100	0,1	460,00	1
200	0,1	920,00	1

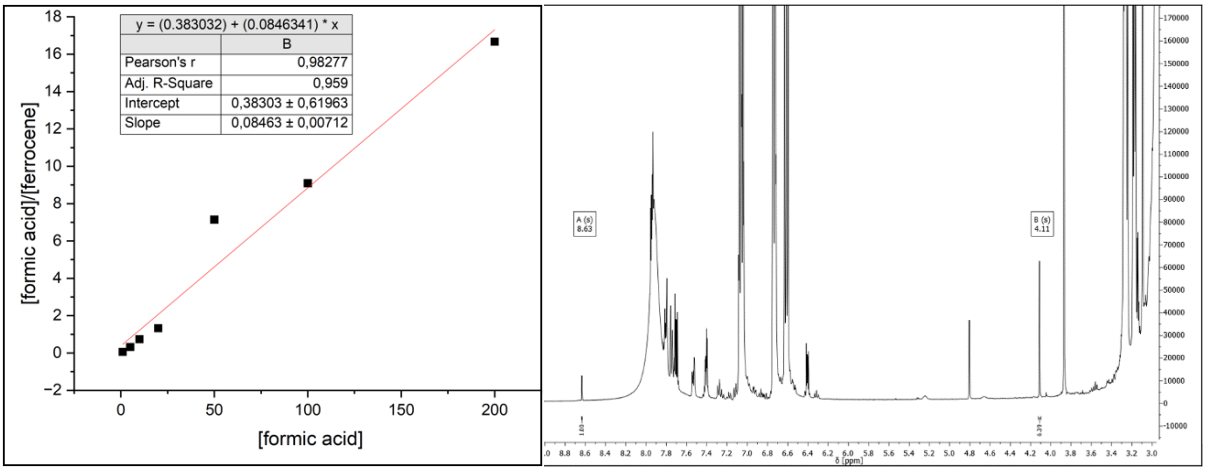

Figure 38: Calibration curve to test the liquid phase of the photoreactions for formate with the quotient of the formic acid to ferrocene concentration over the concentration of formic acid (left). NMR example of the formate detection *via* ^{1}H-NMR (right) with the formic acid peak at 8.63 ppm and the ferrocene peak at 4.11 ppm.

Further analysis of the liquid phase revealed the formation of $HCOO^-$ with an average TON of 54 ± 37, adjusting overall CO selectivity to 97%.

3.2.6 DFT calculations

The target compound could not be crystallized, precluding structural characterization by X-ray crystallography, which would have provided key insights such as the metal–metal distance and potential binding modes of CO_2 to the catalyst. To address this limitation, density functional theory (DFT) and coupled cluster (CC) calculations were employed to model the structure and approximate these critical parameters. DFT calculations revealed the presence of two energetically equivalent enantiomers. The complex lacks any mirror planes or other symmetry elements beyond its own molecular structure, indicating that it belongs to the point group C_1, characterized by the complete absence of symmetry.

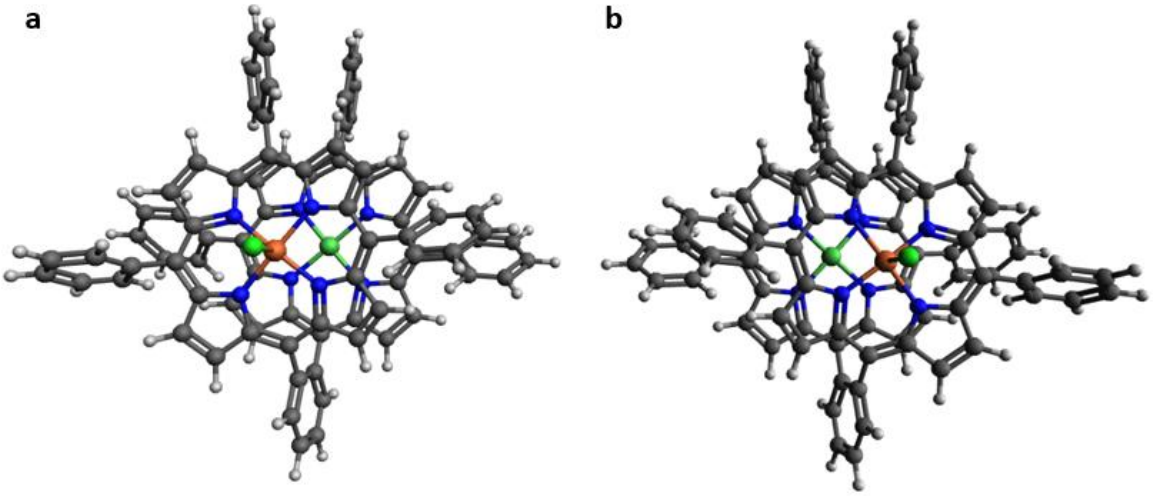

Figure 39: (S)-(+)-enantiomere (**a**) and (R)-(-)-enantiomere (**b**) of the Fe/Ni catalyst **33**. Carbon atoms are marked in grey, hydrogen in white, nitrogen in blue, iron (III) in orange, and Ni (II) in green.

All DFT were carried out using density functional theory (DFT) at the PBE0/def2-SVP level, in combination with Grimme's D3 dispersion correction and the CPCM solvation model for dimethylformamide (DMF). The resolution-of-identity approximation for Coulomb integrals (RI-J) and the RIJCOSX approximation for the exchange part of the hybrid functional were employed to accelerate the computations. For transition metals, higher-quality basis sets were used: def2-TZVP was applied to Ni and Fe atoms. The self-consistent field (SCF) procedure was performed with broken-symmetry constraints to account for open-shell or spin-polarized states. All geometries were first optimized, followed by frequency calculations to verify the nature of the stationary points. The molecular orbital diagram for compound **33** was determined using Domain-based Local Pair Natural Orbital *N*-electron Valence State Perturbation Theory (DLPNO-NEVPT2) calculations. Both Ni(II) and Fe(III) centers adopt high-spin electronic configurations, consistent with antiferromagnetic coupling between their individual spin states

and opposing magnetic dipole moments. This magnetic interaction gives rise to an overall spin state of S = 3/2. The computed metal–metal distance was approximately 4.2 Å, indicating that the magnetic interaction arises solely from dipolar coupling, with no significant orbital overlap or direct exchange interaction.

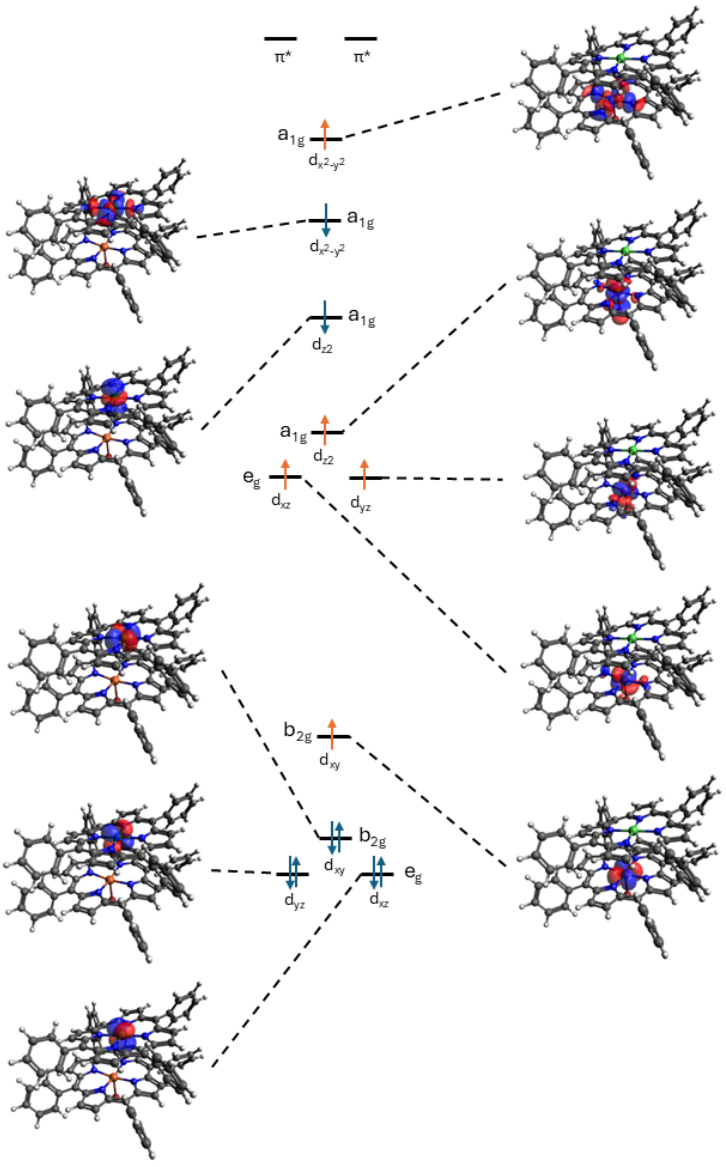

Figure 40: Irreducible representation of molecule **33** through DLPNO-NEVPT2-CASSCF calculations.

The electronic structure of the complex was investigated using a complete active space self-consistent field (CASSCF) approach with an active space of 13 electrons in 14 orbitals [CASSCF(13,14)], considering 30 roots for both doublet and quartet spin states. Dynamic electron correlation was accounted for using the strongly contracted n-electron valence state second-order perturbation theory (NEVPT2). Scalar relativistic and spin–orbit coupling (SOC)

effects were included via the mean-field SOC approach (SOCType 3), incorporating picture-change corrections. Calculations employed the def2-SVP basis set alongside the RIJCOSX approximation with corresponding def2-SVP/C and def2/J auxiliary basis sets. Solvent effects (DMF) were modeled using the conductor-like polarizable continuum model (CPCM). Initial molecular orbitals were generated from AVAS-based guesses, and all computations were carried out using 48 cores with 15 GB of memory allocated per core.

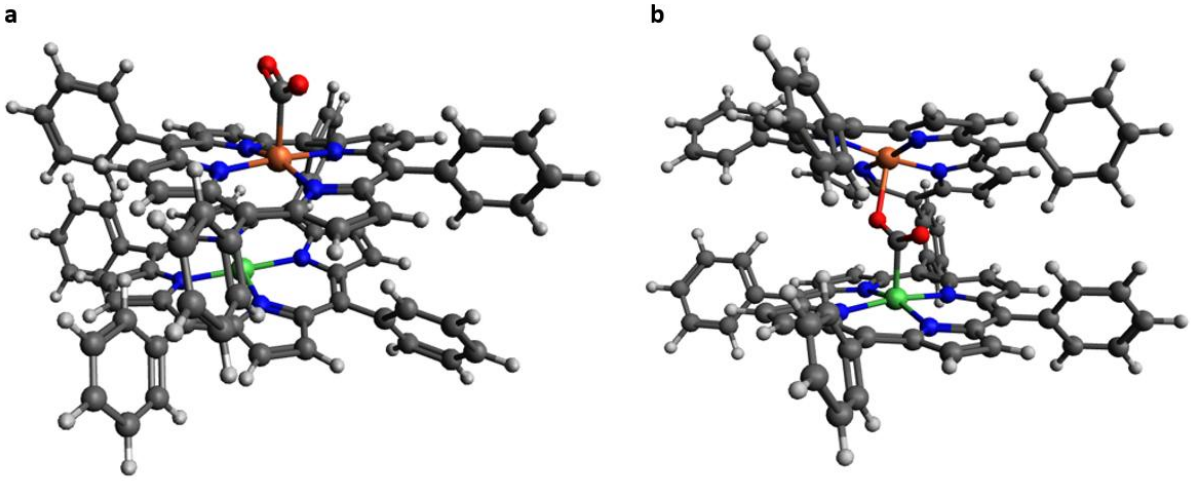

Figure 41: Possible coordination of carbon dioxide to the investigated complex **33**. Displayed is the 'on-top' coordination to the Fe(III) center (**a**) and the 'in-between' coordination (**b**). Carbon atoms are marked in grey, hydrogen in white, nitrogen in blue, oxygen in red, iron (III) in orange, and Ni (II) in green.

Both coordination sides of CO_2 were favorable in terms of energy-gain but the 'in-between' coordination (**Figure 41**, **b**), similar to the coordination of CO_2 to the active center of the CODH, is energetically preferred.

Table 10: Simulated (DELFIN (PBE0)) vs. experimental (CV) redox potentials.

V vs. Fc/Fc^+	DELFIN (PBE0)	CV	Δ
E_{red1}	-1.22	-1.28	+0.06
E_{red2}	-1.44	-1.44	0.00
E_{red3}	-1.68	-1.75	+0.07
E_{red4}	–2.04	-2.23	+0.19
E_{red5}	–2.16	-2.39	+0.23
E_{ox1}	0.54	0.64	-0.10
E_{ox2}	1.07	0.85	+0.22

The OCCUPIER module was unable to automatically determine the preferred electronic occupation, as the required calculations were not performed. Therefore, the redox potentials were estimated manually using DELFIN, based on the occupational data obtained from

CASSCF calculations. This represents a revised computational strategy: electronic occupation patterns are first established *via* multireference methods (CASSCF), followed by a manual redox potential evaluation using DELFIN, enabling a more accurate assessment of redox behavior in systems where automated occupation analysis is insufficient (**Table 10**).

3.3 Non-linear production of singlet oxygen with stacked porphyrin palladium (II) complexes

Despite the clinical success of porphyrin-based photosensitizers, ongoing research continues to focus on improving their efficacy, selectivity, and safety profiles.[170-172] Advances in molecular design, particularly through structural modification and metallation strategies, aim to overcome current limitations such as low ROS yields, poor solubility, and limited tumor specificity. As the understanding of photophysical and biological mechanisms deepens, next-generation porphyrinoid systems hold immense potential to enhance the therapeutic index of PDT.[120, 173] Ultimately, the continued evolution of photosensitizer chemistry, especially leveraging the unique properties of porphyrins, will play a pivotal role in expanding the clinical applications of PDT and advancing it as a cornerstone modality in precision cancer therapy. One promising strategy to enhance the functionality of porphyrin-based PSs involves metalation, incorporating metal ions into the central macrocyclic cavity of the porphyrin scaffold. Thanks to their extended π-conjugation and tetrapyrrolic coordination environment, porphyrins readily chelate a wide array of metal ions. Metallation not only modulates the electronic structure and redox behavior of the porphyrin but also facilitates ISC through the heavy atom effect, thereby significantly boosting triplet state population and enhancing ROS generation. In particular, metalloporphyrins containing transition metals such as platinum or palladium are of exceptional interest.[120, 174, 175] These complexes exhibit dual roles, as efficient photosensitizers and as luminescent oxygen sensors, making them attractive for both therapeutic and diagnostic applications. The rational design of metalloporphyrin-based PSs thus offers a powerful platform for developing advanced PDT agents with tailored photophysical properties, superior tumor specificity, and multifunctional capability. This evolving approach holds great promise for expanding the clinical potential of PDT and improving patient outcomes in the treatment of cancer and beyond.

3.3.1 Molecule design and photoluminescent emission

To advance the design of improved photosensitizers for photodynamic therapy, the cooperative effects of palladium(II) complexes within co-facial porphyrin architectures were investigated. Specifically, a series of mono-, di-, and trimeric porphyrins were synthesized and subsequently metalated with Pd(II) to assess their photophysical and photochemical properties. For the monomeric porphyrin, TPP-Pd(II) was synthesized according to the literature known procedures.[176] The synthesis of the ortho-phenylene-bisporphyrin was reproduced for this study using an optimized synthetic pathway detailed in Section **3.2.2.2**. For the trimeric system,

the construction of an ortho-phenylene-linked trisporphyrin and its palladium(II) complex was performed based on a synthetic protocol reported by the BRÄSE group.[128] The synthetic route began with a SUZUKI–MIYAURA cross-coupling reaction between 5-bromo-10,15,20-triphenylporphyrin and (2-formylphenyl)boronic acid to afford 5-(2-formylphenyl)-10,15,20-triphenylporphyrin. This intermediate was then subjected to a mixed condensation reaction with pyrrole in the absence of an aldehyde component, yielding a "1.5-fold" porphyrin intermediate: 5-(2-(di(1H-pyrrol-2-yl)methyl)phenyl)-10,15,20-triphenylporphyrin. Subsequently, two equivalents of this precursor were condensed with benzaldehyde under acid-catalyzed conditions to furnish the desired trimeric porphyrin scaffold. Metalation of the mono-, di-, and trimeric porphyrins with Pd(II) yielded the corresponding palladium complexes, setting the stage for further investigation of their cooperative photodynamic properties (**Scheme 15**).

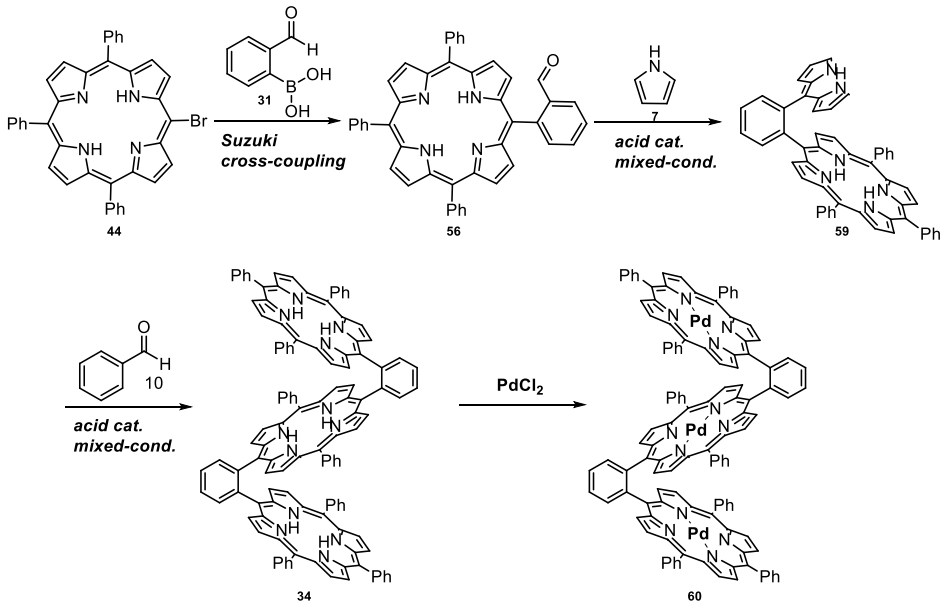

Scheme 15: Synthesis route to yield 5,15-Bis(2-(10,15,20)-triphenylporphyrinylphenyl)-10,20-diphenylporphyrin-tripalladium(II) in a 4-step synthesis.

After sufficient quantities of all three Pd(II) complexes were obtained, photoluminescence emission spectroscopy was revisited to validate their ability to generate singlet oxygen upon photoexcitation. This step was essential to confirm the photodynamic functionality of the metallated porphyrin systems and to corroborate the previously observed emission behavior. By monitoring characteristic phosphorescence signals and emission profiles, particularly in the near-infrared region around 1270 nm, a qualitative efficiency of triplet energy transfer could be evaluated, thereby providing key insights into the therapeutic potential of these Pd(II)-porphyrin complexes in PDT applications. (**Figure *42***).

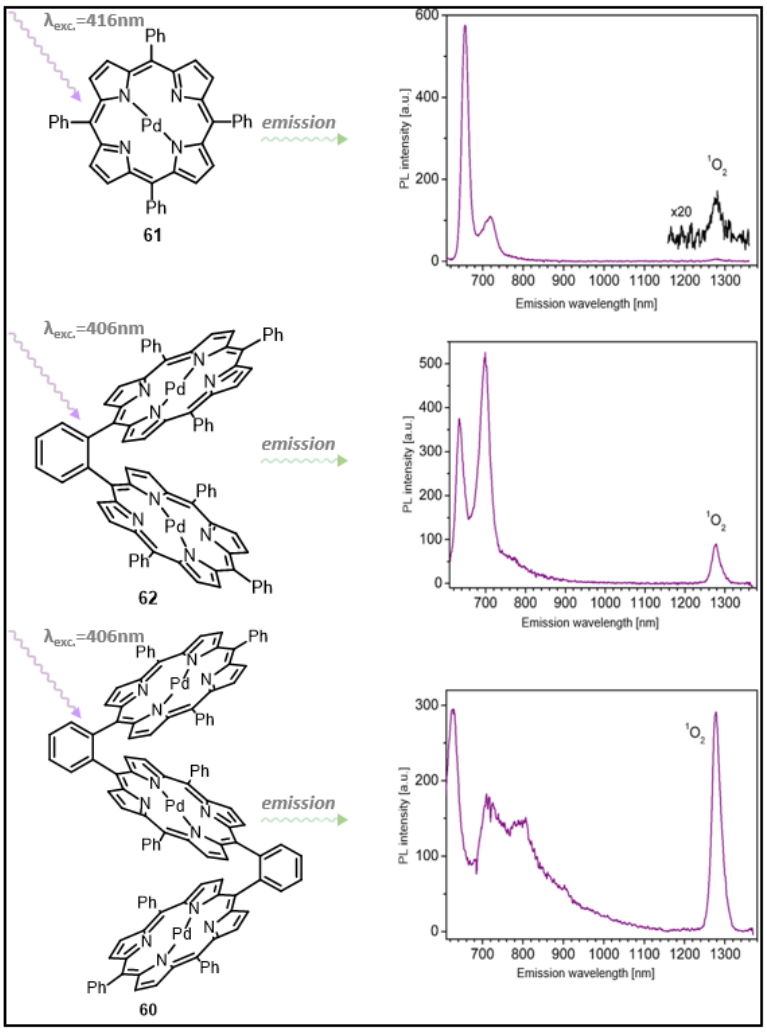

Figure 42: Photoluminescent emission spectra of compounds **61**, **62**, and **60**. Compound **61** was excited with a wavelength of 416 nm, compound **62**, and compound **60** with a wavelength of 406 nm. The respective $^1O_2$ peak in the emission spectrum is visible at 1270 nm.

Photoluminescence emission spectra of all three Pd(II)-porphyrin complexes revealed a distinct emission peak at 1270 nm, characteristic of $^1O_2$ phosphorescence. This confirms that each complex is capable of effectively sensitizing $^1O_2$ upon photoexcitation. Notably, the emission intensity exhibited a pronounced, non-linear trend: the dimeric complex showed significantly enhanced $^1O_2$ emission compared to the monomer, while the trimeric complex displayed an even greater intensity, far surpassing that of the dimer. This progressive amplification of $^1O_2$ generation with increasing number of Pd(II) centers suggests potential cooperative or excitonically coupled effects that may enhance intersystem crossing or energy transfer efficiency. These intriguing non-linear photophysical properties warrant further investigation to elucidate the underlying mechanisms and to optimize the structural features contributing to enhanced photodynamic performance.

3.3.2 Absorption studies

Several strategies exist to quantitatively evaluate the singlet oxygen generation efficiency of photosensitizers. One commonly employed method involves the photooxidation of a probe molecule that exhibits a well-defined absorption band, which diminishes upon oxidation to a non-absorbing product. By monitoring the decrease in the characteristic absorbance of the starting material over time during irradiation, the extent of photoinduced oxidation, and, by extension, the generation of $^1O_2$, can be quantitatively assessed. This time-dependent reduction in absorbance serves as a direct proxy for photosensitizer efficiency and allows for comparative analysis across different compounds under controlled irradiation conditions. For that, this work conducted a series of singlet oxygen generation experiments using the oxidation of diphenylfuran (DPF) as a model reaction. The in-situ generation of $^1O_2$ was achieved *via* photoactivation of the investigated compounds **60 - 62** under 410 nm irradiation over one minute. For this purpose, solutions containing 0.1 µM of each PS and 40 µM DPF were prepared in dimethylformamide (DMF), with corresponding PS-only solutions serving as blanks. Upon reaction with molecular oxygen, DPF undergoes oxidation at the 2- and 5-positions of the furan ring, forming a temperature-sensitive endoperoxide through the insertion of an oxygen bridge.

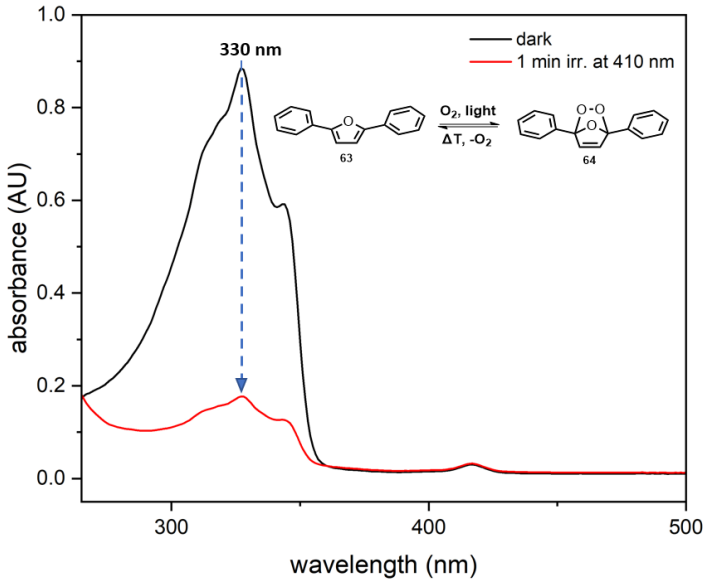

Figure 43: UV-Vis absorption spectrum of DPF without irradiation (black) and with 1 minute of irradiation at 410 nm wavelength as a general representation of the absorption quenching of DPF trough oxidation. All associated experiments are illustrated in **6.1**.

The oxidation process results in a progressive decline of the characteristic DPF absorbance band at 330 nm, serving as a spectroscopic marker for $^1O_2$ generation. The rate of absorbance

loss correlates directly with the amount of reactive oxygen species produced. However, since the efficiency of ROS generation is inherently linked to the extent of light absorbed by each PS, quantification requires correction for individual absorption profiles. To account for this, the molar extinction coefficients of all tested compounds were determined *via* serial dilution. The absorbance data for DPF were subsequently normalized and adjusted using correction factors based on the reference extinction coefficient of TPP, ensuring accurate comparison across the different PSs.

Table 11: Calculated extinction coefficients for the photosensitizers and their respective ligands. The values are based on dilution series of the PS in CH_2Cl_2, described in more detail in section **6.1**.

Photosensitizer	Extinction coefficient (L/mol·cm)
TPP	676600
Pd-TPP	405098
OBBP	690250
Pd-OBBP	532155
OBTP	950663
Pd-OBTP	111354

By normalizing the decrease in DPF absorbance at 330 nm to the respective photosensitizer's light absorption, it became evident that the metal-containing complexes, owing to their comparatively weaker absorbance at the excitation wavelength, were weighted more heavily in the analysis. This adjustment resulted in lower relative efficiency coefficients, reflecting their diminished light-harvesting capability under the standardized conditions (**Table 11**).

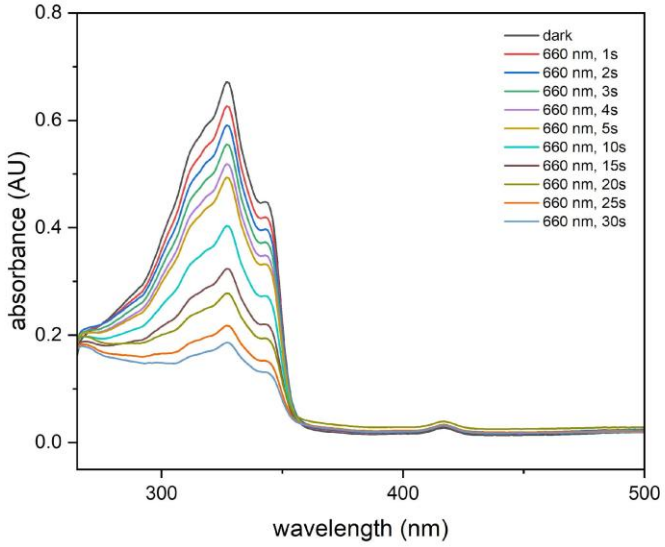

Figure 44: 0.1 µM solutions of methylene blue (MB) as positive control, together with 40 µM DPF in DMF were blanked to a pure solution of 0.1 µM of the respective sensitizer and irradiated at 410 nm over 30 seconds.

As a positive control, methylene blue (MB), a well-established photosensitizer for $^1O_2$ generation, was employed to validate the experimental setup and provide a benchmark for comparison against literature-known standards. **Figure 44** illustrates the photooxidation of DPF in the presence of MB under 660 nm irradiation for a total of 30 seconds. Absorbance measurements were recorded at one-second intervals for the initial five data points, followed by five additional measurements taken at five-second intervals.

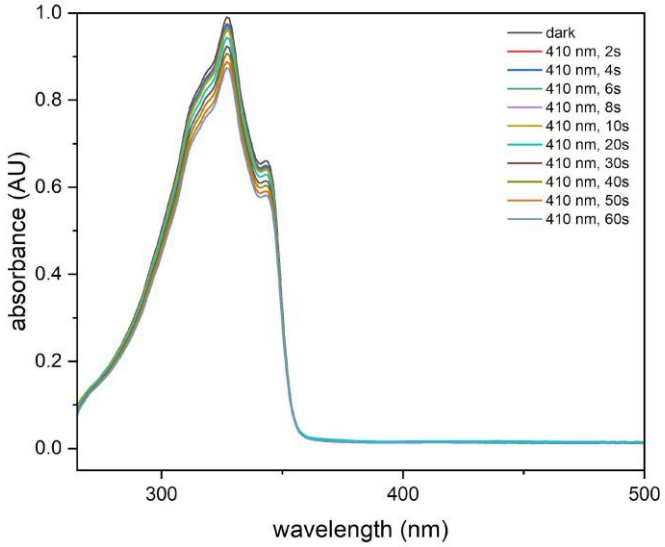

Figure 45: Negative control, 40 µM DPF in DMF were blanked to a pure solution of the solvent and irradiated at 410 nm over 60 seconds.

As a negative control, a solution containing only DPF, without any photosensitizer, was subjected to irradiation at 410 nm for one minute. As shown in **Figure 45**, a minor decrease in absorbance was observed, indicating that a small amount of DPF oxidation can occur under these conditions, likely due to background photoreactions or ambient reactive oxygen species. Nevertheless, this minimal change contrasts sharply with the pronounced spectral shifts observed upon addition of the photosensitizers. The significant enhancement in DPF oxidation in the presence of the tested compounds clearly confirms their efficacy as photosensitizers capable of generating reactive oxygen species upon light activation.

To enable a clearer comparison of the relative efficacies of the different photosensitizers, the maximum absorbance at 330 nm was normalized across all samples. The degree of absorbance decrease following irradiation was then quantitatively compared to assess singlet oxygen production by each photosensitizer. The corresponding UV-Vis spectra for each compound are provided in section **6.1**.

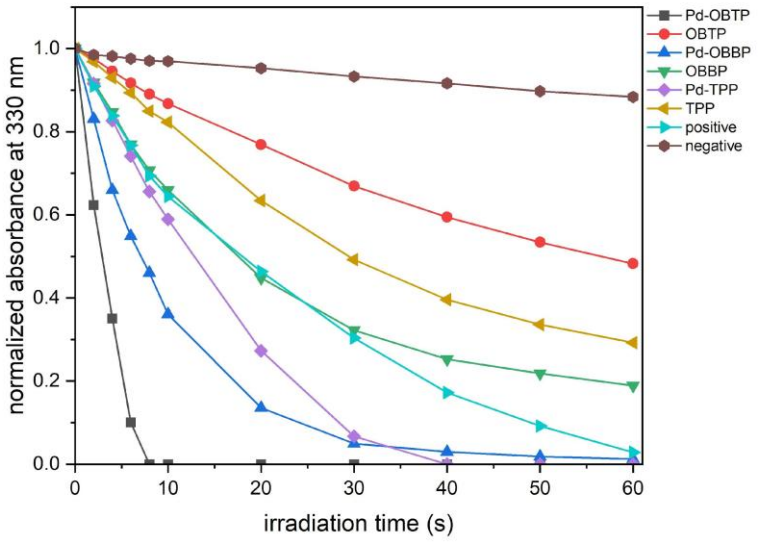

Figure 46: Normalized absorbance of DPF at 330 nm for all investigated compounds, a positive control with 50 µM MB as PS and a negative control without PS irradiated over 1 minute with influence of the absorption coefficient.

As illustrated in **Figure 46**, the three Pd(II) complexes demonstrated the highest photosensitizing efficiency, with Pd-OBTP achieving complete oxidation of DPF within just 8 seconds. In comparison, Pd-OBBP and Pd-TPP required approximately 40 seconds to reach a similar extent of oxidation. The initial rates of DPF degradation, calculated from the average absorbance decline within the first 10 seconds, were 0.150 for Pd-OBTP, 0.0640 for Pd-OBBP, and 0.041 for Pd-TPP. These results highlight the superior efficacy of the oligomeric systems:

the dimeric Pd-OBBP exhibited a 64% higher efficiency than the monomeric Pd-TPP, while the trimeric Pd-OBTP outperformed the monomer by 365% and the dimer by 235%. This nonlinear enhancement suggests a cooperative effect in singlet oxygen generation across the multimeric porphyrin systems.

3.3.3 Solubility exchange of porphyrins

To evaluate the potential of the synthesized PSs for PDT, a comprehensive biological assessment was initiated. This included standard MTT viability assays, studies on cellular uptake, intracellular reactive oxygen species generation, and evaluation of both dark cytotoxicity and light-induced phototoxicity. These experiments require the PSs to be soluble in aqueous media, as typical cell culture environments are predominantly water-based. However, the hydrophobic nature of the synthesized porphyrin complexes prevents their dissolution in such polar systems, posing a significant barrier to biological testing. To address this limitation and enable further biological investigation, structural modification of the porphyrin ligands was undertaken to enhance water solubility. A conventional strategy to improve aqueous compatibility involves the introduction of polar functional groups, such as carboxylic or sulfonic acid moieties, onto the peripheral positions of the porphyrin scaffold. In this case, sulfonation was achieved by treating the monomeric and dimeric porphyrin ligands with concentrated sulfuric acid, facilitating the attachment of sulfonic acid groups to the phenyl substituents. This modification improves solubility in polar solvents, thereby enabling the compounds' compatibility with biological assay conditions.

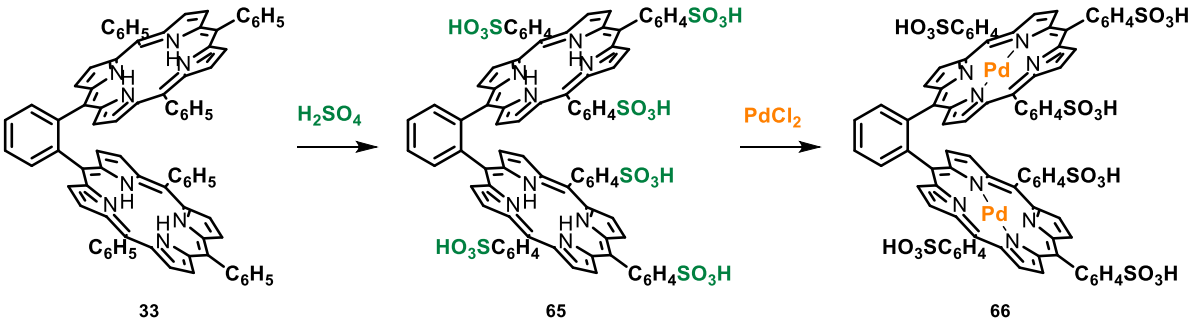

Figure 47: Synthetic polarity enhancement by attaching sulfuric acid groups for subsequent biological studies with Pd-OBBP as an example.

The OBBP ligand was successfully functionalized 6-fold with sulfonic acid groups (OBBP-S) through sulfonation, significantly enhancing its polarity and rendering it readily soluble in a range of conventional polar solvents, including water and methanol. This increased solubility is essential for enabling biological evaluation in aqueous media, such as cell culture environments. The same procedure could be converted to TPP, yielding in a tetraphenylporpyhrin with four sulfuric acid groups (TPP-S). However, the conversion of the trimer (OBTP-S) was unsuccessful; consequently, the biological assays were conducted exclusively on the mono- and dimeric complexes. Before proceeding with biological assays, it is critical to assess whether the introduction of sulfonic acid groups affects the ligand’s

photophysical properties. Structural modifications, especially those altering the electronic environment of the porphyrin core, can influence key parameters such as absorption maxima and emission efficiency.[177, 178]Therefore, a comparative photophysical characterization was performed between the non-polar parent compound and its water-soluble sulfonated derivative. This included the acquisition of UV-Vis absorption spectra to monitor any shifts in the *Sorét*- or *Q*-bands, as well as photoluminescence emission measurements to evaluate singlet oxygen generation potential. These analyses provide a foundational understanding of how sulfonation influences the photosensitizing efficiency of the modified ligand prior to biological application.

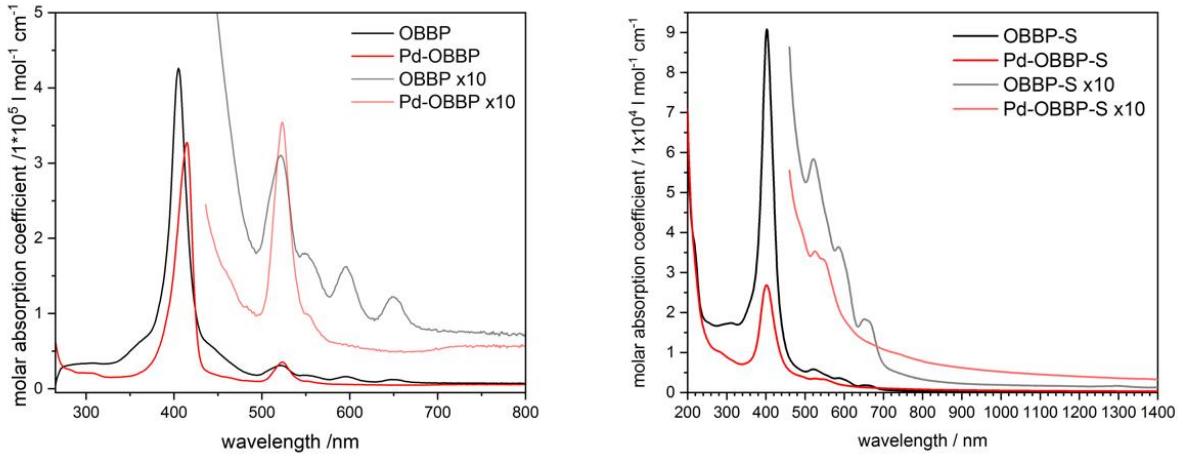

Figure 48: UV-Vis absorption spectrum comparison of the non-polar OBBP ligand and its Pd(II) complex (left) and the polar sulfonated OBBP ligand and its Pd(II) complex (right).

A comparative analysis of the molar absorption coefficients between the non-polar and polar porphyrins revealed a pronounced reduction in light absorption following sulfonation (**Figure *48***). Specifically, the parent OBBP ligand exhibited an absorption maximum around 410 nm that was approximately 4.66 times more intense than that of its sulfonated derivative. This trend was even more pronounced in the corresponding Pd(II) complexes, where the non-polar variant demonstrated a molar absorption coefficient 12.20 times greater than its sulfonated counterpart. These substantial reductions suggest that the introduction of sulfonic acid groups significantly perturbs the electronic structure of the porphyrin macrocycle, likely by disrupting conjugation or inducing conformational changes. This decline in absorbance could have important implications for the photosensitizing efficiency of the sulfonated derivatives, necessitating further investigation into their ROS-generating capability and overall photodynamic performance.

Photoluminescence measurements of the sulfonated porphyrin derivatives revealed the characteristic emission peak for $^1O_2$ at 7874 cm^{-1}, confirming the retention of photosensitizing

capability despite sulfonation. Both the free sulfonated ligand and its corresponding Pd(II) complex exhibited this diagnostic $^1O_2$ emission. For comparative evaluation, *Rose Bengal*, an established photosensitizer known for efficient $^1O_2$ generation, was employed as a literature benchmark.

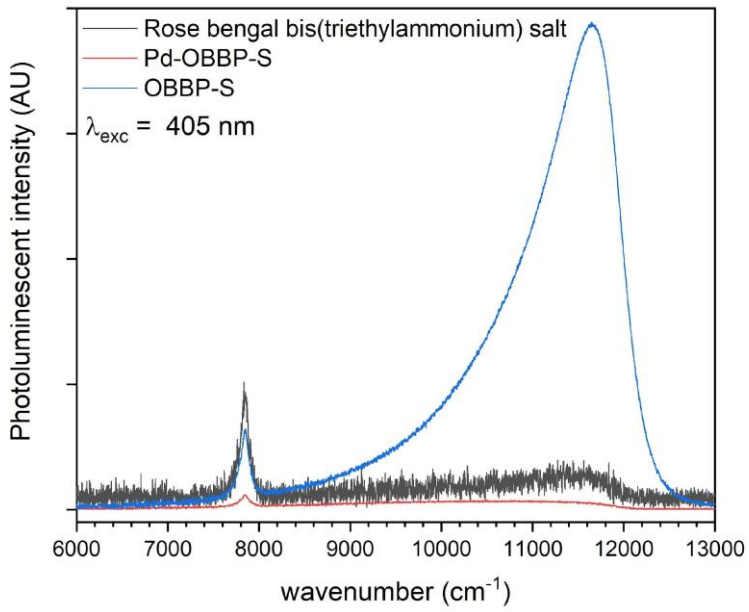

Figure 49: Comparison of the PL intensity of the sulfonated OBBP species vs. a literature-known standard, *Rose Bengal*.

Compared to *Rose Bengal*, the $^1O_2$ generation efficiency of the sulfonated OBBP ligand and its corresponding Pd(II) complex was estimated to be approximately 60% and 10%, respectively, after normalization to their respective molar absorption coefficients. This indicates that, while both compounds retain photodynamic activity, the metal complex exhibits a significantly reduced $^1O_2$ emission efficiency relative to the free ligand.

3.3.4 Biological evaluation

To gain deeper insight into the biological behavior of these novel compounds, a comprehensive biological evaluation was conducted. This includes standard MTT viability assays, studies on cellular uptake, intracellular reactive oxygen species generation, and assessment of both dark cytotoxicity and light-induced phototoxicity. Methods and instruments for this study can be found in section **5.1.3**.

3.3.4.1 Cell permeability and cytotoxicity

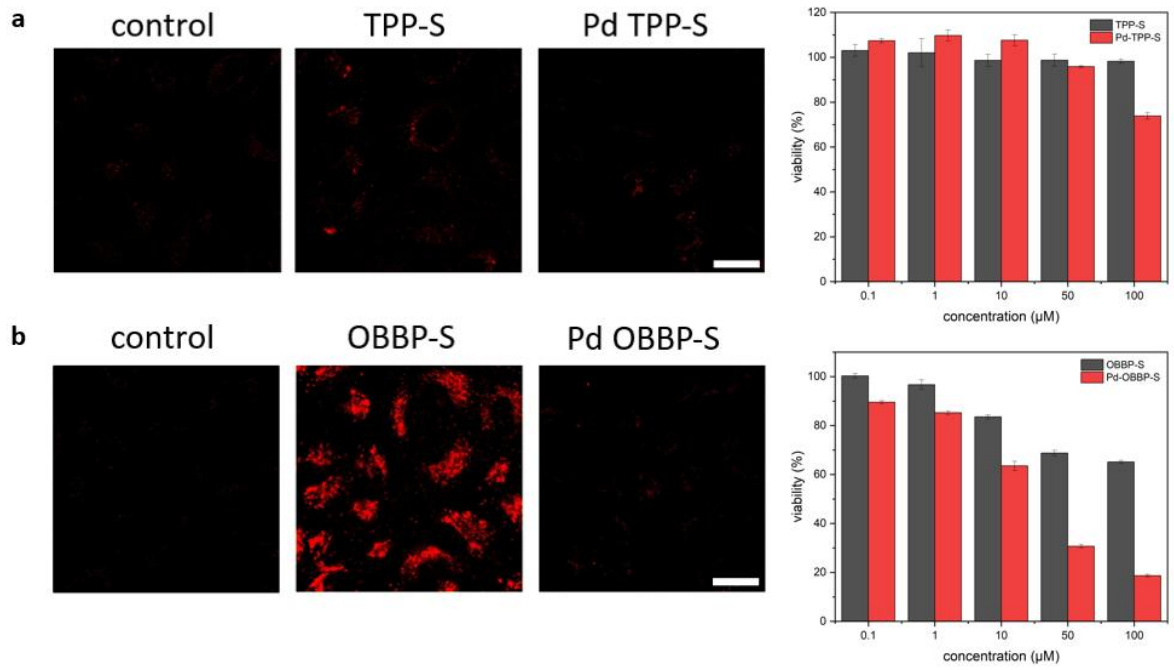

Figure 50: Cell permeability and MTT assays for the sulfonated TPP ligand and its respective Pd(II) complex (**a**) and the sulfonated OBBP ligand and its respective Pd(II) complex (**b**). The images were taken with a *Stellaris 5* confocal microscope (Leica) using a 63x oil objective (λ_{ex} = 405 nm; λ_{em} = 600 nm – 800 nm; zoom: 1.5x). The scale bar corresponds to 25 µm.

Evaluation of cellular uptake revealed that all four sulfonated compounds successfully penetrated the cell membrane, as evidenced by the red fluorescence signals shown in **Figure *50***. Each compound demonstrated measurable intracellular accumulation. Notably, the dimeric ligand exhibited an exceptionally intense fluorescent signal, suggesting significantly enhanced cell permeability relative to the other compounds. As an initial evaluation of cytocompatibility, standard MTT viability assays were performed on all sulfonated compounds. The sulfonated TPP ligand exhibited minimal cytotoxicity across the entire concentration range tested (0.1 µM to 100 µM), maintaining cell viability above 98% at all levels. Consequently, no LD_{50} value could be determined for this compound due to the consistently high cell viability. In contrast, its corresponding Pd(II) complex displayed slightly increased cytotoxicity. While

concentrations from 0.1 µM to 50 µM showed no significant reduction in viability, exposure to 100 µM resulted in a marked decline in cell survival to below 74%, indicating potential cytotoxic effects at higher concentrations. For the dimeric ligand, OBBP-S, a more pronounced concentration-dependent decrease in viability was observed, with cell viability declining to approximately 65% at the upper concentration limit. Notably, the Pd(II)-OBBP-S complex demonstrated considerable cytotoxicity, with viability dropping to approximately 19% at 100 µM, highlighting its potential for significant cellular damage at elevated doses. The LD_{50} values could not be calculated precisely and were approximated to over 100 µM for all substances, except Pd-OBBP, which indicated a higher toxicity. A pronounced trend emerges wherein increasing the molecular size of the porphyrin ligand and the number of coordinated palladium(II) centers markedly enhances cytotoxicity. Specifically, the sulfonated monomeric ligand TPP-S exhibits an estimated LD_{50} of approximately 1287 mg/kg, while its dimeric counterpart, OBBP-S, demonstrates a substantially lower LD_{50} of 131 mg/kg, underscoring the heightened bioactivity and potential toxicity associated with multimetallic porphyrin scaffolds.

3.3.4.2 Dark and light-induced phototoxicity

Given that the excitation of the PS requires irradiation at 405 nm, outside the optimal therapeutic window and known to potentially induce cellular stress or damage independently of the PS, it was essential to differentiate intrinsic compound toxicity from light-induced phototoxic effects. To this end, a comprehensive phototoxicity assessment was conducted by testing four different concentrations of each compound under both dark and light-exposed conditions. This dual-condition experimental setup allowed for the evaluation of compound-specific dark cytotoxicity as well as the quantification of additional phototoxicity induced upon irradiation. By comparing cell viability in the absence of light to that following 405 nm illumination, the contribution of light-activated ROS generation to cytotoxicity could be directly assessed, providing crucial insight into the suitability of each PS for therapeutic application under clinically relevant conditions.

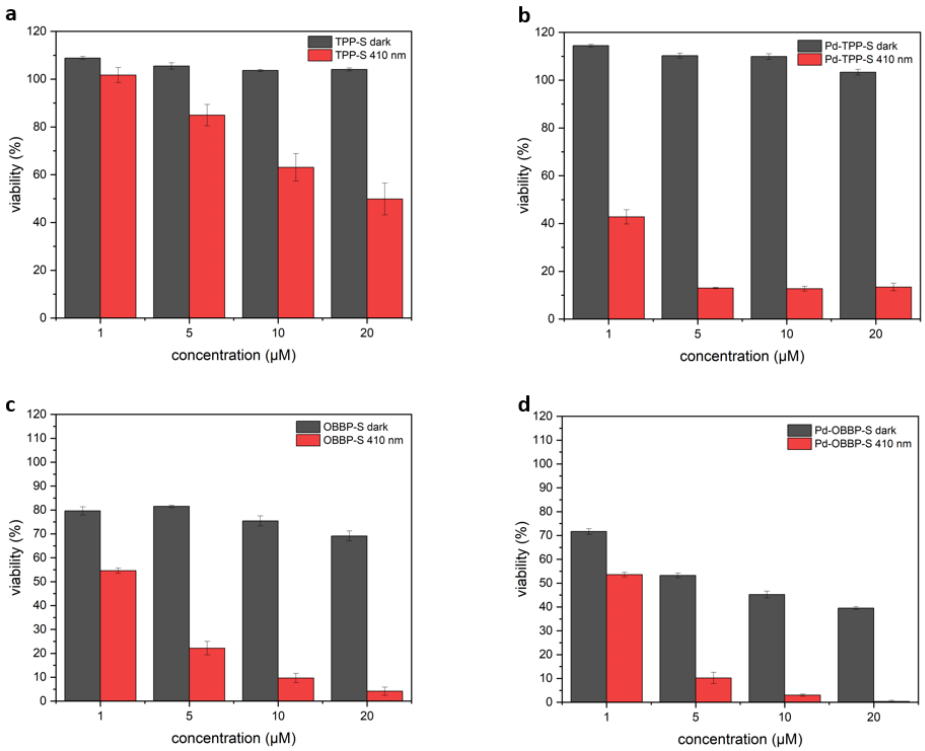

Figure 51: Dark and light-induced phototoxicity for TPP-S (**a**), Pd-TPP-S (**b**), OBBP-S (**c**), and Pd-OBBP-S (**d**).

In the evaluation of dark cytotoxicity, the monomeric compounds TPP-S and Pd-TPP-S (**Figure 51**, **a** and **b**) demonstrated excellent cell viability across the tested concentration range up to 20 µM, corroborating the results obtained from the MTT assays described in section **3.3.4.1**. The MTT data revealed a pronounced decline in viability for the Pd-containing species at 100 µM, suggesting that dark cytotoxicity may increase substantially at concentrations beyond those assessed in this assay. In contrast, the dimeric compounds OBBP-S and Pd-OBBP-S (**Figure 51**, **c** and **d**) exhibited significant cytotoxic effects even at low concentrations. Approximately 20% cell death was observed at 1 µM, with this value increasing to over 30% at 20 µM. The metallated dimer, Pd-OBBP-S, displayed an even more pronounced cytotoxic profile, with roughly 30% cell mortality at 1 µM escalating to approximately 60% at 20 µM. While the absolute cytotoxicity values deviate somewhat from those reported in the earlier MTT assays, the overall concentration-dependent trend of increasing dark toxicity with higher compound concentrations remains consistent.

To evaluate phototoxic effects induced by the PS, the baseline cell death observed in the blank controls was subtracted, thereby isolating cell mortality attributable solely to ROS generation by the PS. For the monomeric ligand TPP-S, a modest increase in phototoxicity was observed, with cell viability decreasing from 100% to approximately 50% across the concentration range of 1 to 20 µM. Its corresponding Pd(II) complex exhibited substantially enhanced

phototoxicity, inducing 57% cell death at 1 µM and escalating to 88% at 20 µM. The dimeric compounds demonstrated a consistent, concentration-dependent increase in ROS-mediated cytotoxicity. The OBBP-S ligand caused 45% cell death at the lowest concentration tested, rising to 95% at 20 µM, while the Pd-OBBP complex induced 46% and 99% cell death at the same concentrations, respectively. These results clearly indicate that, with the exception of the monomeric ligand TPP-S, all investigated compounds effectively generate significant levels of ROS under irradiation, supporting their potential utility as photosensitizers in photodynamic therapy.

3.3.4.3 Intercellular ROS emission

To assess intracellular $^1O_2$ generation, ROS detection assays were performed for all sulfonated compounds. HeLa cells were incubated with each compound, followed by targeted photoirradiation at 405 nm for 1 minute, followed by 10 minutes recording time. This setup enabled the evaluation of ROS production within a cellular environment under physiologically relevant conditions.

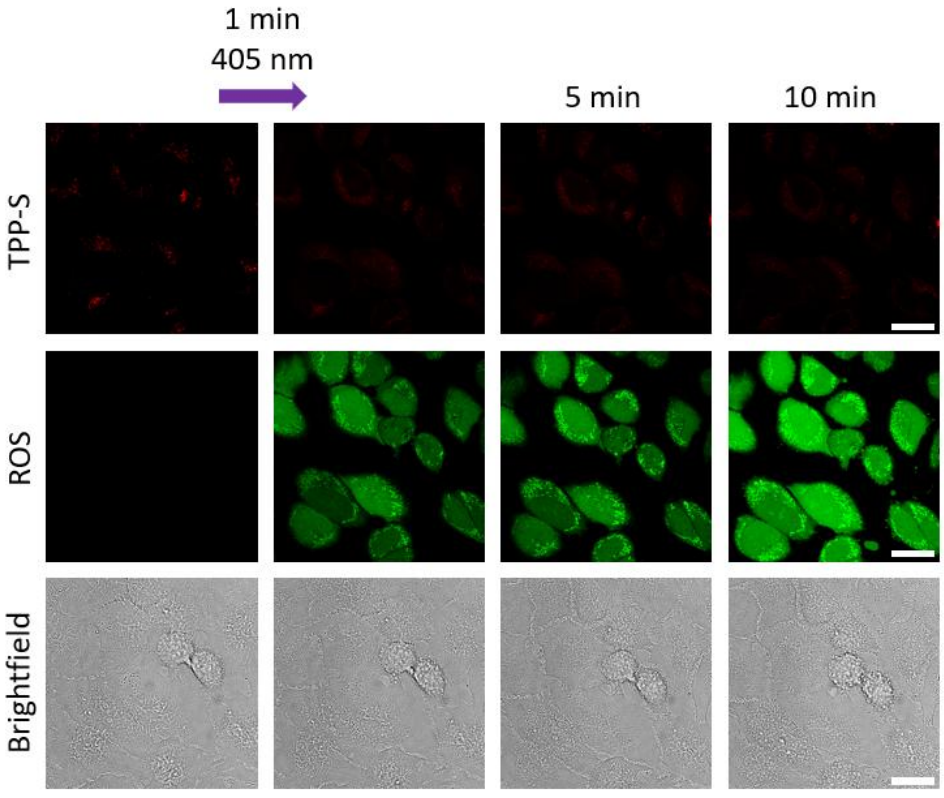

Figure 52: Cellular uptake and intercellular ROS emission under irradiation of 405 nm of a solution of 5 µM TPP-S. The images were taken with the *Stellaris 5* confocal microscope (Leica) using the 63x oil objective (OBBP-S: λ_{ex} = 405 nm; λ_{em} = 650 nm – 800 nm; ROS: λ_{ex} = 504 nm; λ_{em} = 515 nm – 545 nm; zoom: 1.5x). Scale bar corresponds to 25 µm.

As depicted in **Figure 52**, the sulfonated TPP derivative demonstrates moderate cellular uptake, evidenced by the red fluorescence localized within the cytoplasm. Notably, this intracellular presence remains relatively stable over time, suggesting limited efflux or degradation under physiological conditions. Upon irradiation at 405 nm for 1 minute, a measurable increase in intracellular ROS was detected *via* green fluorescence. However, comparative analysis with the negative control (**Figure 80**) indicates that a significant portion of the observed ROS signal may arise from photophysical background effects rather than photosensitizer-mediated $^1O_2$ generation. This is further supported by the brightfield images, which reveal negligible morphological changes over 10 minutes of irradiation. These findings suggest that TPP-S, in its sulfonated free-base form, exhibits limited photodynamic efficacy in cellular environments, likely due to insufficient ROS generation under the applied conditions.

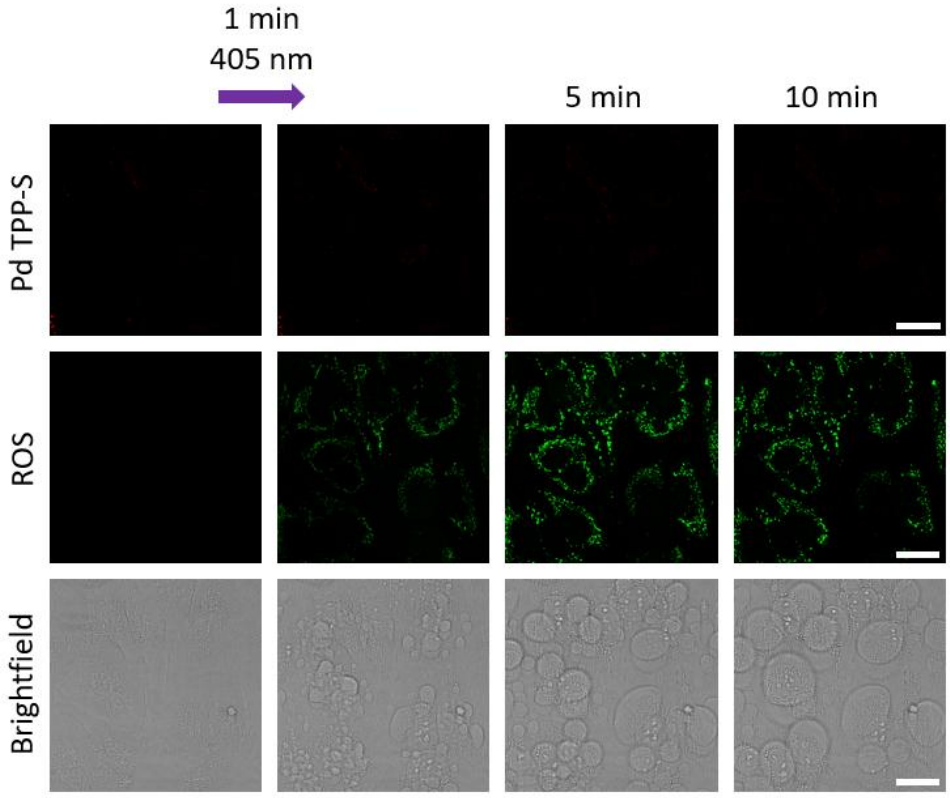

Figure 53: Cellular uptake and intercellular ROS emission under irradiation of 405 nm of a solution of 5 µM Pd-TPP-S. The images were taken with the *Stellaris 5* confocal microscope (Leica) using the 63x oil objective (OBBP-S: λ_{ex} = 405 nm; λ_{em} = 650 nm – 800 nm; ROS: λ_{ex} = 504 nm; λ_{em} = 515 nm – 545 nm; zoom: 1.5x). Scale bar corresponds to 25 µm.

As shown in **Figure 53**, the sulfonated palladium complex Pd-TPP-S exhibits relatively low initial cellular uptake, as evidenced by the modest red fluorescence signal. Nevertheless, once internalized, the compound demonstrates notable retention within the cellular environment, with fluorescence persisting even after 10 minutes of continuous irradiation. In contrast to its non-metallated analog TPP-S, Pd-TPP-S exhibits a markedly enhanced capacity for

intracellular ROS generation. Following just one minute of exposure to 405 nm light, a distinct increase in green fluorescence, indicative of ROS production, was observed. Importantly, this response is significantly elevated compared to the negative control, strongly suggesting that the detected ROS are predominantly the result of efficient photosensitization by the Pd(II) center. This conclusion is further supported by the brightfield microscopy images, which reveal pronounced morphological alterations post-irradiation, consistent with light-induced cytotoxic effects. Together, these findings highlight the improved photodynamic activity of Pd-TPP-S relative to its ligand precursor, attributable to the enhanced intersystem crossing and singlet oxygen sensitization facilitated by the heavy atom effect of palladium.

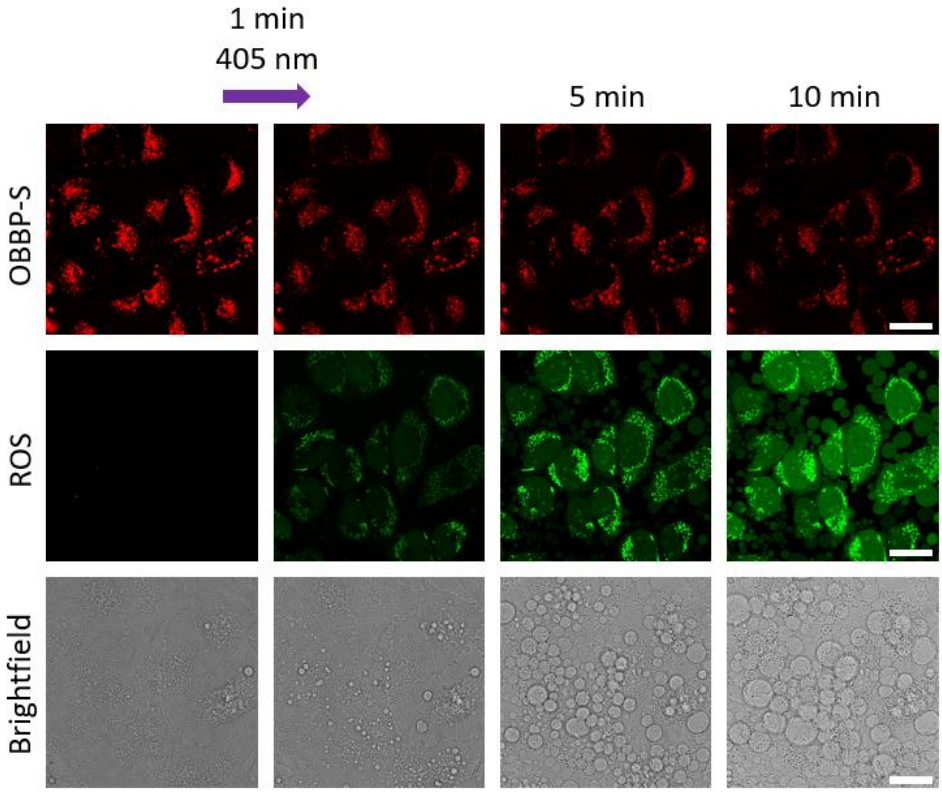

Figure 54: Cellular uptake and intercellular ROS emission under irradiation of 405 nm of a solution of 5 µM OBBP-S. The images were taken with the *Stellaris 5* confocal microscope (Leica) using the 63x oil objective (OBBP-S: λ_{ex} = 405 nm; λ_{em} = 650 nm – 800 nm; ROS: λ_{ex} = 504 nm; λ_{em} = 515 nm – 545 nm; zoom: 1.5x). Scale bar corresponds to 25 µm.

For the sulfonated dimeric ligand OBBP-S, cellular uptake was markedly superior compared to the other tested photosensitizers, as evidenced by the intense red fluorescence observed in the confocal microscopy images (**Figure 54**). This high intracellular accumulation is likely due to the enhanced lipophilicity and favorable interaction of the dimeric structure with cellular membranes. Interestingly, a slight decrease in red fluorescence was noted throughout irradiation, suggesting a potential redistribution, photobleaching, or photodegradation of the compound within the cellular milieu. A redistribution could occur through compound induced

lysosome damage. In terms of intracellular ROS generation, OBBP-S demonstrated robust photodynamic activity. Upon irradiation at 405 nm, a pronounced increase in green fluorescence was observed as early as one minute post-irradiation. This ROS signal intensified progressively from 1 to 10 minutes, indicating sustained photosensitization and efficient $^1O_2$ production over time, likely facilitated by the high intracellular concentration of the sensitizer. The ROS levels recorded in these experiments significantly exceeded those of the blank, confirming that the observed oxidative stress originates predominantly from the activity of OBBP-S rather than light exposure alone. These findings are further corroborated by the brightfield microscopy, which revealed progressive cellular morphological alterations, most notably the formation of intracellular vesicles, that closely correlate with the spatiotemporal distribution of ROS detected *via* fluorescence imaging.

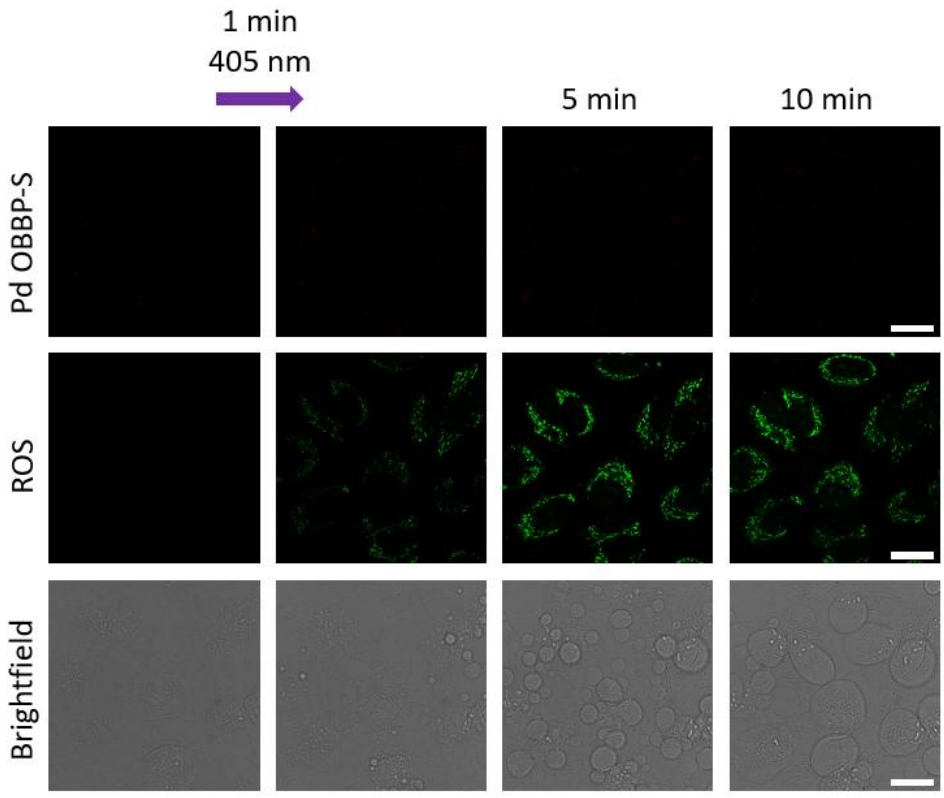

Figure 55: Cellular uptake and intercellular ROS emission under irradiation of 405 nm of a solution of 5 µM Pd-OBBP-S. The images were taken with the *Stellaris 5* confocal microscope (Leica) using the 63x oil objective (OBBP-S: λ_{ex} = 405 nm; λ_{em} = 650 nm – 800 nm; ROS: λ_{ex} = 504 nm; λ_{em} = 515 nm – 545 nm; zoom: 1.5x). Scale bar corresponds to 25 µm.

For the sulfonated dimeric Pd(II) complex, Pd-OBBP-S, cellular uptake was found to be relatively modest, particularly when compared to its non-metallated counterpart. This trend reinforces the observation that Pd(II) coordination significantly reduces the membrane permeability of porphyrin systems, likely due to increased molecular symmetry, altered

polarity, and modified electronic configuration, which collectively hinder passive diffusion across lipid bilayers. Despite its limited intracellular accumulation, Pd-OBBP-S exhibited a notable capacity for intracellular ROS generation upon photoactivation. Following irradiation at 405 nm, a time-dependent increase in green fluorescence intensity was observed, indicating efficient and sustained production of $^1O_2$. The emission profile closely mirrored that of Pd-TPP-S, albeit with a more gradual onset, possibly reflecting its lower intracellular concentration but higher intrinsic photosensitization efficiency. The specificity of ROS generation, comparing the results to a blank control, demonstrated negligible ROS signals under identical experimental conditions. Brightfield microscopy corroborated these findings, showing morphological changes characteristic of photodynamic-induced stress, absent in the control.

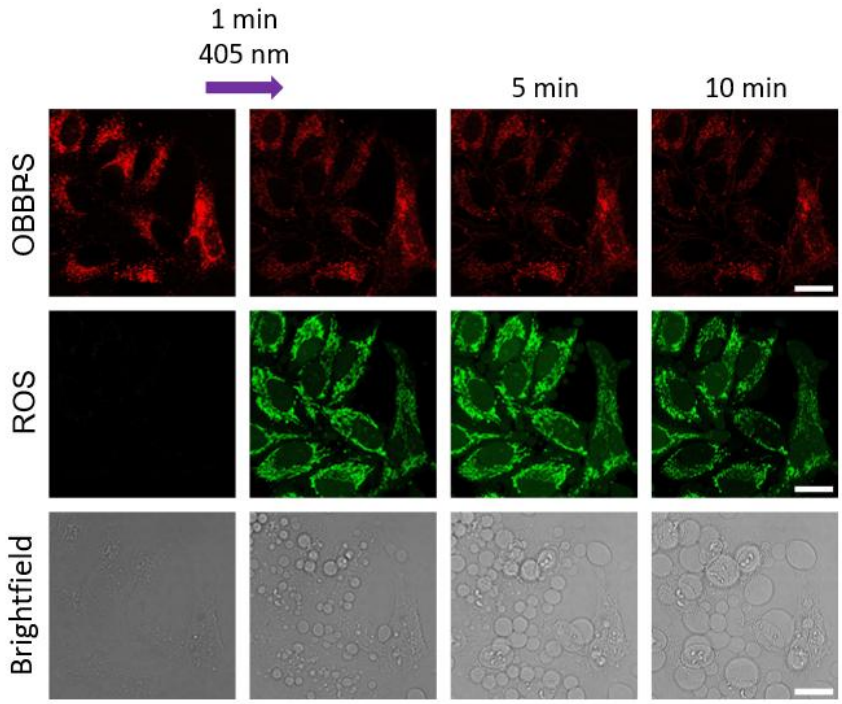

Figure 56: Cellular uptake and intercellular ROS emission under irradiation of 405 nm of a solution of 10 µM OBBP-S. The images were taken with the *Stellaris 5* confocal microscope (Leica) using the 63x oil objective (OBBP-S: λ_{ex} = 405 nm; λ_{em} = 650 nm – 800 nm; ROS: λ_{ex} = 504 nm; λ_{em} = 515 nm – 545 nm; zoom: 1.5x). Scale bar corresponds to 25 µm.

To further elucidate the concentration-dependent behaviour of the most effective PS, additional experiments were performed using a doubled concentration of 10 µM vs. 5 µM. The results, shown in **Figure 56**, reveal that both cellular uptake and intracellular ROS generation remain robust at the elevated concentration, with a slight enhancement compared to the lower dose. Interestingly, at 10 µM, distinct subcellular localization of ROS production becomes apparent, particularly within defined intracellular compartments that were not as prominently affected at

5 µM. The spatial pattern suggests mitochondrial involvement, although this hypothesis requires confirmation through colocalization studies using mitochondrial-specific dyes. If confirmed, this would suggest that ROS were also generated within mitochondria, a process that can occur endogenously and is not necessarily induced by the active compound.. Moreover, the comparison across compounds Pd-TPP-S, OBBP-S, and Pd-OBBP-S versus control and TPP-S shows a consistent trend: targeted ROS generation in subcellular compartments correlates with increased phototoxicity and decreased viability in MTT assays. Conversely, TPP-S, which displays a more diffuse ROS distribution, does not induce significant cell death. This suggests that diffuse or low-level cytosolic ROS production may be effectively mitigated by cellular antioxidant systems, such as glutathione, thereby preserving cell viability. These findings are in line with the observed MTT viability data (**Figure 50**), where TPP-S maintained high cell viability post-irradiation despite visible ROS generation. In contrast, Pd-TPP-S, OBBP-S, and Pd-OBBP-S demonstrated targeted ROS formation and associated cytotoxicity, reinforcing the link between subcellular ROS localization, PS efficacy, and therapeutic potential.

Among the investigated compounds, all except TPP-S demonstrated promising photophysical and biological characteristics for application as PSs in PDT. Notably, substantial intracellular ROS generation upon photoactivation was observed for the Pd(II) complexes as well as for the dimeric ligand, with the latter exhibiting the most pronounced ROS emission. This unexpectedly high photodynamic efficacy of the metal-free OBBP-S ligand stands in contrast to conventional expectations, where metalation, particularly with Pd(II), is known to enhance intersystem crossing and facilitate $^1O_2$ generation. The superior performance of OBBP-S can likely be attributed to its markedly higher cellular uptake and stronger molar absorption coefficient. These combined factors enable more efficient intracellular light absorption and energy transfer, leading to enhanced ROS production despite the absence of a metal center. This hypothesis is further supported by the photoluminescence data (**Figure 49**), which shows that OBBP-S sensitizes singlet oxygen emission nearly sixfold more effectively than its Pd(II)-coordinated counterpart. The results emphasize the importance of not only photophysical properties but also cellular pharmacokinetics when evaluating PS performance, and suggest that in specific structural contexts, non-metalated porphyrin derivatives may outperform their metallated analogs in biological settings.

4 Conclusion and Outlook

In this work, a novel dimeric porphyrin construct featuring an *N*-fused porphyrin linked to a conventional tetraphenylporphyrin unit *via* a mixed condensation approach was successfully synthesized and characterized. The synthetic route began with the preparation of an *N*-confused porphyrin, employing methanesulfonic acid as the acid catalyst. Subsequent bromination and SUZUKI–MIYAURA cross-coupling reactions enabled the introduction of a formyl-functionalized aryl group at the *β*-position of the NCP, yielding an aldehyde-bearing *N*-fused porphyrin intermediate suitable for dimerization. The resulting NFP–TPP dimer was obtained through a controlled acid-catalyzed condensation, and its structure was extensively characterized using a combination of spectroscopic and spectrometric techniques. NMR spectroscopy revealed significant aggregation behavior due to π–π interactions, which could be mitigated through solvent and temperature optimization. UV-Vis absorption spectra confirmed the presence of both monomeric units within the dimer, exhibiting characteristic *Sorét* and *Q*-band features of NFP and TPP subunits. Due to challenges in obtaining single crystals, ion mobility spectrometry coupled with high-resolution mass spectrometry was employed to gain structural insight into the gas-phase conformation of the dimer. The CCS values supported a co-facial arrangement of the porphyrin units, consistent with *π*-stacked architectures observed in analogous systems. Furthermore, coordination studies with $Mn(CO)_5Br$ demonstrated selective metalation of the NFP moiety, yielding a heterobimetallic Mn(I)/Mn(III) complex (**Scheme 16**). TIMS analysis of the complex indicated the presence of a single dominant isomer, which DFT calculations suggested corresponds to an externally coordinated $Mn(I)(CO)_3$ moiety. Together, these findings provide a comprehensive framework for the synthesis and structural analysis of asymmetrical porphyrin dimers incorporating *N*-fused scaffolds, paving the way for future investigations into their electronic, photophysical, and catalytic properties.

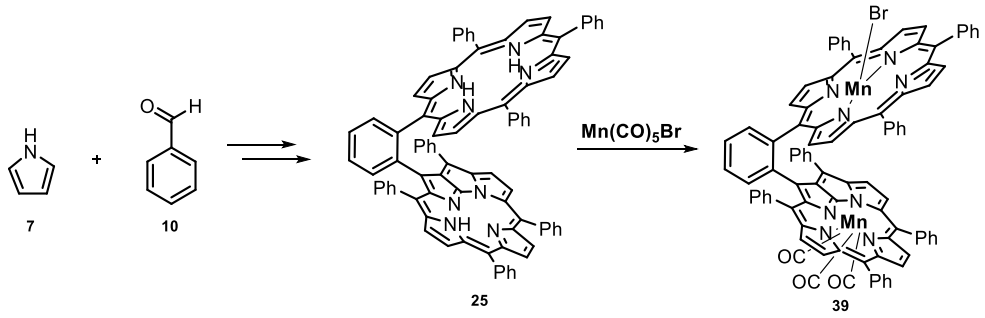

Scheme 16: Successful synthesis of the ortho-linked NFP-TPP dimeric ligand with proove that the subsequent metallation of two different oxidation stated of Mn is possible.

Furthermore, this work demonstrates the significant progress and persistent challenges in the synthesis and characterization of co-facial o-phenylene-bridged bisporphyrins and their metal complexes. Traditional methods employing flexible linkers have given way to more rigid architectures, enabling better control of porphyrin orientation but often suffering from low yields. Among the evaluated synthetic strategies, SUZUKI–MIYAURA cross-coupling offered mechanistic insights and a potential one-step route to OBBP, although product isolation remained elusive due to the instability of intermediates and harsh conditions. Alternatively, a refined stepwise condensation protocol, incorporating controlled catalyst addition, yielded OBBP in up to 44%, representing the most efficient route reported to date. Moreover, post-synthetic metalation of the free-base ligand provided a practical path to homobimetallic and heterobimetallic complexes, with UV-Vis spectroscopy confirming selective Ni(II) insertion. Electrochemical analysis *via* cyclic voltammetry revealed distinct and reversible redox processes for each metal center, confirming the integrity and electronic communication of the dimeric frameworks. Comprehensive experimental and computational investigations demonstrate the high efficiency, selectivity, and robustness of the Fe/Ni heterobimetallic complex for visible-light-driven CO_2 reduction.

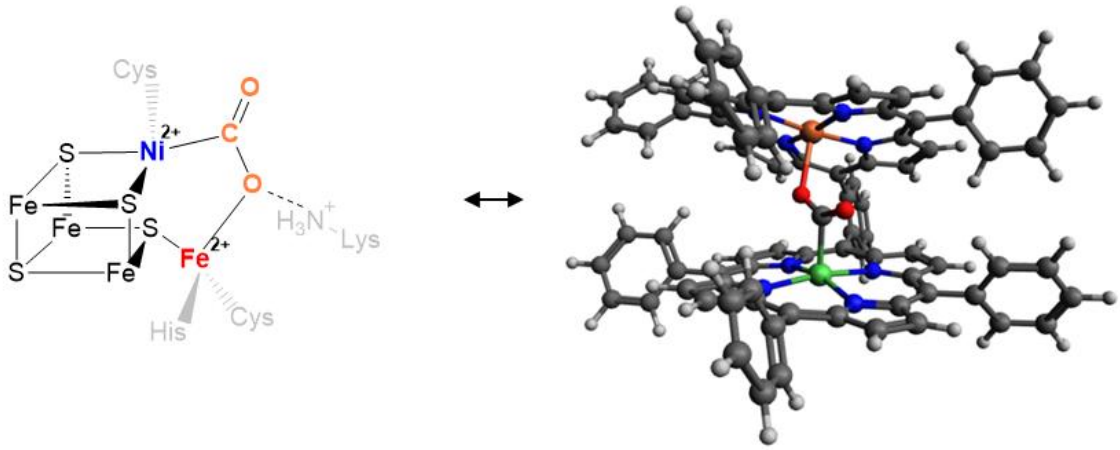

Figure 57: Active center of the CODH (left) capable of reducing CO_2 efficiently under physiological conditions, novel Fe/Ni complex (right) showing the same CO_2 coordination as the natural molecule and proven to efficiently catalyze the photocatalytic CO_2 reduction.

Optimization studies identified phenol as the most effective proton source, 1 µM as the optimal catalyst loading, and $Ru(bpy)_3Cl_2$ as the most selective and productive photosensitizer, although more sustainable alternatives such as Cu-based and organic TADF PSs showed promising activity. The heterobimetallic architecture outperformed both monometallic and homobimetallic analogues, achieving TONs up to 2060 with near-quantitative gas-phase CO

selectivity and demonstrating excellent reproducibility. Liquid-phase analysis confirmed formate as a minor product, adjusting overall selectivity to ~97%. DFT and multireference calculations revealed a magnetically coupled, low-symmetry structure with dipolar interaction between high-spin metal centers, and identified a CODH-like CO_2 binding geometry as energetically preferred (**Figure 57**). Manual redox potential estimation using CASSCF-DELFIN data provided additional insight into the electronic structure and reactivity. Together, these findings underscore the cooperative advantage of heterobimetallic design and offer a mechanistically grounded framework for future development of earth-abundant photocatalytic CO_2 reduction systems.

Another project in this work demonstrates that structural modulation of porphyrin-based photosensitizers, particularly through palladium(II) metalation and multimerization, significantly enhances their photophysical and photochemical performance for photodynamic therapy applications. Photoluminescence emission studies revealed that Pd(II)-coordinated mono-, di-, and trimeric porphyrins efficiently generate singlet oxygen, with multimeric systems exhibiting a pronounced, nonlinear enhancement in $^1O_2$ emission intensity. Quantitative photooxidation assays using diphenylfuran further confirmed the superior ROS generation capacity of the trimeric Pd-OBTP complex, which outperformed its dimeric and monomeric counterparts by over 200% and 350%, respectively. These findings suggest that cooperative or excitonic effects within multimeric architectures may amplify intersystem crossing and energy transfer efficiencies. To enable biological evaluation, sulfonation of the porphyrin ligands was employed to confer water solubility. Although this modification preserved $^1O_2$ generation capability, it substantially reduced molar absorptivity and overall photosensitizer efficiency, particularly in the Pd(II)-complexes. These results underscore the importance of balancing hydrophilicity with photophysical performance in the rational design of next-generation photosensitizers. The comprehensive biological evaluation of the sulfonated porphyrin-based compounds revealed clear structure–activity relationships that govern their photodynamic behavior. All compounds demonstrated measurable cellular uptake, with the dimeric ligand OBBP-S exhibiting notably superior permeability. Cytotoxicity assessments indicated that metalation and molecular dimerization significantly enhance biological activity: the monomeric ligand TPP-S was essentially non-toxic across the tested concentration range, whereas its Pd(II) complex and especially the dimeric forms, OBBP-S and Pd-OBBP-S, showed pronounced concentration-dependent cytotoxic effects.

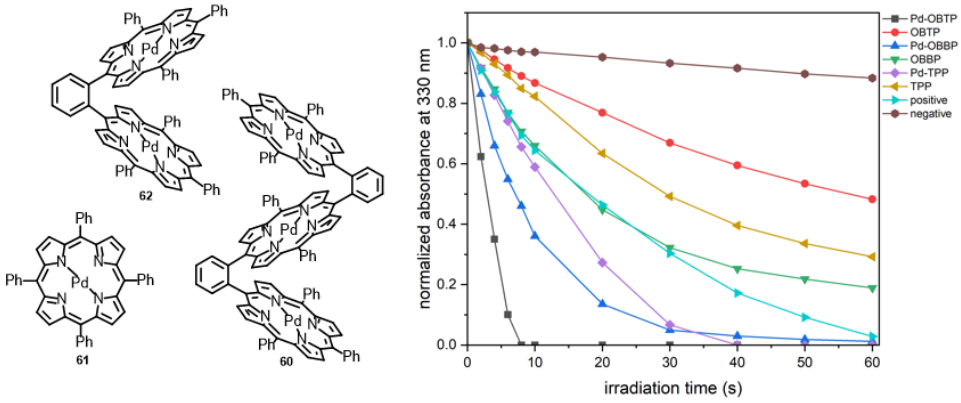

Figure 58: Mono-, dimeric- and trimeric Pd(II) porphyrin complexes that can efficiently sensitize $^1O_2$ production.

LD_{50} analysis corroborated these trends, highlighting the increasing toxicity with greater molecular complexity and metal content. Under photoirradiation, all compounds except TPP-S exhibited substantial phototoxicity, primarily due to intracellular singlet oxygen generation. Pd(II) complexes benefitted from enhanced intersystem crossing *via* the heavy atom effect, while the dimeric ligand OBBP-S surprisingly outperformed its metallated counterpart in ROS emission, likely due to its higher cellular uptake and stronger absorption cross-section. Confocal microscopy confirmed intracellular ROS generation and associated morphological changes, with spatial localization patterns suggesting mitochondrial involvement in the photodynamic response. Together, these findings establish that dimeric sulfonated porphyrins, particularly OBBP-S and Pd-OBBP-S, are promising candidates for photodynamic therapy. The results highlight the complex interplay between photophysical properties, cellular uptake, and subcellular localization in dictating therapeutic performance and suggest that carefully

engineered non-metalated systems may offer advantages over traditional metallated photosensitizers in certain biological contexts.

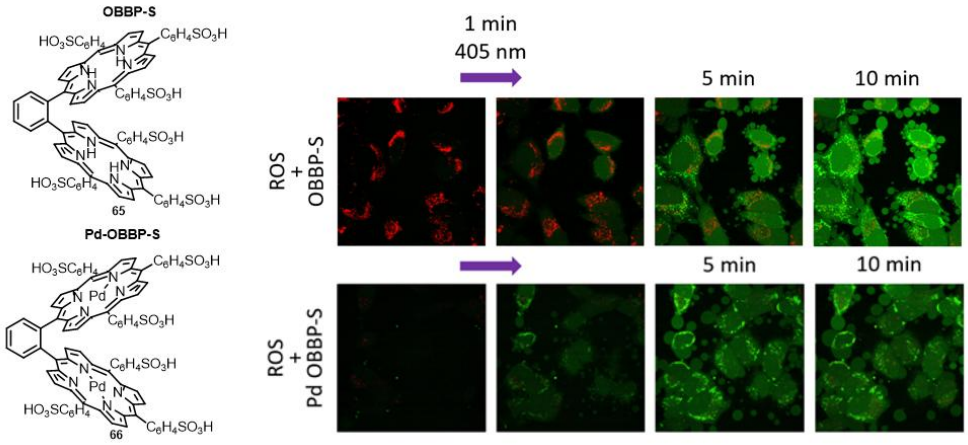

Figure 59: Sulfonated dimeric porphyrin and its respective Pd(II) complex illustrating intercellular ROS generation.

Future investigations could focus on the newly developed dimeric NFP-TPP ligand, particularly exploring its potential for metal coordination and the formation of homo- and heterobimetallic complexes incorporating metal centers with varying oxidation states. Such complexes may exhibit unprecedented cooperative effects, offering promising avenues for applications in areas such as photocatalytic CO_2 reduction and small molecule activation. Additionally, strategic structural modification of the porphyrin scaffold, specifically through the incorporation of NH-containing functional groups at the *meso*-positions, could enhance CO_2 binding affinity *via* hydrogen bonding or secondary coordination sphere effects. This approach may yield more efficient ortho-linked porphyrin dimers with superior catalytic or photochemical performance. From a synthetic standpoint, these functionalized systems can be preliminarily accessed through modified dipyrromethene intermediates using a diverse set of aldehyde precursors bearing NH moieties. This strategy enables modular construction of the desired porphyrin architectures *via* a simplified synthetic route exemplified by the OBBP ligand. Preliminary success in synthesizing 2-(4-(di(1H-pyrrol-2-yl)methyl)phenyl)pyridine and 2-[bis(1H-pyrrol-2-yl)methyl]-5-methylpyridine underscores the feasibility of this approach and lays the groundwork for the rational development of next-generation porphyrinoid ligands with tailored electronic and coordinative properties.

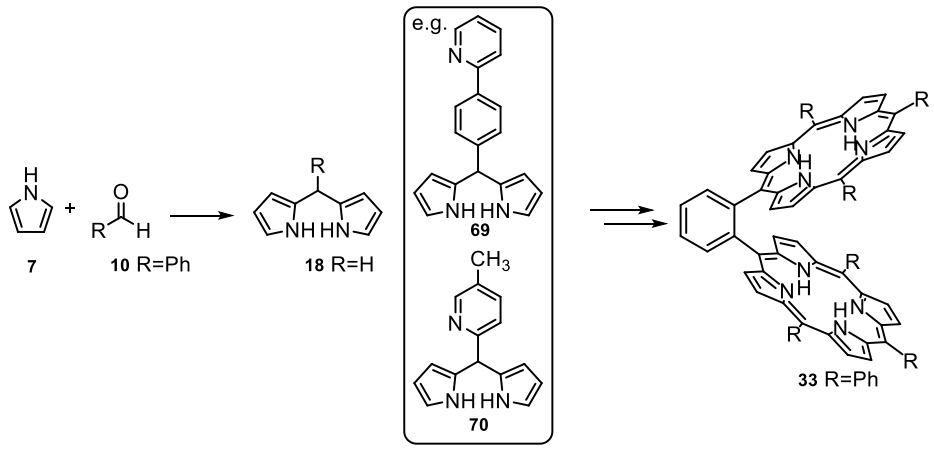

Figure 60: General reaction strategy towards optimized OBBP ligands with higher probability to coordinate CO_2 through additional *N*-containing side-groups.

The successful synthesis of the asymmetric brominated porphyrin derivative, 5-bromo-10,15,20-triphenylporphyrin, opens a versatile synthetic gateway for the construction of structurally diverse porphyrin-based architectures *via* SUZUKI–MIYAURA cross-coupling reactions. This halogenated porphyrin serves as an ideal precursor for the late-stage diversification of the macrocyclic core through coupling with a broad range of boronated linker systems, allowing systematic investigation of how conjugated substituents modulate the electronic, photophysical, and catalytic properties of the porphyrin scaffold. One particularly promising avenue involves the coupling of porphyrin moieties such as 1,2-diphenylethane-1,2-dione (benzil), a known radical initiator used in photoinitiated polymerization. Integration of a benzil linker with a porphyrin chromophore could yield a novel class of light-responsive initiators with significantly enhanced performance. Due to the strong absorption of porphyrins in the visible region, such hybrid systems could enable efficient homolytic cleavage under lower laser intensities, thereby improving the energy efficiency of radical initiation processes. This concept holds strong potential for advanced photonic applications, including high-resolution 3D laser nanoprinting, where reduced power requirements and increased spatial precision are highly desirable.

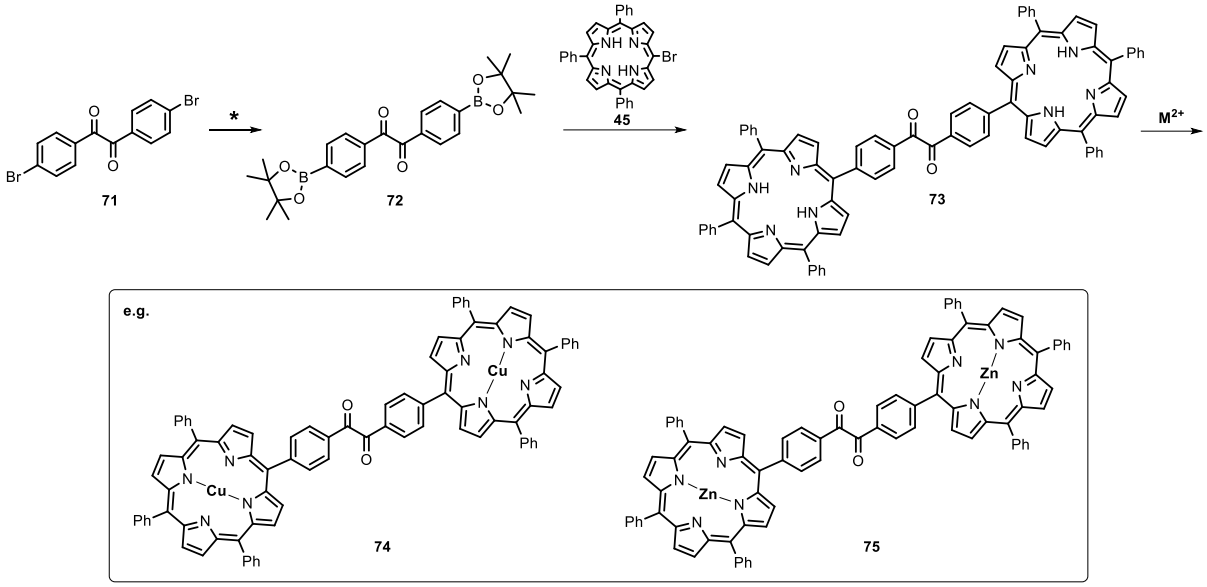

Figure 61: Synthesis strategy to yield dimeric benzil-linked porphyrin scaffold for possible applications in 3D laser nanoprinting.

5 Experimental Section

5.1 General information

5.1.1 Methods and analytics

During the preparation of reactions containing air- or moist-sensitive reagents, the glassware was previously dried with either a heat gun or a gas burner. These reactions were carried out under conventional Schlenk-technique, using argon as an inert gas, and liquids were transferred via plastic syringes and V2A-steel cannulas.[179] Solids were used in pulverized form. For running reactions at low temperature, flat Dewar flasks of the company Isotherm were used for cooling, using the following frigorific mixtures:

0 °C: ice/H_2O

–18 °C: NaCl/ice/H_2O

–78 °C: isopropanol/dry ice

The used solvent mixtures were volumetrically measured. Solvents were removed under reduced pressure using rotary evaporators with a 40 °C water bath.

5.1.2 Solvents and chemicals

Solvents of p.a. (pro analysis) quality were commercially purchased at Acros Organics, Sigma Aldrich, Fisher Scientific, or Alpha Aesar and used without further purification. Under the standard procedure, absolute solvents were used and stored under inert gas or commercially purchased.

Acetone was purchased as an absolute solvent at Fisher Scientific.

Chloroform was purchased as an absolute solvent at Acros Organics.

Dichloromethane	was purchased in p.a. quality and dried over two columns as part of the MBRAUN SPS 800 system.
Dimethylsulfoxide	was purchased as an absolute solvent at Acros Organics.
Dimethylformamide	was purchased as an absolute solvent at Acros Organics.
Ethyl acetate	was purchased as an absolute solvent at Acros Organics.
Methanol	was purchased as an absolute solvent at Acros Organics.
Propionic acid	was purchased as an absolute solvent at Sigma-Aldrich.
Pyridine	was purchased as an absolute solvent at Fisher Scientific.
Pyrrole	was purchased as an absolute solvent at Sigma-Aldrich and distilled before use.
Triethylamine	was purchased as an absolute solvent at Sigma-Aldrich.
Toluene	was purchased in p.a. quality and dried over two columns as part of the MBRAUN SPS 800 system.
O-Xylene	was purchased as an absolute solvent at Sigma-Aldrich.

5.1.3 Methods and instruments for biological studies

Cultivation of HeLa cells

The HeLa cells were cultivated in *Dulbecco's Modified Eagle's Medium* (DMEM; Gibco® Life Technologies) with the addition of 1% penicillin/streptomycin (Gibco® Life Technologies) and 10% fetal calf serum (FCS; Gibco® Life Technologies). Cultivation was performed in 75 cm^2 culture flasks (Greiner Bio-One™, CELLSTAR™) at 37 °C, a CO_2 concentration of 5%, and saturated humidity. To use the cells, they were detached enzymatically. First, the culture medium was removed and the cells were washed with 10 ml *Dulbecco's Phosphate Buffered Saline* (DPBS; Gibco® Life Technologies). Then, 2 ml of 0.25% Trypin-EDTA (Gibco® Life Technologies) was added and incubated for 3 min at 37 °C. The addition of 8 mL DMEM halted the enzymatic detachment, and the cells could be used for further experiments.

MTT assay without irradiation

An MTT assay was performed to determine cytotoxicity. First, 1 x 104 HeLa cells were seeded in 100 µl DMEM per well of a 96-well plate (Greiner Bio-One™ CELLSTAR™) and incubated at 37°C overnight. The next day, the cells were treated with the compounds together with three technical replicates were prepared. From the time of treatment, work was carried out in the dark. In addition, live and dead controls were carried out in triplicates, with a media change on day two. The cells were then incubated for 72 h at 37°C. After incubation, the cells of the dead controls were first killed by adding 5 µl of a 20% *Triton X-100* solution (Carl Roth® GmbH) in dH_2O. Then, 15 µl of 3-(4,5-dimethylthiazol-2-yl)-2,5-diphenyltetrazolium bromide reagent (MTT reagent; Promega) was added to each well and incubated for 3 hours. To stop the reaction, 100 µl of stop solution (Promega) was added and the plate was incubated for 24 h. The absorbance was measured at 596 nm using a microplate reader (Spectra Max iD3). For evaluation, the absorbance of the dead controls was subtracted from all values and the live controls were referenced to determine the relative viability.

MTT assay with irradiation

The preparation and treatment of the cells was identical to the MTT assay without irradiation. After the 72-hour incubation of the treated cells, the medium was removed, the cells were washed with 100 µl DPBS and 100 µl fresh DMEM was added. Subsequently, all wells were irradiated with 410 nm using an LED (405 nm) at a distance of 3 cm from the radiation source

for 5 min and then incubated in the dark for 30 min. In addition, an identically treated plate was used, which was not irradiated. Thereafter, dead controls were prepared by adding 5 µl of 20% Triton X-100, 15 µl of MTT reagent and incubated for 3 h. The reaction was stopped and analyzed according to the MTT test without irradiation.

Treatment of HeLa cells for cell microscopy

In preparation for cell microscopy, 2 x 104 HeLa cells were seeded in 200 µl DMEM per well of a µ-Slide 8 well *ibiTreat* (ibidi® GmbH) and incubated overnight at 37°C. The next day, the cells were incubated with 200 µl DMEM per well. The next day, the cells were treated with 200 µl of a 5 µM solution of the investigated compounds dissolved in DMEM. In addition, one well was left untreated as a negative control, in which only the medium was changed. The cells were incubated for 72 h at 37°C. The *Stellaris 5* confocal microscope (Leica) was used for microscopy of the cells.

Detection of radical oxygen species after irradiation of treated HeLa cells

To analyze the formation of radical oxygen species (ROS) after irradiation with the respective compounds of treated HeLa cells, the cells were spiked with 25 µM 2'-7'-dichlorodihydrofluorescein diacetate (H_2DCFDA) and could be used for cell microscopy (λ_{ex} = 504 nm, λ_{em} = 529 nm) after an incubation time of 45 min. Untreated cells, to which 25 µM H_2DCFDA was also added, served as a negative control. First, images of the initial state were taken with the *Stellaris 5* confocal microscope (Leica). The cells were then irradiated for 1 min with the microscope's 405 nm laser (laser intensity: 20%). To follow the formation of ROS, one image was taken immediately after irradiation, after 5 min and after 10 min.

5.1.4 Devices and analytical instruments

Nuclear magnetic resonance spectroscopy (NMR):

The NMR spectra were recorded on the following devices: ^{1}H- and ^{13}C- NMR spectra were recorded on Bruker Avance (300 MHz, 400 MHz), Bruker DRX (500 MHz) spectrometers in

the solvents indicated. All spectra were recorded at room temperature. As solvents were used: chloroform d[1] ($CDCl_3$), dichloromethane-d_2, or THF-d_8 purchased at Eurisotop. The chemical shift δ is expressed in parts per million (ppm) and referenced to the residual solvent peaks of chloroform (^{1}H: δ = 7.26 ppm; 13C: δ = 77.16 ppm), dichloromethane (^{1}H: δ = 5.32 ppm; ^{13}C: δ = 54.00 ppm), tetrahydrofuran (1H: δ = 3.58 ppm; ^{13}C: δ = 67.57 ppm) and toluene-d8 (^{1}H: δ = 7.09 ppm; 13C: δ = 137.86 ppm).[180] The recorded spectra were evaluated by 1st order. For centrosymmetric signals, it's the median point; for multiplets, the range of the signal was listed. For characterization of the multiplicity the abbreviation s = singlet, d = doublet, t = triplet, q = quartet, p = pentet, m = multiplet, dd = doublet of doublets, td = triplet of doublets ddd = doublet of doublets of doublets and so forth were used. Coupling constants were sorted by absolute values expressed in Hertz (Hz). The number of bonds between the coupling counterparts was expressed as indices as nJ. The assignment of the signals via 1H NMR spectra was based on the multiplicity and the chemical shift by using the following abbreviations: Hpyrrole = proton of the pyrrolic subunit of the porphyrin ring, H~~aromatic~~ = proton of the aryl-residues in meso-position. In the course of the assignment of the aromatic proton signals of the residues in meso-position, the porphyrin residue was allocated to the highest value. The assignment of the signals via ^{13}C NMR spectra was based on the chemical shift and the multiplicity obtained via DEPT 90- and DEPT 135-spectra (DEPT = distortionless enhancement by polarization transfer) or by phase edited HSQC (heteronuclear single quantum coherence) and are described as follows: + = primary or tertiary C-atom (positive DEPT- or HSQC-signal), – = secondary C-atom (negative signal) and Cq = quaternary C-atom (no signal). Common solvent and solvent impurity signals as followed were not explicitly listed: in CDCl3: 1H NMR 1.55 (H2O), 1.25 (H grease), 0.84 – 0.87 (H grease), 0.07 (silicon grease) ppm; 13C NMR 29.7 (H grease), 1.20 (silicon grease) ppm; DCM-d2: 1H NMR 1.52 (H2O), 1.29 (H grease), 0.84 – 0.90 (H grease), 0.09 (silicon grease) ppm; 13C NMR 30.1 (H grease), 1.2 (silicon grease) ppm; THF-d8: 1H NMR 10.84 (THF-d8 impurity), 3.26 (THF-d8 impurity), 2.50 (THF-d8 impurity), 2.49 (H2O), 1.29 (H grease), 0.85 – 0.91 (H grease), 0.11 (silicon grease) ppm; 13C NMR 29.9 ppm (H grease) 1.2 (silicon grease) ppm. In low resolution, the signals were listed based on the 1H-broadband-decoupled 13C NMR spectra without phases.

Infrared spectroscopy (IR):

IR spectra were recorded on an FT-IR Bruker Alpha P spectrometer. All samples were measured by the ATR technique (attenuated total reflection), ranging from 3600 cm–1 to

500 cm–1. The positions of the absorption bands are given in wavenumbers ṽ in cm–1. The signal intensity was listed and characterized as followed (T = transmission): vs = very strong (0 – 10% T), s = strong (10 – 40% T), m = middle (40 – 70% T), w = weak (70 – 90% T), vw = very weak (90 – 100% T).

Mass spectrometry (MS):

Mass spectra were measured either by FAB-MS (Fast Atom Bombardment) recorded on a Finnigan MAT 95 with m-nitrobenzyl alcohol (3-NBA) like matrix, by EI-MS (electron ionization) recorded on Finnigan MAT 95, or by ESI-MS (electron spray ionization) recorded on a Thermo Scientific Q Exactive Plus or a Bruker timsTOF™.

For the o-phenylene bisporphyrins and trisporphyrins, the mass spectra and ion mobility spectra, the porphyrins were dissolved in a 1:2 mixture of CH_2Cl_2 and DMF. A capillary voltage of up to 6 kV was necessary to ionize the neutral porphyrins. For the already charged and the free base porphyrins, a voltage of 2.5 kV was sufficient. The source pressure was 1.3 bar, and the dry gas temperature was 200 °C.

In general, the molecular peak $[M]^+$ or $[M+H]^+$ and the characteristic fragmentation peaks [M – fragment]$^+$ or [fragment]$^+$ were given, as far as they were significant, as the mass-to-charge ratio (m/z) with their intensity relative to the basic signal (100%). Under HRMS, the molecular mass was determined, whereby “calc.” represents the theoretical value of the exact mass and “found” represents the obtained value in the spectra.

UV-Vis spectroscopy (UV-Vis):

All UV-Vis spectra were recorded on a Specord 50 Plus made by Q Analytik Jena. Before the measurement, the samples were dissolved in CH_2Cl_2, MeOH, or $CHCl_3$ filled in glass cuvettes with a thickness of 0.1 cm or 0.5 cm.

Analytical thin-layer chromatography (TLC):

TLC was carried out on Merck silica gel coated aluminum plates (silica 60, F254). Solvent mixtures were measured volumetrically. If an assignment was not possible under daylight, fluorescence quenching under UV light was used at $\lambda = 254$ nm or $\lambda = 365$ nm via a UV lamp UV-6 S/L purchased at Hereolab or $\lambda = 395$ nm via a UV flashlight Veetop Schwarzlicht UV purchased by QVQ EU.

Column chromatography:

If not stated otherwise, the crude products were purified via flash column chromatography using p.a. solvents as described after Still et al.[308] Silica gel 60 (0.040 × 0.063 mm, Geduran®, Merck) was used as a stationary phase. Alternatively, aluminum oxide 150 basic (particle size: 70% between 0.063 – 0.200 mm, Sigma Aldrich) Brockmann activity III (6% H2O (w/w)) was used.

Analytical balance:

Weight measurements were done on an HR-250A purchased at A&D Company.

Minimum weight: 10 mg, maximum weight: 252 g, calibrated value: 1 mg.

5.2 Synthesis of non-porphyrin moieties

Di(1*H*-pyrrol-2-yl)methane (**18**)[181]

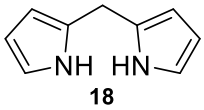

18

To 233 mL of freshly distilled 1*H*-pyrrole (225 g, 3.36 mol, 92.5 equiv), paraformaldehyde (1.09 g, 36.3 mmol, 1.00 equiv) was added and the resulting suspension was stirred for 10 min at 55 °C. Then, indium trichloride (800 mg, 3.62 mmol, 0.0996 equiv) was added and the resulting mixture was stirred for additional 3 h at 55 °C. After cooling down to 25 °C, powdered sodium hydroxide (4.81 g, 120 mmol, 3.31 equiv) was added and the mixture was stirred for another hour, followed by filtration. The obtained crude product was purified *via* flash-chromatography on silica gel (cyclohexane/ethyl acetate 7:1 to 5:1) to yield the desired product 2-(1*H*-pyrrol-2-ylmethyl)-1*H*-pyrrole (3.12 g, 21.3 mmol, 59% yield) **18** as a colorless solid.

***R*$_f$** (*c*Hex/EtOAc, 2:1) = 0.58. – **^{1}H NMR** (400 MHz, $CDCl_3$): δ = 7.67 (bs, 2H, N*H*), 6.62 (td, ^3J = 2.7, 1.6 Hz, 2H), 6.18 (q, ^3J = 2.9 Hz, 2H), 6.03 – 6.09 (m, 2H), 3.94 (s, 2H, CH_2) ppm. – **^{13}C NMR** (101 MHz, $CDCl_3$): δ = 129.2 (C_q), 117.5 (+, CH), 108.4 (+, CH), 106.6 (+, CH), 26.4 (–, CH_2) ppm. – **IR** (ATR): $\tilde{\nu}$ = 3325, 1561, 1439, 1422, 1327, 1244, 1181, 1119, 1108, 1095, 1024, 960, 884, 806, 798, 747, 720, 683, 666, 625, 599, 585, 496, 469 cm^{-1}. – **MS** (EI, 70 eV, 20 °C): *m/z* (%) =146.1 (100) $[M]^+$, 118.1 (12), 80.1 (30), 67.1 (18). – **HRMS** ($C_{10}H_{10}O_3$): calc.: 146.0844, found: 146.0844.

Additional information on the chemical synthesis is available *via* Chemotion repository:

https://doi.org/10.14272/reaction/SA-FUHFF-UHFFFADPSC-PBTPREHATA-UHFFFADPSC-NUHFF-NUHFF-NUHFF-ZZZ.8

Additional information on the analysis of the target compound is available *via* Chemotion repository:

https://doi.org/10.14272/PBTPREHATAFBEN-UHFFFAOYSA-N.5

2-[(4-Bromophenyl)-(1*H*-pyrrol-2-yl)methyl]-1*H*-pyrrole (**76**)[181]

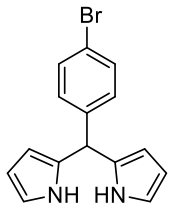

76

To 34.7 mL of freshly distilled 1*H*-pyrrole (33.6 g, 501 mmol, 92.7 equiv) was added 4-bromobenzaldehyde (1.00 g, 5.40 mmol, 1.00 equiv). Then indium trichloride (119 mg, 539 µmol, 0.0996 equiv) was added and the resulting mixture was stirred for 3 h at 55 °C. After cooling down to 25 °C, powdered sodium;hydroxide (713 mg, 17.8 mmol, 3.30 equiv) were added and the mixture was stirred for another hour, followed by filtration. The obtained crude product was purified *via* flash-chromatography on silica gel (cyclohexane/ethyl acetate 7:1 to 5:1). 2-[(4-Bromophenyl)-(1*H*-pyrrol-2-yl)methyl]-1*H*-pyrrole (1.29 g, 4.27 mmol, 79% yield) **76** was obtained as colorless solid.

***R*$_f$** = 0.68 (*c*Hex/EtOAc, 2:1). **^{1}H NMR** (500 MHz, $CDCl_3$ [7.26 ppm], ppm) δ = 7.91 (s, 2H, H_{NH}), 7.45–7.42 (m, 2H, H_{Ar}), 7.11–7.07 (m, 2H, H_{Ar}), 6.71 (td, J = 2.6, 1.5 Hz, 2H, H_{Ar}), 6.16 (q, J = 2.9 Hz, 2H, H_{Ar}), 5.89 (ddt, J = 3.6, 2.4, 1.1 Hz, 2H, H_{Ar}), 5.44 (s, 1H, H_{Ar}). Impurities: spectrum contains cyclohexane (1.44 ppm), ethyl acetate (4.12, 2.05, 1.25 ppm), water (1.53 ppm) and grease (0.08 ppm); **^{13}C NMR** (126 MHz, $CDCl_3$ [77.16], ppm) δ = 141.3 (C_q, 1C), 132.0 (C_q, 2C), 131.8 (+, CH_{Ar}, 2C), 130.3 (+, CH_{Ar}, 2C), 121.0 (C_q, 1C), 117.6 (+, CH_{Ar}, 2C), 108.7 (+, CH_{Ar}, 2C), 107.6 (+, CH_{Ar}, 2C), 43.6 (+, CH, 1C); **MS** (ESI), m/z (%): 303/301 (34/61) [M]+, 299 (61), 177 (100), 102 (51). **HRMS** (ESI) ($C_{15}H_{14}{}^{79}BrN_2^+$): calc. 301.0340, found 301.0333 303.0316 (34), 301.0335 (33), 301.0161 (61), 299.0181 (61), 177.1123 (100), 102.1283 (51); IR (ATR, $\tilde{\nu}$) = 3373 (w), 2924 (m), 2849 (w), 1558 (w), 1486 (m), 1465 (w), 1449 (w), 1425 (w), 1401 (w), 1254 (w), 1113 (w), 1088 (m), 1071 (m), 1027 (s), 1010 (s), 969 (w), 884 (w), 847 (w), 793 (m), 762 (s), 713 (vs), 646 (w), 527 (m), 503 (vs), 397 (m) cm^{-1}.

Additional information on the chemical synthesis is available *via* Chemotion repository:

https://doi.org/10.14272/reaction/SA-FUHFF-UHFFFADPSC-SJDXTHJAKN-UHFFFADPSC-NUHFF-NUHFF-NUHFF-ZZZ

Additional information on the analysis of the target compound is available *via* Chemotion repository:

https://doi.org/10.14272/SJDXTHJAKNMBFS-UHFFFAOYSA-N.2

2-(4-(Di(1*H*-pyrrol-2-yl)methyl)phenyl)pyridine (**69**)[181]

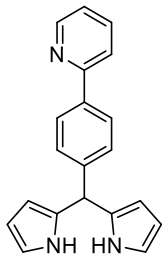

69

To freshly distilled pyrrole (6.79 g, 7.00 mL, 101 mmol, 18.5 equiv) was added 4-(2-pyridyl)benzaldehyde (1.00 g, 5.46 mmol, 1.00 equiv) and the resulting suspension was stirred for 30 min at 55 °C. Then indium trichloride (24.1 mg, 109 µmol, 0.0200 equiv) was added and the resulting mixture was stirred for additional 3 h at 55 °C. After cooling down to 25 °C, powdered sodium hydroxide (145 mg, 3.61 mmol, 3.31 equiv) was added and the mixture was stirred for another hour, followed by filtration. The solvent was removed under reduced pressure. The obtained crude product was purified via flash-chromatography on silica gel (cyclohexane/ethyl acetate 10:1 to 7:1). 2-(4-(di(1*H*-pyrrol-2-yl)methyl)phenyl)pyridine (467 mg, 1.56 mmol, 29% yield) **69** was obtained as a yellow solid.

***R*$_f$** = 0.36 (*c*Hex/EtOAc, 3:1). **^{1}H NMR** (500 MHz, $CDCl_3$ [7.26], ppm) δ = 8.68 (d, J = 4.9 Hz, 1H), 8.00 (s, 2H), 7.93 (d, J = 8.2 Hz, 2H), 7.75 (td, J = 7.9, 1.7 Hz, 1H), 7.70 (d, J = 7.8 Hz, 1H), 7.33 (d, J = 8.2 Hz, 2H), 7.25–7.19 (m, 1H), 6.82–6.59 (m, 2H), 6.17 (q, J = 2.8 Hz, 2H), 5.98–5.94 (m, 2H), 5.54 (s, 1H). Impurities: spectrum contains ethyl acetate (1.26 (t), 2.05 (s), 4.12 (q) ppm) and silicon grease (0.07 (s) ppm); **^{13}C NMR** (126 MHz, $CDCl_3$ [77.16], ppm) δ = 157.3 (C_q, 1C), 149.8 (+, CH_{Ar}, 1C), 143.1 (Cq, 1C), 138.4 (Cq, 1C), 136.9 (+, CH_{Ar}, 1C), 132.4 (C_q, 2C), 129.0 (+, CH_{Ar}, 2C), 127.4 (+, CH_{Ar}, 2C), 122.3 (+, CH_{Ar}, 1C), 120.7 (+, CH_{Ar}, 1C), 117.4 (+, CH_{Ar}, 2C), 108.7 (+, CH_{Ar}, 2C), 107.4 (+, CH_{Ar}, 2C), 43.9 (+, CH, 1C) Impurities: ethyl acetate (171.3, 60.5, 21.2, 14.3 ppm), silicon grease (1.2 ppm); **MS** (ESI), m/z (%): 298 (100) [M–H]-, 199 (1), 118 (12), 116 (2), 111 (2), 103 (2), 102 (33). **HRMS** (ESI) ($C_{20}H_{18}N_3^-$): calc.: 298.1349, found: 298.1333; UV-Vis (abs., CH_2Cl_2, 21 °C), λ_{max} = 282 nm; **IR** (ATR, $\tilde{\nu}$) = 2959 (w), 2921 (w), 2856 (w), 1691 (m), 1679 (m), 1606 (m), 1588 (s), 1574 (m), 1562 (m), 1469 (s), 1434 (s), 1404 (m), 1305 (m), 1261 (m), 1177 (m), 1153 (m), 1115 (s), 1095 (s), 1030 (s), 1016 (s), 990 (m), 884 (s), 858 (s), 844 (s), 803 (s), 776 (vs), 761 (vs), 721 (vs) cm^{-1}.

Additional information on the chemical synthesis is available *via* Chemotion repository:

https://doi.org/10.14272/reaction/SA-FUHFF-UHFFFADPSC-ILSHJPHOTB-UHFFFADPSC-NUHFF-NUHFF-NUHFF-ZZZ

Additional information on the analysis of the target compound is available *via* Chemotion repository:

https://doi.org/10.14272/ILSHJPHOTBMRGU-UHFFFAOYSA-N.1

2-[Bis(1*H*-pyrrol-2-yl)methyl]-5-methyl-pyridine (**70**)[181]

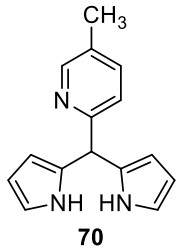

70

To freshly distilled pyrrole (10.3 g, 10.6 mL, 153 mmol, 18.5 equiv) was added 5-methylpicolinaldehyde (1.00 g, 8.26 mmol, 1.00 equiv) and the resulting suspension was stirred for 30 min at 55 °C. Then indium trichloride (36.5 mg, 165 µmol, 0.0200 equiv) was added and the resulting mixture was stirred for additional 3 h at 55 °C. After cooling down to 25 °C, powdered sodium hydroxide (219 mg, 5.46 mmol, 0.662 equiv) was added and the mixture was stirred for another hour, followed by filtration. The solvent was removed under reduced pressure. The obtained crude product was purified *via* flash-chromatography on silica gel (cyclohexane/ethyl acetate 10:1 to 7:1). 2-(Di(1*H*-pyrrol-2-yl)methyl)-5-methylpyridine (991 mg, 4.18 mmol, 51% yield) **70** was obtained as a grey solid.

R_f = 0.43 (*c*Hex/EtOAc, 1:1). **^{1}H NMR** (500 MHz, $CDCl_3$ [7.26], ppm) δ = 8.87 (s, 2H), 8.43 (dt, J = 2.4, 0.8 Hz, 1H), 7.46 (ddd, J = 7.9, 2.3, 0.8 Hz, 1H), 7.18 (dd, J = 7.8, 0.8 Hz, 1H), 6.69 (dt, J = 2.7, 1.3 Hz, 2H), 6.12 (q, J = 2.9 Hz, 2H), 5.92 (td, J = 1.7, 0.9 Hz, 2H), 5.46 (s, 1H), 2.32 (s, 3H). Impurities: spectrum contains ethyl acetate (1.26 (t), 2.05 (s), 4.12 (q)); **^{13}C NMR** (126 MHz, $CDCl_3$ [77.16], ppm) δ = 158.3 (+, C_q, 1C), 149.9 (+, CH_{Ar}, 1C), 137.6 (+, CH_{Ar}, 1C), 131.9 (+, C_q, 2C), 131.4 (+, C_q, 1C), 122.7 (+, CH_{Ar}, 1C), 117.3 (+, CH_{Ar}, 2C), 108.2 (+, CH_{Ar}, 2C), 106.3 (+, CH_{Ar}, 2C), 44.8 (+, CH_{Ar}, 1C), 18.1 (+, CH_3, 1C); **MS** (ESI), m/z (%): 238 (17) $[M+H]^+$, 236 (14), 224 (24), 171 (100). Unknown adducts: 489 (80). **HRMS** (ESI) ($C_{15}H_{16}N_3^+$): calc.: 238.1344, found: 238.1335; **UV-Vis** (CH_2Cl_2), λmax = 243 nm; **IR** (ATR, ṽ) = 3346 (m), 3275 (vw), 3160 (w), 3126 (w), 3121 (w), 3092 (w), 3048 (w), 3021 (vw), 2985 (w), 2961 (w), 2921 (w), 2864 (w), 2851 (w), 1601 (vw), 1568 (w), 1558 (w), 1480 (w), 1459 (w), 1438 (w), 1422 (w), 1414 (w), 1404 (w), 1378 (w), 1316 (w), 1278 (vw), 1265 (w), 1247 (vw), 1220 (w), 1186 (w), 1167 (vw), 1130 (w), 1116 (w), 1095 (m), 1040 (w), 1023 (m), 976 (w), 965 (w), 885 (w), 874 (w), 857 (w), 810 (w), 796 (m), 768 (s), 714 (vs), 662 (m), 643 (w), 612 (m), 579 (vs), 557 (w), 511 (m), 477 (w), 469 (w), 449 (vw), 432 (vw), 408 (w) cm^{-1}.

Additional information on the chemical synthesis is available *via* Chemotion repository:

https://doi.org/10.14272/reaction/SA-FUHFF-UHFFFADPSC-NJRVDFUNQH-UHFFFADPSC-NUHFF-NUHFF-NUHFF-ZZZ

Additional information on the analysis of the target compound is available *via* Chemotion repository:

https://doi.org/10.14272/NJRVDFUNQHSZOA-UHFFFAOYSA-N.1

1,2-Bis[4-(4,4,5,5-tetramethyl-1,3,2-dioxaborolan-2-yl)phenyl]ethane-1,2-dione (**72**)

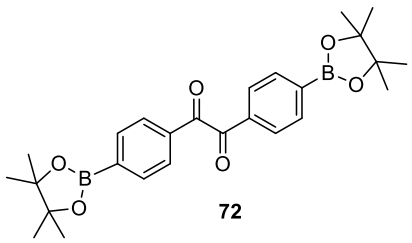

72

1,2-Bis(4-bromophenyl)ethane-1,2-dione (2.00 g, 5.43 mmol, 1.00 equiv), 4,4,5,5-tetramethyl-2-(4,4,5,5-tetramethyl-1,3,2-dioxaborolan-2-yl)-1,3,2-dioxaborolane (4.14 g, 16.3 mmol, 3.00 equiv), Pd(dppf)Cl_2 (408 mg, 543 µmol, 0.100 equiv), and potassium acetate (3.73 g, 38.0 mmol, 7.00 equiv), were dissolved in degassed dioxane (50 mL) under argon atmosphere. The reaction mixture was stirred and heated at 100 °C for 16 h. After cooling down to 25 °C, the reaction mixture was added to water and extracted with hexane and CH_2Cl_2. The organic layers were combined and washed with water and brine, then dried with $MgSO_4$ and the solvent was evaporated under reduced pressure. The crude residue was adsorbed on a small amount of silica gel and was purified *via* column chromatography (CH_2Cl_2/MeOH 20:1). The target compound was isolated after recrystallization from methanol. 1,2-Bis[4-(4,4,5,5-tetramethyl-1,3,2-dioxaborolan-2-yl)phenyl]ethane-1,2-dione (1.46 g, 3.17 mmol, 58% yield) **72** was obtained as a colorless solid.

***R*$_f$** = 0.47 (CH_2Cl_2/MeOH 50:1). **^{1}H NMR** (500 MHz, $CDCl_3$ [7.26], ppm) δ = 7.93 (s, 8H), 1.35 (s, 24H); **^{13}C NMR** (126 MHz, $CDCl_3$ [77.16], ppm) δ = 194.8 (CO, 2C), 135.2 (+, CH, 4C), 134.8 (C_q, 2C), 128.8 (+, CH, 4C), 84.4 (C_q, 4C), 24.9 (+, CH_3, 8C). Missing signals: C_q (2C) not visible in the spectrum due to the coupling with boron; **^{11}B NMR** (128 MHz, $CDCl_3$, ppm) δ = 30.44 (s, 2B); **MS** (ESI), m/z (%): 463 (100) $[M+H]^+$, 462 (45) $[M]^+$. **HRMS** (ESI) ($C_{26}H_{33}B_2O_6^+$): calc. 463.2463, found 463.2471; **IR** (ATR, ṽ) = 2979 (w), 1676 (s), 1507 (m), 1400 (s), 1357 (vs), 1298 (w), 1272 (m), 1208 (s), 1177 (w), 1167 (w), 1140 (vs), 1112 (w), 1089 (vs), 1016 (w), 963 (w), 891 (s), 856 (s), 827 (w), 809 (m), 765 (m), 705 (s), 656 (vs), 647 (vs), 630 (w), 578 (w), 518 (w), 499 (vw), 431 (w), 422 (w) cm^{-1}.

Additional information on the chemical synthesis is available *via* Chemotion repository:

https://doi.org/10.14272/reaction/SA-FUHFF-UHFFFADPSC-BDTMRQVYWG-UHFFFADPSC-NUHFF-NUHFF-NUHFF-ZZZ

Additional information on the analysis of the target compound is available *via* Chemotion repository:

https://doi.org/10.14272/BDTMRQVYWGTPFO-UHFFFAOYSA-N.1

5.3 Synthesis of conventional porphyrins and their complexes

5,15-Diphenylporphyrin (**19**)[127]

In a 4 L flask, 2-([1]*H*-pyrrol-2-ylmethyl)-[1]*H*-pyrrole (1.33 g, 9.10 mmol, 1.00 equiv) was dissolved in 3.7 L DCM and benzaldehyde (2.03 g, 1.95 mL, 19.1 mmol, 2.10 equiv) was added. Argon gas was passed through the mixture for 15 min to remove dissolved oxygen. Afterwards, TFA (1.27 g, 853 µL, 11.1 mmol, 1.22 equiv) was added dropwise over 30 min. The mixture was stirred for 4 h in the dark. Then, 4,5-dichloro-3,6-dioxocyclohexa-1,4-diene-1,2-dicarbonitrile (5.00 g, 22.0 mmol, 2.42 equiv) was added to the mixture, which was further stirred for 1 h before the addition of 10 mL of triethylamine. The crude mixture was concentrated under reduced pressure and the resulting crude product was filtered through a short column eluting with CH_2Cl_2. After removing the solvent again, a final thorough wash of the remaining solid with MeOH yielded the desired product 5,10-diphenylporphyrin (2.43 g, 5.25 mmol, 58% yield) **19** as a purple solid.

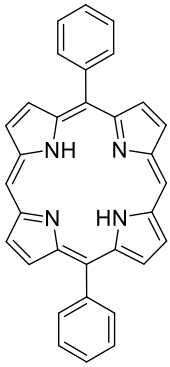

19

***R*$_f$** (CH_2Cl_2/*c*Hex, 1:1) = 0.48. – **^{1}H NMR** (400 MHz, $CDCl_3$): δ = 10.32 (s, 2H, H_{meso}), 9.40 (d, ^3J = 4.6 Hz, 4H, $H_{pyrrole}$), 9.10 (d, ^3J = 4.6 Hz, 4H, $H_{pyrrole}$), 8.32 – 8.25 (m, 4H, $H_{aromatic}$), 7.85 – 7.79 (m, 6H, $H_{aromatic}$), –3.11 (bs, 2H, N*H*) ppm. – **^{13}C NMR** (101 MHz, $CDCl_3$): δ = 147.3 (C_q), 145.4 (C_q), 141.5 (C_q), 135.0 (+, CH), 131.8 (+, CH), 131.2 (+, CH), 127.9 (+, CH), 127.1 (+, CH), 119.3 (C_q), 105.4 (+, CH) ppm. – **UV-Vis** ($CHCl_3$): λ_{max} (rel. absorption) = 407 (5.44), 503 (4.23), 537 (3.70), 575 (3.74), 630 (3.18) nm. – **IR** (ATR): $\tilde{\nu}$ = 3050, 1578, 1532, 1482, 1438, 1406, 1324, 1237, 1196, 1145, 1051, 1000, 985, 972, 955, 851, 784, 745, 717, 688, 649, 558, 500, 432, 414, 396 cm^{-1}. – **MS** (ESI): *m/z* (%) = 463 (100) $[M+H]^+$. – **HRMS** ($C_{32}H_{23}N_4$): calc.: 463.1917, found: 463.1900.

Additional information on the chemical synthesis is available *via* Chemotion repository:

https://doi.org/10.14272/reaction/SA-FUHFF-UHFFFADPSC-FNNOEKVUXX-UHFFFADPSC-NUHFF-NZWZG-NUHFF-ZZZ.2

Additional information on the analysis of the target compound is available *via* Chemotion repository:

https://doi.org/10.14272/FNNOEKVUXXVPAI-DUVOQLPESA-N.3

5,10,15-Triphenylporphyrin (**44**)[127]

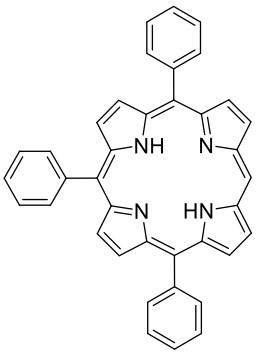

44

Under argon atmosphere 5,10-diphenylporphyrin (1.26 g, 2.72 mmol, 1.00 equiv) was dissolved in dry THF (600 ml) and cooled to 0 °C. Subsequently, cyclohexatriene lithium (3.04 g, 19.1 mL, 36.2 mmol, 1.90 M, 13.3 equiv) was added. The reaction mixture was stirred at room temperature for 30 min and then quenched with H_2O. After stirring for 10 min, 4,5-dichloro-3,6-dioxocyclohexa-1,4-diene-1,2-dicarbonitrile (1.24 g, 5.45 mmol, 2.00 equiv) was added and stirred for further 15 min. The solvent was removed under reduced pressure and the crude product was filtered through a short layer of silica gel eluting with CH_2Cl_2. A final thorough wash with MeOH afforded the title compound 5,10,15-triphenylporphyrin (1.39 g, 2.58 mmol, 95% yield) **44** as a purple solid.

R_f (CH_2Cl_2/*c*Hex, 1:1) = 0.47. – **^{1}H NMR** (400 MHz, $CDCl_3$): δ = 10.22 (s, 1H, H_{meso}), 9.34 (d, ^3J = 4.6 Hz, 2H, $H_{pyrrole}$), 9.04 (d, ^3J = 4.6 Hz, 2H, $H_{pyrrole}$), 8.93 (d, ^3J = 4.8 Hz, 2H, $H_{pyrrole}$), 8.90 (d, ^3J = 4.8 Hz, 2H, $H_{pyrrole}$), 8.30 – 8.21 (m, 6H, $H_{aromatic}$), 7.84 – 7.73 (m, 9H, $H_{aromatic}$). –2.98 (bs, 2H, N*H*) ppm. – **^{13}C NMR** (101 MHz, $CDCl_3$): δ = 142.7 (C_q), 141.9 (C_q), 134.8 (+, CH), 134.6 (+, CH), 131.6 (+, CH), 131.4 (+, CH), 130.8 (+, CH), 127.9 (+, CH), 127.0 (+, CH), 126.7 (+, CH), 120.7 (C_q), 119.8 (C_q), 104.9 (+, CH) ppm. – **UV-Vis** ($CHCl_3$): λ_{max} (rel. Absorption) = 413 (2.83), 509 (0.41), 543 (0.12), 583 (0.12), 638 (0.05) nm. – **IR** (ATR): $\tilde{\nu}$ = 2330, 1592, 1555, 1471, 1438, 1405, 1341, 1220, 1191, 1150, 1065, 1051, 1031, 1000, 977, 959, 854, 794, 784, 745, 726, 701, 654, 638, 555, 512, 494 cm^{-1}. – **MS** (FAB, 3-NBA): *m/z* (%) = 539 (100) $[M+H]^+$. – **HRMS** ($C_{38}H_{27}N_4$): calc.: 539.2236, found: 539.2234.

Additional information on the chemical synthesis is available *via* Chemotion repository:

https://doi.org/10.14272/reaction/SA-FUHFF-UHFFFADPSC-ONZNTVWSXS-UHFFFADPSC-NUHFF-NBVCV-NUHFF-ZZZ.2

Additional information on the analysis of the target compound is available *via* Chemotion repository:

https://doi.org/10.14272/ONZNTVWSXSVUHQ-WIYWIPGRSA-N.3

5-Bromo-10,15,20-triphenylporphyrin (**45**)[127]

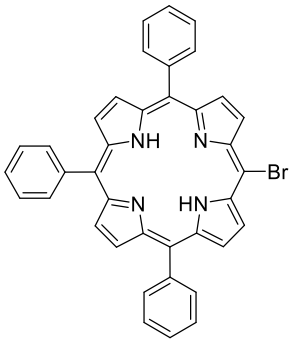

45

5,10,15-Triphenylporphyrin (1.30 g, 2.41 mmol, 1.00 equiv) was dissolved in CH2Cl2 and cooled to 0 °C. 1-Bromopyrrolidine-2,5-dione (450 mg, 2.53 mmol, 1.05 equiv) was added and the resulting mixture was stirred for 60 min. The solvent was removed under reduced pressure. The crude product was purified *via* column chromatography (CH_2Cl_2/*n*-pentane 1:3) to afford the title compound 5-bromo-10,15,20-triphenylporphyrin (1.44 g, 2.33 mmol, 97% yield) **45** as a purple solid. $\boldsymbol{R_f}$ (CH_2Cl_2/*c*Hex, 1:1) = 0.66. – **^{1}H NMR** (400 MHz, $CDCl_3$): δ = 9.67 (d, ^3J = 4.8 Hz, 2H, $H_{pyrrole}$), 8.91 (d, ^3J = 4.9 Hz, 2H, $H_{pyrrole}$), 8.80 (s, 4H, $H_{pyrrole}$), 8.23 – 8.15 (m, 6H, $H_{aromatic}$), 7.83 – 7.71 (m, 9H, $H_{aromatic}$), –2.14 (bs, 2H, N*H*) ppm. – **^{13}C NMR** (101 MHz, $CDCl_3$): δ = 142.0 (C_q), 141.9 (C_q), 134.7 (+, CH), 134.6 (+, CH), 128.0 (+, CH), 128.0 (+, CH), 121.1 (C_q), 120.9 (C_q), 103.0 (C_q) ppm. – **UV-Vis** ($CHCl_3$): λ_{max} (rel. absorption) = 418 (5.34), 518 (4.22), 553 (3.93), 595 (3.70), 652 (3.61) nm. – **IR** (ATR): $\tilde{\nu}$ = 1594, 1469, 1439, 1341, 1216, 1176, 1071, 1000, 979, 963, 843, 793, 743, 718, 697, 633, 554, 517, 418 cm^{-1}. – **MS** (ESI): *m/z* (%) = 617/618/619/620 (100/43/99/41) $[M+H]^+$. – **HRMS** ($C_{38}H_{26}N_4{}^{79}Br$): calc.: 617.1335, found: 617.1323.

Additional information on the chemical synthesis is available via Chemotion repository:

https://doi.org/10.14272/reaction/SA-FUHFF-UHFFFADPSC-SSDAPHKBPY-UHFFFADPSC-NUHFF-NCEIP-NUHFF-ZZZ.2

Additional information on the analysis of the target compound is available via Chemotion repository:

https://doi.org/10.14272/SSDAPHKBPYAYKP-YVFGNCJRSA-N.3

5,10,15-Triphenyl-20-(4,4,5,5-tetramethyl-1,3,2-dioxaborolan-2-yl)porphyrin (**53**)

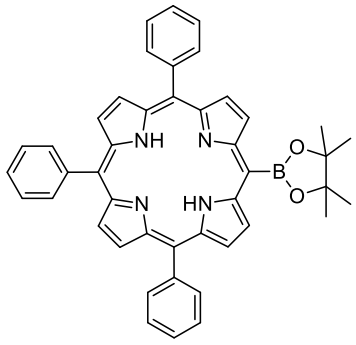

53

Under argon atmosphere, 5-bromo-10,15,20-triphenylporphyrin (200 mg, 324 µmol, 1.00 equiv), pinacolborane (829 mg, 940 µL, 6.48 mmol, 20.0 equiv), dichloropalladium triphenylphosphane (56.8 mg, 81.0 µmol, 0.250 equiv) and triethylamine (426 mg, 584 µL, 4.21 mmol, 13.0 equiv) were dissolved in 1,2-dichloroethane. The mixture was stirred for 16 h at 75 °C. The solvent was removed under reduced pressure and redissolved in CH_2Cl_2. The organic phase was consecutively washed with H_2O, dried over Na_2SO_4, filtered and the solvent was removed under reduced pressure. The obtained crude product was purified via flash-chromatography on silica gel (CH_2Cl_2/ *n*-pentane 1:1) to afford the title compound 5,10,15-triphenyl-20-(4,4,5,5-tetramethyl-1,3,2-dioxaborolan-2-yl)porphyrin (92.9 mg, 140 µmol, 43% yield) **53** as purple solid.

***R*$_f$** = 0.58 (CH_2Cl_2/n-pentane 1:1). **^{1}H NMR** (400 MHz, CDCl3 [7.26], ppm): δ = 9.86 (d, 3J = 4.8 Hz, 2H), 8.96 (d, 3J = 4.8 Hz, 2H), 8.87 – 8.78 (m, 4H), 8.24-8.17 (m, 6H), 7.81 – 7.71 (m, 9H), 1.84 (s, 12H), –2.80 (s, 2H) ppm Impurities: 9.35 - 9.33 (aromatic side product), 1.53 (water), 1.28 (H grease), 0.94–0.82 (H grease), 0.08 (silicon grease); **^{13}C NMR** (101 MHz, $CDCl_3$ [77.16], ppm): δ = 142.51 (Cq), 142.16 (Cq), 134.71 (+, CH, 4C), 134.65 (+, CH, 4C), 127.90 (Cq, 4C), 127.82 (Cq, 4C), 126.81 (+, CH, 6C), 126.77 (+, CH, 6C), 121.93 (Cq, 4C), 120.17 (Cq, 4C), 85.37 (Cq, 2C), 25.47 (CH3, 4C) Impurities: H-grease (29.71), Silicon-graese (1.19); MS (ESI), m/z (%): 667 (9), 666 (42), 665 (100), 664 (20), 288 (9). HRMS (ESI) ($C_{44}H_{38}BN_4O_2^+$): calc.: 665.3082, found: 665.3086; **UV-Vis** (abs., CH_2Cl_2, 20 °C), λ_{max} = 417 nm.

Additional information on the chemical synthesis is available *via* Chemotion repository:

https://doi.org/10.14272/reaction/SA-FUHFF-UHFFFADPSC-ZEJJPPPXVV-UHFFFADPSC-NUHFF-NOKYX-NUHFF-ZZZ

Additional information on the analysis of the target compound is available *via* Chemotion repository:

https://doi.org/10.14272/ZEJJPPPXVVFSRQ-UAVNSCBQSA-N.1

5-(2-Formylphenyl)-10,15,20-triphenylporphyrin (**56**)[127]

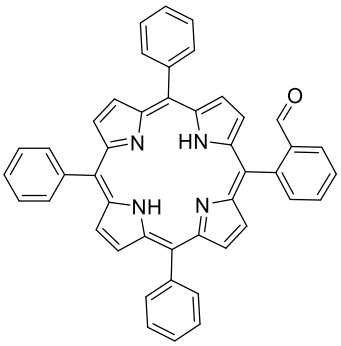

56

Under argon atmosphere, 5-bromo-10,15,20-triphenylporphyrin (362 mg, 586 µmol, 1.00 equiv), (2-formylphenyl)boronic acid (1.05 g, 7.02 mmol, 12.0 equiv), palladium triphenylphosphane (162 mg, 140 µmol, 0.239 equiv) and tripotassium phosphate (1.24 g, 5.86 mmol, 10.0 equiv) were dissolved in dry THF (80 mL). The mixture was stirred for 16 h at 80 °C. The solvent was removed under reduced pressure and the crude was re-dissolved in CH_2Cl_2. The organic phase was consecutively washed with H_2O, dried over Na_2SO_4, filtered and the solvent removed under reduced pressure. The crude product was purified by flash column chromatography on silica gel (CH_2Cl_2/ *n*-pentane 1:1) to afford the title compound 2-(10,15,20-triphenylporphyrin-5-yl)benzaldehyde (286 mg, 445 µmol, 76% yield) **56** as a purple solid.

***R*$_f$** (*c*Hex/EtOAc, 4:1) = 0.64. – **^{1}H NMR** (400 MHz, $CDCl_3$): δ = 9.52 (s, 1H, C*H*O), 8.93 – 8.86 (m, 6H, $H_{pyrrole}$), 8.67 (d, ^3J = 4.8 Hz, 2H), 8.46 – 8.41 (m, 1H, $H_{aromatic}$), 8.29 – 8.20 (m, 7H, $H_{aromatic}$), 7.99 – 7.90 (m, 2H, $H_{aromatic}$), 7.83 – 7.73 (m, 9H, $H_{aromatic}$), –2.67 (bs, 2H, N*H*) ppm. – **^{13}C NMR** (101 MHz, $CDCl_3$): δ = 191.2 (+, *C*HO), 145.6 (C_q), 142.1 (C_q), 142.0 (C_q), 138.2 (C_q), 135.8 (+, CH), 134.7 (+, CH), 134.7 (+, CH), 131.5 (+, CH), 129.1 (+, CH), 128.0 (+, CH), 127.0 (+, CH), 126.9 (+, CH), 126.3 (+, CH), 121.1 (C_q), 120.9 (C_q), 114.1 (C_q) ppm. – **UV-Vis** (CH_2Cl_2): λ_{max} (rel. absorption) = 243 (0.33), 372 (0.40), 418 (3.19), 516 (0.28), 551 (0.11), 591 (0.08), 647 (0.05) nm. – **IR (ATR)**: $\tilde{\nu}$ = 415, 518, 557, 574, 620, 642, 657, 663, 680, 696, 707, 724, 748, 786, 800, 915, 963, 980, 1000, 1058, 1071, 1157, 1176, 1184, 1193, 1214, 1220, 1349, 1383, 1439, 1470, 1592, 1694 (*ν*-CO), 1810, 1952, 2728, 2822, 2919, 3021, 3051, 3129, 3320 cm^{-1}. – **MS** (FAB, 3-NBA): *m/z* (%) = 642.2 (100) $[M]^+$, 419.3 (92). – **HRMS** ($C_{45}H_{31}O_1N_4$): calc.: 643.2498, found: 643.2497.

Additional information on the chemical synthesis is available *via* Chemotion repository:

https://doi.org/10.14272/reaction/SA-FUHFF-UHFFFADPSC-IXMWRMWFCF-UHFFFADPSC-NUHFF-NAGQZ-NUHFF-ZZZ.2

Additional information on the analysis of the target compound is available *via* Chemotion repository:

https://doi.org/10.14272/IXMWRMWFCFDTKE-HIXPDHBDSA-N.3

1,2-Phenylene-bis-5-(10,15,20-triphenylporphyrin) (**33**)[127]

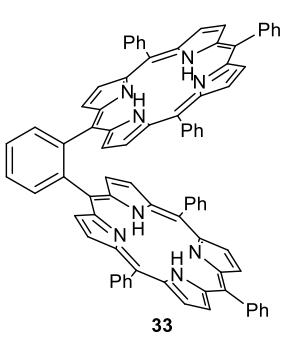

33

Under an argon atmosphere 2-(10,15,20-triphenylporphyrin-5-yl)benzaldehyde (200 mg, 311 µmol, 1.00 equiv) was dissolved in 40 mL of dry CH_2Cl_2. Argon gas was passed through the mixture for 15 min to remove dissolved oxygen. Subsequently benzaldehyde (99.1 mg, 933 µmol, 3.00 equiv), ^1H-pyrrole (83.5 mg, 1.24 mmol, 4.00 equiv) and $BF_3{\cdot}OEt_2$ (47.7 mg, 336 µmol, 1.08 equiv) were added while stirring the mixture in the dark. Three times a day, TLC was undertaken to check if the target compound is formed, if not, another batch of each compound was added until no starting material was left, which took 3 days. Afterwards 4,5-dichloro-3,6-dioxocyclohexa-1,4-diene-1,2-dicarbonitrile (706 mg, 3.11 mmol, 10.0 equiv) was added and stirred for further 1 h. Then, 5 mL NEt_3 were added and the crude mixture was concentrated under reduced pressure and filtered through a short layer of silica gel eluting with CH_2Cl_2, before concentrating the mixture again under reduced pressure. The crude product was purified by flash chromatography on silica gel twice (CH_2Cl_2/n-pentane 1:1, followed by CH_2Cl_2/*n*-pentane 2:1 to afford the title compound ortho-phenylene-bisporphyrin (158 mg, 137 µmol, 44% yield) **33** as a purple solid.

R_f (CH_2Cl_2/*n*-pentane, 1:1) = 0.63. – **^{1}H NMR** (500 MHz, THF-d_8): δ = 9.28 (d, ^3J = 4.7 Hz, 4H, $H_{pyrrole}$), 8.87 (dd, J = 5.7, 3.4 Hz, 2H, $H_{aromatic}$), 8.39 – 8.28 (m, 14H, $12H_{pyrrole}$, $2H_{aromatic}$), 8.03 – 7.97 (m, 2H $H_{aromatic}$), 7.80 (d, ^3J = 7.3 Hz, 4H, $H_{aromatic}$), 7.74 – 7.69 (m, 4H, $H_{aromatic}$), 7.68 – 7.52 (m, 14H), $H_{aromatic}$, 7.50 – 7.40 (m, 6H, $H_{aromatic}$), –3.82 (bs, 4H, N*H*) ppm. – **^{13}C NMR** (126 MHz, THF-d_8): δ = 146.7 (C_q), 143.1 (C_q), 143.1 (C_q), 135.5 (+, CH), 135.2 (+, CH), 135.1 (+, CH), 135.0 (+, CH), 128.4 (C_q), 128.2 (C_q), 127.5 (+, CH), 127.5 (+, CH), 127.4 (+, CH), 120.6 (C_q), 120.2 (C_q), 119.1 (C_q) ppm. – **UV-Vis** (CH_2Cl_2): λ_{max} (rel. absorption) = 218 (0.24), 409 (1.33), 419 (1.48), 520 (0.12), 552 (0.06), 594 (0.05), 649 (0.03) nm. – **IR** (ATR): $\tilde{\nu}$ = 3313, 2921, 2846, 1714, 1693, 1595, 1470, 1439, 1349, 1071, 1033, 1001, 980, 965, 798, 749, 727, 700 cm^{-1}. – **HRMS** (ESI) ($H_5C_{82}H_{50}N_8$): calc.: 1151.4544, found: 1151.4598.

Additional information on the chemical synthesis is available *via* Chemotion repository:

https://doi.org/10.14272/reaction/SA-FUHFF-UHFFFADPSC-GCDCSJMXKZ-UHFFFADPSC-NUHFF-NWDCB-NUHFF-ZZZ.1

Additional information on the analysis of the target compound is available *via* Chemotion repository:

https://doi.org/10.14272/GCDCSJMXKZHSKI-XZDYDVNVSA-N.2

5-(2-(Di(1*H*-pyrrol-2-yl)methyl)phenyl)-10,15,20-triphenylporphyrin (**69**)

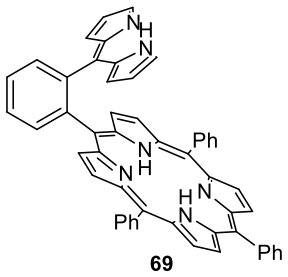

69

Under an argon atmosphere, 5-(2-formylphenyl)-10,15,20-triphenylporphyrin (60.0 mg, 93,3 µmol, 1.00 equiv.) was dissolved in pyrrole (6.5 mL, 6288 mg, 93.7 mmol, 1004 equiv.). A stream of argon was passed through the mixture for 15 min to remove dissolved oxygen. Then, TFA (24.7 mL, 36.5 g, 338 µmol, 3.62 equiv.) was added dropwise. The mixture was stirred for 4 h in the dark. Afterward, triethylamine (0.5 mL) was added and stirred for 15 min. Subsequently, the solvent was removed under reduced pressure in the absence of air. The crude product was purified by flash column chromatography on silica gel (toluene) to afford the title compound **69** as a purple solid (66.0 mg, 87.2 µmol, 93%).

***R*$_f$** (toluene) = 0.58. – **^{1}H NMR** (500 MHz, toluene-d$_8$): δ = 8.88 – 8.83 (m, 4H, H$_{pyrrole}$), 8.79 (d, ^3J = 4.7 Hz, 2H, H$_{pyrrole}$), 8.66 (d, ^3J = 4.8 Hz, 2H, H$_{pyrrole}$), 8.13 – 8.04 (m, 6H, H$_{aromatic}$), 7.95 (dd. J = 7.5, 1.4 Hz, 1H, H$_{aromatic}$), 7.69 (dd, J = 8.1, 1.4 Hz, 1H, H$_{aromatic}$), 7.53 – 7.42 (m, 10H, H$_{aromatic}$), 7.34 (td, J = 7.5, 1.4 Hz, 1H, H$_{aromatic}$), 6.30 (bs, 2H, NH$_{dipyrromethane}$), 6.04 (dd, J = 6.5, 2.8 Hz, 2H, H$_{dipyrromethane}$), 5.93 – 5.85 (m, 4H, H$_{dipyrromethane}$), 4.98 (s, 1H, H$_{dipyrromethane}$), –2.19 (bs, 2H, NH) ppm. – **^{13}C NMR** (126 MHz, toluene-d$_8$) : δ = 145.9 (C$_q$), 143.3 (C$_q$), 143.1 (C$_q$), 141.6 (C$_q$), 134.0 (C$_q$), 135.3 (+, CH), 135.3 (+, CH), 135.2 (+, CH), 134.5 (+, CH), 132.8 (C$_q$), 129.6 (+, CH), 128.6 (+, CH), 128.5 (+, CH), 128.3 (+, CH), 128.2 (+, CH), 127.3 (+, CH), 127.3 (+, CH), 126.0 (+, CH), 121.2 (C$_q$), 121.0 (C$_q$), 118.6 (+, CH), 116.7 (+, CH), 42.4 (+, CH) ppm. – **UV-Vis** (CH_2Cl_2): λ_{max} (rel. absorption) = 217 (0.21), 298 (0.07), 419 (1.61), 482 (0.02), 516 (0.08), 550 (0.04), 590 (0.03), 646 (0.02) nm. – **IR (ATR)**: $\tilde{\nu}$ = 3410, 3309, 3050, 3017, 2919, 2847, 1691, 1595, 1554, 1469, 1439, 1400, 1347, 1213, 1176, 1153, 1111, 1069, 1054, 1030, 1000, 979, 965, 798, 748, 720, 698, 656, 640, 463, 452, 439, 425, 416, 398, 382 cm^{-1}. – **MS** (ESI): *m/z* (%) = 759.3 (33) $[M+H]^+$, 643.2 (100). – **HRMS** (ESI) ($C_{53}H_{38}N_6$): calc.: 759.3236, found: 759.3225.

Additional information on the reaction details is available *via* the Chemotion repository: https://dx.doi.org/10.14272/reaction/SA-FUHFF-UHFFFADPSC-FJGPNDURHC-UHFFFADPSC-NUHFF-NXVFY-NUHFF-ZZZ

Additional information on the analysis of the target compound is available *via* the Chemotion repository:

https://dx.doi.org/10.14272/FJGPNDURHCLNNX-IIFGQYIMSA-N.1

5,15-Bis(2-(10,15,20)-triphenylporphyrinylphenyl)-10,20-diphenylporphyrin (**34**)[182]

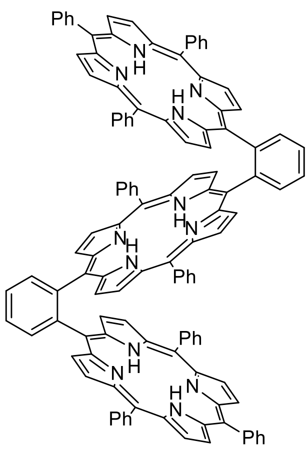

34

Under an argon atmosphere, 5-(2-(di(1*H*-pyrrole-2-yl)methyl)phenyl)-10,15,20-triphenylporphyrin (150 mg, 198 µmol, 2.00 equiv.) was dissolved in CH_2Cl_2, (60 mL) previously degassed by three freeze-pump-thaw-cycles. Subsequently, benzaldehyde (73.0 µL, 75.9 mg, 715 µmol, 7.22 equiv.) and TFA (64.6 µL, 95.6 mg, 1.18 mmol, 8.46 equiv.) were added within 26.5 h while stirring the mixture in the dark until all starting material was consumed. Afterward, DDQ (47.2 mg, 208 µmol, 2.10 equiv.) was added and stirred for 1 h under air, whereas oxygen supported oxidation. Then, NEt_3 (5 mL) was added and the crude mixture was concentrated under reduced pressure, filtered through a short layer of silica gel (CH_2Cl_2 + 1% NEt_3) and purified by flash column chromatography on silica gel (1 × CH_2Cl_2/*n*-pentane, 1:1 + 1% NEt_3); (1 × toluene/*c*Hex, 5:1) to afford the title compound **34** as a purple solid (2,3 mg, 1.3 µmol, 1%).

R_f (CH_2Cl_2) = 0.60. – **^{1}H NMR** (500 MHz, CD_2Cl_2): δ = 9.10 (d, ^3J = 4.8 Hz, 4H, $H_{pyrrole}$), 9.06 (d, ^3J = 4.8 Hz, 4H, $H_{pyrrole}$), 8.56 (d, ^3J = 4.8 Hz, 4H, $H_{pyrrole}$), 8.48 (dd, J = 6.5, 2.9 Hz, 2H, $H_{linker\text{-}benzene}$), 8.48 (dd, J = 6.3, 2.9 Hz, 2H, $H_{linker\text{-}benzene}$), 8.27 (d, ^3J = 4.8 Hz, 4H, $H_{pyrrole}$), 8.12 (d, ^3J = 4.8 Hz, 4H, $H_{pyrrole}$), 8.07 (d, ^3J = 4.7 Hz, 4H, $H_{pyrrole}$), 8.06 – 8.02 (m, 4H, $H_{aromatic}$), 7.99 (d, ^3J = 7.6 Hz, 2H, $H_{aromatic}$), 7.86 (d, ^3J = 7.8 Hz, 2H, $H_{aromatic}$), 7.75 (t, ^3J = 7.4 Hz, 3H, $H_{aromatic}$), 7.72 – 7.67 (m, 6H, $H_{aromatic}$), 7.66 – 7.60 (m, 5H, $H_{aromatic}$), 7.56 – 7.53 (m, 2H, $H_{aromatic}$), 7.53 – 7.41 (m, 10H, $H_{aromatic}$), 7.12 (d, ^3J = 7.3 Hz, 2H, $H_{aromatic}$), 6.73 – 6.65 (m, 4H, $H_{aromatic}$), 6.65 – 6.56 (m, 4H, $H_{aromatic}$), –3.79 (bs, 4H, NH_{out}), –4.20 (bs, 2H, NH_{in}) ppm. – **^{13}C NMR** (126 MHz, CD_2Cl_2) : δ = 144.9 (C_q), 144.7 (C_q), 142.5 (C_q), 142.1 (C_q), 142.1 (C_q), 136.9 (C_q), 136.5 (C_q), 135.3 (+, CH), 135.0 (+, CH), 134.8 (+, CH), 134.8 (+, CH), 134.4 (+, CH), 134.3 (+, CH), 132.5 – 128.9 (m, C_q), 128.1 (+, CH), 127.8 (+, CH), 127.6 (+, CH), 127.2 (+, CH), 127.2 (+, CH), 127.2 (+, CH), 126.8 (+, CH), 126.6 (+, CH), 120.3 (C_q), 119.8 (C_q),

119.6 (C_q), 119.2 (C_q), 118.9 (C_q) ppm. – **UV-Vis** (CH_2Cl_2): λ_{max} (rel. absorption) = 288 (3.12), 404 (4.14), 522 (3.01), 549 (2.72), 596 (2.59), 651 (2.34) nm. – **IR (ATR)**: $\tilde{\nu}$ = 2953, 2919, 2854, 1666, 1596, 1468, 1439, 1349, 1259, 1181, 1153, 1088, 1072, 1031, 967, 800, 798, 749, 730, 703, 577, 511, 418, 397 cm^{-1}. – **HRMS** (ESI) ($C_{120}H_{78}N_{12}H$): calc.: 1687.6551, found: 1687.6552.

Additional information on the reaction details is available *via* the Chemotion repository: https://dx.doi.org/10.14272/reaction/SA-FUHFF-UHFFFADPSC-MGTQLOOLBA-UHFFFADPSC-NUHFF-NZPNZ-NUHFF-ZZZ

Additional information on the analysis of the target compound is available *via* the Chemotion repository:

https://dx.doi.org/10.14272/MGTQLOOLBARGGW-FOTJXGMTSA-N.1

1,2-Bis(4-(10,15,20-triphenylporphyrin-5-yl)phenyl)ethane-1,2-dione (**73**)

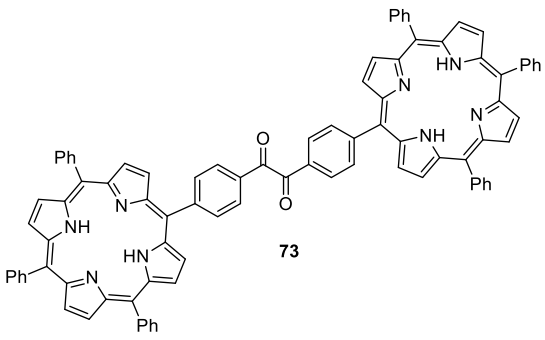

73

Under argon atmosphere, 5-bromo-10,15,20-triphenylporphyrin (200 mg, 324 µmol, 1.00 equiv), 1,2-bis[4-(4,4,5,5-tetramethyl-1,3,2-dioxaborolan-2-yl)phenyl]ethane-1,2-dione (150 mg, 324 µmol, 1.00 equiv), tetrakis(triphenylphosphine)palladium(0) (89.8 mg, 77.7 µmol, 0.240 equiv) and tripotassium phosphate (687 mg, 3.24 mmol, 10.0 equiv) were dissolved in dry THF (40 mL). The mixture was stirred for 2 days at 80 °C. The solvent was removed under reduced pressure and the residue re-dissolved in CH_2Cl_2. The organic phase was consecutively washed with H_2O, dried over Na_2SO_4, filtered and the solvent was removed under reduced pressure. The crude product was purified by flash column chromatography on silica gel (CH_2Cl_2/n-pentane 1:1). 1,2-bis(4-(10,15,20-triphenylporphyrin-5-yl)phenyl)ethane-1,2-dione (24.0 mg, 18.7 µmol, 6% yield) **73** was obtained as a purple solid.

R_f = 0.84 (CH_2Cl_2). **^{1}H NMR** (500 MHz, $CDCl_3$ [7.26], ppm) δ = 8.99 – 8.90 (m, 8H), 8.89 (s, 8H), 8.63 (d, *J* = 8.2 Hz, 4H), 8.52 (d, *J* = 8.1 Hz, 4H), 8.25 (dt, *J* = 7.9, 1.7 Hz, 12H), 7.78 (dtd, *J* = 8.7, 7.0, 1.5 Hz, 18H), -2.72 (s, 4H). Impurities: 5.31 (CH_2Cl_2), 1.53 (water), 1.45 (cHex), 1.28 (H grease), 0.94–0.82 (H grease), 0.08 (silicon grease); **^{13}C NMR** (126 MHz, $CDCl_3$ [77.16], ppm) δ = 194.7 (+, CCO, 2C), 149.6 (+, C_{Ar}, 2C), 142.1 (+, C_{Ar}, 8C), 135.5 (+,

C_{Ar}, 8C), 134.7 (+, C_{Ar}, 16C), 132.4 (+, C_{Ar}, 2C), 128.7 (+, C_{Ar}, 8C), 128.0 (+, C_{Ar}, 16C), 126.9 (+, C_{Ar}, 18C), 121.0 (+, C_{Ar}, 4C), 120.7 (+, C_{Ar}, 2C), 118.0 (+, C_{Ar}, 4C). Impurities: 53.5 (CH_2Cl_2), 29.7 (H grease), 26.9 (cHex), 1.19 (silicon grease); **MS** (ESI), m/z (%): 1283 (100) $[M+H]^+$, 1127 (28), 1126 (33), 1125 (64), 1124 (47), 1123 (84), 1122 (50), 1121 (46), 1120 (31). **HRMS** (ESI) ($C_{90}H_{59}N_8O_2^+$): calc.: 1283.4755, found: 1283.4761; UV-Vis (abs., CH_2Cl_2, 21 °C), λ_{max} = 419 nm; **IR** (ATR, $\tilde{\nu}$) = 3316 (w), 3024 (w), 1673 (w), 1596 (m), 1557 (w), 1472 (w), 1439 (w), 1400 (w), 1349 (w), 1210 (m), 1184 (w), 1171 (m), 1154 (w), 1072 (w), 1000 (w), 989 (w), 979 (w), 965 (s), 895 (m), 875 (w), 853 (w), 795 (vs), 748 (m), 727 (vs), 701 (vs), 671 (s), 657 (s), 639 (m), 629 (m), 620 (m), 558 (w), 524 (w), 486 (w), 412 (w), 390 (w) cm^{-1}.

Additional information on the chemical synthesis is available *via* Chemotion repository:

https://doi.org/10.14272/reaction/SA-FUHFF-UHFFFADPSC-AQVUHQULPB-UHFFFADPSC-NUHFF-NQEHY-NUHFF-ZZZ

Additional information on the analysis of the target compound is available *via* Chemotion repository:

https://doi.org/10.14272/AQVUHQULPBGHSX-GMCFREGPSA-N.1

1,2- Phenylene -bis-5-(10,15,20 (4-trisulfonicacidphenylporphyrin (**65**)

1,2-Phenylene-bis-5-(10,15,20-triphenylporphyrin) (10.0 mg, 8.69 µmol, 1.00 equiv) was dissolved in sulfuric acid (4.26 mg, 43.4 µmol, 5.00 equiv) and stirred at 100 °C for 16 h. Subsequently, a 7 M ammonia solution in MeOH was added while cooling the reaction mixture to 0 °C, until the color changed from green to red. The solvent was removed under reduced pressure and the crude product was extracted with ethanol to afford the title compound 1,2-Phenylene-bis-5-(10,15,20 (4-trisulfonicacidphenylporphyrin (12.0 mg, 7.35 µmol, 85% yield) **65** as purple solid.

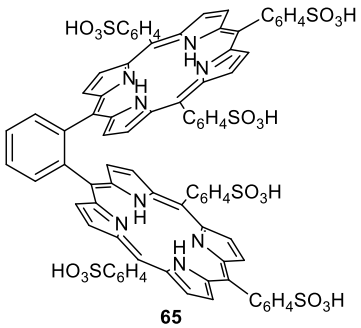

HRMS (ESI): ($C_{82}H_{51}N_8O_{18}S_6^{-3}$): calc.: 542.389, found: 542.389. ($C_{82}H_{50}N_8O_{18}S_6^{-4}$): calc.: 406.540, found: 406.540. ($C_{82}H_{49}N_8O_{18}S_6^{-5}$): calc.: 325.030, found: 325.031. ($C_{82}H_{48}N_8O_{18}S_6^{-6}$): calc.: 270.691, found: 270.691; **UV-Vis** (CH_3OH), λ_{max} = 405 nm; **IR** (ATR, $\tilde{\nu}$) = 3200 (m), 3193 (m), 3187 (m), 3064 (m), 3054 (m), 3048 (m), 2958 (w), 2914 (w), 2871 (w), 1662 (s), 1431 (s), 1180 (vs), 1133 (vs), 1058 (vs), 1034 (s), 1026 (s), 1004 (s), 972 (vs), 950 (vs), 890

(w), 839 (m), 799 (vs), 739 (m), 722 (vs), 625 (s), 582 (vs), 517 (m), 435 (s), 424 (s), 394 (m), 391 (m), 377 (m) cm^{-1}.

Additional information on the chemical synthesis is available *via* Chemotion repository:

https://dx.doi.org/10.14272/reaction/SA-FUHFF-UHFFFADPSC-LNKIVBRISP-UHFFFADPSC-NUHFF-NWDCB-NUHFF-ZZZ

Additional information on the analysis of the target compound is available *via* Chemotion repository:

https://dx.doi.org/10.14272/LNKIVBRISPYABL-XZDYDVNVSA-N.1

1,2- Phenylene -bis-5-(10,15,20-(4-trisulfonicacidphenylporphyrin))]-dipalladium(II) (**66**)

1,2- Phenylene -bis-5-(10,15,20 (4-trisulfonicacidphenylporphyrin (30.0 mg, 18.4 µmol, 1.00 equiv) was dissolved in MeOH and 38% HCl solution in H_2O was added until the color changed from red to green. Afterward, dichloropalladium (26.1 mg, 147 µmol, 8.00 equiv) was added and stirred at 60 °C for 12 h while the color of the reaction mixture changed from green to red. The solvent was removed under reduced pressure, the residue was redissolved in boiling EtOH, cooled to 0 °C and filtered the precipitate. This was repeated three times, before the solvent was removed under reduced pressure to afford the title compound 1,2- Phenylene -bis-5-(10,15,20-(4-trisulfonicacidphenylporphyrin))]-dipalladium(II) (28.0 mg, 15.2 µmol, 83% yield) **66** as purple solid.

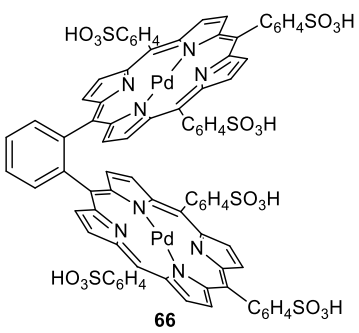

66

HRMS (ESI): ($C_{82}H_{47}N_8O_{18}Pd_2S_6^{-3}$): calc.: 612.315, found: 611.981. ($C_{82}H_{46}N_8O_{18}Pd_2S_6^{-4}$): calc.: 458.984, found: 458.734. ($C_{82}H_{45}N_8O_{18}Pd_2S_6^{-5}$): calc.: 366.986, found: 366.794; **UV-Vis** (CH_3OH), λ_{max} = 405 nm; **IR** (ATR, $\tilde{\nu}$) = 3174 (vs), 3047 (vs), 2962 (m), 2870 (m), 2813 (m), 1639 (w), 1463 (w), 1397 (vs), 1180 (vs), 1044 (vs), 1017 (vs), 950 (m), 921 (m), 863 (s), 789 (m), 620 (m), 581 (s), 433 (m) cm^{-1}.

Additional information on the chemical synthesis is available *via* Chemotion repository:

https://dx.doi.org/10.14272/reaction/SA-FUHFF-UHFFFADPSC-DVGZSBRSCW-UHFFFADPSC-NUHFF-NCDDW-NUHFF-ZZZ

Additional information on the analysis of the target compound is available *via* Chemotion repository:

https://dx.doi.org/10.14272/DVGZSBRSCWJYPO-IGJFLPGISA-N.1

1,2-Phenylene-bis-5-(10,15,20-triphenylporphyrin)-nickel(II) (**58**)

1,2-Phenylene-bis-5-(10,15,20-triphenylporphyrin) (80.0 mg, 69.5 µmol, 1.00 equiv) together with nickel pentane-2,4-dione (18.0 mg, 69.5 µmol, 1.00 equiv) were dissolved in 5 mL of DMF. The mixture was stirred for 30 min at 100 °C. After cooling down to 25 °C, the solvent was removed under reduced pressure. The crude product was purified *via* column chromatography on silca gel (CH_2Cl_2), to afford the title compound 1,2-Phenylene-bis-5-(10,15,20-triphenylporphyrin)-nickel(II) (63.0 mg, 52.2 µmol, 75% yield) **58** as purple solid.

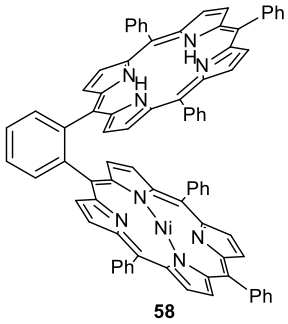

58

***R*$_f$** = 0.46 (CH_2Cl_2/n-pentane 1:1). **^{1}H NMR** (500 MHz, Chloroform-d [7.26], ppm) δ = 9.12 (d, J = 4.9 Hz, 2H), 8.98 (dd, J = 7.0 Hz, 1H), 8.92 (d, J = 4.7 Hz, 2H), 8.61 (dd, J = 7.5 Hz, 1H), 8.51–8.40 (m, 4H), 8.35 (d, J = 4.9 Hz, 2H), 8.32–8.26 (m, 3H), 8.25 (s, 1H), 8.23 (q, 4H), 8.17 (td, J = 7.1 Hz, 1H), 8.06 (s, 1H), 8.02 (s, 1H), 7.82 (d, J = 7.0 Hz, 2H), 7.70 (t, J = 7.6 Hz, 4H), 7.62 (q, J = 7.3 Hz, 13H), 7.55 (s, 3H), 7.44 (d, J = 7.0 Hz, 5H), -3.81 (s, 2H) Impurities (ppm): 8.02/2.96/2.88 (DMF), 1.53 (water), 1.28 (H grease), 0.94–0.82 (H grease), 0.08 (silicon grease); **^{13}C NMR** (126 MHz, $CDCl_3$ [77.16], ppm) δ = 144.6 (C_q), 143.8 (C_q), 142.7 (C_q), 142.1 (C_q), 142.1 (C_q), 142.0 (C_q), 141.7 (C_q), 141.6 (C_q), 140.8 (C_q), 140.6 (C_q), 134.5 (CH), 134.4 (CH), 134.2 (CH), 133.6 (CH), 133.5 (CH), 132.6 (CH), 131.5 (CH), 131.5 (CH), 131.3 (CH), 127.6 (CH), 127.5 (CH), 127.2 (CH), 127.1 (CH), 126.7 (CH), 126.7 (CH), 126.6 (CH), 126.6 (CH), 126.6 (CH), 119.7 (C_q), 119.4 (C_q), 118.5 (C_q), 118.2 (C_q), 117.7 (C_q), 117.0 (C_q). Missing signals (48 C) due to signal overlap. Impurities (ppm): 162.6/36.5/31.5 (DMF), 29.7 (H grease), 22.8/14.3 (n-pentane), 1.2 (silicon grease); **MS** (ESI), m/z (%): 1207/1208/1209/1210/1211 (7/6/3/3/2) $[M+H]^+$, 1151 (21), 459 (68), 447 (10), 274 (20), 240 (61), 223 (7), 170 (75), 150 (48), 112 (6), 102 (100). **HRMS** (ESI): ($C_{82}H_{53}N_8Ni^+$): calc.: 1207.3741, found: 1207.3697; **UV-Vis** (abs., CH_2Cl_2, 21 °C), λ_{max} = 405 nm; **IR** (ATR, $\tilde{\nu}$) = 3053 (w), 3020 (w), 2951 (w), 2919 (w), 2850 (w), 1596 (w), 1458 (w), 1439 (w), 1350 (m), 1176 (w), 1154 (w), 1071 (m), 1004 (s), 980 (m), 965 (s), 795 (vs), 748 (s), 722 (s), 711 (s),

698 (vs), 657 (m), 650 (m), 640 (m), 620 (w), 558 (w), 518 (w), 467 (m), 446 (w), 435 (w), 421 (w), 412 (w), 399 (w) cm^{-1}.

Additional information on the chemical synthesis is available *via* Chemotion repository:

https://doi.org/10.14272/reaction/SA-FUHFF-UHFFFADPSC-QYFQNSKAHG-UHFFFADPSC-NUHFF-NZLTO-NUHFF-ZZZ.1

Additional information on the analysis of the target compound is available *via* Chemotion repository:

https://doi.org/10.14272/QYFQNSKAHGLVQL-XRTKQMIRSA-N.2

1,2-Phenylene-bis-5-(10,15,20-triphenylporphyrin)-nickel(II)iron(III) (**36**)

1,2-Phenylene-bis-5-(10,15,20-triphenylporphyrin)-nickel(II) (10.00 mg, 8.28 µmol, 1.00 equiv) together with iron dibromide (17.85 mg, 82.78 µmol, 10.0 equiv) were dissolved in 9 mL DMF. The mixture was stirred for 2 h at 140 °C. After cooling down to 25 °C, the solvent was removed under reduced pressure. The crude product was purified via column chromatography on silca gel (CH_2Cl_2 to CH_2Cl_2/MeOH 20:1) to yield the desired product 1,2-Phenylene-bis-5-(10,15,20-triphenylporphyrin)-nickel(II)iron(III) (8.70 mg, 6.89 µmol, 83% yield) **36** as purple solid.

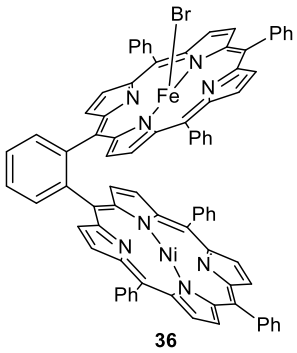

36

R_f = 0.68 (CH_2Cl_2/MeOH 20:1). **MS** (ESI), m/z (%): 1339/1340/1341/1342/1343 (10/10/5/4/2) [M]+, 1292 (17), 1269 (6), 1260 (12), 1186 (6), 492 (8), 374 (100), 339 (18), 312 (49), 264 (10), 225 (19). **HRMS** (ESI) ($C_{82}H_{50}BrFeN_8Ni$): calc.: 1339.2045, found: 1339.3914; **UV-Vis** (abs., CH_2Cl_2, 21 °C), λ_{max} = 401 nm; **IR** (ATR, $\tilde{\nu}$) = 3050 (w), 2919 (m), 2849 (w), 1439 (m), 1350 (m), 1337 (w), 1071 (m), 1003 (vs), 994 (vs), 870 (w), 793 (vs), 751 (vs), 713 (s), 700 (vs), 670 (m) cm^{-1}.

Additional information on the chemical synthesis is available *via* Chemotion repository:

https://doi.org/10.14272/reaction/SA-FUHFF-UHFFFADPSC-DAELOXDKKK-UHFFFADPSC-NUHFF-MVIHC-NUHFF-ZZZ

Additional information on the analysis of the target compound is available *via* Chemotion repository:

https://doi.org/10.14272/DAELOXDKKKKEJN-LKHNKGCCSA-M.1

[1,2-Phenylene-bis-5-(10,15,20-triphenylporphyrin)]-dipalladium(II) (**62**)[127]

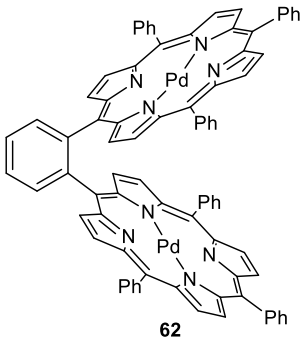

62

1,2-Phenylene-bis-5-(10,15,20-triphenyporphyrin) (4.5 mg, 3.91 µmol, 1.00 equiv.) and $PdCl_2$ (5.55 mg, 31.27 µmol, 8.00 equiv.) were dissolved in DMF (5 mL). The reaction mixture was stirred for 16 h at 100 °C. Subsequently, the solvent was removed under reduced pressure. The crude product was purified by flash column chromatography on silica gel (CH_2Cl_2/*n*-pentane, 1:1) to afford the title compound **62** as a red-purple solid (4.10 mg, 3.01 µmol, 77%).

***R*$_f$** (CH_2Cl_2/*n*-pentane, 1:2) = 0.61. – **^{1}H NMR** (500 MHz, THF-d_8): δ = 8.96 (dd, *J* = 5.6, 3.4 Hz, 2H, $H_{aromatic}$), 8.82 (d, ^3J = 4.9 Hz, 4H, $H_{pyrrole}$), 8.35 (dd, *J* = 5.4, 3.7 Hz, 2H, $H_{aromatic}$), 8.33 (d, ^3J = 4.9 Hz, 4H, $H_{pyrrole}$), 8.16 (d, ^3J = 4.8 Hz, 4H, $H_{pyrrole}$), 7.98 – 7.94 (m, 2H, $H_{aromatic}$), 7.90 (d, ^3J = 4.9 Hz, 4H, $H_{pyrrole}$), 7.79 – 7.76 (m, 2H, $H_{aromatic}$), 7.69 – 7.58 (m, 10H, $H_{aromatic}$), 7.58 – 7.53 (m, 4H, $H_{aromatic}$), 7.50 –7.45 (m, 8H, $H_{aromatic}$), 6.74 (dd, *J* = 7.4, 1.4 Hz, 4H, $H_{aromatic}$) ppm. – **^{13}C NMR** (126 MHz, THF-d_8): δ = 141.5 (C_q), 135.1 (+, CH), 134.7 (+, CH), 134.5 (+, CH), 133.2 (+, CH), 130.9 (+, CH), 130.6 (+, CH), 130.1 (+, CH), 127.4 (+, CH), 127.3 (+, CH), 110.5 (C_q) ppm.– **UV-Vis** (CH_2Cl_2): λ_{max} (rel. absorption) = 218 (0.11), 274 (0.04), 309 (0.03), 406 (0.28), 531 (0.02) nm. – **IR** (ATR): $\tilde{\nu}$ = 3027, 2959, 2914, 2851, 2166, 1717, 1659, 1595, 1448, 1350, 1262, 1077, 1009, 798, 749, 705 cm^{-1}. – **HRMS** (ESI) ($Pd_2C_{82}H_{50}N_8$): calc.: 1360.2259, found: 1360.2267.

Additional information on the reaction details is available *via* the Chemotion repository: https://dx.doi.org/10.14272/reaction/SA-FUHFF-UHFFFADPSC-XSSRUEVVUK-UHFFFADPSC-NUHFF-NCDDW-NUHFF-ZZZ

Additional information on the analysis of the target compound is available *via* the Chemotion repository: https://dx.doi.org/10.14272/XSSRUEVVUKKETO-IGJFLPGISA-N.1

1,2-Bis(4-(10,15,20-triphenylporphyrin-5-yl)phenyl)ethane-1,2-dione(2-Zn(II)) (**74**)

1,2-Bis(4-(10,15,20-triphenylporphyrin-5-yl)phenyl)ethane-1,2-dione (10.0 mg, 7.79 µmol, 1.00 equiv) and $Zn(OAc)_2$ (19.6 mg, 107 µmol, 13.7 equiv) were dissolved in DMF. The mixture was stirred for 1 h at 25 °C. The solvent was removed under reduced pressure. Purification *via* column chromatography on silica gel (CH_2Cl_2/*n*-pentane 1:1) afforded the title compound 1,2-bis(4-(10,15,20-triphenylporphyrin-5-yl)phenyl)ethane-1,2-dione(2-Zn(II)) (8.60 mg, 6.10 µmol, 78% yield) **74** as a purple solid.

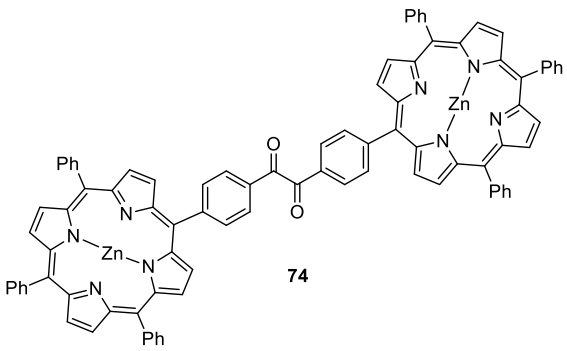

***R*$_f$** = 0.46 (CH_2Cl_2/n-pentane 1:3). **^{1}H NMR** (500 MHz, $CDCl_3$ [7.26], ppm) δ = 8.99 – 8.90 (m, 8H), 8.89 (s, 8H), 8.63 (d, *J* = 8.2 Hz, 4H), 8.52 (d, *J* = 8.1 Hz, 4H), 8.25 (dt, *J* = 7.9, 1.7 Hz, 12H), 7.78 (dtd, *J* = 8.7, 7.0, 1.5 Hz, 18H) Impurities: methylene chloride (5.30 (s)), CHex (1.43 (s)), H grease (0.85 (m), 1,25 (br s)); **^{13}C NMR** (126 MHz, $CDCl_3$ [77.16], ppm) δ = 194.7 (+, C_{CO}, 2C), 149.6 (+, C_{Ar}, 2C), 142.1 (+, C_{Ar}, 8C), 135.5 (+, C_{Ar}, 8C), 134.7 (+, C_{Ar}, 16C), 132.4 (+, C_{Ar}, 2C), 128.7 (+, C_{Ar}, 8C), 128.0 (+, C_{Ar}, 16C), 126.9 (+, C_{Ar}, 18C), 121.0 (+, C_{Ar}, 4C), 120.7 (+, C_{Ar}, 2C), 118.0 (+, C_{Ar}, 4C).

Additional information on the chemical synthesis is available *via* Chemotion repository:

https://doi.org/10.14272/reaction/SA-FUHFF-UHFFFADPSC-KNKGJCLDPO-UHFFFADPSC-NUHFF-LGYGG-NUHFF-ZZZ

Additional information on the analysis of the target compound is available *via* Chemotion repository:

https://doi.org/10.14272/KNKGJCLDPOCENO-VVKHVWBYSA-L.1

1,2-Bis(4-(10,15,20-triphenylporphyrin-5-yl)phenyl)ethane-1,2-dione-dicopper(II) (**75**)

1,2-bis(4-(10,15,20-triphenylporphyrin-5-yl)phenyl)ethane-1,2-dione (10.4 mg, 8.10 µmol, 1.00 equiv) and copper diacetate (8.83 mg, 48.6 µmol, 6.00 equiv) were dissolved in THF. The mixture was stirred for 1 h at 140 °C. The solvent was removed under reduced pressure.

Purification *via* coloumn chromatography on silica gel (CH_2Cl_2 / *n*-pentane 1:1) to afford the title compound 1,2-bis(4-(10,15,20-triphenylporphyrin-5-yl)phenyl)ethane-1,2-dione-dicopper(II) (4.60 mg, 3.27 µmol, 40% yield) **75** as orange solid.

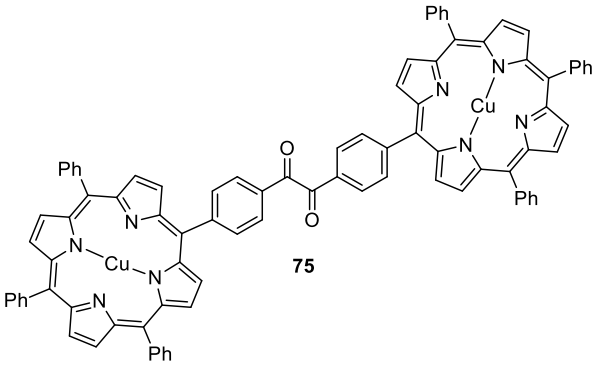

75

***R*$_f$** = 0.7 (CH_2Cl_2/n-pentane 1:1). **MS** (ESI), m/z (%): 1409 (8), 1408 (36), 1407 (74), 1406 (100), 1405 (71) $[M+H]^+$, 1404 (55), 1171 (7), 1170 (20), 1169 (26), 1035 (10), 1034 (10), 1033 (5), 1014 (23), 1013 (66), 1012 (89), 1011 (11), 1010 (16). **HRMS** (ESI) ($C_{90}H_{55}Cu_2N_8O_2^+$): calc.: 1405.3035, found: 1405,3038; **UV-Vis** (abs., CH_2Cl_2, 20 °C), λ_{max} = 416 nm; **IR** (ATR, $\tilde{\nu}$) = 3051 (w), 2951 (w), 2918 (s), 2849 (m), 2776 (w), 2749 (w), 2738 (w), 1667 (m), 1598 (s), 1455 (w), 1439 (w), 1344 (s), 1204 (s), 1174 (s), 1157 (w), 1071 (m), 1001 (vs), 996 (vs), 969 (w), 891 (w), 875 (w), 851 (w), 840 (w), 815 (w), 795 (vs), 769 (w), 748 (vs), 713 (vs), 698 (vs), 684 (s), 667 (s), 659 (m), 643 (m), 632 (m), 620 (w), 568 (w), 562 (w), 534 (w), 526 (w), 503 (w), 446 (w), 436 (w), 405 (w) cm^{-1}.

Additional information on the chemical synthesis is available *via* Chemotion repository:

https://doi.org/10.14272/reaction/SA-FUHFF-UHFFFADPSC-RVYYJCTVPS-UHFFFADPSC-NUHFF-LGYGG-NUHFF-ZZZ

Additional information on the analysis of the target compound is available *via* Chemotion repository:

https://doi.org/10.14272/RVYYJCTVPSSVFG-VVKHVWBYSA-L.1

5,15-Bis(2-(10,15,20)-triphenylporphyrinylphenyl)-10,20-diphenylporphyrin-tripalladium(II) (**60**)[128]

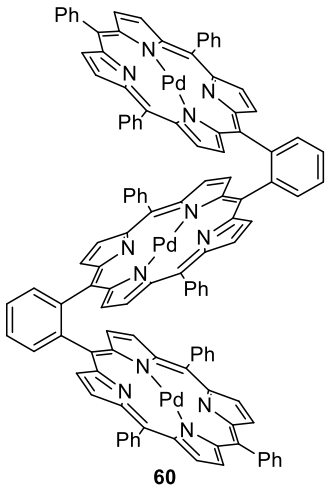

5,15-Bis(2-(10,15,20)-triphenylporphyrinylphenyl)-10,20-diphenylporphyrin (2.2 mg, 1.30 µmol, 1.00 equiv.) and $Pd(OAc)_2$ (5.0 mg, 2.96 µmol, 1.00 equiv.) were dissolved in CH_2Cl_2. The reaction mixture was stirred for 16 h at 80 °C, changing its color from brown to orange. Subsequently, the solvent was removed under reduced pressure. The crude product was purified by flash column chromatography on silica gel (CH_2Cl_2) to afford the title compound **60** as a red solid (1.9 mg, 0.95 µmol, 32%).

***R*$_f$** (CH_2Cl_2/*n*-pentane, 1:2) = 0.24. – **^{1}H NMR** (500 MHz, CD_2Cl_2): δ = 9.07 (d, ^3J = 5.0 Hz, 4H, $H_{pyrrole}$), 9.03 (d, ^3J = 5.0 Hz, 4H, $H_{pyrrole}$), 8.50 (d, ^3J = 4.9 Hz, 4H, $H_{pyrrole}$), 8.46 – 8.43 (m, 2H, $H_{linker\text{-}benzene}$), 8.42 – 8.39 (m, 2H, $H_{linker\text{-}benzene}$), 8.16 (d, ^3J = 4.9 Hz, 4H, $H_{pyrrole}$), 8.14 (d, ^3J = 5.0 Hz, 4H, $H_{pyrrole}$), 8.06 – 8.03 (m, 4H, $H_{linker\text{-}benzene}$), 8.02 (d, ^3J = 5.0 Hz, 4H, $H_{pyrrole}$), 7.98 – 7.95 (m, 2H, $H_{aromatic}$), 7.75 – 7.72 (m, 2H, $H_{aromatic}$), 7.71 (dt, *J* = 7.5, 1.4 Hz, 2H, $H_{aromatic}$), 7.69 – 7.66 (m, 2H, $H_{aromatic}$), 7.65 – 7.58 (m, 6H, $H_{aromatic}$), 7.57 – 7.52 (m, 2H, $H_{aromatic}$), 7.50 – 7.47 (m, 4H, $H_{aromatic}$), 7.46 – 7.38 (m, 10H, $H_{aromatic}$), 7.19 (dd, *J* = 7.4, 1.4 Hz, 2H, $H_{aromatic}$), 6.57 (d, ^3J = 7.3 Hz, 4H, $H_{aromatic}$), 6.50 (dd, *J* = 7.3, 1.7 Hz, 4H, $H_{aromatic}$) ppm.– **UV-Vis** (CH_2Cl_2): λ_{max} (rel. absorption) = 218 (0.44), 273 (0.07), 309 (0.02), 406 (0.19), 529 (0.02) nm. – **IR (ATR)**: $\tilde{\nu}$ = 2955, 2922, 2853, 1660, 1598, 1538, 1460, 1442, 1378, 1351, 1310, 1261, 1078, 1013, 970, 868, 795, 751, 724, 711, 703, 664, 533, 404, 385 cm^{-1}. – **HRMS** (ESI) ($C_{120}H_{72}N_{12}Pd_3$): calc.: 1998.3107, found: 1998.3202.

Additional information on the reaction details is available *via* the Chemotion repository:

https://dx.doi.org/10.14272/reaction/SA-FUHFF-UHFFFADPSC-WGFBNGVGII-UHFFFADPSC-NUHFF-NBPXK-NUHFF-ZZZ

Additional information on the analysis of the target compound is available *via* the Chemotion repository: https://dx.doi.org/10.14272/WGFBNGVGIIZZAE-SMDKEBRUSA-N/CHMO0000593

5.4 Synthesis of porphyrin derivatives and their metal complexes

5,10,15,20-Tetraphenyl-2-aza-21-carbaporphyrin: (**2**)[183]

^1H-pyrrole (310 mg, 321 µL, 4.62 mmol, 1.00 equiv) and benzaldehyde (1.96 g, 1.89 mL, 18.5 mmol, 4.00 equiv) were dissolved in degassed CH_2Cl_2. methanesulfonic acid (1.24 g, 840 µL, 12.9 mmol, 2.80 equiv) was added and the reaction mixture was stirred under the exclusion of light for 30 min at 25°C. 4,5-Dichloro-3,6-dioxo-cyclohexa-1,4-diene-1,2-dicarbonitrile (6.29 g, 27.7 mmol, 6.00 equiv) was added and the reaction mixture was stirred for 2 h at 25 °C. Then, NEt_3 was added. The crude product was purified by flash column chromatography on silica gel (CH_2Cl_2/MeOH 97-99:1-3), "Brockmann activity III" basic alumina (7.5% water)(*n*-pentane/CH_2Cl_2 2:1 to 1:1, 1% NEt_3) and on silica gel (CH_2Cl_2/MeOH 99:1 to 98.5/1.5). The title compound 5,10,15,20-tetraphenyl-2-aza-21-carbaporphyrin (499 mg, 812 µmol, 18% yield) **2** was obtained as a purple solid.

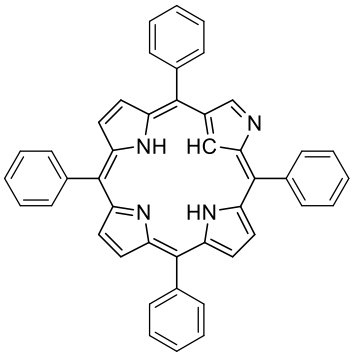

2

***R*$_f$** (CH_2Cl_2/MeOH, 50:1) = 0.71. – **^{1}H NMR** (400 MHz, $CDCl_3$): δ = 8.99 (d, ^3J = 4.9, 1H, $H_{pyrrole}$), 8.92 (d, ^3J = 4.9, 1H, $H_{pyrrole}$), 8.77 (s, 1H, $H_{confused,outer}$), 8.62 (d, ^3J = 4.9, 1H, $H_{pyrrole}$), 8.63–8.55 (m, 3H, $H_{pyrrole}$), 8.39–8.35 (m, 4H, $H_{aromatic}$), 8.19–8.15 (m, 4H, $H_{aromatic}$), 7.87–7.74 (m, 12H, $H_{aromatic}$), –2.43 (bs, 2H, N*H*), –4.99 (s, 1H, $H_{confused,inner}$) ppm. – **^{13}C NMR** (126 MHz, $CDCl_3$) : δ = 157.4, 156.4, 156.1, 149.6, 141.9, 140.5, 140.0, 139.8, 139.8, 137.3, 137.0, 135.2, 134.8, 134.7, 134.7, 134.2, 128.5, 128.5, 128.2, 128.0, 127.9, 127.8, 127.6, 127.1, 127.1, 126.5, 125.7, 125.2, 119.2, 117.6 ppm. Missing signals (14Cs) due to signal overlap. – **IR** (ATR): $\tilde{\nu}$ = 2955, 2924, 2868, 2853, 1737, 1711, 1462, 1377, 1265, 1186, 1160, 1084, 1026, 976, 888, 820, 803, 741, 705 cm^{-1}. **HRMS** (ESI) ($C_{44}H_{31}N_4^+$): calc.: 615.2549, found: 615.2544. - **UV-Vis** (CH_2Cl_2), λ_{max} = 440 nm.

Additional information on the chemical synthesis is available *via* Chemotion repository:

https://doi.org/10.14272/reaction/SA-FUHFF-UHFFFADPSC-WATPLABZTN-UHFFFADPSC-NUHFF-NRPDS-NUHFF-ZZZ.1

Additional information on the analysis of the target compound is available *via* Chemotion repository:

https://doi.org/10.14272/WATPLABZTNQXNG-QUILPVNTSA-N.2

19-Bromo-3,8,13,16-tetraphenyl-4,7-imino-2,17-methano-9,12-nitrilo[1,3]diazacyclohexadecino[2,1,16-*cd*]pyrrolizine: (**6**)[183]

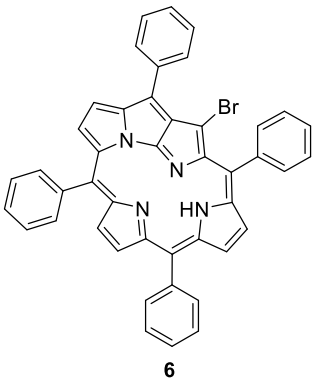

6

5,10,15,20-Tetraphenyl-2-aza-21-carbaporphyrin (250 mg, 407 µmol, 1.00 equiv) was dissolved in CH_2Cl_2 and *N*-Bromosuccinimide (166 mg, 935 µmol, 2.30 equiv) was added. The reaction mixture was stirred for 5 min. Subsequently, the solvent was removed under reduced pressure. The residue was purified by flash column chromatography on silica gel (CH_2Cl_2 to CH_2Cl_2/MeOH, 99:1) and the solvent was removed under reduced pressure to obtain the dibromo-*N*-confused-porphyrin as unstable intermediat. The residue was redissolved in pyridine (48.3 g, 49.1 mL, 610 mmol, 1500 equiv) and stirred for 8 h at 21 °C. The solvent was removed under reduced pressure. Purification by flash column chromatography (CH_2Cl_2/MeOH, 98:2) afforded the title compound 19-Bromo-3,8,13,16-tetraphenyl-4,7-imino-2,17-methano-9,12-nitrilo[1,3]diazacyclohexadecino[2,1,16-cd]pyrrolizine (81.0 mg, 84.0 µmol, 29% yield) **6** as a red solid.

R_f (CH_2Cl_2/MeOH, 25:1) = 0.56. – **^{1}H NMR** (400 MHz, $CDCl_3$): δ = 8.98 (d, ^3J = 5.1 Hz, 1H, $H_{pyrrole}$), 8.63 (d, ^3J = 5.1 Hz, 1H, $H_{pyrrole}$), 8.57–8.53 (m, 2H, $H_{pyrrole}$), 8.09–8.03 (m, 5H, $H_{aromatic}$), 8.00–7.95 (m, 3H, $H_{aromatic}$), 7.96–7.95 (m, 1H, $H_{aromatic}$), 7.77–7.65 (m, 11H, $H_{aromatic}$), 7.61–7.55 (m, 2H, $H_{pyrrole}$) ppm. The internal NH peak are in some samples present at 8.34 (bs, N*H*), in this sample it is too broad do be assigned. – **^{13}C NMR** (500 MHz, $CDCl_3$): δ = 150.6, 146.8, 146.1, 145.8, 139.8, 139.0, 137.5, 136.9, 134.7, 134.5, 133.8, 133.4, 133.2, 132.7, 132.2, 130.3, 129.2, 129.2, 128.6, 128.6, 128.0, 127.8, 127.3, 125.4, 124.6, 120.4 ppm. Missing signals (18Cs) due to signal overlap. – **UV-Vis** (CH_2Cl_2): λ_{max} (rel. absorption) = 279 (0.04), 373 (0.03), 424 (0.03), 450 (0.03), 465 (0.03), 497 (0.03), 543 (0.02) nm. – **IR** (ATR): $\tilde{\nu}$ = 3054, 3029, 2953, 2924, 2851, 1775, 1706, 1594, 1574, 1531, 1465, 1441, 1391, 1356, 1264, 1228, 1204, 1177, 1154, 1072, 1044, 1018, 1001, 958, 919, 881, 846, 827, 799, 786, 752, 728, 698, 662, 647, 626, 598, 571, 557, 544, 530, 404 cm^{-1}. – **HRMS** (ESI) ($C_{44}H_{28}BrN_4^+$) calc.: 691.1497, found: 691.1490.

Additional information on the chemical synthesis is available *via* Chemotion repository:

https://doi.org/10.14272/reaction/SA-FUHFF-UHFFFADPSC-PWPXEVLOSG-UHFFFADPSC-NUHFF-NNESF-NUHFF-ZZZ.1

Additional information on the analysis of the target compound is available *via* Chemotion repository:

https://doi.org/10.14272/PWPXEVLOSGZCKX-GJPCLHIXSA-N.2

19-Formylphenyl-3,8,13,16-tetraphenyl-4,7-imino-2,17-methano-9,12-nitrilo[1,3]diazacyclohexadecino[2,1,16-cd]pyrrolizine (**32**)[183]

Under argon atmosphere, 19-bromo-3,8,13,16-tetraphenyl-4,7-imino-2,17-methano-9,12-nitrilo[1,3]diazacyclohexadecino[2,1,16-cd]pyrrolizine (50.0 mg, 51.9 µmol, 1.00 equiv), (2-formylphenyl)boronic acid (933 mg, 6.22 mmol, 120 equiv), palladium triphenylphosphane (14.4 mg, 12.4 µmol, 0.240 equiv) and tripotassium phosphate (275 mg, 1.30 mmol, 25.0 equiv) were dissolved in dry THF, which was dried through multiple freeze-pump-thaw cycles. The mixture was stirred for 10 min at 120 °C in a pressure vial. The solvent was removed under reduced pressure and redissolved in CH_2Cl_2. The organic phase was consecutively washed with H_2O, dried over Na_2SO_4, filtered and the solvent was removed under reduced pressure. The crude product was purified by flash column chromatography on silica gel (CH_2Cl_2/MeOH 1/500 – 1/100) Nto afford the title compound 19-formylphenyl-3,8,13,16-tetraphenyl-4,7-imino-2,17-methano-9,12-nitrilo[1,3]diazacyclohexadecino[2,1,16-cd]pyrrolizine (9.00 mg, 12.6 µmol, 24% yield) **32** as purple solid.

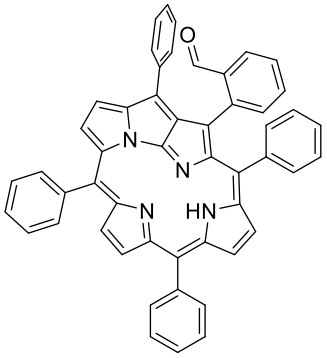

32

***R*$_f$** = 0.50 (CH_2Cl_2/MeOH 50:1). – **^{1}H NMR** (500 MHz, CD_2Cl_2 [5.31], ppm): δ = 10.16 (s, 1H, CHO), 9.21 (d, 3J = 5.0 Hz, 1H), 8.85 (d, 3J = 5.0 Hz, 1H), 8.59 (d, 3J = 5.0 Hz, 1H), 8.29 – 8.27 (m, 2H), 8.22 (d, 3J = 7.5 Hz, 1H), 8.07 (d, 3J = 5.0 Hz, 1H), 8.00 (bs, 1H), 7.84 – 7.80 (m, 5H), 7.80 – 7.71 (m, 5H), 7.70 – 7.61 (m, 4H), 7.60 – 7.32 (m, 9H) Impurities: 1.53 (water), 1.28 (H grease), 0.94–0.82 (H grease), 0.08 (silicon grease); **^{13}C NMR** (500 MHz, CD_2Cl_2 [53.8], ppm): δ =192.2, 158.0, 154.6, 153.3, 150.7, 149.4, 147.8, 147.0, 146.9, 142.2, 142.2, 139.6, 137.9, 137.5, 137.0, 135.6, 135.4, 135.0, 134.8, 134.7, 134.3, 134.3, 133.9, 133.7, 133.6, 133.5, 133.3, 133.0, 132.7, 131.7, 130.2, 129.8, 129.6, 129.3, 129.2, 128.8, 128.7, 128.4, 128.3, 128.2), 128.1, 127.7, 127.6), 126.7, 125.7, 125.4, 125.2, 125.1, 120.4, 120.0, 119.5, 110.3. signals are missing due to signal overlap (12C); **MS** (ESI), m/z (%): 719 (15), 718 (58), 717

(100). **HRMS** (ESI) ($C_{51}H_{33}N_4O^+$) calc.: 717.2654, found: 717.2645; **UV-Vis** (abs., CH_2Cl_2, 21 °C), λ_{max} = 490 nm.

Additional information on the chemical synthesis is available *via* Chemotion repository:

https://doi.org/10.14272/reaction/SA-FUHFF-UHFFFADPSC-WSNZFGVLLG-UHFFFADPSC-NUHFF-NDEDO-NUHFF-ZZZ.1

Additional information on the analysis of the target compound is available *via* Chemotion repository:

https://doi.org/10.14272/WSNZFGVLLGJFMK-VDICBCJWSA-N.2

1,2-phenylene(*N*-fused-tetraphenylporphyrin-triphenylporphyrin) (**25**)[183]

Under an argon atmosphere, a crimp vial was charged with 2-formylphenyl-*N*-fused-TPP **5**

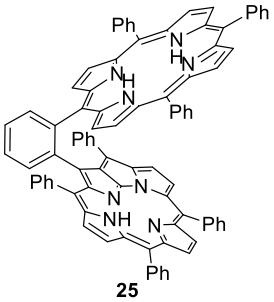

25

(64.0 mg, 89.2 µmol, 1.00 equiv.) and CH_2Cl_2 (20 mL). Pyrrole (**1**) (51.0 µL, 49.3 mg, 735 µmol, 8.23 equiv.), benzaldehyde (56.0 µL, 58.2 mg, 548 µmol, 6.15 equiv.) and TFA (12.7 µL, 18.9 mg, 166 µmol, 1.86 equiv.) were all added dropwise while stirring for 19 h at room temperature. Afterwards, DDQ (20.3 mg, 89.0 µmol, 1.00 equiv.) was added and stirred for 1 h under air. Then, NEt_3 (0.5 mL) was added, and the solvent was removed under reduced pressure. The crude product was purified three times by flash column chromatography on silica gel (CH_2Cl_2/MeOH, 9:1), (toluene/EtOAc, 7:1→ 5:1) and (CH_2Cl_2/MeOH, 93:7) to afford the title compound as a red solid (23.8 mg, 19.0 µmol, 22%).

R_f (CH_2Cl_2/MeOH, 97:3 + 1% NEt_3) = 0.45. – **^{1}H NMR** (500 MHz, CD_2Cl_2 / pyridine-d_5, 25:1): δ = 8.87 (d, *J* = 4.6 Hz, 1H, $H_{pyrrole}$), 8.66 (d, *J* = 7.7 Hz, 1H, $H_{aromatic}$), 8.53 (d, *J* = 4.6 Hz, 1H, $H_{pyrrole}$), 8.51 (d, *J* = 4.7 Hz, 1H, $H_{pyrrole}$), 8.45 (d, *J* = 4.5 Hz, 1H, $H_{pyrrole}$), 8.37 (d, *J* = 4.6 Hz, 1H, $H_{pyrrole}$), 8.26 (d, *J* = 7.5 Hz, 1H, $H_{aromatic}$), 8.16 – 8.10 (m, 1H), 8.10 – 8.01 (m, 2H), 8.01 – 7.92 (m, 4H), 7.90 – 7.85 (m, 3H), 7.84 – 7.75 (m, 9H), 7.72 – 7.68 (m, 6H), 7.65 – 7.57 (m, 8H), 7.57 – 7.47 (m, 5H), 7.45 – 7.34 (m, 5H), 7.25 – 7.18 (m, 2H), 7.09 (d, *J* = 4.7 Hz, 2H, $H_{pyrrole}$). –4.14 (bs, 2H, NH) ppm. – **^{13}C NMR** (126 MHz, DMF-d_7): δ = 149.6, 149.4, 149.2, 148.5, 145.8, 141.5, 137.7, 137.1, 135.8, 134.5, 134.3, 134.1, 133.9, 130.2, 129.9, 129.5, 129.4 128.8, 128.5, 128.3, 128.2, 128.0, 127.4, 127.3, 127.0, 126.8, 124.7, 123.7, 119.8, 119.6, 119.4,

118.0 ppm. Missing signals (56 Cs) due to signal overlap. – **UV-Vis** (CH_2Cl_2): λ_{max} (rel. absorption) = 420 (1.61), 504 (0.41), 558 (0.32), 650 (0.15), 720 (0.10) nm. – **IR** (ATR): $\tilde{\nu}$ = 2955, 2921, 2851, 1455, 1441, 1374, 1259, 1173, 1086, 1072, 1014, 966, 878, 798, 752, 722, 698, 663, 407, 399, 390 cm^{-1}. – **HRMS** ($C_{88}H_{56}N_8H$) calc.: 1225.4706, found: 1225.4663.

6 Appendix

6.1 Experimental spectra

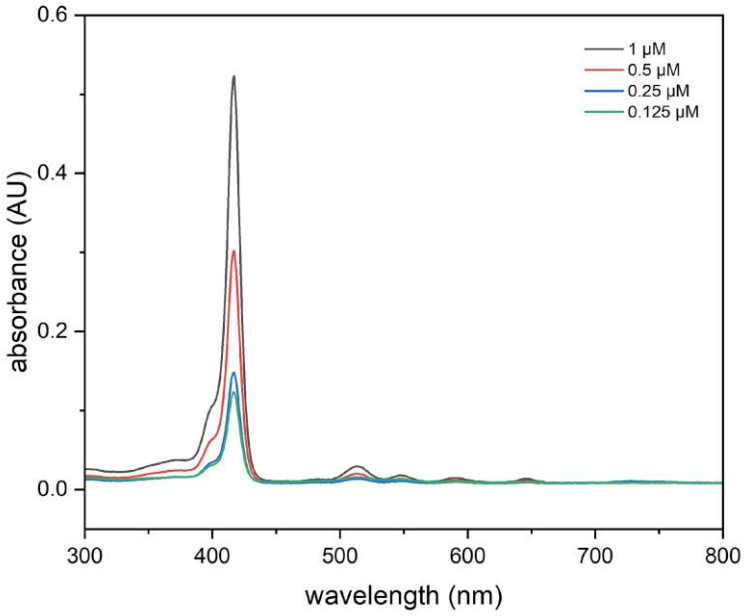

Figure 62: Absorption spectrum of a dilution series of TPP to calculate the extinction coefficient.

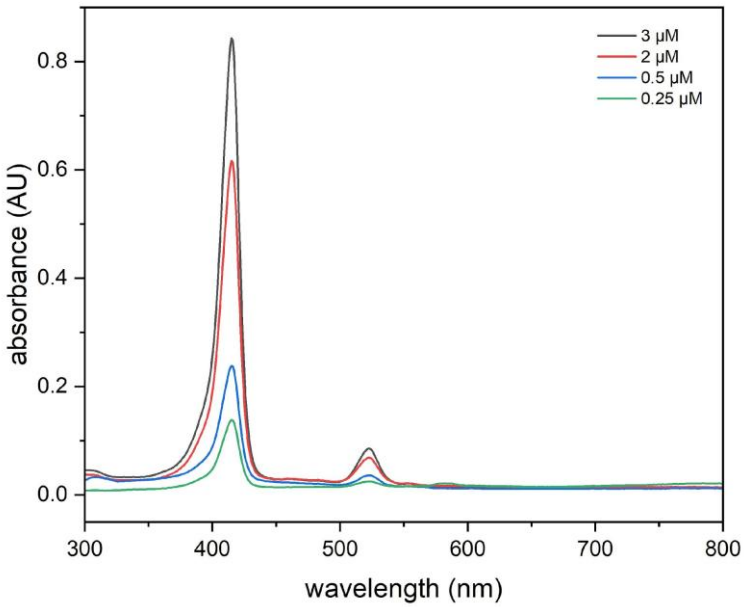

Figure 63: Absorption spectrum of a dilution series of Pd-TPP to calculate the extinction coefficient.

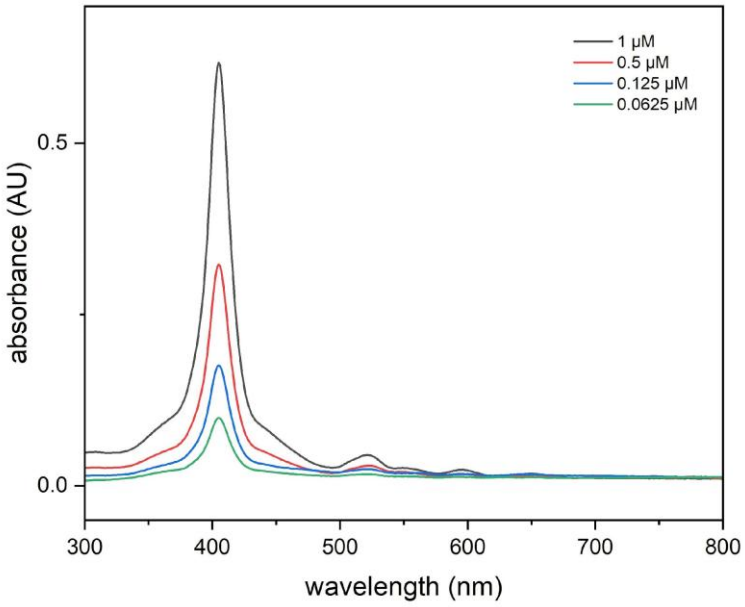

Figure 64: Absorption spectrum of a dilution series of OBBP to calculate the extinction coefficient.

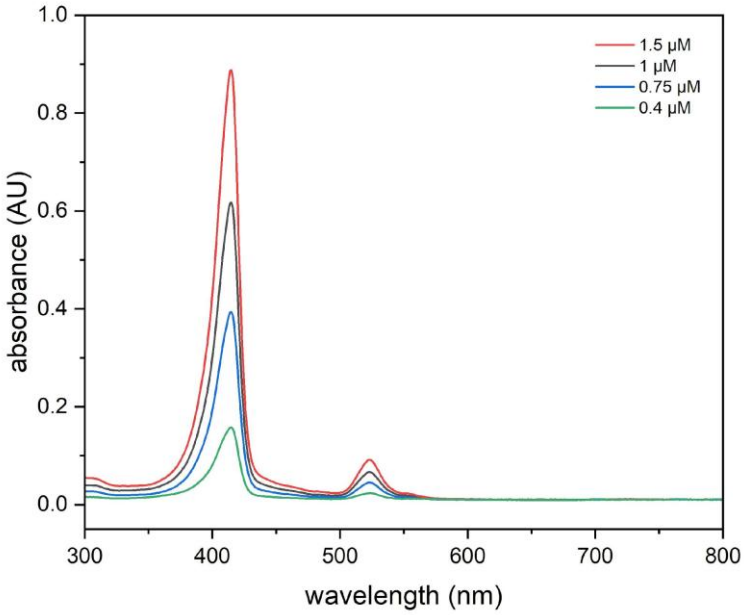

Figure 65: Absorption spectrum of a dilution series of Pd-OBBP to calculate the extinction coefficient.

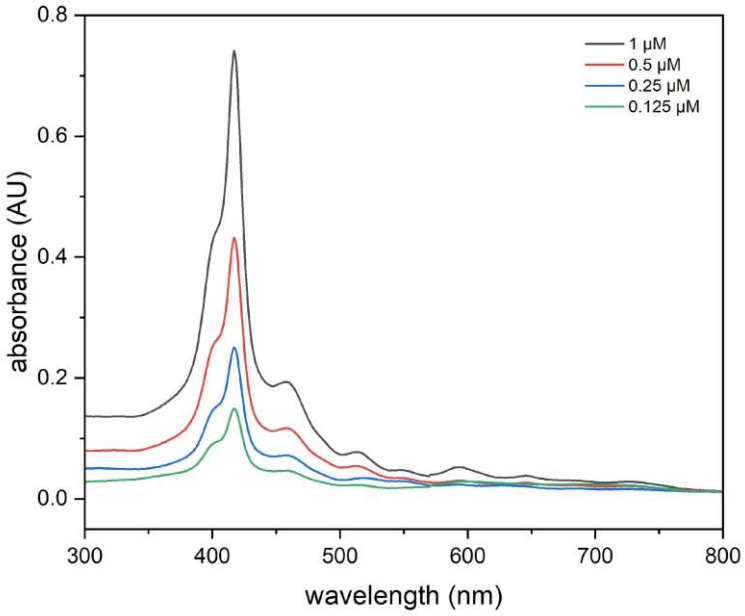

Figure 66: Absorption spectrum of a dilution series of OBTP to calculate the extinction coefficient.

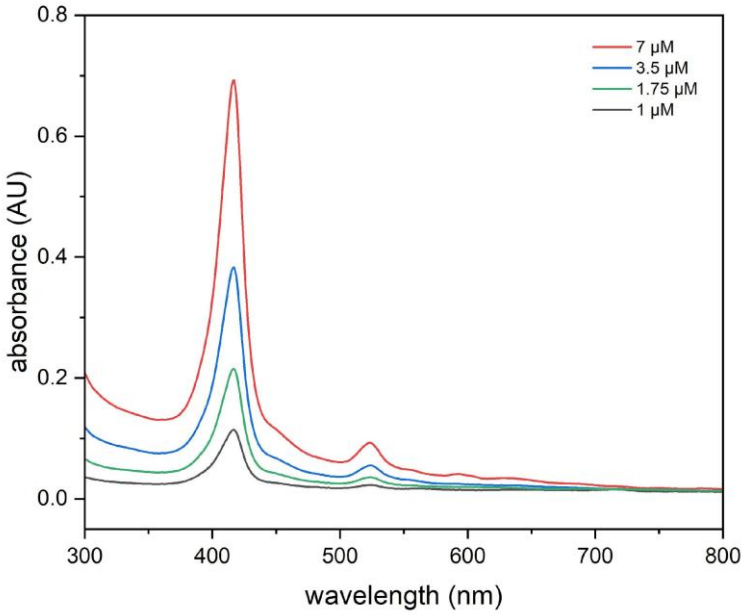

Figure 67: Absorption spectrum of a dilution series of Pd-OBTP to calculate the extinction coefficient.

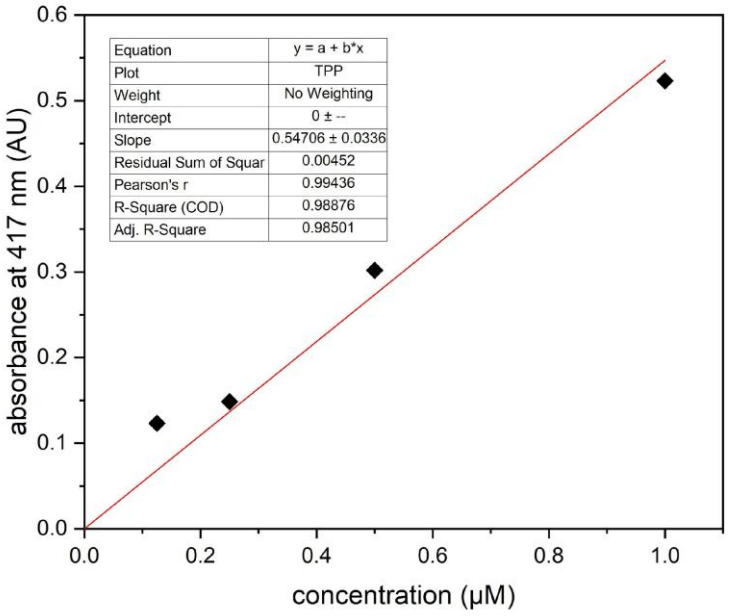

Figure 68: Extinction coefficient determination of TPP. The absorbance to concentration was linearly fitted with intercept = 0.

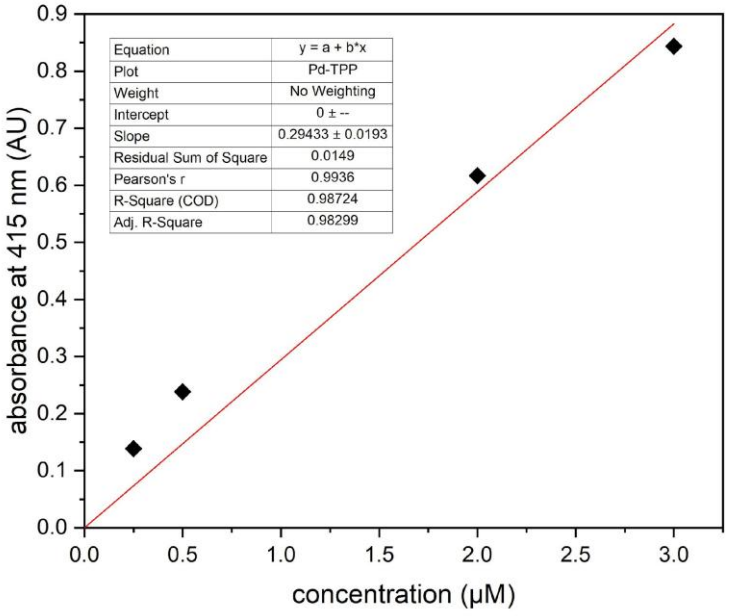

Figure 69: Extinction coefficient determination of Pd-TPP. The absorbance to concentration was linearly fitted with intercept = 0.

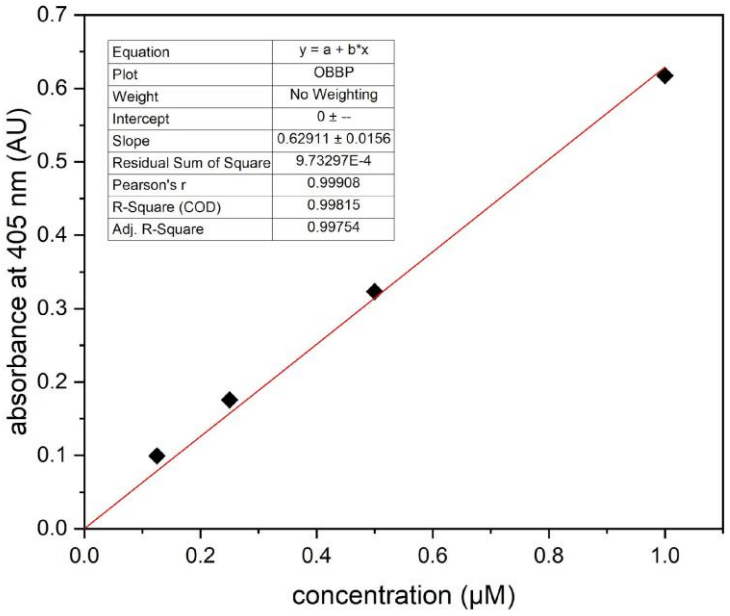

Figure 70: Extinction coefficient determination of OBBP. The absorbance to concentration was linearly fitted with intercept = 0.

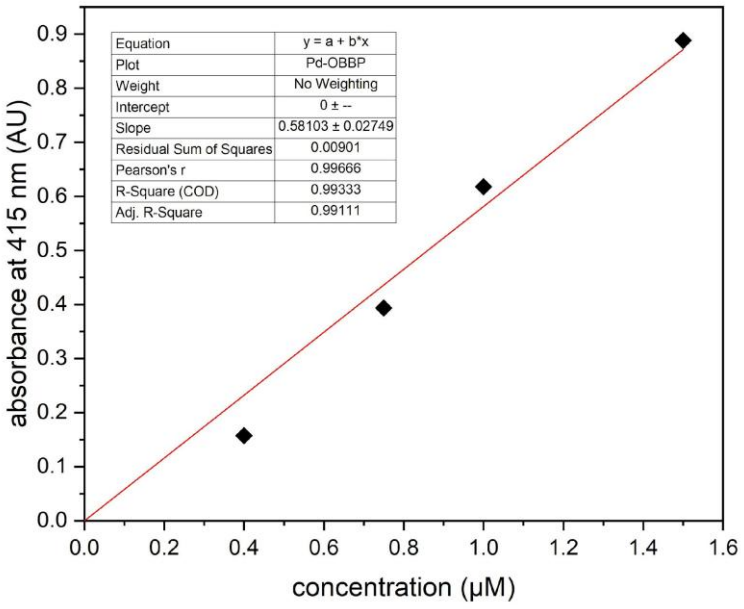

Figure 71: Extinction coefficient determination of Pd-OBBP. The absorbance to concentration was linearly fitted with intercept = 0.

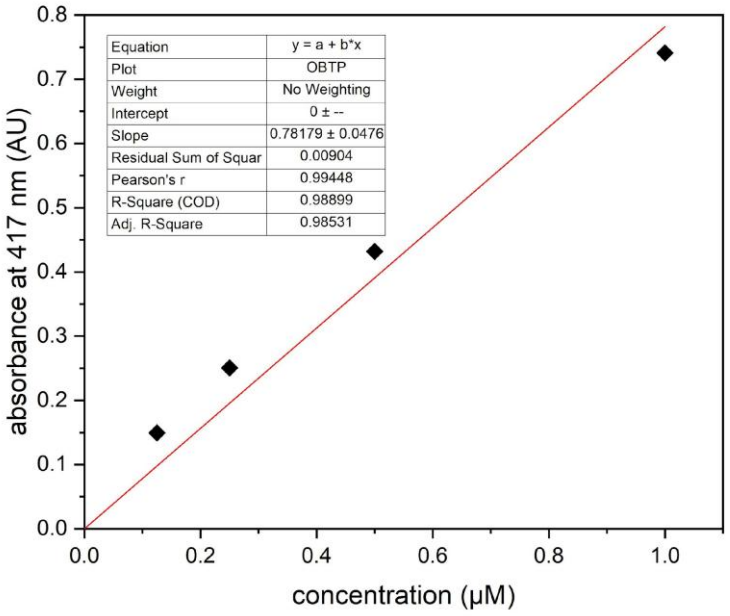

Figure 72: Extinction coefficient determination of OBTP. The absorbance to concentration was linearly fitted with intercept = 0.

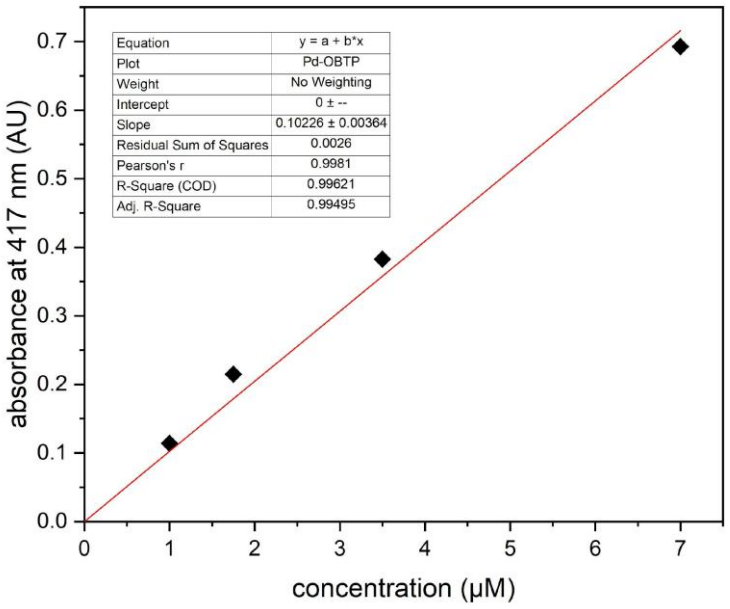

Figure 73: Extinction coefficient determination of Pd-OBTP. The absorbance to concentration was linearly fitted with intercept = 0.

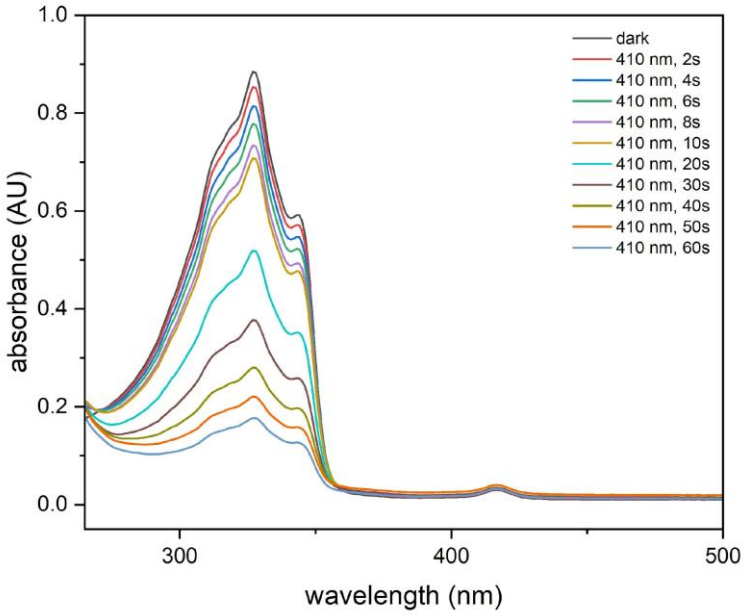

Figure 74: 0.1 µM solutions of TPP, together with 40 µM DPF in DMF were blanked to a pure solution of 0.1 µM of the respective sensitizer and irradiated at 410 nm over 1 minute.

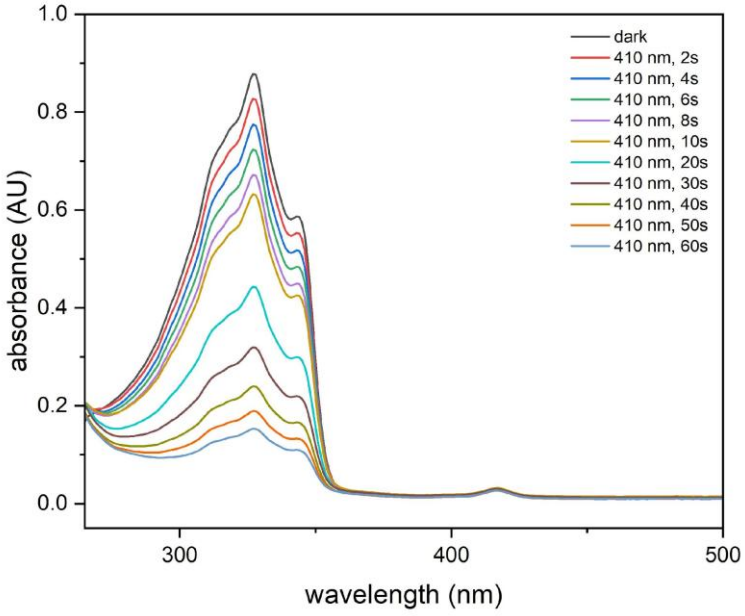

Figure 75: 0.1 µM solutions of Pd-TPP, together with 40 µM DPF in DMF were blanked to a pure solution of 0.1 µM of the respective sensitizer and irradiated at 410 nm over 1 minute.

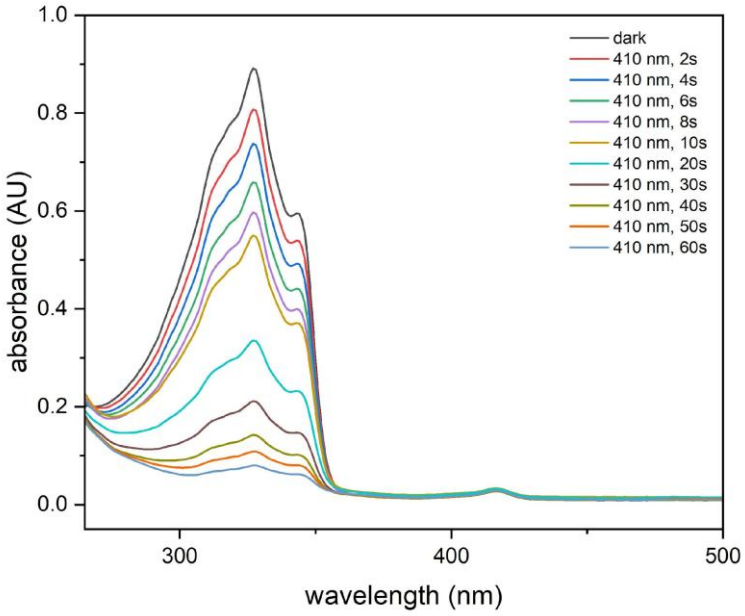

Figure 76: 0.1 µM solutions of OBBP, together with 40 µM DPF in DMF were blanked to a pure solution of 0.1 µM of the respective sensitizer and irradiated at 410 nm over 1 minute.

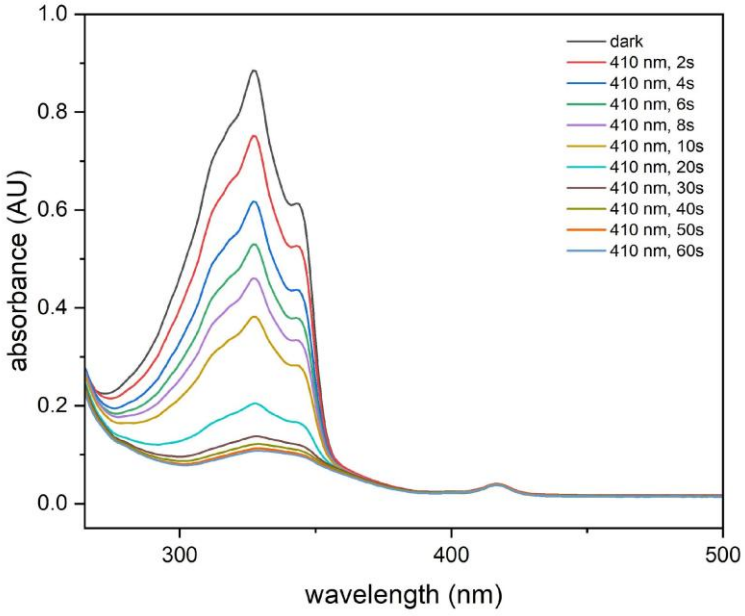

Figure 77: 0.1 µM solutions of Pd-OBBP, together with 40 µM DPF in DMF were blanked to a pure solution of 0.1 µM of the respective sensitizer and irradiated at 410 nm over 1 minute.

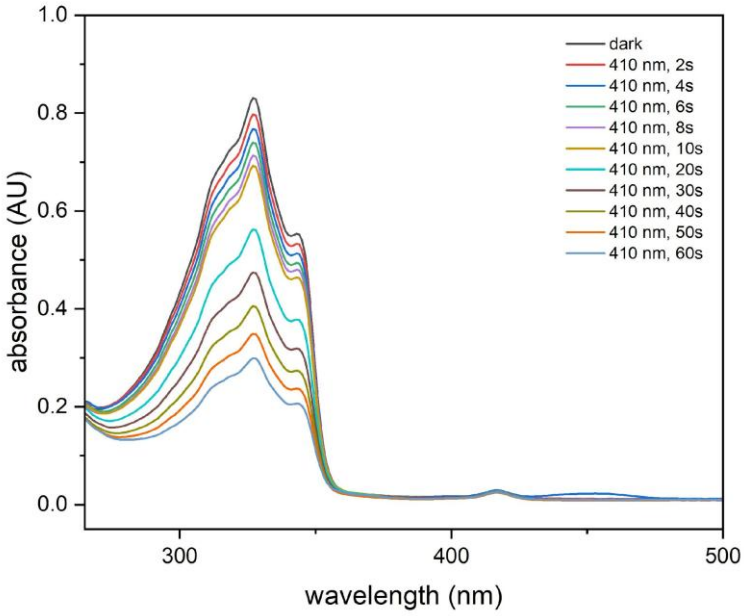

Figure 78: 0.1 µM solutions of OBTP, together with 40 µM DPF in DMF were blanked to a pure solution of 0.1 µM of the respective sensitizer and irradiated at 410 nm over 1 minute.

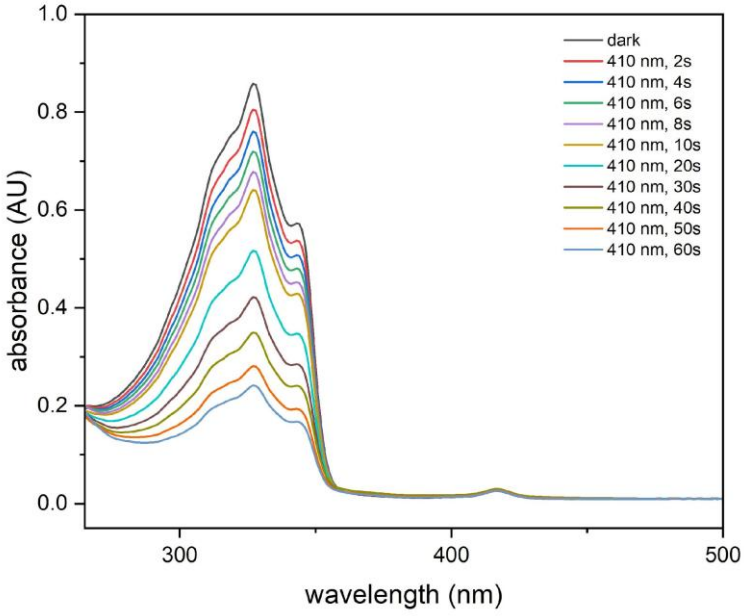

Figure 79: 0.1 µM solutions of Pd-OBTP, together with 40 µM DPF in DMF were blanked to a pure solution of 0.1 µM of the respective sensitizer and irradiated at 410 nm over 1 minute.

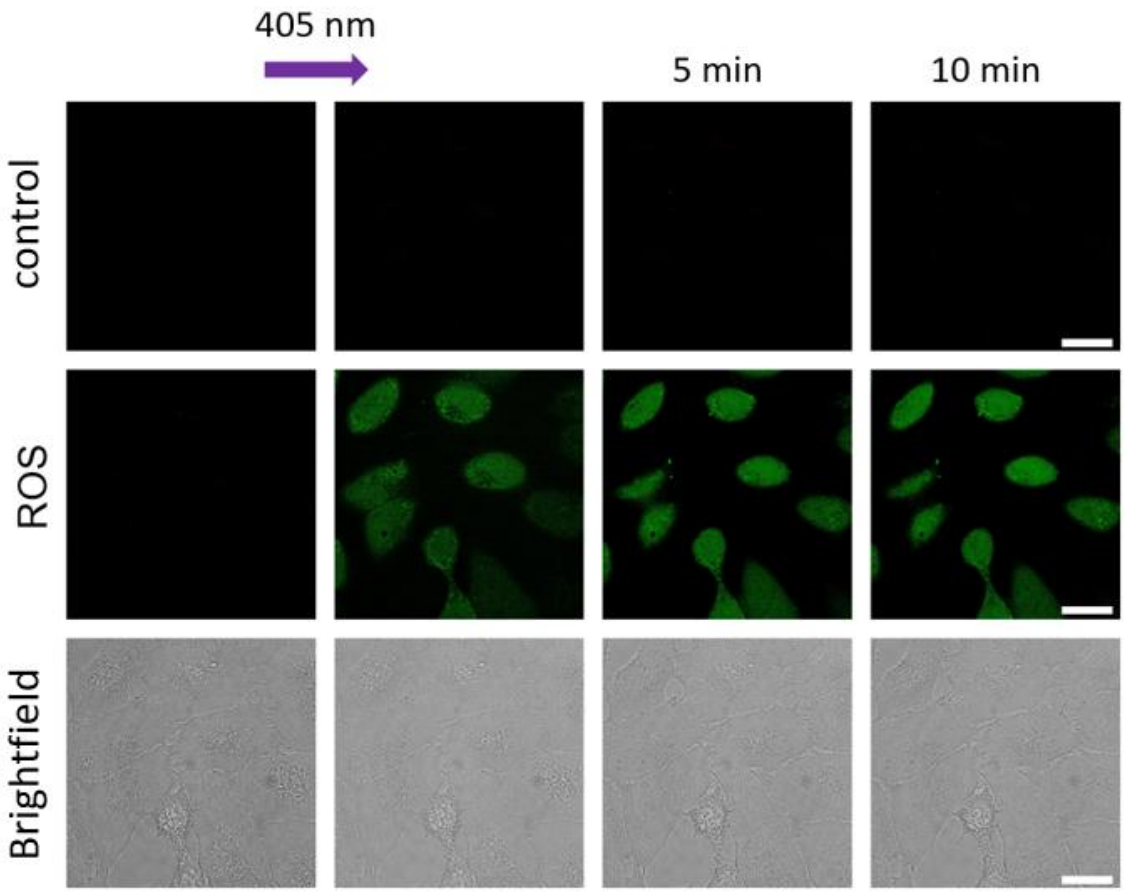

Figure 80: Blanked ROS build-up experiment. The pure irradiation of the cells results in a ROS formation without photosensitizer. (green). The images were taken with the *Stellaris 5* confocal microscope (Leica) using the 63x oil objective (OBBP-S: λ_{ex} = 405 nm; λ_{em} = 650 nm – 800 nm; ROS: λ_{ex} = 504 nm; λ_{em} = 515 nm – 545 nm; zoom: 1.5x). Scale bar corresponds to 25 µm.

6.2 List of abbreviations

Å	*Angström*
abs.	absolut
acac	acetylacetonate
aq.	aqueous
ATR	Attenuated Total Reflection (IR)
Bu	Butyl-
°C	Grad *Celsius*
c	concentration
calc.	calculated
$CDCl_3$	Chloroform-d_1
CH_2Cl_2	Dichloromethane
$CHCl_3$	Chloroform
cm	centimeter
CODH	Carbon Monoxide Dehydrogenase
COSY	Correlation Spectroscopy (NMR)
cp	cyclopentadienyl
d	day, doublet (NMR), path length
DDQ	2,3-Dichloro-5,6-Dicyano-1,4-benzoquinone
DEPT	Distortionless Enhancement by Polarization Transfer (NMR)
DFT	Density Functional Theory
DMF	Dimethylformamide
DMSO	Dimethylsulfoxide
E	potential

E^0	standard potential
e.g.	lat. *Exempli gratia*
EOAc	Ethylacetate
equiv.	equivalents
ESI	Electrospray Ionization (MS)
et al.	*et alia* (and others)
EtOH	Ethanol
eV	electron volt
FAB	Fast Atom Bombardment (MS)
g	gram
GC	Gas Chromatography
GC-MS	Gas Chromatography Mass Spectrometry
h	hour(s)
HMBC	Heteronuclear Multiple Bond Correlation (NMR)
HPLC	High-Pressure Liquid Chromatography
HRMS	High-Resolution Mass Spectrometry (MS)
HSQC	Heteronuclear Single Quantum Coherence (NMR)
IR	Infrared (-Spectroscopy)
^{i}Pr	*iso*-Propyl
IUPAC	International Union of Pure and Applied Chemistry
J	coupling constant
K	Kelvin
kJ	kilojoule
Ln	Lanthanide

M	molar
m	multiplett (NMR), medium (IR), *milli*
m	*meta*
m/z	mass/charge-ratio
Me	Methyl-
MeOH	Methanol
min	minutes
mL	milliliter
mmol	millimole
µmol	micromole
M	Metal
mol%	mole percent
MeOH	Methanol
MHz	*mega* Hertz
MS	Mass Spectrometry, Molecular Sieve
n	*nano*
NBS	N-Bromosuccinimide
nm	nanometer
NMR	Nuclear Magnetic Resonance
NOESY	Nuclear *Overhauser* Effect Spectroscopy (NMR)
o	*ortho*
OAc	acetate
OBBP	*o*-Phenylene bisporphyrin
p	*para*

Ph	phenyl-
ppm	parts per million
q	quartet (NMR)
quant.	quantitative
r.t.	room temperature
R_f	Retardation factor
s	singlet (NMR), strong (IR)
sat	sitting-atop, saturated
S_EAr	Electrophilic aromatic substitution
T	Temperature
t	triplet (NMR), tertiary
^{t}Bu	*tert*-butyl
TFA	Trifluoro Acetic acid
THF	Tetrahydrofuran
TLC	Thin Layer Chromatography
TMS	trimethylsilyl-
Tol	Toluene
TPP	Tetraphenylporphyrin
V	Volt
Vis	visible
via	through
vs	very strong (IR)
vs	*versus* (against)
UV	Ultraviolet

w	week, weak (IR)
w/w	weight percent
Y	Yield
δ	chemical shift
ε	extinction coefficient
λ	wavelength
$h\nu$	light
Φ	quantum yield
$\tilde{\nu}$	wavenumber

6.3 Literature

(1) Abbass, K.; Qasim, M. Z.; Song, H.; Murshed, M.; Mahmood, H.; Younis, I. A review of the global climate change impacts, adaptation, and sustainable mitigation measures. *Environ Sci Pollut Res Int* **2022**, *29* (28), 42539-42559. DOI: 10.1007/s11356-022-19718-6 From NLM Medline.

(2) PEREIRA, M. M. C. a. J. S. Water Stress, C02 and Climate Change. *Journal of Experimental Botany* **1992**, *43*, 1131 - 1139.

(3) Sesana, E.; Gagnon, A. S.; Ciantelli, C.; Cassar, J.; Hughes, J. J. Climate change impacts on cultural heritage: A literature review. *WIREs Climate Change* **2021**, *12* (4). DOI: 10.1002/wcc.710.

(4) Jones, T. M. L. W. P. D. Detecting CO2-induced climatic change. *Nature* **1981**, *292*, 206 - 208.

(5) Keith P. Shine, P. M. d. F. F. The effect of human activity on radiative forcing of climate change: a review of recent developments. *Global Environmental Change* **1999**, *20*, 205 - 225.

(6) Trenberth, K. E. Climate change caused by human activities is happening and it already has major consequences. *Journal of Energy & Natural Resources Law* **2018**, *36* (4), 463-481. DOI: 10.1080/02646811.2018.1450895.

(7) Wu, Z.; Zhang, H.; Krause, C. M.; Cobb, N. S. Climate change and human activities: a case study in Xinjiang, China. *Climatic Change* **2010**, *99* (3-4), 457-472. DOI: 10.1007/s10584-009-9760-6.

(8) Hitz, S.; Smith, J. Estimating global impacts from climate change. *Global Environmental Change* **2004**, *14* (3), 201-218. DOI: 10.1016/j.gloenvcha.2004.04.010.

(9) Postt, J. P. W. M. Response of northern forests to

C02-induced climate change. *Nature* **1988**, *334*.

(10) Bellard, C.; Bertelsmeier, C.; Leadley, P.; Thuiller, W.; Courchamp, F. Impacts of climate change on the future of biodiversity. *Ecol Lett* **2012**, *15* (4), 365-377. DOI: 10.1111/j.1461-0248.2011.01736.x From NLM Medline.

(11) Calzadilla, A.; Rehdanz, K.; Betts, R.; Falloon, P.; Wiltshire, A.; Tol, R. S. J. Climate change impacts on global agriculture. *Climatic Change* **2013**, *120* (1-2), 357-374. DOI: 10.1007/s10584-013-0822-4.

(12) Doney, S. C.; Ruckelshaus, M.; Duffy, J. E.; Barry, J. P.; Chan, F.; English, C. A.; Galindo, H. M.; Grebmeier, J. M.; Hollowed, A. B.; Knowlton, N.; et al. Climate change impacts on marine ecosystems. *Ann Rev Mar Sci* **2012**, *4*, 11-37. DOI: 10.1146/annurev-marine-041911-111611 From NLM Medline.

(13) Tol, R. S. J. The Economic Impacts of Climate Change. *Review of Environmental Economics and Policy* **2018**, *12* (1), 4-25. DOI: 10.1093/reep/rex027.

(14) Bernicker, E.; Averbuch, S. D.; Edge, S.; Kamboj, J.; Khuri, F. R.; Pierce, J. Y.; Schiller, J.; Sirohi, B.; Thomas, A.; Moushey, A.; et al. Climate Change and Cancer Care: A Policy Statement From ASCO. *JCO Oncol Pract* **2024**, *20* (2), 178-186. DOI: 10.1200/OP.23.00637 From NLM Medline.

(15) Ramamoorthy, T.; Nath, A.; Singh, S.; Mathew, S.; Pant, A.; Sheela, S.; Kaur, G.; Sathishkumar, K.; Mathur, P. Assessing the Global Impact of Ambient Air Pollution on Cancer

Incidence and Mortality: A Comprehensive Meta-Analysis. *JCO Glob Oncol* **2024**, *10*, e2300427. DOI: 10.1200/GO.23.00427 From NLM Medline.

(16) Hadid, M.; Elomri, A.; El Mekkawy, T.; Kerbache, L.; El Omri, A.; El Omri, H.; Taha, R. Y.; Hamad, A. A.; Al Thani, M. H. J. Bibliometric analysis of cancer care operations management: current status, developments, and future directions. *Health Care Manag Sci* **2022**, *25* (1), 166-185. DOI: 10.1007/s10729-021-09585-x From NLM Medline.

(17) Hiatt, R. A.; Beyeler, N. Cancer and climate change. *Lancet Oncol* **2020**, *21* (11), e519-e527. DOI: 10.1016/S1470-2045(20)30448-4 From NLM Medline.

(18) Parker, E. R. The influence of climate change on skin cancer incidence - A review of the evidence. *Int J Womens Dermatol* **2021**, *7* (1), 17-27. DOI: 10.1016/j.ijwd.2020.07.003 From NLM PubMed-not-MEDLINE.

(19) Yu, P.; Xu, R.; Yang, Z.; Ye, T.; Liu, Y.; Li, S.; Abramson, M. J.; Kimlin, M.; Guo, Y. Cancer and Ongoing Climate Change: Who Are the Most Affected? *ACS Environ Au* **2023**, *3* (1), 5-11. DOI: 10.1021/acsenvironau.2c00012 From NLM PubMed-not-MEDLINE.

(20) Turner, M. C.; Andersen, Z. J.; Baccarelli, A.; Diver, W. R.; Gapstur, S. M.; Pope, C. A., 3rd; Prada, D.; Samet, J.; Thurston, G.; Cohen, A. Outdoor air pollution and cancer: An overview of the current evidence and public health recommendations. *CA Cancer J Clin* **2020**. DOI: 10.3322/caac.21632 From NLM Publisher.

(21) Dimitrova, A.; Marois, G.; Kiesewetter, G.; K C, S.; Rafaj, P.; Tonne, C. Health impacts of fine particles under climate change mitigation, air quality control, and demographic change in India. *Environmental Research Letters* **2021**, *16* (5). DOI: 10.1088/1748-9326/abe5d5.

(22) Park, S.; Allen, R. J.; Lim, C. H. A likely increase in fine particulate matter and premature mortality under future climate change. *Air Quality, Atmosphere & Health* **2020**, *13* (2), 143-151. DOI: 10.1007/s11869-019-00785-7.

(23) Turner, M. C.; Krewski, D.; Diver, W. R.; Pope, C. A., 3rd; Burnett, R. T.; Jerrett, M.; Marshall, J. D.; Gapstur, S. M. Ambient Air Pollution and Cancer Mortality in the Cancer Prevention Study II. *Environ Health Perspect* **2017**, *125* (8), 087013. DOI: 10.1289/EHP1249 From NLM Medline.

(24) Miraglia, M.; Marvin, H. J.; Kleter, G. A.; Battilani, P.; Brera, C.; Coni, E.; Cubadda, F.; Croci, L.; De Santis, B.; Dekkers, S.; et al. Climate change and food safety: an emerging issue with special focus on Europe. *Food Chem Toxicol* **2009**, *47* (5), 1009-1021. DOI: 10.1016/j.fct.2009.02.005 From NLM Medline.

(25) Misiou, O.; Koutsoumanis, K. Climate change and its implications for food safety and spoilage. *Trends in Food Science & Technology* **2022**, *126*, 142-152. DOI: 10.1016/j.tifs.2021.03.031.

(26) Smith, B. A.; Ruthman, T.; Sparling, E.; Auld, H.; Comer, N.; Young, I.; Lammerding, A. M.; Fazil, A. A risk modeling framework to evaluate the impacts of climate change and adaptation on food and water safety. *Food Research International* **2015**, *68*, 78-85. DOI: 10.1016/j.foodres.2014.07.006.

(27) Mac Dowell, N.; Fennell, P. S.; Shah, N.; Maitland, G. C. The role of CO2 capture and utilization in mitigating climate change. *Nature Climate Change* **2017**, *7* (4), 243-249. DOI: 10.1038/nclimate3231.

(28) Yu, B.; Zou, B.; Hu, C.-W. Recent applications of polyoxometalates in CO2 capture and transformation. *Journal of CO2 Utilization* **2018**, *26*, 314-322. DOI: 10.1016/j.jcou.2018.05.021.

(29) Nocera, N. S. L. a. D. G. Powering the planet: Chemical challenges in solar

energy utilization. *Proc Natl Acad Sci U S A* **2006**, *103*, 15729 - 15735.

(30) Lemaire, O. N.; Wagner, T. All-in-One CO(2) Capture and Transformation: Lessons from Formylmethanofuran Dehydrogenases. *Acc Chem Res* **2024**, *57* (24), 3512-3523. DOI: 10.1021/acs.accounts.4c00623 From NLM Medline.

(31) Ma, H.; Liu, S.; Wang, H.; Li, G.; Zhao, K.; Cui, X.; Shi, F. In situ CO2 capture and transformation into cyclic carbonates using flue gas. *Green Chemistry* **2023**, *25* (6), 2293-2298. DOI: 10.1039/d2gc04757h.

(32) Wu, J.; Huang, Y.; Ye, W.; Li, Y. CO(2) Reduction: From the Electrochemical to Photochemical Approach. *Adv Sci (Weinh)* **2017**, *4* (11), 1700194. DOI: 10.1002/advs.201700194 From NLM PubMed-not-MEDLINE.

(33) Xu, S.; Carter, E. A. Theoretical Insights into Heterogeneous (Photo)electrochemical CO(2) Reduction. *Chem Rev* **2019**, *119* (11), 6631-6669. DOI: 10.1021/acs.chemrev.8b00481 From NLM PubMed-not-MEDLINE.

(34) Felsher, D. W. Cancer revoked: oncogenes as therapeutic targets. *Nat Rev Cancer* **2003**, *3* (5), 375-380. DOI: 10.1038/nrc1070 From NLM Medline.

(35) Kim, T. E.; Chang, J. E. Recent Studies in Photodynamic Therapy for Cancer Treatment: From Basic Research to Clinical Trials. *Pharmaceutics* **2023**, *15* (9). DOI: 10.3390/pharmaceutics15092257 From NLM PubMed-not-MEDLINE.

(36) Robertson, C. A.; Evans, D. H.; Abrahamse, H. Photodynamic therapy (PDT): a short review on cellular mechanisms and cancer research applications for PDT. *J Photochem Photobiol B* **2009**, *96* (1), 1-8. DOI: 10.1016/j.jphotobiol.2009.04.001 From NLM Medline.

(37) Grin, M.; Suvorov, N.; Ostroverkhov, P.; Pogorilyy, V.; Kirin, N.; Popov, A.; Sazonova, A.; Filonenko, E. Advantages of combined photodynamic therapy in the treatment of oncological diseases. *Biophys Rev* **2022**, *14* (4), 941-963. DOI: 10.1007/s12551-022-00962-6 From NLM PubMed-not-MEDLINE.

(38) Gupta, M.; Sahu, A.; Mukherjee, T.; Mohanty, S.; Das, P.; Nayak, N.; Kumari, S.; Singh, R. P.; Pattnaik, A. Divulging the potency of naturally derived photosensitizers in green PDT: an inclusive review Of mechanisms, advantages, and future prospects. *Photochem Photobiol Sci* **2025**, *24* (1), 191-214. DOI: 10.1007/s43630-024-00669-5 From NLM Medline.

(39) Taylor, E. L.; Brown, S. B. The advantages of aminolevulinic acid photodynamic therapy in dermatology. *J Dermatolog Treat* **2002**, *13 Suppl 1*, S3-11. DOI: 10.1080/095466302317414645 From NLM Medline.

(40) Mário J.F. Calvete, A. V. C. S., César A. Henriques, Sara M.A. Pinto and Mariette M. Pereira. Tetrapyrrolic Macrocycles: Potentialities in Medical Imaging Technologies. *Current Organic Synthesis* **2014**, *11*, 127-140.

(41) Martinez De Pinillos Bayona, A.; Mroz, P.; Thunshelle, C.; Hamblin, M. R. Design features for optimization of tetrapyrrole macrocycles as antimicrobial and anticancer photosensitizers. *Chem Biol Drug Des* **2017**, *89* (2), 192-206. DOI: 10.1111/cbdd.12792 From NLM Medline.

(42) Martynov, A. G.; Safonova, E. A.; Tsivadze, A. Y.; Gorbunova, Y. G. Functional molecular switches involving tetrapyrrolic macrocycles. *Coordination Chemistry Reviews* **2019**, *387*, 325-347. DOI: 10.1016/j.ccr.2019.02.004.

(43) Rossifanelli, A.; Antonini, E.; Caputo, A. Hemoglobin and Myoglobin. *Adv Protein Chem* **1964**, *19*, 73-222. DOI: 10.1016/s0065-3233(08)60189-8 From NLM Medline.

(44) Ivano Bertini, G. C., and Antonio Rosato. Cytochrome c: Occurrence and Functions. *Chem. Rev.* **2006**, *106*, 90−115.

(45) Ilia G. Denisov, T. M. M., Stephen G. Sligar, and Ilme Schlichting. Structure and Chemistry of Cytochrome P450. *Chem. Rev.* **2005**, *105*, 2253−2277.

(46) Vlasits, J.; Jakopitsch, C.; Bernroitner, M.; Zamocky, M.; Furtmuller, P. G.; Obinger, C. Mechanisms of catalase activity of heme peroxidases. *Arch Biochem Biophys* **2010**, *500* (1), 74-81. DOI: 10.1016/j.abb.2010.04.018 From NLM Medline.

(47) Bjorn, L. O.; Papageorgiou, G. C.; Blankenship, R. E.; Govindjee. A viewpoint: why chlorophyll a? *Photosynth Res* **2009**, *99* (2), 85-98. DOI: 10.1007/s11120-008-9395-x From NLM Medline.

(48) Passaris, I.; Van Gaelen, P.; Cornelissen, R.; Simoens, K.; Grauwels, D.; Vanhaecke, L.; Springael, D.; Smets, I. Cofactor F430 as a biomarker for methanogenic activity: application to an anaerobic bioreactor system. *Appl Microbiol Biotechnol* **2018**, *102* (3), 1191-1201. DOI: 10.1007/s00253-017-8681-y From NLM Medline.

(49) Kumar, S. W. R. a. M. Nickel-Containing Carbon Monoxide Dehydrogenase/Acetyl-CoA Synthase. *Chem. Rev.* **1996**, *96*, 2515−2539.

(50) Decker, H.; Hellmann, N.; Jaenicke, E.; Lieb, B.; Meissner, U.; Markl, J. Minireview: Recent progress in hemocyanin research. *Integr Comp Biol* **2007**, *47* (4), 631-644. DOI: 10.1093/icb/icm063 From NLM PubMed-not-MEDLINE.

(51) Auwarter, W.; Ecija, D.; Klappenberger, F.; Barth, J. V. Porphyrins at interfaces. *Nat Chem* **2015**, *7* (2), 105-120. DOI: 10.1038/nchem.2159 From NLM Medline.

(52) Mukhopadhyay, R. D.; Kim, Y.; Koo, J.; Kim, K. Porphyrin Boxes. *Acc Chem Res* **2018**, *51* (11), 2730-2738. DOI: 10.1021/acs.accounts.8b00302 From NLM PubMed-not-MEDLINE.

(53) Sakthitharan Shanmugathasan, C. E. a. R. W. B. Advances in Modern Synthetic Porphyrin Chemistry. *Tetrahedron* **2000**, *56*, 1025 - 1046.

(54) C. RIMINGTON, S. F. M. a. K. Porphin. *Spectrochimica Acta* **1957**, *12*, 65 - 77.

(55) Webb, L. E.; Fleischer, E. B. Crystal Structure of Porphine. *The Journal of Chemical Physics* **1965**, *43* (9), 3100-3111. DOI: 10.1063/1.1697283.

(56) Dolphin, T. P. W. a. D. *SOME PREPARATIONS AND PROPERTIES OF PORPHYRINS*; Plenum Press, 1985.

(57) P. J. Brothers, M. O. S. *Fundamentals of Porphyrin Chemistry: A 21st Century Approach*; Wiley, 2022.

(58) MOSS, G. P. NOMENCLATURE OF TETRAPYRROLES. *Pure & Appl. Chem.* **1986**, *59*, 779 - 832.

(59) SESSLER, J. L. Porphyrin analogues. *Journal of Porphyrins and Phthalocyanines* **2000**, *4*, 331 - 336.

(60) Hiroyuki Furuta, T. A., and Takuji Ogawa. "N-Confused Porphyrin": A New Isomer of Tetraphenylporphyrin. *J Am Chem Soc* **1994**, *116*, 767 - 768.

(61) Hiroyuki Furuta, T. I., Atsuhiro Osuka, Hirohisa Dejima, Hidenori Nakagawa, and Yuichi Ishikawa. NH Tautomerism of N-Confused Porphyrin. *J Am Chem Soc* **2001**, *123*, 6207 - 6208.

(62) Hiroyuki Furuta, T. I., Atsuhiro Osuka, and Takuji Ogawa. "N-Fused Porphyrin": A New Tetrapyrrolic Porphyrinoid with a Fused Tri-pentacyclic Ring. *J Am Chem Soc* **2000**, *122*, 5748 - 5757.

(63) Toganoh, M.; Furuta, H. N-Fused Porphyrin: A Maverick Member of the Porphyrin Family. *Chemistry Letters* **2019**, *48* (7), 615-622. DOI: 10.1246/cl.190250.

(64) Furuta, M. T. a. H. *Handbook of Porphyrin Science: 10 Synthesis and Metal Coordination of N-Confused and N-Fused Porphyrinoids*; 2010.

(65) Ikeda, S.; Toganoh, M.; Furuta, H. Synthesis, reactivity, and properties of N-fused porphyrin manganese(I) tricarbonyl complexes. *Inorg Chem* **2011**, *50* (13), 6029-6043. DOI: 10.1021/ic2000393 From NLM Medline.

(66) Osuka, A.; Saito, S. Expanded porphyrins and aromaticity. *Chem Commun (Camb)* **2011**, *47* (15), 4330-4339. DOI: 10.1039/c1cc10534e From NLM PubMed-not-MEDLINE.

(67) Broring, M. How should aromaticity be described in porphyrinoids? *Angew Chem Int Ed Engl* **2011**, *50* (11), 2436-2438. DOI: 10.1002/anie.201007442 From NLM PubMed-not-MEDLINE.

(68) Shin, J. Y.; Kim, K. S.; Yoon, M. C.; Lim, J. M.; Yoon, Z. S.; Osuka, A.; Kim, D. Aromaticity and photophysical properties of various topology-controlled expanded porphyrins. *Chem Soc Rev* **2010**, *39* (8), 2751-2767. DOI: 10.1039/b925417j From NLM PubMed-not-MEDLINE.

(69) Abraham, R. J.; Plant, J.; Bedford, G. R. The NMR spectra of porphyrins 20—proton and 13C characterization of porphyrin atropisomers. *Organic Magnetic Resonance* **2005**, *19* (4), 204-210. DOI: 10.1002/mrc.1270190409.

(70) Smith, K. M.; Goff, D. A.; Abraham, R. J. The NMR spectra of porphyrins. 27—proton NMR spectra of chlorophyll-a and pheophytin-a. *Organic Magnetic Resonance* **2005**, *22* (12), 779-783. DOI: 10.1002/mrc.1270221210.

(71) GOUTERMAN, M. Spectra of Porphyrins. *JOURNAL OF MOLECULAR SPECTROSCOPY* **1961**, *6*, 138 - 163.

(72) Albers, V. M.; Knorr, H. V. Spectroscopic Studies of the Simpler Porphyrins I. The Absorption Spectra of Porphin, ms-Methyl Porphin, ms-Ethyl Porphin, ms-Propyl Porphin and ms-Phenyl Porphin. *The Journal of Chemical Physics* **1936**, *4* (7), 422-425. DOI: 10.1063/1.1749873.

(73) R. BONNETT, D. J. M., A. HARRIMAN, E. J. LAND4, T. G. TRUSCO and U-J. WINFIE. PHOTOPHYSICAL PROPERTIES OF meso-TETRAPHENYLPORPHYRIN AND SOME meso-TETRA(HYDR0XYPHENYL)PORPHYRIN. *Photochem Photobiol Sci* **1988**, *48*, 271 - 276.

(74) Dadeko, A. V.; Murav'eva, T. D.; Starodubtsev, A. M.; Gorelov, S. I.; Dobrun, M. V.; Kris'ko, T. K.; Bagrov, I. V.; Belousova, I. M.; Ponomarev, G. V. Photophysical properties of porphyrin photosensitizers. *Optics and Spectroscopy* **2015**, *119* (4), 633-637. DOI: 10.1134/s0030400x15100094.

(75) Giovanelli, L.; Lee, H. L.; Lacaze-Dufaure, C.; Koudia, M.; Clair, S.; Lin, Y. P.; Ksari, Y.; Themlin, J. M.; Abel, M.; Cafolla, A. A. Electronic structure of tetra(4-aminophenyl)porphyrin studied by photoemission, UV–Vis spectroscopy and density functional theory. *Journal of Electron Spectroscopy and Related Phenomena* **2017**, *218*, 40-45. DOI: 10.1016/j.elspec.2017.05.005.

(76) Fleischer, E. B. The Structure of Porphyrins and Metalloporphyrins. **1969**.

(77) Magdalena Biesaga, K. P. s., Marek Trojanowicz Porphyrins in analytical chemistry. A review. *Talanta* **2000**, *51*, 209 - 224.

(78) BUCHLER, J. W. Coordination chemistry of metal tetrapyrrole complexes— unusual geometries and stoichiometries. *Journal of Porphyrins and Phthalocyanines* **2000**, *4*, 337 - 339.

(79) Treibs, A. [Metal complexes of porphyrins]. *Justus Liebigs Ann Chem* **1969**, *728*, 115-148. DOI: 10.1002/jlac.19697280115 From NLM Medline.

(80) Bulach, V.; Sguerra, F.; Hosseini, M. W. Porphyrin lanthanide complexes for NIR emission. *Coordination Chemistry Reviews* **2012**, *256* (15-16), 1468-1478. DOI: 10.1016/j.ccr.2012.02.027.

(81) Hoffmann, K. T. a. R. Metalloporphyrins with Unusual Geometries. 1. Mono-, Di-, Triatom-Bridged Porphyrin Dimers. *J Am Chem Soc* **1980**, *81*.

(82) Barbe, J. M.; Burdet, F.; Espinosa, E.; Guilard, R. Synthesis and Physicochemical Characterization of Bis(macrocycles) Involving a Porphyrin and a meso-Substituted Corrole – X-ray Crystal Structure of a [(Free-base porphyrin)–corrole]bis(pyridine)cobalt Complex. *European Journal of Inorganic Chemistry* **2005**, *2005* (6), 1032-1041. DOI: 10.1002/ejic.200400756.

(83) Moreno-Pineda, E.; Klyatskaya, S.; Du, P.; Damjanovic, M.; Taran, G.; Wernsdorfer, W.; Ruben, M. Observation of Cooperative Electronic Quantum Tunneling: Increasing Accessible Nuclear States in a Molecular Qudit. *Inorg Chem* **2018**, *57* (16), 9873-9879. DOI: 10.1021/acs.inorgchem.8b00823 From NLM PubMed-not-MEDLINE.

(84) Hiroyuki Furuta, T. I., Atsuhiro Osuka, Hirohisa Dejima, Hidenori Nakagawa, and Yuichi Ishikawa. NH Tautomerism of N-Confused Porphyrin. *J Am Chem Soc* **2001**, *123*, 6207-6208.

(85) Ishizuka, T.; Sakashita, R.; Iwanaga, O.; Morimoto, T.; Mori, S.; Ishida, M.; Toganoh, M.; Takegoshi, K.; Osuka, A.; Furuta, H. NH Tautomerism of N-Confused Porphyrin: Solvent/Substituent Effects and Isomerization Mechanism. *J Phys Chem A* **2020**, *124* (28), 5756-5769. DOI: 10.1021/acs.jpca.0c04779 From NLM PubMed-not-MEDLINE.

(86) Anna Młodzianowska, L. L.-G. y. s., Ludmiła Szterenberg, and Marcin Ste¸pien´. Single-Boron Complexes of N-Confused and N-Fused Porphyrins. *Inorg Chem* **2007**, *46*, 6950−6957.

(87) Pal, N.; Singha, D.; Mukherjee, A. K. Review on N-confused porphyrin. *International Journal of Experimental Research and Review* **2022**, *29*, 55-66. DOI: 10.52756/ijerr.2022.v29.006.

(88) Hiromitsu Maeda, A. O., Yuichi Ishikawa, Isao Aritome, Yoshio Hisaeda, and Hiroyuki Furuta. N-Confused Porphyrin-Bearing meso-Perfluorophenyl Groups: A Potential Agent That Forms Stable Square-Planar Complexes with Cu(II) and Ag(III). *Organic Letters* **2003**, *5*, 1293-1296.

(89) Alagar Srinivasan, M. T., Teppei Niino, Atsuhiro Osuka, and Hiroyuki Furuta. Synthesis of N-Confused Tetraphenylporphyrin Rhodium Complexes Having Versatile Metal Oxidation States. *Inorg Chem* **2008**, *47*, 11305-11313.

(90) Boggavarapu Kiran, M. T. N. Density functional studies on N-fused porphyrin. Electronic, magnetic and metal binding properties. *Journal of Organometallic Chemistry* **2002**, 265 - 271.

(91) Ou, Z.; Chen, X.; Ye, L.; Xue, S.; Fang, Y.; Jiang, X.; Kadish, K. M. N-confusedmeso-tetraaryl-substituted free-base porphyrins: determination of protonation and deprotonation constants in nonaqueous media. *Journal of Porphyrins and Phthalocyanines* **2015**, *19* (01-03), 251-260. DOI: 10.1142/s1088424614501132.

(92) Toganoh, M.; Matsuo, H.; Sato, A.; Furuta, H. Ruthenocene-Type Complexes of N-Fused Porphyrins. *Chemistry* **2016**, *22* (24), 8316-8322. DOI: 10.1002/chem.201600813 From NLM Medline.

(93) Touden, S.; Ikawa, Y.; Sakashita, R.; Toganoh, M.; Mori, S.; Furuta, H. Sulfur-assisted interconversion between N-confused porphyrin and N-fused porphyrin. *Tetrahedron Letters* **2012**, *53* (45), 6071-6074. DOI: 10.1016/j.tetlet.2012.08.131.

(94) Lee, J. S.; Lim, J. M.; Toganoh, M.; Furuta, H.; Kim, D. Comparative spectroscopic studies on porphyrin derivatives: electronic perturbation of N-confused and N-fused porphyrins. *Chem Commun (Camb)* **2010**, *46* (2), 285-287. DOI: 10.1039/b916521e From NLM Medline.

(95) Willstätter, S., Küster. *Physiology. Chem.* **1912**.

(96) H. Fischer, K. Z. *Ann. Chem. Ber. Dtsch. Chem.* **1929**.

(97) Rothemund, P. Formation of Porpyhrins from Pyrroles and Aldehydes. *J Am Chem Soc* **1935**.

(98) Rothemund, P. A New Porphyrin Synthesis. The Synthesis of Porphin. *J Am Chem Soc* **1936**.

(99) Menotti, P. R. a. A. R. Porphyrin Studies. IV.1 The Synthesis of a,0,7,5-Tetraphenylporphine. *J Am Chem Soc* **1941**. DOI: 10.1021/ja01846a065,.

(100) Alan D. Adler, F. R. L., and William Shergalis. Mechanistic Investigations of Porphyrin Syntheses. Preliminary Studies on ms-Tetraphenylporphin. **1964**.

(101) Jonathan S. Lindsey, I. C. S., Henry C. Hsu, Patrick C. Kearney, and Anne M. Marguerettaz. Rothemund and Adler-Longo Reactions Revisited: Synthesis of Tetraphenylporphyrins under Equilibrium Conditions. *J. Org. Chem.* **1987**, *52*, 827-836.

(102) Fazekas, M.; Pintea, M.; Senge, M. O.; Zawadzka, M. Synthetic strategies and porphyrin building blocks for unsymmetrical multichromophores. *Tetrahedron Letters* **2008**, *49* (14), 2236-2239. DOI: 10.1016/j.tetlet.2008.02.029.

(103) Polisetti Dharma Rao, S. D., Benjamin J. Littler, and Jonathan S. Lindsey. Rational Syntheses of Porphyrins Bearing up to Four Different Meso Substituents. *J. Org. Chem.* **2000**, *65*, 7323-7344.

(104) Senge, M. O. Nucleophilic Substitution as a Tool for the Synthesis of Unsymmetrical Porphyrins. *Acc. Chem. Res.* **2005**, *38*, 733-743.

(105) Liu, D.-C.; Zhong, D.-C.; Lu, T.-B. Non-noble metal-based molecular complexes for CO2 reduction: From the ligand design perspective. *EnergyChem* **2020**, *2* (3). DOI: 10.1016/j.enchem.2020.100034.

(106) Fujita, E. Photochemical carbon dioxide reduction with metal complexes. *Coordination Chemistry Reviews* **1999**.

(107) Ting, L. R. L.; Yeo, B. S. Recent advances in understanding mechanisms for the electrochemical reduction of carbon dioxide. *Current Opinion in Electrochemistry* **2018**, *8*, 126-134. DOI: 10.1016/j.coelec.2018.04.011.

(108) Ali, S. A.; Sadiq, I.; Ahmad, T. Deep insight of CO2 reduction reaction mechanism through experimental and theoretical anticipations. *Materials Today Sustainability* **2023**, *24*. DOI: 10.1016/j.mtsust.2023.100587.

(109) Chen, J. Y.; Li, M.; Liao, R. Z. Mechanistic Insights into Photochemical CO(2) Reduction to CH(4) by a Molecular Iron-Porphyrin Catalyst. *Inorg Chem* **2023**, *62* (24), 9400-9417. DOI: 10.1021/acs.inorgchem.3c00402 From NLM PubMed-not-MEDLINE.

(110) Kuramochi, Y.; Ishitani, O.; Ishida, H. Reaction mechanisms of catalytic photochemical CO2 reduction using Re(I) and Ru(II) complexes. *Coordination Chemistry Reviews* **2018**, *373*, 333-356. DOI: 10.1016/j.ccr.2017.11.023.

(111) Thomas J. Dougherty, C. J. G., Barbara W. Henderson, Giulio Jori, David Kessel, Mladen Korbelik, Johan Moan, Qian Peng. Photodynamic Therapy. *Journal of the National Cancer Institute* **1998**, *90*, 889 - 905.

(112) Dos Santos, A. l. F.; De Almeida, D. R. Q.; Terra, L. F.; Baptista, M. c. S.; Labriola, L. Photodynamic therapy in cancer treatment - an update review. *Journal of Cancer Metastasis and Treatment* **2019**, *2019*. DOI: 10.20517/2394-4722.2018.83.

(113) Silva, E. F.; Serpa, C.; Dabrowski, J. M.; Monteiro, C. J.; Formosinho, S. J.; Stochel, G.; Urbanska, K.; Simoes, S.; Pereira, M. M.; Arnaut, L. G. Mechanisms of singlet-oxygen and superoxide-ion generation by porphyrins and bacteriochlorins and their implications in photodynamic therapy. *Chemistry* **2010**, *16* (30), 9273-9286. DOI: 10.1002/chem.201000111 From NLM Medline.

(114) Algorri, J. F.; Ochoa, M.; Roldan-Varona, P.; Rodriguez-Cobo, L.; Lopez-Higuera, J. M. Photodynamic Therapy: A Compendium of Latest Reviews. *Cancers (Basel)* **2021**, *13* (17). DOI: 10.3390/cancers13174447 From NLM PubMed-not-MEDLINE.

(115) Niculescu, A.-G.; Grumezescu, A. M. Photodynamic Therapy—An Up-to-Date Review. *Applied Sciences* **2021**, *11* (8). DOI: 10.3390/app11083626.

(116) Pass, H. I. Photodynamic Therapy in Oncology: Mechanisms and Clinical Use. *Journal of the National Cancer Institute* **1993**, *85*, 443-456.

(117) Ravindra K. Pandey, K. M. S., and Thomas J. Dougherty. Porphyrin Dimers as Photosensitizers in Photodynamic Therapy. *J. Med. Chem.* **1990**, *33*, 2032-2038.

(118) K. W. Wood Burn, N. J. V., J. S. Hill, A. H. Kaye, J. A. Reiss and D. R. Phillips. Evaluation of Porphyrin Characteristics Required for Photodynamic Therapy. *Photochemistry and Photobiology* **1992**, *55*, 697-704.

(119) Baskaran, R.; Lee, J.; Yang, S. G. Clinical development of photodynamic agents and therapeutic applications. *Biomater Res* **2018**, *22*, 25. DOI: 10.1186/s40824-018-0140-z From NLM PubMed-not-MEDLINE.

(120) Deng, J.; Li, H.; Yang, M.; Wu, F. Palladium porphyrin complexes for photodynamic cancer therapy: effect of porphyrin units and metal. *Photochem Photobiol Sci* **2020**, *19* (7), 905-912. DOI: 10.1039/c9pp00363k.

(121) Forson, M.; Bashiru, M.; Macchi, S.; Singh, S.; Anderson, A. D.; Sayyed, S.; Ishtiaq, A.; Griffin, R.; Ali, N.; Oyelere, A. K.; et al. Cationic Porphyrin-Based Ionic Nanomedicines for Improved Photodynamic Therapy. *ACS Appl Bio Mater* **2023**, *6* (12), 5662-5675. DOI: 10.1021/acsabm.3c00809 From NLM Medline.

(122) McCormick, B. P. P.; Pansa, M. F.; Sanabria, L. N. M.; Carvalho, C. M. B.; Faustino, M. A. F.; Neves, M. G. P. M. S.; Cavaleiro, J. A. S.; Vittar, N. B. R.; Rivarola, V. A. Cationic porphyrin derivatives for application in photodynamic therapy of cancer. *Laser Physics* **2014**, *24* (4). DOI: 10.1088/1054-660x/24/4/045603.

(123) Jiayuan Kou, D. D. a. L. Y. Porphyrin photosensitizers in photodynamic therapy and its applications. *Oncotarget* **2017**, *8*, 81591-81603.

(124) Karges, J. Clinical Development of Metal Complexes as Photosensitizers for Photodynamic Therapy of Cancer. *Angew Chem Int Ed Engl* **2022**, *61* (5), e202112236. DOI: 10.1002/anie.202112236 From NLM Medline.

(125) Klein Couto, G.; Rodrigues, J. C. J.; Pacheco, B. S.; Dame Simoes, L.; Paschoal, J. D.; Seixas, F. K.; Acunha, T. V.; Iglesias, B. A.; Collares, T. Zinc(II), copper(II) and nickel(II) ions improve the selectivity of tetra-cationic platinum(II) porphyrins in photodynamic therapy and stimulate antioxidant defenses in the metastatic melanoma lineage (A375). *Photodiagnosis Photodyn Ther* **2020**, *31*, 101942. DOI: 10.1016/j.pdpdt.2020.101942 From NLM Medline.

(126) Rees, T. W.; Ho, P. Y.; Hess, J. Recent Advances in Metal Complexes for Antimicrobial Photodynamic Therapy. *Chembiochem* **2023**, *24* (16), e202200796. DOI: 10.1002/cbic.202200796 From NLM Medline.

(127) Schissler, C.; Schneider, E. K.; Felker, B.; Weis, P.; Nieger, M.; Kappes, M. M.; Brase, S. A Synthetic Strategy for Cofacial Porphyrin-Based Homo- and Heterobimetallic Complexes. *Chemistry* **2021**, *27* (9), 3047-3054. DOI: 10.1002/chem.202002394.

(128) Schissler, C.; Schneider, E. K.; Lebedkin, S.; Weis, P.; Niedner-Schatteburg, G.; Kappes, M. M.; Brase, S. Novel Cofacial Porphyrin-Based Homo- and Heterotrimetallic Complexes of Transition Metals. *Chemistry* **2021**, *27* (61), 15201-15207.

(129) Holger Dobbek, V. S., Lothar Gremer, Robert Huber, Ortwin Meyer. Crystal Structure of a Carbon Monoxide Dehydrogenase Reveals a [Ni-4Fe-5S] Cluster. *Science* **2001**, *293*, 1281-1285.

(130) Buchwald, K. B. a. S. L. Highly Efficient Monophosphine-Based Catalyst for the Palladium-Catalyzed Suzuki-Miyaura Reaction of Heteroaryl Halides and Heteroaryl Boronic Acids and Esters. *J Am Chem Soc* **2007**, *129*, 3358-3366.

(131) Li, P.; Zhao, C.; Smith, M. D.; Shimizu, K. D. Comprehensive experimental study of N-heterocyclic pi-stacking interactions of neutral and cationic pyridines. *J Org Chem* **2013**, *78* (11), 5303-5313. DOI: 10.1021/jo400370e From NLM Medline.

(132) Liang, F. G. a. W. Z. Vibrationally Resolved Absorption and Emission Spectra of Rubrene Multichromophores: Temperature and Aggregation Effects. *J Phys Chem A* **2009**, *113*, 12847–12856.

(133) Paavo H. Hynninen, a. S. L. Effects of π–π interactions on the 1H-NMR spectra and solution structures of pheophytin a and a' dimers. *Biochemica et Biophysica Acta* **1993**, 374-380.

(134) G. Richard Geier III, D. M. H., and Jonathan S. Lindsey. An Efficient One-Flask Synthesis of N-Confused Tetraphenylporphyrin. *J Am Chem Soc* **1999**, *1*, 1455-1458.

(135) H. E. Revercomb, a. E. A. M. Theory of Plasma Chromatography/Gaseous Electrophoresis — A Review. *Anal Chem* **1975**, *47*, 970-983.

(136) Stow, S. M.; Causon, T. J.; Zheng, X.; Kurulugama, R. T.; Mairinger, T.; May, J. C.; Rennie, E. E.; Baker, E. S.; Smith, R. D.; McLean, J. A.; et al. An Interlaboratory Evaluation of Drift Tube Ion Mobility-Mass Spectrometry Collision Cross Section Measurements. *Anal Chem* **2017**, *89* (17), 9048-9055. DOI: 10.1021/acs.analchem.7b01729 From NLM Medline.

(137) Nakul C. Maiti, S. M., and N. Periasamy. J- and H-Aggregates of Porphyrin-Surfactant Complexes: Time-Resolved Fluorescence and Other Spectroscopic Studies. *J Phys Chem B* **1998**, *102*, 1528-1538.

(138) Poyer, S.; Comby-Zerbino, C.; Choi, C. M.; MacAleese, L.; Deo, C.; Bogliotti, N.; Xie, J.; Salpin, J. Y.; Dugourd, P.; Chirot, F. Conformational Dynamics in Ion Mobility Data. *Anal Chem* **2017**, *89* (7), 4230-4237. DOI: 10.1021/acs.analchem.7b00281 From NLM PubMed-not-MEDLINE.

(139) Reinhart Ahlrichs Michael Bär, M. H., Hans Horn and Christoph Kölmel. Electronic Structure Calculations on Workstation Computers: The Program System Trubomole. *Chemical Physics Letters* **1989**, *162*.

(140) Mohamed, E. A.; Zahran, Z. N.; Naruta, Y. Efficient electrocatalytic CO2 reduction with a molecular cofacial iron porphyrin dimer. *Chem Commun (Camb)* **2015**, *51* (95), 16900-16903. DOI: 10.1039/c5cc04273a From NLM PubMed-not-MEDLINE.

(141) Zahran, Z. N.; Mohamed, E. A.; Naruta, Y. Bio-inspired cofacial Fe porphyrin dimers for efficient electrocatalytic CO2 to CO conversion: Overpotential tuning by substituents at the porphyrin rings. *Sci Rep* **2016**, *6*, 24533. DOI: 10.1038/srep24533 From NLM PubMed-not-MEDLINE.

(142) Mohamed, E. A.; Zahran, Z. N.; Naruta, Y. Efficient Heterogeneous CO2 to CO Conversion with a Phosphonic Acid Fabricated Cofacial Iron Porphyrin Dimer. *Chemistry of Materials* **2017**, *29* (17), 7140-7150. DOI: 10.1021/acs.chemmater.7b01115.

(143) Zhang, C.; Gotico, P.; Guillot, R.; Dragoe, D.; Leibl, W.; Halime, Z.; Aukauloo, A. Bio-Inspired Bimetallic Cooperativity Through a Hydrogen Bonding Spacer in CO(2) Reduction. *Angew Chem Int Ed Engl* **2023**, *62* (8), e202214665. DOI: 10.1002/anie.202214665.

(144) Xiao, Y.; Zhang, H. T.; Zhang, M. T. Heterobimetallic NiFe Complex for Photocatalytic CO(2) Reduction: United Efforts of NiFe Dual Sites. *J Am Chem Soc* **2024**, *146* (42), 28832-28844. DOI: 10.1021/jacs.4c08510 From NLM PubMed-not-MEDLINE.

(145) James P. Coliman, C. S. B., Craig E. Barnes, and Bryan D. Miller. Two New Members of the Dimeric ß-Linked Face-to-Face Porphyrin Family: FTF4 and FTF3. *J Am Chem Soc* **1983**, *105*, 2704-2710.

(146) James P. Coliman, P. D., Yutaka Konai, Matt Marrocco, Carl Koval, and Fred C. Anson. Electrode Catalysis of the Four-Electron Reduction of Oxygen to Water by Dicobalt Face-to-Face Porphyrins. *J Am Chem Soc* **1980**, *102*, 6027-6036.

(147) John T. Landrum, D. G., Kenneth J. Haller, W. Robert Scheldt, and Christopher A. Reed. Imidazolate- and Oxo-Bridged Metalloporphyrins. *J Am Chem Soc* **1981**, *103*, 2640-2650.

(148) J. P. Fillers, K. G. R., I. Abdalmuhdi, A. Tulinsky, and C. K. Chang. Crystal and Molecular Structure of Anthracene and Biphenylene Pillared Cofacial Diporphyrins. *J Am Chem Soc* **1986**, *108*, 417-424.

(149) Abdalmuhdi, C. K. C. a. I. Anthracene Pillared Cofacial Diporphyrin. *J Am Chem Soc* **1983**, *48*, 5388-5390.

(150) Yongqi Deng, C. J. C., and Daniel G. Nocera. Direct Observation of the "Pac-Man" Effect from Dibenzofuran-Bridged Cofacial Bisporphyrins. *J Am Chem Soc* **2000**, *122*, 410-411.

(151) Christopher J. Chang, Y. D., Alan F. Heyduk, C. K. Chang, and Daniel G. Nocera. Xanthene-Bridged Cofacial Bisporphyrins. *J Am Chem Soc* **2000**, *39*, 959-966.

(152) Meier, H., Kobuke, Y. Chromophoric interactions of an" ortho-gable-porphyrin". A novel tetraphenylporphyrin dimer *Chem. Soc.* **1989**, 923-924.

(153) Osuka, A.; Nakajima, S.; Nagata, T.; Maruyama, K.; Toriumi, K. A 1,2-Phenylene-Bridged Porphyrin Dimer—Synthesis, Properties, and Molecular Structure. *Angewandte Chemie International Edition in English* **2003**, *30* (5), 582-584. DOI: 10.1002/anie.199105821.

(154) Bruno, N. Cross-Coupling Reaction Manual: Desk Reference. Merck, Ed.; 2017.

(155) R. Martin, S. L. B. Palladium-Catalyzed Suzuki-Miyaura CrossCoupling Reactions Employing Dialkylbiaryl Phosphine Ligands. *Accounts of Chemical Research* **2008**, *41*, 1461-1473.

(156) Adriana I. Moncada, S. M., Joseph M. Tanski, and LeGrande M. Slaughter. Modular Chelated Palladium Diaminocarbene Complexes: Synthesis, Characterization, and Optimization of Catalytic

Suzuki-Miyaura Cross-Coupling Activity by Ligand Modification. *Organometallics* **2006**, *25*, 491-505.

(157) Banerjee, S.; Karunananda, M. K.; Bagherzadeh, S.; Jayarathne, U.; Parmelee, S. R.; Waldhart, G. W.; Mankad, N. P. Synthesis and characterization of heterobimetallic complexes with direct Cu-M bonds (M = Cr, Mn, Co, Mo, Ru, W) supported by N-heterocyclic carbene ligands: a toolkit for catalytic reaction discovery. *Inorg Chem* **2014**, *53* (20), 11307-11315. DOI: 10.1021/ic5019778 From NLM PubMed-not-MEDLINE.

(158) Lee, J. L.; Oswald, V. F.; Biswas, S.; Hill, E. A.; Ziller, J. W.; Hendrich, M. P.; Borovik, A. S. Stepwise assembly of heterobimetallic complexes: synthesis, structure, and physical properties. *Dalton Trans* **2021**, *50* (23), 8111-8119. DOI: 10.1039/d1dt01021b From NLM Medline.

(159) Termühlen, S.; Wilm, L. F. B.; Dutschke, P. D.; Hepp, A.; Hahn, F. E. Synthesis of Heterobimetallic Complexes through Chemoselective 2,4-Metalation of a Thiazolium Salt. *Organometallics* **2021**, *40* (11), 1565-1570. DOI: 10.1021/acs.organomet.1c00243.

(160) Kim, Y. H.; Sun, Y. Y.; Choi, W. I.; Kang, J.; Zhang, S. B. Enhanced dihydrogen adsorption in symmetry-lowered metal-porphyrin-containing frameworks. *Phys Chem Chem Phys* **2009**, *11* (48), 11400-11403. DOI: 10.1039/b913711d From NLM Medline.

(161) W. Ding, A. B., J. Gussone, T. Bauer. Cyclic Voltammetry for Monitoring Corrosive Impurities in Molten Chlorides for Thermal Energy Storage. *Energy Procedia* **2017**, *135*, 82-91.

(162) Huang, X.; Wang, Z.; Knibbe, R.; Luo, B.; Ahad, S. A.; Sun, D.; Wang, L. Cyclic Voltammetry in Lithium–Sulfur Batteries—Challenges and Opportunities. *Energy Technology* **2019**, *7* (8). DOI: 10.1002/ente.201801001.

(163) López Zavala, M. Á.; González Peña, O. I.; Cabral Ruelas, H.; Delgado Mena, C.; Guizani, M. Use of Cyclic Voltammetry to Describe the Electrochemical Behavior of a Dual-Chamber Microbial Fuel Cell. *Energies* **2019**, *12* (18). DOI: 10.3390/en12183532.

(164) Elgrishi, N.; Rountree, K. J.; McCarthy, B. D.; Rountree, E. S.; Eisenhart, T. T.; Dempsey, J. L. A Practical Beginner's Guide to Cyclic Voltammetry. *Journal of Chemical Education* **2017**, *95* (2), 197-206. DOI: 10.1021/acs.jchemed.7b00361.

(165) Takeda, H.; Irimajiri, M.; Mizutani, T.; Nozawa, S.; Matsuura, Y.; Kurosu, M.; Ishitani, O. Photocatalytic CO(2) Reduction Using Mixed Catalytic Systems Comprising an Iron Cation with Bulky Phenanthroline Ligands. *Inorg Chem* **2024**, *63* (16), 7343-7355. DOI: 10.1021/acs.inorgchem.4c00247 From NLM PubMed-not-MEDLINE.

(166) Wakabayashi, T.; Kamada, K.; Sekizawa, K.; Sato, S.; Morikawa, T.; Jung, J.; Saito, S. Photocatalytic CO2 Reduction Using an Iron–Bipyridyl Complex Supported by Two Phosphines for Improving Catalyst Durability. *Organometallics* **2022**, *41* (14), 1865-1871. DOI: 10.1021/acs.organomet.2c00171.

(167) Yamazaki, Y.; Takeda, H.; Ishitani, O. Photocatalytic reduction of CO2 using metal complexes. *Journal of Photochemistry and Photobiology C: Photochemistry Reviews* **2015**, *25*, 106-137. DOI: 10.1016/j.jphotochemrev.2015.09.001.

(168) Marx, M.; Mele, A.; Spannenberg, A.; Steinlechner, C.; Junge, H.; Schollhammer, P.; Beller, M. Addressing the Reproducibility of Photocatalytic Carbon Dioxide Reduction. *ChemCatChem* **2019**, *12* (6), 1603-1608. DOI: 10.1002/cctc.201901686.

(169) Manafe, S. Y.; Le, N.; Lambert, E. C.; Curiac, C.; Nugegoda, D.; Das, S.; Hunt, L. A.; Qu, F.; Whitt, L. M.; Fedin, I.; et al. Sensitized and Self-Sensitized Photocatalytic CO2 Reduction to HCO2– and CO under Visible Light with Ni(II) CNC-Pincer Catalysts. *ACS Catalysis* **2024**, *14* (9), 6589-6602. DOI: 10.1021/acscatal.3c03787.

(170) Ethirajan, M.; Chen, Y.; Joshi, P.; Pandey, R. K. The role of porphyrin chemistry in tumor imaging and photodynamic therapy. *Chem Soc Rev* **2011**, *40* (1), 340-362. DOI: 10.1039/b915149b.

(171) Park, J. M.; Hong, K. I.; Lee, H.; Jang, W. D. Bioinspired Applications of Porphyrin Derivatives. *Acc Chem Res* **2021**, *54* (9), 2249-2260. DOI: 10.1021/acs.accounts.1c00114.

(172) Xue, X.; Lindstrom, A.; Li, Y. Porphyrin-Based Nanomedicines for Cancer Treatment. *Bioconjug Chem* **2019**, *30* (6), 1585-1603. DOI: 10.1021/acs.bioconjchem.9b00231.

(173) Zhang, J.; Xu, X.; Wei, H.; Wu, D.; Zeng, L. Pt/Pd dual-modified porphyrin metal-organic frameworks for NIR-II photothermal-enhanced photodynamic/catalytic therapy. *J Colloid Interface Sci* **2025**, *678* (Pt A), 42-52. DOI: 10.1016/j.jcis.2024.08.154 From NLM Medline.

(174) Makoto Obata, S. H., Rika Tanaka, Isamu Kinoshita, Kei Ohkubo, Shunichi Fukuzumi, Masao Tanihara, and Shigenobu Yano. In Vitro Heavy-Atom Effect of Palladium(II) and Platinum(II) Complexes of Pyrrolidine-Fused Chlorin in Photodynamic Therapy. *J. Med. Chem.* **2009**, *52*, 2747–2753.

(175) Pinto, S. C.; Acunha, T. V.; Santurio, J. M.; Denardi, L. B.; Iglesias, B. A. Investigation of powerful fungicidal activity of tetra-cationic platinum(II) and palladium(II) porphyrins by antimicrobial photodynamic therapy assays. *Photodiagnosis Photodyn Ther* **2021**, *36*, 102550. DOI: 10.1016/j.pdpdt.2021.102550 From NLM Medline.

(176) Rao, K. U.; Appa, R. M.; Lakshmidevi, J.; Vijitha, R.; Rao, K. S. V. K.; Narasimhulu, M.; Venkateswarlu, K. C(sp2)–C(sp2) Coupling in Water: Palladium(II) Complexes of N-Pincer Tetradentate Porphyrins as Effective Catalysts. *Asian Journal of Organic Chemistry* **2017**, *6* (6), 751-757. DOI: 10.1002/ajoc.201700068.

(177) Shrotriya, V.; Ouyang, J.; Tseng, R. J.; Li, G.; Yang, Y. Absorption spectra modification in poly(3-hexylthiophene):methanofullerene blend thin films. *Chemical Physics Letters* **2005**, *411* (1-3), 138-143. DOI: 10.1016/j.cplett.2005.06.027.

(178) Wu, H.; Du, L.; Luo, J.; Wang, Z.; Phillips, D. L.; Qin, A.; Tang, B. Z. Structural modification on tetraphenylpyrazine: from polarity enhanced emission to polarity quenching emission and its intramolecular charge transfer mechanism. *Journal of Materials Chemistry C* **2022**, *10* (21), 8174-8180. DOI: 10.1039/d2tc01142e.

(179) Schwetlick, K. *Organikum*; Wiley-VCH, 2015.

(180) H.E.Gottlieb, V. K., A. Nudelman. NMR Chemical Shifts of Common Laboratory Solvents as Trace Impurities. *J. Org. Chem.* **1977**, *43*, 7512 - 7515.

(181) Haldar, R.; Batra, K.; Marschner, S. M.; Kuc, A. B.; Zahn, S.; Fischer, R. A.; Brase, S.; Heine, T.; Woll, C. Bridging the Green Gap: Metal-Organic Framework Heteromultilayers Assembled from Porphyrinic Linkers Identified by Using Computational Screening. *Chemistry* **2019**, *25* (33), 7847-7851.

(182) Götz, D. C.; Bruhn, T.; Senge, M. O.; Bringmann, G. Synthesis and stereochemistry of highly unsymmetric β, meso-linked porphyrin arrays. *J. Org. Chem.* **2009**, *74* (21), 8005-8020.

(183) Schissler, C.; Schneider, E. K.; Rotter, M.; Notter, S.; Geier, C.; Weis, P.; Kappes, M. M.; Bräse, S. Marriage of an N-Fused and a Regular Porphyrin in a Cofacial Ligand System. *Organometallics* **2023**, *42* (15), 1882-1889.

6.4 Acknowledgements

First, I would like to thank my doctoral supervisor, Prof. Dr. Stefan Bräse for the support, trust and freedom granted in the context of the preparation of this work. Your guidance opened the door to countless scientific explorations and made it possible to pursue various chemical adventures. Thank you sincerely for supervising my doctoral thesis and for the many years of collaboration.

I would also like to express my heartfelt thanks to Prof. Dr. Claudia Bizzarri, who introduced and guided me through all aspects of analyzing, characterizing, and developing new compounds for the photochemical reduction of carbon dioxide. Your expertise and continuous feedback were invaluable, and I truly cannot imagine having written this thesis without your support. I am deeply grateful for everything.

A special thank is dedicated to Prof. Dr. Manfred Kappes and Dr. Patrick Weis. Their constant support and expertise in tackling analytical challenges, especially with measurements beyond the capabilities of our institute, were indispensable. Without their contribution, these results of this work would not have been possible.

I also want to thank Lisa Wanner and Silas Leidenheimer. Thank you for working alongside me in the laboratory during your third-year traineeships. Your consistent help and support were incredibly helpful. I truly could not have completed everything on time without you. I feel fortunate to have had the opportunity to supervise both of you and to always rely on your dedication.

I thank Ahmet Acan, Andreas Bischoff, Hannah Schroeder, Maximilian Mörtl, Rebecca Margarit-Puri, and Sophia Raubach, who chose to write their theses supervised by me. Also, Brett Boyle, Mitchell Walsh, and Corinn Richards for helping me and my laboratory work in their international internship.